

# IN-situ Debris Inventorisation near the Geostationary Orbit (INDIGO): a feasibility study

Ishita Sinha

Delft University of Technology





# IN-situ Debris Inventorisation near the Geostationary Orbit (INDIGO): a feasibility study

by

Ishita Sinha

to obtain the degree of Master of Science  
at Delft University of Technology,  
to be defended publicly on Monday August 28, 2023 at 14:00 PM

Student number: 4873165  
Project duration: January 24, 2023 – August 28, 2023  
Thesis committee: Ir. R. Noomen, TU Delft, daily supervisor  
Dr. ir. E. J. O. Schrama, TU Delft, committee chair  
Dr. R. M. Groves, TU Delft, external examiner



---

# Acknowledgements

---

“ Baba has the perfect timing - never early, never late. It takes some patience and faith, but it is worth the wait. Turn your worries into worship, and watch him turn your battles into blessings. Om Sai Ram. ”

---

Hemadpant Dabholkar, Shri Sai Satcharitra

In the name of my spiritual Guru, Shri Sai Baba, the divine source of inspiration and wisdom, I offer my heartfelt prayers for guiding me through this journey which has transformed my intellectual and emotional soul. His constant divine presence and miracles have infused my efforts with unwavering faith and made me reach where I am today.

This thesis marks the culmination of my five-year journey at the Faculty of Aerospace Engineering at TU Delft: first as a Bachelor and then as a Master's student. I have received unwavering support, guidance, and encouragement from incredible people. I extend my sincere gratitude to my supervisor Ir. Ron Noomen, whose invaluable guidance and patience have been pivotal in shaping the trajectory of this thesis. His profound knowledge, constructive feedback, and encouragement have been inspirational in bringing out the best in me. Thank you, Ron.

I am immensely thankful to my friends for the cherished memories and laughter we shared at TU Delft. I want to mention my girl gang (Panini Rabbits) members: Nico, Naishadha, Irina, and Ayushi. Five years is a long time for people to drift apart but fortunately, not us. Thank you, girls, for bringing out the fun in me and standing by me during difficult times. I also want to mention my study group friends from Master Room 2.44: Fabrizio, Michael, Jan, Punit, Advait, Ajay, Emma, Vikram, and Kubra, for being present in my journey and cheering me up during our coffee breaks.

I want to mention two lovely people in my life here. My best friend, guide, and constant source of energy and inspiration: Pratik Rindhe. He believed in my abilities more than I ever did and has been there with me throughout my academic and emotional journey. Thank you, Pratik, for taking time despite being busy and supporting me relentlessly. My senior, Mayukh Sarkar, whose unwavering support and belief in my potential brought joy, laughter, and a sense of companionship, making this journey much more beautiful. Thank you, Mayukh, for never questioning my crazy side, showering me with immense emotional support, and rewarding me with your cooked Bengali delicacies, which reminded me of home while working on my dreams day and night.

Finally, I want to thank my extraordinary parents for their endless sacrifices. My father, Hirak Sinha, for being my Rock of Gibraltar, always motivating me to keep my head high but my feet grounded. Thank you, Baba, for prioritising my dreams over everything and supporting me whenever I doubted my abilities. My beautiful mother, Indrani Sinha, for nurturing and guiding me with values of respect, humility, and discipline along the way. Thank you, Mumma, for your immense sacrifices while raising me and for motivating me to be a better human above everything.

Ishita Sinha  
Delft, August 2023



---

# Abstract

---

Recent launches of satellite constellations in the Low Earth Orbit (LEO) region have increased the collision probability of existing debris objects with active satellites. Monitoring the trajectories of these debris objects is crucial for Space Situational Awareness (SSA) to prevent the creation of more debris due to unwanted collisions. Much focus is on the LEO regime, with little awareness of the higher Geostationary orbit (GEO) debris population. To date, the explosion of the Russian Ekran 2 satellite in 1978 as well as the disintegration of the Titan IIIC Trans-stage in 1992, have been recorded. These incidents have increased the number of small-sized debris objects in GEO. More unnoticed fragmentation events have been speculated to have occurred, which pose a significant risk of collisions and damage to all weather and communication satellites in use today. The NASA Debris Office confirms that current ground-based radar or optical sensing methods can only be performed for objects of size 1 m and larger, leaving a gap in the precise orbit determination of sub-meter-sized objects in GEO. Moreover, limited observations and atmospheric losses hinder the quality of orbit determination, thus limiting present ground-based SSA techniques. Attempting to bridge this gap in current space surveillance and tracking methods is the objective of this thesis. It evaluates the feasibility of using space-based sensing methods to enhance SSA in the GEO regime. In this research, a satellite in a sub-GEO orbit is deployed to collect in situ radar measurements, which are processed to determine the orbit of a single object in GEO. Different satellite geometries (altitudes and inclinations) and measurement types such as range, range-rate, and direction (azimuth and elevation angles) and combinations thereof have been analysed. A simple grid search optimisation has been performed to assess the feasibility of such a technique and propose a possible favourable observation configuration, which improves the quality and accuracy of orbit determination. It also analyses the uncertainties in the debris state for future epochs to assess the errors in orbit prediction. The limitations of the geometry and measurement model are identified in this study and provided as recommendations and suggestions for further research. INDIGO is hence a feasibility study or a proof-of-concept of space-based debris state observations in GEO. It can be considered a stepping stone towards inventorying the small-sized GEO debris population catalogue and exploring enhanced SSA techniques in the future.



---

# Contents

---

<b>Acknowledgements</b>	<b>i</b>
<b>Abstract</b>	<b>ii</b>
<b>Nomenclature</b>	<b>vi</b>
<b>1 Introduction</b>	<b>1</b>
<b>2 Relevance</b>	<b>3</b>
2.1 Space debris . . . . .	3
2.2 Space Situational Awareness: current limitations in GEO . . . . .	6
2.3 Research objective and questions . . . . .	9
<b>3 Theoretical background</b>	<b>12</b>
3.1 Orbital dynamics . . . . .	12
3.1.1 Reference frames . . . . .	12
3.1.2 State-vector representations . . . . .	14
3.1.3 Modeling of forces in GEO . . . . .	15
3.1.3.1 Spherical harmonics . . . . .	16
3.1.3.2 Lunar third-body perturbation . . . . .	19
3.1.3.3 Solar third-body perturbation . . . . .	20
3.1.3.4 Aerodynamic drag . . . . .	20
3.1.3.5 Solar radiation pressure . . . . .	21
3.1.3.6 Summary of perturbations . . . . .	21
3.2 Radar system theory . . . . .	22
3.2.1 Motivation for space-based radar . . . . .	22
3.2.2 Radar link budget . . . . .	23
3.2.3 Radar functions . . . . .	26
3.2.4 Selection of waveform and configuration . . . . .	27
3.2.5 Measurement accuracy . . . . .	28
3.3 Orbit Determination theory . . . . .	29
3.3.1 Fundamentals of Least squares (LSQ) . . . . .	30
3.3.2 Variational Equations . . . . .	32
<b>4 Methodology</b>	<b>34</b>
4.1 INDIGO system design . . . . .	34
4.1.1 Parameters and Link Budget Analysis . . . . .	35
4.1.2 Measurement acquisition strategy . . . . .	40
4.1.3 Selected configuration . . . . .	42
4.2 Simulation setup . . . . .	42
4.2.1 Propagating orbital model . . . . .	42
4.2.1.1 Problem initialisation and assumptions . . . . .	43
4.2.1.2 Integrator selection . . . . .	44
4.2.1.3 Reference ephemeris generation . . . . .	45
4.2.2 Generation of observations . . . . .	47
4.2.2.1 Ideal pseudo-measurements . . . . .	47

4.2.2.2	Simulating reality: addition of radar noise and bias . . . . .	49
4.2.3	Precise orbit determination (POD) process . . . . .	52
4.3	Framework for analysis of results . . . . .	57
4.3.1	POD performance metrics . . . . .	57
4.3.2	Parametric study cases . . . . .	58
4.3.3	Approach for optimisation . . . . .	59
<b>5</b>	<b>Verification and Validation</b>	<b>60</b>
5.1	Verification with TUDATPy . . . . .	60
5.1.1	$J_2$ . . . . .	61
5.1.2	$J_{2,2}$ . . . . .	62
5.1.3	Third-body Moon perturbation . . . . .	64
5.1.4	Third-body Sun perturbation . . . . .	66
5.1.5	SRP perturbation . . . . .	68
5.1.6	Other orbital regimes . . . . .	69
5.2	Radar design verification . . . . .	71
5.3	Validation with TLE orbital data . . . . .	73
<b>6</b>	<b>Results and Discussion</b>	<b>76</b>
6.1	Case 1: Nominal case . . . . .	76
6.1.1	Ideal measurements case . . . . .	77
6.1.2	Addition of Gaussian noise only . . . . .	78
6.1.3	Addition of noise and bias . . . . .	79
6.1.4	Overall nominal case analysis . . . . .	81
6.2	Case 2: Different integration step sizes . . . . .	83
6.3	Case 3a: Different satellite altitudes . . . . .	84
6.3.1	Altitude difference 250 km . . . . .	84
6.3.2	Altitude difference 500 km . . . . .	85
6.3.3	Altitude difference 1000 km . . . . .	86
6.3.4	Overall altitude analysis . . . . .	87
6.4	Case 3b: Different satellite inclinations . . . . .	88
6.4.1	Inclination difference 0.1° . . . . .	90
6.4.2	Inclination difference 1° . . . . .	90
6.4.3	Inclination difference 2.5° . . . . .	91
6.4.4	Inclination difference 5° . . . . .	92
6.4.5	Overall inclination analysis . . . . .	92
6.5	Case 4: Different measurement types . . . . .	93
6.5.1	Overall quality for all measurement types . . . . .	95
6.5.2	Selective prediction performance for measurement types . . . . .	96
6.6	Case 5: Different satellites and configurations . . . . .	98
6.6.1	Two-satellite framework . . . . .	98
6.6.2	Three-satellite framework . . . . .	100
6.7	Sensitivity Analysis . . . . .	103
6.7.1	Uncertainty in initial guess of debris state for WLS . . . . .	103
6.7.2	Different noise and bias . . . . .	107
6.7.3	Different debris masses . . . . .	109
6.7.4	Different debris sizes . . . . .	110
6.7.5	Different SRP coefficients . . . . .	111
<b>7</b>	<b>Application of the study</b>	<b>113</b>
7.1	Revisit time . . . . .	113

---

7.2	Optimisation of design space and parameters . . . . .	117
7.3	Research Questions revisited . . . . .	123
<b>8</b>	<b>Conclusions and Recommendations</b>	<b>128</b>
8.1	Conclusions . . . . .	128
8.2	Recommendations . . . . .	129
	<b>References</b>	<b>130</b>
<b>A</b>	<b>Frame transformations</b>	<b>134</b>
A.1	Reference frame transformations . . . . .	134
A.1.1	ECI to ECEF: . . . . .	134
A.1.2	ECEF to ECI: . . . . .	135
A.1.3	ECI to LVLH: . . . . .	135
A.1.4	LVLH to ECI: . . . . .	136
A.2	Coordinate frame transformations . . . . .	137
A.2.1	Cartesian to Spherical: . . . . .	137
A.2.2	Spherical to Cartesian: . . . . .	138
A.2.3	Cartesian to Kepler elements: . . . . .	138
A.2.4	Kepler orbital elements to Cartesian elements: . . . . .	139



# Nomenclature

## Abbreviations

Abbreviation	Definition
CCD	Charged-Coupled Device
CTIO	Cerro Tololo Inter-American Observatory
CW	Continuous Wave
DLR	German Aerospace Centre
DOA	Direction Of Arrival
DoD	Department of Defence
ECEF	Earth-Centred Earth-Fixed
ECI	Earth-Centred Inertial
ESA	European Space Agency
FFT	Fast Fourier Transform
FMCW	Frequency Modulated Continuous Wave
FOV	Field-Of-View
FY-1C	Fengyun-1C Chinese satellite
GEO	Geostationary Earth Orbit
GWN	Gaussian White Noise
HPBW	Half Power Beam Width
IAA	International Academy of Astronautics
IADC	Inter-Agency Space Debris Coordination Committee
INDIGO	IN-situ Debris Inventorisation near the Geostationary Orbit
JD	Julian Day
JPL	Jet Propulsion Laboratory
JSpOC	Joint Space Operation Centre
KF	Kalman Filter
LEO	Low Earth Orbit
LIDAR	Light Detection and Ranging
LOS	Line-Of-Sight
LSQ	Least Squares
LVLH	Local-Vertical Local-Horizontal
MASTER	Meteoroid and Space debris Terrestrial Environment Reference
MODEST	Michigan Orbital Debris Survey Telescope
NASA	National Aeronautics and Space Administration
NORAD	North American Aerospace Defense Command
OD	Orbit Determination

Abbreviation	Definition
PC	Pulse Compression ratio
POD	Precise Orbit Determination
PROOF	Program for Radar and Optical Observation Forecasting
RAAN	Right Ascension of the Ascending Node
RADAR	Radio Detection and Ranging
RCS	Radar-Cross-Section
RK4	Runge-Kutta 4
RMS	Root Mean Square
RMS	Root-Mean-Square
RMSE	Root Mean Square Error
RSO	Resident Space Objects
RTN	Radial-Tangential-Normal
SGP	Simplified General Perturbation
SLR	Satellite Laser Ranging
SNR	Signal-to-Noise Ratio
SRP	Solar Radiation Pressure
SSA	Space Situational Awareness
SSN	Space Surveillance Network
STM	Space Traffic Management
STM	State Transition Matrix
TIRA	Tracking and Imaging Radar
TLE	Two-Line-Element
TUDAT	TU Delft's Astrodynamics Toolbox
TWS	Track-While-Scan
UNOOSA	United Nations Office for Outer Space Affairs
UTT	Union Terrestrial Time
WLS	Weighted Batch Least Squares
ZimSMART	Zimmewald Small-Aperture Robotic Telescope

## Roman Symbols

Symbol	Definition	Unit
<b>A</b>	Partial derivative matrix	—
$A_e$	Radar antenna effective radiative area	[m <sup>2</sup> ]
$A/m$	Area-to-Mass Ratio	[m <sup>2</sup> /kg]
$a$	Semi-major axis	[m]
$B$	Radar noise bandwidth	[Hz]
$\mathbf{b}_{sum}$	Cumulative LSQ parameter from <b>W</b> and measurement residuals	—
$C_{n,m}$	Un-normalised spherical harmonics cosine coefficient	—
$C_D$	Drag coefficient of an object	—
$C_r$	Surface reflection coefficient of an object	—

Symbol	Definition	Unit
$c$	Speed of light in vacuum	[m/s <sup>2</sup> ]
$D_{ant}$	Diameter of a parabolic radar antenna	[m]
$D_{lobe}$	Diameter of antenna main lobe	[m]
$dt$	Simulation time step	[s]
$e$	Eccentricity	–
$\vec{f}$	Ordinary differential equation function	–
$f_c$	Radar carrier frequency	[Hz]
$f_d$	Doppler frequency	[Hz]
$\vec{f}_{drag}$	Atmospheric drag perturbation vector acting on an Earth-orbiting object	[kg m/s <sup>2</sup> ]
$\vec{f}_{Moon}$	Third-body perturbation vector due to the Moon acting on an Earth-orbiting object	[kg m/s <sup>2</sup> ]
$\vec{f}_{SRP}$	Solar radiation pressure perturbation vector acting on an Earth-orbiting object	[kg m/s <sup>2</sup> ]
$\vec{f}_{Sun}$	Third-body perturbation vector due to the Sun acting on an Earth-orbiting object	[kg m/s <sup>2</sup> ]
$f_x$	Force component along the x-axis	[kg m/s <sup>2</sup> ]
$f_y$	Force component along the y-axis	[kg m/s <sup>2</sup> ]
$f_z$	Force component along the z-axis	[kg m/s <sup>2</sup> ]
$G_r$	Gain of receiving antenna	[dB]
$G_t$	Gain of transmitting antenna	[dB]
$G$	Gain of monostatic radar antenna	[dB]
$\mathbf{H}$	Jacobian matrix	–
$h$	Step size for RK4 integration	[s]
$\vec{h}$	Observation module function	–
$i$	Inclination	[°]
$J_{2,2}$	Spherical harmonic of degree 2 and order 2	–
$J_2$	Spherical harmonic of degree 2 and order 0	–
$J_{n,m}$	Spherical harmonic gravity coefficient	–
$J$	WLS Cost function	–
$\vec{K}_1$	Function evaluation for RK4 integrator	–
$\vec{K}_2$	Function evaluation for RK4 integrator	–
$\vec{K}_3$	Function evaluation for RK4 integrator	–
$\vec{K}_4$	Function evaluation for RK4 integrator	–
$k_{J_{2,2}}$	Constant defined in description of $J_{2,2}$ spherical harmonic gravity	[m <sup>2</sup> /s <sup>2</sup> ]
$k_M$	Monopulse pattern difference slope	–
$k$	Boltzmann constant	[J deg <sup>-1</sup> K <sup>-1</sup> ]
$L$	Total radar losses	[dB]
$m$	Mass of object	[kg]
$m$	Order of associated Legendre polynomial	–
$\mathbf{N}_{sum}$	Cumulative LSQ parameter from $\mathbf{W}$ and Jacobian matrix	–
$\hat{N}_{sat}$	Normal unit vector for satellite in LVLH frame	–
$n_{comb}$	Number of epochs for which measurements are available	–

Symbol	Definition	Unit
$n_{el}$	Number of elements in the phased array radar	–
$n_{fa}$	Number of false alarms	–
$n_{meas}$	Number of measurements available for OD	–
$n_c$	Number of radar coherent pulses	–
$N_f$	Noise figure for radar	[dB]
$n_i$	Number of radar incoherent pulses	–
$n$	Degree of associated Legendre polynomial	–
$\mathbf{P}_0$	Covariance matrix	–
$P_d$	Probability of detection for a radar	–
$P_{fa}$	Probability of false alarm for a radar	–
$P_{n,m}$	Associated Legendre Polynomials	–
$P_1, P_2$	Half power beam width points in radar beam	–
$p_t$	Radar transmission power	[W]
$\vec{p}$	A general perturbing force	[kg m/s <sup>2</sup> ]
$R_E$	Radius of the Earth	[m]
$R$	Target range	[m]
$\hat{R}_{sat}$	Radial unit vector for satellite in LVLH frame	–
$\vec{r}_0$	Position vector at initial epoch	–
$\vec{r}$	Cartesian position vector	[m]
$\vec{r}_{Moon}$	Position vector of the Moon relative to the Earth	[m]
$\vec{r}_{Sun}$	Position vector of the Sun relative to the Earth	[m]
$\vec{r}$	Cartesian acceleration vector	[m/s <sup>2</sup> ]
$r$	Magnitude of position vector	[m]
$\text{SNR}_{ref}$	Reference Signal-to-Noise Ratio	[dB]
$\text{SNR}$	Signal-to-Noise Ratio	[dB]
$S_{n,m}$	Un-normalised spherical harmonics sine coefficient	–
$S_r$	Solar radiation flux	[W/m <sup>2</sup> ]
$t_{end}$	Ending simulation epoch	[s]
$\hat{T}_{sat}$	Tangential unit vector for satellite in LVLH frame	–
$T_{sim}$	Total simulation time	[s]
$t_{start}$	Initial simulation epoch	[s]
$t_0$	Initial epoch	[s]
$T_s$	System noise temperature of radar	[K]
$t$	A general epoch	[s]
$\vec{U}_{EB}$	Gravitational potential	[m <sup>2</sup> /s <sup>2</sup> ]
$\vec{U}_{J_2}$	Gravitational potential due to $J_2$ term	[m <sup>2</sup> /s <sup>2</sup> ]
$\vec{v}$	Velocity of object relative to rotating Earth at-mosphere	[m/s]
$\vec{v}$	Cartesian velocity vector	[m/s]
$\vec{v}_0$	Velocity vector at initial epoch	–
$v_r$	Radial velocity of debris along the LOS vector	[m/s]

Symbol	Definition	Unit
$v_x$	Cartesian velocity component along the x-axis	[m/s]
$v_y$	Cartesian velocity component along the y-axis	[m/s]
$v_z$	Cartesian velocity component along the z-axis	[m/s]
$v$	Magnitude of velocity vector	[m/s]
$\mathbf{W}$	Weighting matrix for OD	—
$\vec{X}_{J2000}$	Cartesian unit vector of the ECI J2000 reference frame along the x-axis	—
$\vec{x}_{LVLH}$	Cartesian unit vector of the LVLH reference frame along the x-axis	—
$\dot{x}_D$	Velocity in x-coordinate for the debris object	[m/s]
$\dot{x}_S$	Velocity in x-coordinate for observation satellite	[m/s]
$\vec{x}_0$	State vector at initial epoch	—
$\vec{x}^{apr}$	Approximate state vector guess for debris for WLS	—
$\vec{x}^{ref}$	Reference state vector guess for debris for WLS	—
$\vec{x}_e$	Cartesian unit vector of a general ECEF reference frame along the x-axis	—
$\vec{x}_i$	Cartesian unit vector of a general ECI reference frame along the x-axis	—
$x_D$	Position in x-coordinates for the debris object	[m]
$x_S$	Position in x-coordinates for observation satellite	[m]
$x$	Cartesian position component along the x-axis	[m]
$\vec{y}$	State vector to estimate	—
$\dot{y}_D$	Velocity in y-coordinate for the debris object	[m/s]
$\dot{y}_S$	Velocity in y-coordinate for observation satellite	[m/s]
$\vec{y}_e$	Cartesian unit vector of a general ECEF reference frame along the y-axis	—
$\vec{y}_i$	Cartesian unit vector of a general ECI reference frame along the y-axis	—
$\vec{y}_{i+1}$	Function evaluation by RK4 integrator at next epoch i+1	—
$\vec{Y}_{J2000}$	Cartesian unit vector of the ECI J2000 reference frame along the y-axis	—
$\vec{y}_{LVLH}$	Cartesian unit vector of the LVLH reference frame along the y-axis	—
$\vec{y}_i$	Function evaluation by RK4 integrator at epoch i	—
$y_D$	Position in y-coordinates for the debris object	[m]

Symbol	Definition	Unit
$y_S$	Position in y-coordinates for observation satellite	[m]
$y$	Cartesian position component along the y-axis	[m]
$\dot{z}_D$	Velocity in z-coordinate for the debris object	[m/s]
$\dot{z}_S$	Velocity in z-coordinate for observation satellite	[m/s]
$\vec{z}_e$	Cartesian unit vector of a general ECEF reference frame along the z-axis	—
$\vec{z}_i$	Cartesian unit vector of a general ECI reference frame along the z-axis	—
$\vec{Z}_{J2000}$	Cartesian unit vector of the ECI J2000 reference frame along the z-axis	—
$\vec{z}_{LVLH}$	Cartesian unit vector of the LVLH reference frame along the z-axis	—
$\vec{z}$	Measured observations vector	—
$z_D$	Position in z-coordinates for the debris object	[m]
$z_S$	Position in z-coordinates for observation satellite	[m]
$z$	Cartesian position component along the z-axis	[m]

## Greek Symbols

Symbol	Definition	Unit
$\alpha$	Right ascension	[°]
$\beta$	Radar metric parameter	—
$\delta$	Declination	[°]
$\dot{\rho}$	Range-rate measurements	[m/s]
$\epsilon_{conv}$	Tolerance for WLS convergence	—
$\eta$	Radar antenna efficiency	—
$\Lambda_{2,2}$	Spherical harmonics gravity field coefficient for $J_{2,2}$ spherical harmonic coefficient	[°]
$\Lambda_{n,m}$	Spherical harmonics gravity field coefficient	[°]
$\Lambda$	Geocentric longitude	[°]
$\lambda$	Wavelength	[m]
$\mu_{Moon}$	Gravitational parameter of the Moon	[m <sup>3</sup> /s <sup>2</sup> ]
$\mu_n$	Mean of a Gaussian Normal distribution	—
$\mu_{Sun}$	Gravitational parameter of the Sun	[m <sup>3</sup> /s <sup>2</sup> ]
$\mu$	Gravitational parameter of the Earth	[m <sup>3</sup> /s <sup>2</sup> ]
$\omega$	argument of pericentre	[°]
$\Omega$	Right Ascension of Ascending Node	[°]
$\Phi$	State transition matrix for OD	—
$\vec{\epsilon}$	Residual vector for measurements	—

Symbol	Definition	Unit
$\rho_{atm}$	Atmospheric density	[kg/m <sup>3</sup> ]
$\rho_{v_x v_y}$	Correlation between x velocity and y velocity	—
$\rho_{v_x v_z}$	Correlation between x velocity and z velocity	—
$\rho_{v_y v_z}$	Correlation between y velocity and z velocity	—
$\rho_{x v_x}$	Correlation between x position and x velocity	—
$\rho_{x v_y}$	Correlation between x position and y velocity	—
$\rho_{x v_z}$	Correlation between y position and z velocity	—
$\rho_{xy}$	Correlation between x position and y position	—
$\rho_{xz}$	Correlation between x position and z position	—
$\rho_{y v_x}$	Correlation between y position and x velocity	—
$\rho_{y v_y}$	Correlation between y position and y velocity	—
$\rho_{y v_z}$	Correlation between y position and z velocity	—
$\rho_{yz}$	Correlation between y position and z position	—
$\rho_{z v_x}$	Correlation between z position and x velocity	—
$\rho_{z v_y}$	Correlation between z position and y velocity	—
$\rho_{z v_z}$	Correlation between z position and z velocity	—
$\rho$	Range measurements	[m]
$\sigma_{\dot{\rho}}$	Standard deviation in range measurements	[m/s]
$\sigma_{\rho}$	Standard deviation in range measurements	[m]
$\sigma_{az}$	Standard deviation in azimuth measurements	[°]
$\sigma_{bias}$	Standard deviation for bias	—
$\sigma_{dev}$	Standard deviation of a Gaussian Normal distribution	—
$\sigma_{el}$	Standard deviation in elevation measurements	[°]
$\sigma_{pos}$	Formal uncertainty in position	[m]
$\sigma_{std}$	Standard deviation for Gaussian noise	—
$\sigma_{v_x}$	Standard deviation in x-coordinate velocity	[m/s]
$\sigma_{v_y}$	Standard deviation in x-coordinate velocity	[m/s]
$\sigma_{v_z}$	Standard deviation in z-coordinate velocity	[m/s]
$\sigma_{vel}$	Formal uncertainty in velocity	[m/s]
$\sigma_x$	Standard deviation in x-coordinate position	[m]
$\sigma_y$	Standard deviation in y-coordinate position	[m]
$\sigma_z$	Standard deviation in z-coordinate position	[m]
$\sigma$	Radar Cross Sectional area	[m <sup>2</sup> ]
$\tau$	Radar pulse duration	[s]
$\theta_{az}$	Azimuth angle measurements	[°]
$\theta_{BW}$	Radar antenna beamwidth	[°]
$\theta_{el}$	Elevation angle measurements	[°]
$\theta$	True Anomaly	[°]

## Other Symbols

Symbol	Definition	Unit
$\Delta h$	Altitude difference	[m]
$\Delta i$	Inclination difference	[°]
$\Delta R$	Range accuracy of a radar	[m]
$\Delta T$	Trip time of a radar signal to and from a target	[s]
$\Delta V$	Velocity accuracy of a radar	[m/s]
$\Delta x_0^{\text{lsq}}$	Least squares solution	—
$\Upsilon$	Vernal Equinox	—

# 1

## Introduction

---

Since the launch of the first satellite Sputnik-I, on October 4, 1957, humans have rapidly progressed into space exploration. With the increasing number of space missions and satellite deployments, the potential for collisions and the generation of additional space debris has increased to the point that it comes close to creating a cascading effect known as Kessler's Syndrome. Collisions with debris objects traveling at high speeds can generate more debris, jeopardising communication links and compromising the functionality of vital space infrastructure [1].

Monitoring debris trajectories is crucial for Space Situational Awareness (SSA), which is significant for managing space assets in higher orbits. At 35,786 km from the Earth's surface lies the Geostationary Earth orbit (GEO), a unique orbital regime. A satellite in this orbit appears stationary for an observer on the ground, making it attractive for communication and meteorological satellites. Due to their high altitude and lack of significant atmospheric drag, these satellites remain in orbit far beyond their operational lifetime and are subjected to explosions or fragmentation over time [2]. The gradual onset of crowding in the GEO regime due to dysfunctional satellites and their debris fragments has sparked concerns among the scientific community. The threats of debris collisions in higher orbits call for relevant monitoring and mitigation methods, which require precise knowledge of their behaviour and trajectories.

Ground-based observations performed by the National Aeronautics and Space Administration (NASA) and the United States Department of Defence (DoD) can predict the trajectories of objects as small as 5 cm in Low Earth Orbit (LEO) and as small as 1 m in GEO [3], which keeps the existence and cataloguing of smaller debris objects at higher orbits vastly unknown. These objects as small as 1 cm can be catastrophic for active satellites currently and in the future. Moreover, these small-sized objects are infrequently visible to the sensors due to atmospheric and illumination conditions, which makes tracking them even more difficult.

To overcome the shortcomings of ground-based systems, this research focuses on exploring the feasibility of using a novel space-based tracking platform or an observation satellite framework to conduct in-situ measurements. The motivation for this new concept is that the drawbacks of ground-based observations are discerning, which is attempted to be solved by resorting to space-based observations. Since space-based radars have the potential to collect multiple in-situ measurements [4], it is explored in this thesis to assess whether the gap in research can be fulfilled by formulating three main research questions, mentioned as follows.

1. Is using a space-based radar system **feasible** for space surveillance and tracking small objects in GEO?
2. How do the dynamic model parameters, observation types and trajectory prediction outcome contribute to the **feasibility assessment** of the system?
3. How **sensitive** is the orbit determination **accuracy** of small-sized debris objects in GEO to changes in uncertainties and satellite geometric configurations?

To answer these main questions and their sub-questions (defined later in Section 2.3), a numerical model will be developed as part of this thesis. This model will simulate the orbital dynamics of one debris object in GEO and one (or more) observation satellite(s) in a sub-GEO orbit. The thesis will involve studying the fundamentals of the problem, supporting the usefulness of in-situ measurement collection techniques. The innovation point of this research is to develop and analyse the results from an orbital simulation model to solve a two-fold objective. This consists of first, determining trajectories of small-sized debris which are currently not observed and second, quantifying and optimising the accuracy with which these objects are known, ideally higher than what is achieved with ground-based sensing.

This report documents the research conducted for the thesis and comprehensively presents them as chapters with the following structure. The relevance or justification of the research is provided in Chapter 2, which highlights the problem of space debris and the shortcomings of the current SSA capabilities. After identifying the research gap and formulating the sub-research questions to the three main research questions mentioned above, Chapter 3 discusses the fundamental theoretical aspects whose strong understanding is required during the research. After that, the research approach followed by applying the theory in the previous chapter is described in Chapter 4, which is used to generate results for the study. However, before the results are generated and reviewed, they are verified and validated in Chapter 5. The results obtained for different case studies are presented in Chapter 6, which is followed by Chapter 7, where a feasibility outcome is discussed, and the research questions are answered based on the conducted study. The report ends with conclusions in Chapter 8, summarising the problem, methodology, and results of this research report, along with recommendations for further study.

# 2

## Relevance

Before embarking upon any research project, it is essential to understand its overall purpose. Once a big problem has been identified, a more directed and relevant segment can be chosen for study. Following this principle, this chapter aims to familiarise the reader with the relevance of this thesis and research area.

In Section 2.1 of this chapter, the comprehensive threat due to the rising number of space debris is explained. The state-of-the-art techniques along with their associated challenges and limitations, for monitoring and tracking debris objects in higher orbits, are discussed in Section 2.2. The knowledge gap is identified here and is further motivated in Section 2.3, which defines the overall goal or objective to be fulfilled and research questions that will be answered as a result at the end of the thesis.

### 2.1. Space debris

October 4, 1957, marked the beginning of a new era for mankind with the launch of the first artificial satellite Sputnik-I by the Soviet Union. More than six decades of space exploration have led to the growth of a particle environment in the Earth orbit collectively known as “space debris”, endangering all active satellites today [1]. Debris mitigation experts have studied the classification of orbital debris and their sources. Abandoned launch vehicles filled with residual propellant and high-pressure fluids exposed to temperature and pressure fluctuations can suffer explosions in orbit, thus creating debris objects. The primary debris sources are mission-related operations, accidental collisions, and intentional creation [5]. In more collective words, space debris can be defined as stated below.

#### Space debris definition

The International Academy of Astronautics (IAA) defines **space** or **orbital debris** as “any man-made object orbiting the Earth which is non-functional with no reasonable expectation of assuming or resuming its intended function or any other function for which it is or can be expected to be authorized, including fragments and parts thereof” [6].

The United Nations Office for Outer Space Affairs (UNOOSA) states that currently about 33750 objects are being regularly tracked by the United States Space Surveillance Network or SSN. Approximately 640 fragments are expected to have evolved from explosions of defunct satellites, increasing the risk of further collisions [7]. The European Space Agency (ESA) maintains and

distributes several models for characterising the environment and evolution of debris objects through their risk assessment tool known as MASTER (Meteoroid and Space debris Terrestrial Environment Reference). This tool estimates about 365,000 objects greater than 10 cm in size, about 1,000,000 objects between sizes 1 cm and 10 cm, and more than 130 million objects between 1 mm and 1 cm in size [8]. The evolution of the debris population in all orbital regimes as of 2020 can be visualised in Figure 2.1. The trend of the total object population in orbit (brown curve) can be largely attributed to the fragmentation debris (pink curve). [9].

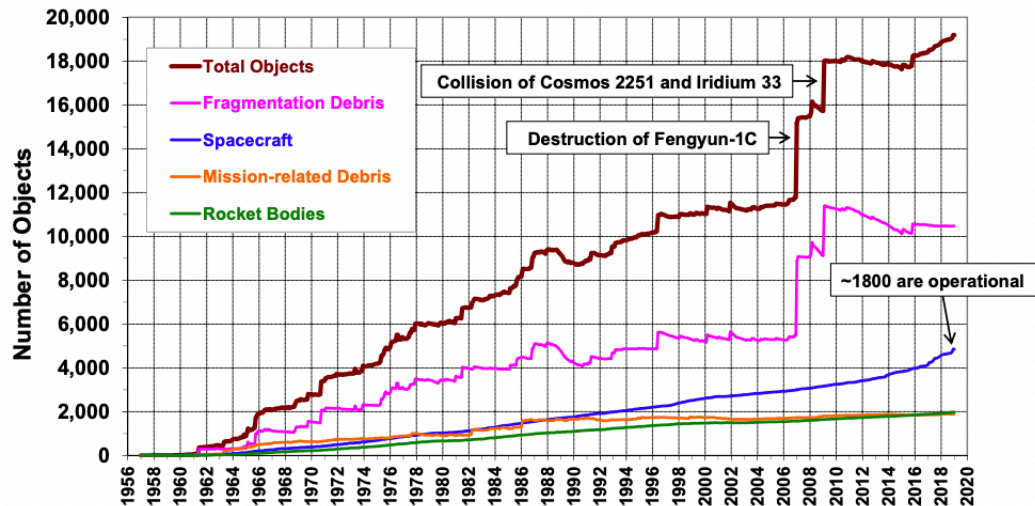


**Figure 2.1:** Evolution of the total number of space debris objects in LEO since 1957. This has been catalogued by the US Combined Space Operations over the years, which shows the trend is rising. As of 2020, out of approximately 5000 satellites, only about 1800 satellites are operational in orbit [9].

Two jumps in the fragmentation debris population curve are also reflected in the total object population. The first spike was seen in 2007, when China destroyed its defunct weather satellite, **Fengyun-1C** (FY-1C), through a ballistic missile from the Earth. This act created a cloud of debris particles around the original satellite orbit at 863 km. The SSN has tracked about 3037 pieces originating from this incident and predicts that more than 32000 smaller untracked pieces will remain in orbit for as long as the year 2108 [10]. This incident produced the largest debris cloud ever generated by a single event in orbit. In a matter of two years, on February 10, 2009, an active American communication satellite **Iridium 33** accidentally collided with a defunct Russian communication satellite **Cosmos 2251** at an altitude of 770 km. Approximately 2000 pieces of debris larger than 10 cm and more than thousands of smaller pieces were produced, marking this incident in the history of accidental collisions. The SSN catalogued 528 pieces from Iridium 33 and 1347 pieces from Cosmos 2251, predicting 1000 additional smaller and untracked pieces [11].

In a theoretical study by NASA scientist Donald Kessler in 1978, it was speculated that this exponential uncontrolled rise in the number of orbiting objects in LEO would lead to a chain of collisions creating more debris. Fragmentation from these debris objects would cause more collisions making it infeasible to launch new satellites and inhibit space-based activity with active satellites. This scenario was named the Kessler's Syndrome and drew quite some concern in the scientific community [9]. This scenario may render space unusable for several centuries [12]. After contemplation, it has been deduced that the threshold for a low-intensity Kessler Syndrome has already been crossed [13]. Any added number of space debris objects would amplify this effect, thus really making space inaccessible for further use.

The **Geostationary** or **Geosynchronous Equatorial Orbit (GEO)** is a unique orbit with an altitude of 35,786 km and 0° inclination. The specialty of this orbital regime is that a satellite launched in this orbit remains above the same point on the Earth's surface, making it highly popular for communication and Earth observation satellites. At high altitudes, the effect of atmospheric drag acting on the satellites is negligible. De-orbiting of GEO satellites after their operational lives to make them re-enter the Earth's atmosphere would be very propellant expensive, which is why they should ideally be manoeuvred and placed in a graveyard orbit, about 300 km above their nominal orbit. However, a study in 2017 concluded that only two-thirds of the satellites move to this disposal orbit, while the remaining fail to succeed or do not even try, which only delays the developing problem of debris in GEO rather than solving it [14].

The Inter-Agency Space Debris Coordination Committee (IADC) spotted a significant rise in the GEO regime of the uncatalogued objects as big as 20 cm in diameter. They were a result of two major breakup events near GEO from the Ekran 2 and Titan IIIC Transtage satellites [2]. It is expected that there is more debris of smaller sizes that are unidentified or uncatalogued, posing a risk of collisions with the active satellites in GEO. The cumulative probability of collisions in GEO is estimated to be close to  $3.2 \times 10^{-4}$ , equivalent to one collision once every 3000 years. The satellites in GEO orbit in the same direction, with the same speed and inclination, which reduces the probability of collisions with each other [15]. However, recent studies suggest that the collision likelihood in GEO is four orders of magnitude higher than suggested before [16]. Figure 2.2 illustrates the possibility of collision with all active satellites in GEO distributed over their longitude bins with different resident space objects (RSO). It can be seen that there are peaks at 75° E and 105° W or 255° E, which represent the geopotential wells. These locations are more likely to witness collisions due to the larger concentration of satellites and RSOs.

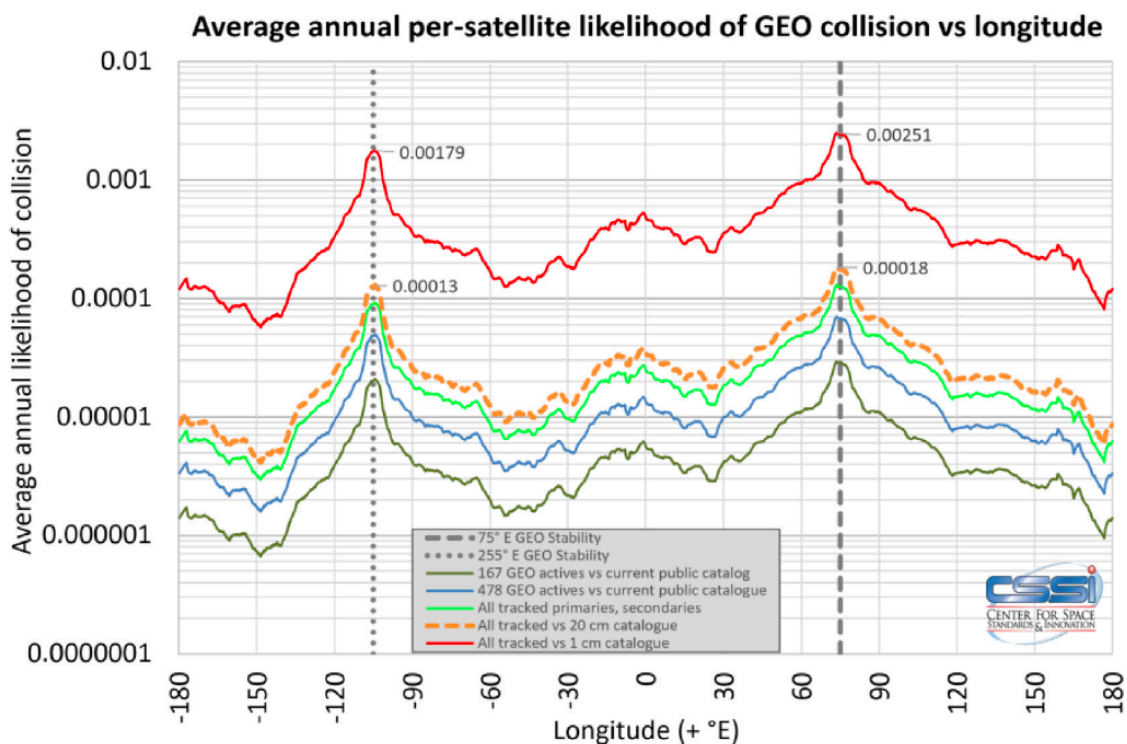


**Figure 2.2:** The likelihood of GEO collision as a function of longitude for active satellites in GEO for 2018. The red and orange curves depict the likelihood of collision of the entire GEO population against an object catalogued with size 1 cm and 20 cm, respectively. The vertical lines represent the two geopotential wells [16].

The work of Oltrogge et al. [16] estimates the average annual likelihood of collision with the GEO active satellites against 1912 RSO objects of size larger than 20 cm to be 0.0152. Similarly, when estimated for 33932 objects larger than 1 cm, the average annual likelihood is estimated to be 0.1929. Multiplying each likelihood by a scaling factor of 1.29 and taking its inverse yields the average latency time between two collisions. The Joint Space Operation Centre (JSpOC) uses this method to perform conjunction analysis assessments using models for a 5-meter miss distance. It evaluates that a collision with the entire GEO population against a **1 cm** RSO catalogue is likely to happen **once every four years**. The exact likelihood changes to **once every 50 years** when evaluated against a **20 cm** RSO catalogue [16]. Although the risk of collision in GEO is less than in LEO, collision avoidance manoeuvres must be conducted to safeguard active satellites in GEO. However, this can only be done when the orbit of the debris object at that altitude is sufficiently known. Moreover, for objects which are new and uncatalogued due to an unknown explosion, it is essential to identify and detect them first, to be able to monitor their orbital behaviour regularly and accurately track them to make conjunction predictions.

## 2.2. Space Situational Awareness: current limitations in GEO

Obtaining up-to-date information on space debris objects in GEO is essential to monitor their trajectories. Space surveillance observations aim to establish and maintain a catalogue containing the orbital and physical characteristics of existing and new objects. The knowledge and characterisation of space objects and their operational environment to support safe, stable, and sustainable space activities is commonly referred to as Space Situational Awareness or SSA, which is crucial for efficient Space Traffic Management (STM) and conjunction analysis [3]. There are typically three measurement techniques for surveillance or tracking from ground-based facilities to obtain information about the orbit of an object: radar ranging or Doppler tracking, Satellite Laser Ranging (SLR), and optical tracking. A literature study was conducted before this thesis, which reviewed these techniques in more detail to evaluate their utility as possible options for enhanced SSA.

**Light Detection and Ranging, or LIDAR**, involves sending coherent and high-intensity light pulses into space to measure the reflection on a Charged-Coupled Device or CCD sensor. SLR is a similar technique in which the time laser pulses take to travel from a global network of observing stations to satellites and back is measured. Although distance accuracy in the order of millimeters could be obtained, the object tracked would need to be equipped with passive reflectors to reflect the light off its surface. A study in 2016 by ESA and the German Aerospace Centre (DLR) demonstrated 60% success in precise orbit determination from the ground of LEO objects by combining optical sensors and laser-ranging observations [17]. It showed that a high-power laser is needed to avoid diffuse scattering of light and concentrate the light beam in the desired direction. Although they perform well for tracking due to their precise beam, their limited Field-Of-View (FOV) hinders the possibility of space surveillance for detecting new objects with LIDAR and optical systems. Due to the gap in surveillance and tracking of possible non-reflective debris, this technique was decided not to be further analysed in the research.

**Passive electro-optical sensors** can detect space debris by recording them on images, such that they are distinguished as moving objects relative to the stellar background. These sensors record the reflection of sunlight from debris objects against a dark background at night. Since objects in LEO have higher orbital velocities, they move quicker across the sky. As a result, the observation window for LEO objects is shorter to collect useful information on them. However, passive sensors are attractive for objects in GEO. This is because these objects are relatively stationary with

the ground, which facilitates data collection throughout the night, given that clear sky conditions are met. Moreover, the brightness or signal strength of the object is inversely proportional to the square of the distance from the passive observing facility, which makes them interesting for GEO object surveillance [18].

The detection ability of a sensor greatly depends on its light receiving area or aperture and the angular velocity of the object of interest. A fast and faint object will make it difficult for the sensor to discriminate the signal from the background sky, which can be solved by tracking the object. However, this requires knowledge of an object's trajectory, which is impossible for unknown or uncatalogued objects. To fulfill this, wide-FOV optical survey sensors are operating worldwide, which scan the area of interest for objects with unknown orbits. For instance, the Russian-based optical sensor network ISON has 50 telescopes in 27 positions, which detect objects in the LEO region several times a day [3].

To observe and maintain the orbits of GEO objects, wide-field optical designs are needed, which introduce a trade-off in the FOV and the aperture size, constrained by the telescope's mechanical design. Objects larger than 1 meter in diameter in GEO can be surveyed by the Zimmewald small-aperture robotic telescope known as ZimSMART, which has a 0.2 m aperture and 10° squared FOV. ESA collects observations through its 1 m aperture telescope at the Optical Ground Station in Tenerife, Canary Islands, to better understand the small-sized debris population. NASA too collects optical data with the Michigan Orbital Debris Survey Telescope (MODEST) located at the Cerro Tololo Inter-American Observatory (CTIO) in Chile to have a statistically complete data set for the GEO small-sized object population [19].

Although ground-based telescopes are very common methods of SSA, they also have limitations. A study on the performance of ground-based optical telescopes in 1994 showed the limiting size of objects detected depending on their orbital altitudes and sensor apertures as seen in Figure 2.3.

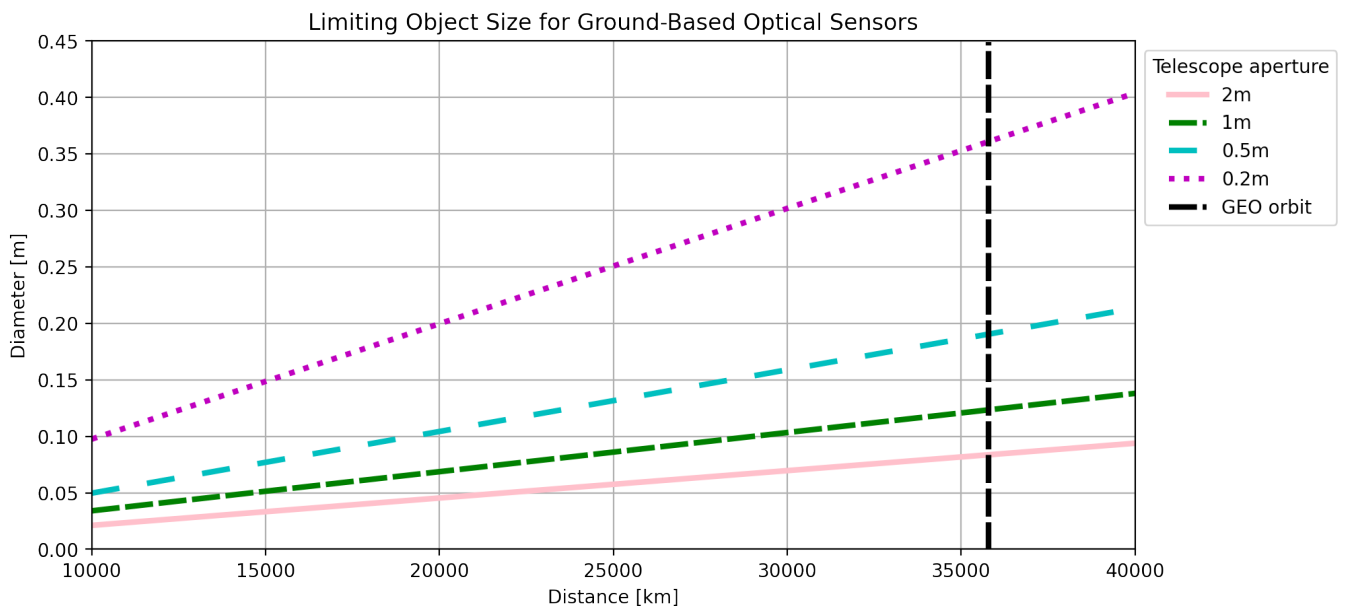


**Figure 2.3:** Limiting object size for ground-based optical sensors. The size is shown as a function of the sensor aperture and the orbital altitude. The graph assumes perfect measurement conditions such as a dark site, optimal atmosphere and weather, and a bond albedo 0.2 [20].

The black dashed line signifies the GEO regime objects and shows that with a telescope aperture of 2 m, an object as small as 8 cm in diameter can be detected. However, it must be noted that the results in this study are obtained with assumptions of conducting the observations in the dark with optimal illumination and atmospheric conditions. When errors and background clutter are considered, the objects are limited to 1 m in diameter [20][19].

To overcome these limitations in optical sensing methods, proposals and studies have been conducted to use a space-based optical system for collecting measurements. The advantages are that they are at a shorter distance and are no longer constrained by weather or illumination conditions. The brightness of the sky is reduced, which reduces signal atmospheric attenuation. A study by ESA proposes using a 20 cm aperture folded Schmidt telescope with a 6° FOV, coupled with a four-megapixel CCD sensor camera. Simulations with ESA's software MASTER-99 and PROOF showed this instrument operating in a circular orbit 1000 km below the GEO ring to detect 120 objects in 24 hours, facing away from the Sun [21].

As motivated previously in the literature study, optical tracking yields angles-only measurements but not much about its distance or velocity relative to the observing system. For SSA purposes, collecting one type of measurement information is not always enough to accurately determine the trajectory. Since optical systems are only constrained to the directional measurement type, there is no evaluation of the effect of different measurements or their combinations on precise trajectory computation of small-sized objects. Moreover, prior knowledge of the object's position is required to precisely aim the telescope in the desired direction, which is not possible for unknown objects. Hence, the research does not further analyze passive or optical sensing methods.

**Radio Detection and Ranging or RADAR** works on the principle of sending short bursts of radio energy at the speed of light to transmit and receive an echo from a target. Radars are independent of weather conditions and can be operated continuously, although at the cost of high power. Compared to optical sensing methods, the strength of the radar signal decreases with the fourth power of distance, constraining it from observing objects in GEO [22]. Currently, most surveillance and tracking for space debris in LEO is through ground-based radars. Information on the object's trajectory can be obtained by measuring the distance, velocity, and direction of the space object relative to the observation facility. The orbital parameters of these objects can then be estimated from their motion. A network of tracking sensors on the ground can track the path of a satellite by using three widely used types of measurements, as explained below [23].

- **Range:** The absolute distance between an object and a tracking system is known as range. This is computed by measuring the time delay between transmitted and reflected echoes. The geometric range is known as the true range. In contrast, the distance which accounts for measurement errors due to various factors such as clock errors and atmospheric losses is known as the pseudo range.
- **Range rate:** The velocity of a target in the radial direction along the Line-Of-Sight (LOS) of the object and radar is known as range rate. They are measured by differentiating successive range measurements over time or by measuring the Doppler shift of the tracking signal frequency.
- **Direction:** The angular orientation of an object with respect to the radar pointing axis gives the directional information of the object in azimuth and elevation. In the case of an interferometer, directional measurement of a target object is obtained by measuring the phase

difference between signals arriving at two antenna elements separated by a known distance.

As studied in the literature review report, radars have different modes of operation and functions. Surveillance radars operate in a beam park mode and have a large FOV. They emit radio waves and wait for detections to arrive at the receiver, counting the objects traveling through its beam. Once detected, the signal is processed, providing information on its distance, instantaneous Doppler frequency, and directional position in the sky. Tracking radars operate in a chasing mode and have a much narrower FOV, suited for following an object until it disappears below its detection threshold. Their main application is the refinement of orbital trajectories and the physical characterisation of objects, such as their shape, size, and composition. A third mode, known as the stare and chase mode, combines both modes and can switch between operations [24]. The Tracking and Imaging Radar (TIRA), located in Germany, is a unique 34 m diameter radar system that facilitates gathering information for precise orbit determination of LEO objects. Equipped with a high target resolution, it plays a big role in SSA from the ground. NASA also regularly performs observations using the US 34 m diameter Haystack antenna, which operates in the beam park mode to detect debris in LEO [25].

Although little is known about the exact detection threshold of known radar systems, ground-based radars can typically detect objects as small as 10 cm in diameter in the LEO regime, but not much is known about the performance of small-sized objects in GEO [3]. With the increasing population of space debris objects, their regular observation becomes a necessity. Radar techniques offer the advantage of multiple measurement types with no dependencies on weather or illumination. The major drawback of ground-based radars is the large distance between the target and the observing ground station through which the radio wave has to travel twice. If this propagation distance can be reduced by resorting to space-based radars, they could potentially be an asset for the future of SSA. This approach is still novel, contrary to space-based optical solutions, which have been previously studied by space agencies, partly due to their lower power and cost requirements [26]. However, the viability in terms of the performance of an **in-situ radar observation concept** has not been explicitly studied for GEO by space agencies to date. This research gap is aimed to be bridged through this thesis project.

## 2.3. Research objective and questions

The gap in research directly follows into a goal, which is to be fulfilled through this research. The research objective for INDIGO is

**To assess the space situational awareness capability of a space-based radar system, which surveys and detects small-sized debris objects in the geostationary orbital regime.**

The above goal is quite broad, and several related aspects need to be tackled systematically. Bridging the gap caused by current SSA practices from the ground is not simply overcome by moving the platform to space. Planning, manufacturing, executing, and maintaining a space mission requires a large amount of labour and cost. Moreover, a fair comparison with ground-based systems must be drawn before switching to a space-based radar system for SSA in practice. Several aspects determine whether or not the idea or concept is viable for a long-term purpose, out of which some will be assessed to answer the first research question of the thesis.

### Research question 1

Is using a space-based radar system **feasible** for space surveillance and tracking of small-sized debris objects in GEO?

- What are the **performance metrics** that determine the system's feasibility?
- How does the performance of the space-based system **compare** with conventional ground-based SSA systems?

The thesis explores the primary feasibility by analysing how well the orbit of an object in GEO is reproduced by the observations collected by the INDIGO system. Based on the metrics determined from research question 1, more specific questions about the system's modeling, measurement collection, and orbit prediction performance can be formulated. The second research question of this thesis is then formulated.

### Research question 2

How do the dynamic model parameters, observation types, and trajectory prediction outcome contribute to the **feasibility assessment** of the system?

- For which **type** or **settings** of the **orbit propagation model** is the system's feasibility assessed, given a requirement on orbit accuracy?
- Which **category** or **combinations** of collected **in-situ measurements** lead to the optimal performance of the space-based system?
- How well is the orbit determination scheme capable of **predicting the debris orbit** when the system collects no measurements?

To prove the system's workability, several cases will be studied to analyse the system's sensitivity to changing geometries and configurations. The prediction performance due to these changes will be catered to in the last research question of the thesis. A design space will be optimised for the performance metrics defined in research questions 1 and 2 to recommend a feasible space-based radar observation system to fulfill the overall research goal.

### Research question 3

How **sensitive** is the orbit determination **accuracy** of small-sized debris objects in GEO to changes in uncertainties and satellite geometric configuration?

- How do changes in the **system noise** and **uncertainties** affect the accuracy of the orbit determination and prediction?
- At what optimal **orbital altitude** and **inclination** must the system be positioned to obtain the best possible orbit determination and prediction accuracy?
- To what extent does the performance of the system **improve** if **extra tracking satellites** are introduced, and what would be the optimal geometric **configuration**?

Space debris is a growing hindrance to the future of space exploration and earth observation missions. Due to the increasing threat to active satellites, especially in GEO, it is important to build and maintain space object catalogues. As highlighted in this chapter, obtaining accurate and up-to-date data on the state and characteristics of small-sized objects is crucial for STM to predict conjunctions. Current SSA activities in GEO are limited by object size, distance, and accuracy.

Optical telescope networks scan the GEO belt for a limited observation time every night with clear sky conditions. Each object is analysed for a short period, not enough to accurately predict its orbit for longer. This knowledge gap in SSA is identified in this chapter, laying the foundation for this thesis. Three research questions originated from this goal to investigate the topic deeper, which will be answered at the end of this study.

In the subsequent chapter, the underlying concepts for conducting the research will be discussed comprehensively. It will lay the foundation for understanding the space-based radar system, the orbital model parameters, and the theory of orbit determination. The research approach, set-up, and results of the study will follow from Chapter 3 on the theoretical framework and will help the reader better understand them.



# 3

## Theoretical background

This chapter is the theoretical backbone of the thesis, dedicated to laying the necessary background for the research. The relevant concepts such as the dynamics of an object in the GEO regime, parameters of a space-based radar system, and the orbit determination process followed to determine performance metrics for the system are defined here. Upon reading the chapter, it is expected that the reader will be able to connect the research outlook described previously in Chapter 2, to the methodology adopted and results obtained from it in the later chapters of this thesis report.

The chapter is structured in the following way. Section 3.1 gives a general but short overview of the frames of reference, relevant forces acting on an object, and the representation of its orbital trajectory over time. This is followed by Section 3.2, which describes the space-based radar system. The selected radar parameters of the system are presented along with their motivation, which is conceptualised to collect in-situ measurements for GEO debris objects. The chapter ends with an overview of the orbit determination theory provided in Section 3.3. It describes the estimation method and the evaluation of performance parameters, which are later studied to assess the system's feasibility.

### 3.1. Orbital dynamics

This section is dedicated to presenting a physical understanding of satellite orbit dynamics in GEO. A numerical model will be developed in the thesis, which will simulate the motion of a debris object and the space-based radar observation satellite. It is important to understand the representation of their motion around the Earth influenced by acting perturbing forces. The detailed explanation and choices related to the selection of reference frames, coordinate systems, and perturbations were discussed earlier during the literature review phase of the thesis. They will be revisited briefly in the subsequent sections.

#### 3.1.1. Reference frames

According to Wakker [27], a reference frame consists of a set of identifiable fiducial points on the sky along with their coordinates, which specify how the origin and orientation of a celestial body can be incorporated to construct a system of reference. The development of a dynamic model for the GEO environment originates from the choice of appropriate model coordinates, described with respect to a convenient frame of reference. Frame transformations will be performed for

ease of computation and interpretation. Three reference frames are adopted in this thesis, which are mentioned as follows.

### **Earth-Centred Inertial (ECI)**

As the name suggests, this frame is fixed with respect to the inertial space, with its origin at the Earth's centre. Representing the motion of objects in space is possible in a simple way using this representation. The x-axis of an ECI frame is aligned in the direction of the intersection between the equatorial plane (plane passing through the Earth's equator) and the ecliptic plane (the orbital plane of the Earth around the Sun), also referred to as the direction of the vernal equinox. The vernal equinox varies for different epochs due to the precession and nutation of the Earth's rotational axis and must be selected to define the ECI frame. The most commonly used ECI frame is the J2000 frame, which defines the x-axis to be pointed towards the vernal equinox measured on 1st January 2000 at 12:00 terrestrial time [28]. The z-axis of the frame is aligned with the Earth's rotational axis (in the direction of the North Pole), and the y-axis coincides with the equatorial frame, completing the orthogonal basis.

In this thesis, the J2000 frame is adopted to represent the orbital motion of GEO objects around the Earth in a non-rotating inertial frame. This simplifies the propagation of the equations of motion by neglecting the effect of Earth's rotation and makes computation straightforward.

### **Earth-Centred Earth-Fixed (ECEF)**

This reference frame originates at the Earth's centre but is not inertial, unlike the ECI frame. Fixed with respect to the Earth, the rotation of the frame coincides with the Earth's rotation. The x-axis of this frame is aligned in the direction of the Greenwich Meridian, and the z-axis is in the direction of the Earth's rotational axis, similar to the convention in the ECI representation. The y-axis of the ECEF frame is defined accordingly to complete the orthogonal basis with the previously defined x-axis and z-axis.

This is very useful in representing the position and velocity of terrestrial objects and tracking satellites from the ground. Since the thesis is focused on space-based tracking, a simple inertial Earth-centred system (J2000) is sufficient for the orbital model. However, the Earth's gravitational field is fixed with respect to the Earth's centre and defined in the geocentric rotating frame [27]. Hence, the acceleration components due to the Earth's gravity field are computed throughout the simulation period in the ECEF frame per epoch. They are transformed to the J2000 frame before propagating to the next epoch.

### **Local-Vertical Local-Horizontal (LVLH)**

Space-based measurements are taken with respect to a satellite whose orbit is simulated in the J2000 frame, as discussed earlier. In principle, the measurements are collected with respect to the body-fixed reference frame, which coincides with its centre of mass. In this thesis, the observing satellite is assumed to be a point mass whose rotational dynamics are not considered in the simulation. For simplification, the body-fixed reference frame is assumed to coincide with the local orbital frame, also known as the Local-Vertical Local-Horizontal (LVLH) frame.

In this thesis, the LVLH frame (also known as the Radial-Tangential-Normal or RTN frame) is adopted to represent the simulation of pseudo-measurements from the space-based system to collect observation data on the debris object. The x-axis of this frame is oriented in the radial direction of the instantaneous position of the user satellite, while the y-axis points along the velocity vector, which is tangential for a circular orbit. The z-axis completes the orthogonal basis,

normal to the x-y plane, in the direction of the orbit's angular momentum [28]. An illustration of the J2000 and the LVLH frames adopted in the thesis is presented in Figure 3.1.

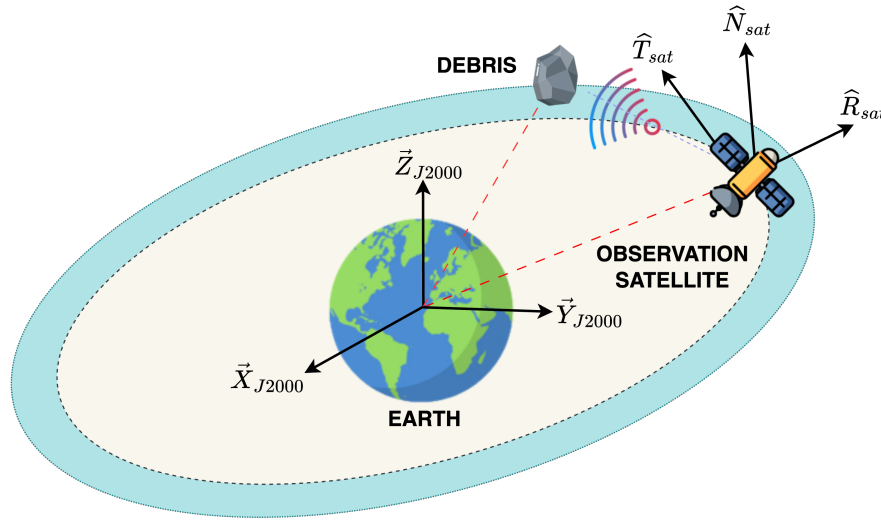


**Figure 3.1:** Overview of the inertial and orbital reference frames of the observation satellite and the debris object. The J2000 frame originates at the Earth's centre, with axes marked as  $\vec{X}_{J2000}$ ,  $\vec{Y}_{J2000}$  and  $\vec{Z}_{J2000}$ . The spacecraft and the debris are modeled as point masses, with the local orbital frame coinciding with their centres of masses. Unit vectors represent the observation satellite LVLH frame in the radial  $\hat{R}_{sat}$ , tangential  $\hat{T}_{sat}$  and normal  $\hat{N}_{sat}$  directions.

The frame transformations performed during the simulation are discussed in Appendix A.

### 3.1.2. State-vector representations

A suitable coordinate system presents the origin and orientation of a reference frame. To know the trajectory of an object in orbit, they are represented in the form of state vectors. The motion of the object in orbit can be represented in various forms. Depending on the ease of computation or interpretation, they may be transformed from one form to another. Two sets of coordinate systems have been used to represent the state of an object (satellite and debris) throughout the thesis, which is as follows.

#### Cartesian system

An object's position and velocity in orbit can be expressed in three-dimensional space in Cartesian coordinates, with  $x$ ,  $y$ , and  $z$  describing the position and  $\dot{x}$ ,  $\dot{y}$  and  $\dot{z}$  representing the velocity. The state vector combines the position and velocity vectors computed at a given epoch  $t$ , as defined in Equation 3.1.

$$\vec{X}(t) = [x(t) \quad y(t) \quad z(t) \quad \dot{x}(t) \quad \dot{y}(t) \quad \dot{z}(t)]^T \quad (3.1)$$

The computation of state vectors is easy and fast for Cartesian coordinates. They are used in the propagation and estimation of orbits in this thesis.

#### Kepler orbital elements

Defining the state of an object in Cartesian coordinates is often difficult to interpret since the position and velocity elements precisely vary over time. This is where representing the state in

terms of Kepler orbital elements is advantageous. It helps easily understand the orbit's geometry and position of an object in orbit at any given epoch. The state vector containing the Kepler orbital elements is given in Equation 3.2.

$$\vec{X}_{Kepler}(t) = [a \ e \ i \ \Omega \ \omega \ \theta(t)]^T \quad (3.2)$$

In the above equation,  $a$  is the semi-major axis,  $e$  is the eccentricity,  $i$  is the inclination,  $\omega$  is the argument of the pericentre,  $\Omega$  is the right ascension of the ascending node (RAAN), and  $\theta$  is the time-dependent true anomaly. An illustration of some of the orbital elements can be seen in Figure 3.2.

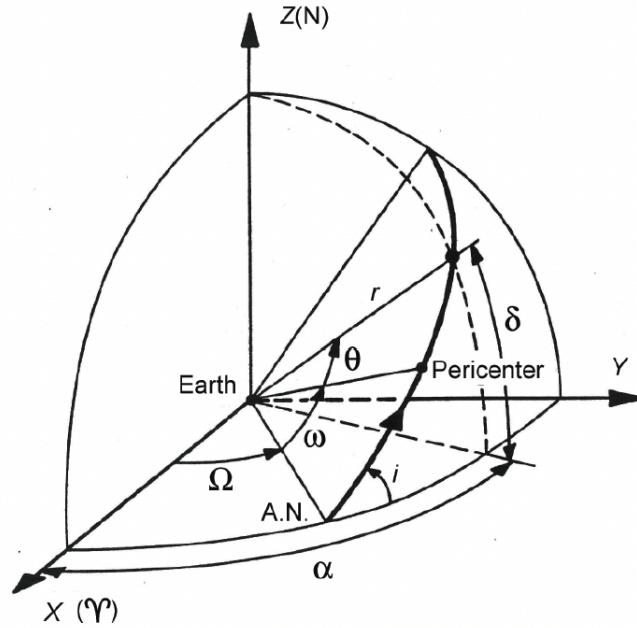


Figure 3.2: The orbital elements of a satellite in spherical coordinates as illustrated in Wakker [27].

The six Kepler orbital parameters mentioned in Equation 3.2 are provided in the model as inputs to specify the initial position at the first simulation epoch. The transformation algorithm between Cartesian and Keplerian representations of the state vector is presented in Appendix A.

### 3.1.3. Modeling of forces in GEO

According to Newton's law of universal gravitation, an object's motion around the Earth can be expressed as an ordinary differential equation. The point-mass gravity acceleration of the Earth is the most dominant acceleration acting on the object and is expressed by Equation 3.3 [27].

$$\ddot{\vec{r}} = -\frac{\mu}{r^3} \vec{r} \quad (3.3)$$

where  $\mu$  is the gravitational parameter of the Earth, which has a value of  $398600.4418 \text{ km}^3/\text{s}^2$ ,  $\vec{r}$  is the object's position vector, defined as the Cartesian position components of the state vector defined earlier in Equation 3.1. The result of Equation 3.3 is a Kepler orbit.

In reality, the orbit of an object is not purely Keplerian. Perturbations are acting on it, which causes a change in the dynamics of the orbital behaviour. Perturbations may be of large magnitude or may also seem to be small. However, the small effects may keep aggregating over a long period to the point when they are no longer insignificant. The thesis focuses on the GEO orbital regime, which makes it important to understand the different perturbing forces acting on the object to simulate a model close to reality. Hence, this section will describe the theory behind the different orbital perturbations used in the model for the reader to understand the physics of the problem.

### 3.1.3.1 Spherical harmonics

The point-mass expression in Equation 3.3 originates from the assumption that the Earth is spherically symmetric in shape and radially symmetric in density. This results in a non-uniform gravitational field of the Earth. In other words, the latitudinal and longitudinal variations in the shape and mass distribution of the Earth contribute to the gravitational field deviating from that of a perfect sphere. The gravitational potential  $\vec{U}_{EB}$  is defined in terms of spherical harmonics, as described in Equation 3.4. Here, the potential is assumed to be static, independent of the effect of solid Earth and ocean tides [27].

$$U_{EB}(\vec{r}_{EB}) = -\frac{\mu}{r_{EB}} \left[ 1 + \sum_{n=2}^{\infty} \sum_{m=0}^n \left( \frac{R_E}{r_{EB}} \right)^n P_{n,m}(\sin \phi) (C_{n,m} \cos m\Lambda + S_{n,m} \sin m\Lambda) \right] \quad (3.4)$$

Here  $\vec{r}_{EB}$  is the position vector of a general orbiting body B w.r.t. the Earth,  $R_E$  is the mean radius of the Earth at the equator,  $\phi$  is the geocentric latitude and  $\Lambda$  is the geographic longitude.  $P_{n,m}(\sin \phi)$  is known as the associated Legendre polynomial of degree  $n$  and order  $m$ , with argumentation of  $\sin \phi$ . The two scaling terms  $C_{n,m}$  and  $S_{n,m}$  depict the constant model scaling parameters, where each combination of  $n$  and  $m$  represents a distinct gravity field variation. They are generally expressed as spherical gravity field coefficients in terms of  $J_{n,m}$  and  $\Lambda_{n,m}$  as shown in Equation 3.5.

$$\begin{aligned} J_{n,m} &= \sqrt{C_{n,m}^2 + S_{n,m}^2} \\ \Lambda_{n,m} &= \frac{1}{m} \text{atan2}^1(S_{n,m}, C_{n,m}) \end{aligned} \quad (3.5)$$

Spherical harmonics can be categorised into three types, depending on the type of mass density deviations. When the deviations are only in the north-south direction i.e. in the latitude bands, they are known as zonal harmonics ( $m = 0$ ). On the other hand, when they are in the east-west direction i.e. in the longitudinal bands, they are known as sectorial harmonics ( $m = n$ ). When they are both in north-south and east-west directions, they are known as tesseral harmonics ( $m \neq n$ ).

In the current available detailed model, these spherical harmonic coefficients can be evaluated for orders and degrees as high as 2150. For most applications in astrodynamics, a truncated version of the spherical harmonics model is used, considering only a limited number of terms that have a significant contribution to the acceleration [27]. For the thesis, the two most relevant spherical harmonic coefficients  $J_2$  and  $J_{2,2}$  are considered for analysis and application in the model. The coefficient values for these two spherical harmonics have been extracted from the GRACE GGM02C Earth gravity field model and are presented in Table 3.1 [29].

<sup>1</sup>As atan returns an angle lying between  $-\pi/2$  and  $\pi/2$ , atan2 is used in this study when calculating an angle that can lie between  $-\pi$  and  $\pi$ .

**Table 3.1:** Overview of the two spherical harmonic coefficients used in this thesis.

Degree $n$	Order $m$	$J_{n,m}$	$\Lambda_{n,m} [^\circ]$
2	0	$1082.6357 \times 10^{-6}$	0
2	2	$1.8155628 \times 10^{-6}$	-14.9287

In the rest of Section 3.1.3.1, the two spherical harmonic coefficients  $J_2$  and  $J_{2,2}$  considered in this study are explained and motivated for their inclusion in the model.

### Term $J_2$

The value of the  $J_2$  coefficient is  $1082.6357 \times 10^{-6}$  as seen in Table 3.1. It is the largest among all other coefficients [30]. When the gravitational potential function described by Equation 3.4 is expanded till degree and order 2, the gravitational potential as a result of only the  $J_2$  coefficient is obtained. This is given by Equation 3.6.

$$\vec{U}_{J_2}(r, \phi) = \frac{1}{2} \mu J_2 \frac{R_E^2}{r^3} (3 \sin^2 \phi - 1) \quad (3.6)$$

When the gradient of this potential function is calculated, the perturbing acceleration due to the  $J_2$  zonal harmonic coefficient can be expressed in Cartesian coordinates as given by Equation 3.7 [27].

$$\begin{aligned} f_x &= -\frac{3}{2} \mu J_2 x \frac{R_E^2}{r^5} \left(1 - 5 \frac{z^2}{r^2}\right) \\ f_y &= -\frac{3}{2} \mu J_2 y \frac{R_E^2}{r^5} \left(1 - 5 \frac{z^2}{r^2}\right) \\ f_z &= -\frac{3}{2} \mu J_2 z \frac{R_E^2}{r^5} \left(3 - 5 \frac{z^2}{r^2}\right) \end{aligned} \quad (3.7)$$

The effect of the  $J_2$  spherical harmonics can be interpreted by computing these accelerations for a point on the Earth's surface. In a physical sense, the  $J_2$  effect originates from the Earth's rotation, which causes the oblateness of the gravity field [31]. This effect is also commonly known as polar flattening and can be visualised in two dimensions (in the equatorial plane) as seen in Figure 3.3, as well as in three dimensions as seen in Figure 3.4.

The magnitude of  $J_2$  acceleration is plotted on the Earth's surface and visualised in the figures above. The magnitude of the acceleration is in the order of  $10^{-5}$  km/s<sup>2</sup>, symmetrically distributed across the latitude belts. The Earth's oblateness is also visualised with slightly higher acceleration values at the poles compared to the equator.

### Term $J_{2,2}$

Deviations due to the shape and distribution of mass density in the east-west direction cancel out for satellites with an orbital period greater than a sidereal day. The effects of sectorial harmonics are thus ignored since their contribution is negligible. However, an object in geostationary orbit stays at the same point over the Earth's equator, with an orbital period of exactly one sidereal day. This causes the orbit to be perturbed relatively strongly by accelerations due to  $J_{n,m}$  harmonic coefficients with  $n = m$ . Although  $J_{2,2}$  has a small value of  $1.8155628 \times 10^{-6}$ , it is dominant over the rest of the sectorial harmonics terms and is the only  $J_{n,m}$  term considered in this thesis.

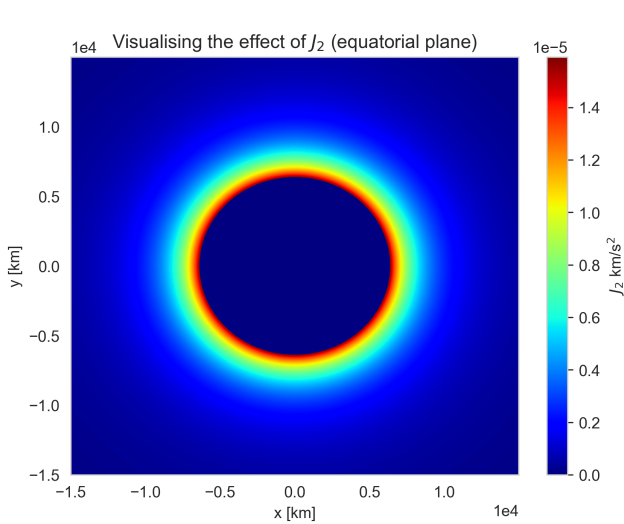


**Figure 3.3:** The magnitude of the  $J_2$  acceleration visualised in two-dimensional space in the equatorial plane. The acceleration pattern can be seen as circular rings, whose magnitude in  $\text{km/s}^2$  decreases with increasing distance from the Earth's surface.

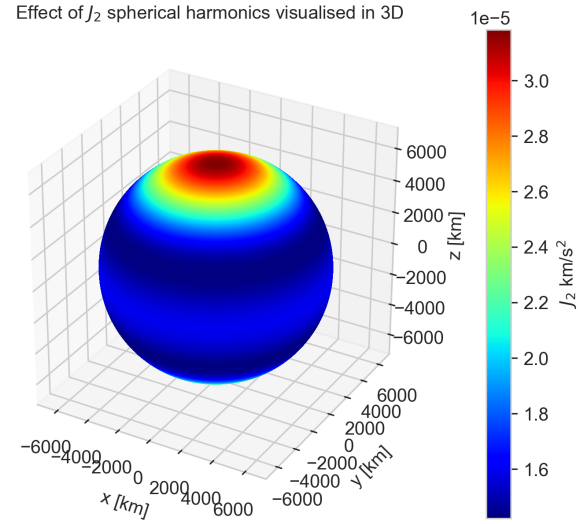


**Figure 3.4:** The magnitude of the  $J_2$  acceleration visualised in three-dimensional space on the surface of the Earth. The acceleration pattern can be seen varying as latitude bands, whose magnitude in  $\text{km/s}^2$  increases when moving towards either pole away from the equator.

When the gradient of the potential function is calculated, including terms with order and degree 2, the perturbing acceleration due to the  $J_{2,2}$  zonal harmonic coefficient is expressed in Cartesian coordinates as given by Equation 3.8.

$$\begin{aligned}
 f_x &= k_{J_{2,2}} \left[ x \left( 5 \frac{z^2}{r^4} - \frac{3}{r^2} \right) \cos(2 \operatorname{atan2}^2(y, x) - \Lambda_{2,2}) + \frac{y}{\sqrt{x^2 + y^2}} \left( 1 - \frac{z^2}{r^2} \right) 2 \sin(2 \operatorname{atan2}(y, x) - \Lambda_{2,2}) \right] \\
 f_y &= k_{J_{2,2}} \left[ y \left( 5 \frac{z^2}{r^4} - \frac{3}{r^2} \right) \cos(2 \operatorname{atan2}(y, x) - \Lambda_{2,2}) - \frac{x}{\sqrt{x^2 + y^2}} \left( 1 - \frac{z^2}{r^2} \right) 2 \sin(2 \operatorname{atan2}(y, x) - \Lambda_{2,2}) \right] \\
 f_z &= \frac{5k_{J_{2,2}}}{r^2} \left[ z \left( \frac{z^2}{r^2} - 1 \right) \cos(2 \operatorname{atan2}(y, x) - \Lambda_{2,2}) \right]
 \end{aligned} \tag{3.8}$$

where  $k_{J_{2,2}}$  is a constant defined as follows :

$$k_{J_{2,2}} = 3\mu J_{2,2} \frac{R_E^2}{r^3}$$

Similar to what was done for  $J_2$ , the effect of spherical harmonics due to  $J_{2,2}$  can also be visualised. The  $J_{2,2}$  term contributes to the equatorial stretching or squeezing of the Earth's gravitational field, which subjects an object in GEO to significant east-west perturbations [31]. This effect can be visualised in two dimensions in Figure 3.5, and in three dimensions in Figure 3.6.

The magnitude of the  $J_{2,2}$  acceleration is also plotted on the Earth's surface and visualised in the figures above. The magnitude of the acceleration is in the order of  $10^{-7} \text{ km/s}^2$ , symmetrically distributed across the longitude belts, in contrast to  $J_2$  earlier. Compared to a uniform distribution for the  $J_2$  effect, the  $J_{2,2}$  term shows longitudinal variations with four points with a higher acceleration magnitude.

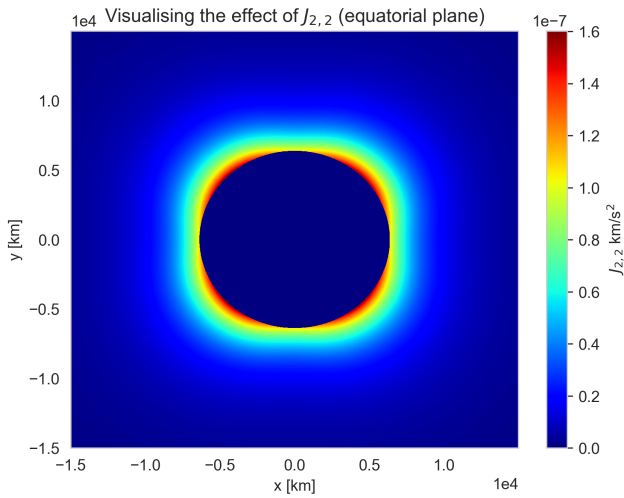


Figure 3.5: The magnitude of the  $J_{2,2}$  acceleration in  $\text{km/s}^2$  is visualised in two-dimensional space in the equatorial plane. The acceleration pattern can be seen as four peaks, showing longitudinal variations.

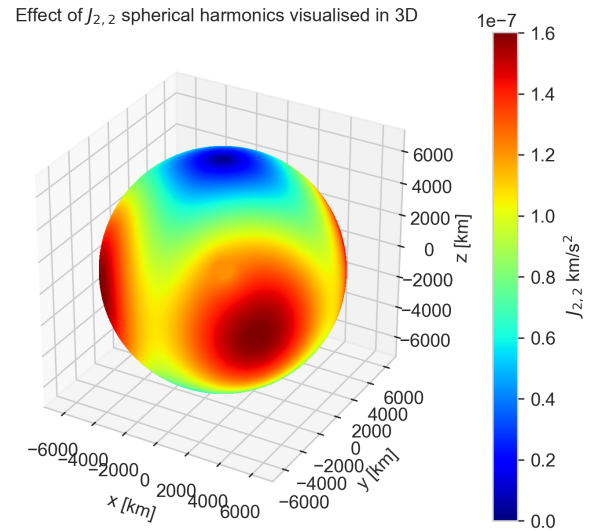


Figure 3.6: The magnitude of the  $J_{2,2}$  acceleration visualised in three-dimensional space on the surface of the Earth. It can be seen that the magnitude of the acceleration  $\text{km/s}^2$  is rather smaller at the poles and more at the four longitude positions.

### 3.1.3.2 Lunar third-body perturbation

Apart from the Earth's point mass and spherical harmonics gravity, third bodies in the environment affect the orbits of satellites. Third-body perturbations on an Earth-orbiting satellite due to the Moon can be expressed by Equation 3.9.

$$\vec{f}_{Moon} = \mu_{Moon} \left[ \frac{\vec{r}_{Moon} - \vec{r}}{\|\vec{r}_{Moon} - \vec{r}\|^3} - \frac{\vec{r}_{Moon}}{\|\vec{r}_{Moon}\|^3} \right] \quad (3.9)$$

As seen in the equation, the perturbation depends on the gravitational parameter of the Moon  $\mu_{Moon}$  which has a value of  $4902.8001 \text{ km}^3/\text{s}^2$  and three position vectors. Here,  $\vec{r}$  represents the position vector of the satellite w.r.t. the Earth,  $\vec{r}_{Moon}$  represents the position of the Moon, relative to the Earth while  $\vec{r}_{Moon} - \vec{r}$  denotes the position of the Moon w.r.t. the satellite. An illustration denoting the vectors can be seen in Figure 3.7.

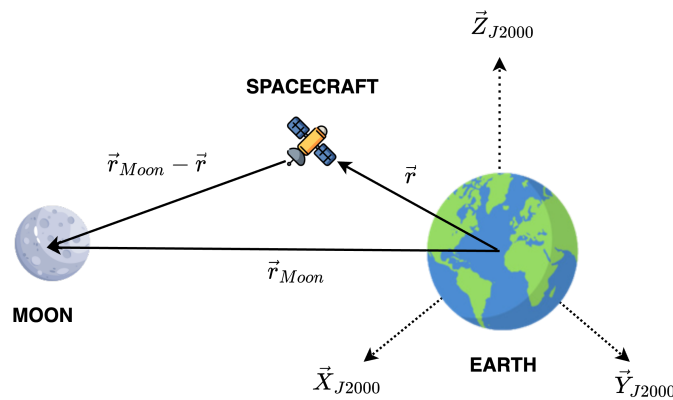


Figure 3.7: Position vectors for visualisation of a satellite's perturbation due to the Moon as a third body.

The geocentric position of the Moon w.r.t. the Earth or  $\vec{r}_{Moon}$  is epoch-dependent since the positions of the Moon and the Earth keep changing. The ephemerides of the Moon can be downloaded from the Horizons website provided by the Jet Propulsion Laboratory (JPL) given an epoch [32]. However, for the sake of versatility, the position vector of the Moon at a given epoch is analytically computed by the algorithm specified in Curtis [30].

### 3.1.3.3 Solar third-body perturbation

The Sun's influence on Earth-orbiting satellites' orbits is also significant. Similar to what was done for the Moon, third-body perturbations on an Earth-orbiting satellite due to the Sun can be expressed by Equation 3.10.

$$\vec{f}_{Sun} = \mu_{Sun} \left[ \frac{\vec{r}_{Sun} - \vec{r}}{\|\vec{r}_{Sun} - \vec{r}\|^3} - \frac{\vec{r}_{Sun}}{\|\vec{r}_{Sun}\|^3} \right] \quad (3.10)$$

As seen in the equation, the perturbation depends on the gravitational parameter of the Sun  $\mu_{Sun}$  which is equal to  $1.327 \times 10^{11} \text{ km}^3/\text{s}^2$  and three position vectors. Here,  $\vec{r}$  represents the position vector of the satellite w.r.t. the Earth,  $\vec{r}_{Sun}$  represents the position of the Sun, relative to the Earth while  $\vec{r}_{Sun} - \vec{r}$  denotes the position of the Sun w.r.t. the satellite. An illustration denoting the vectors can be seen in Figure 3.8.

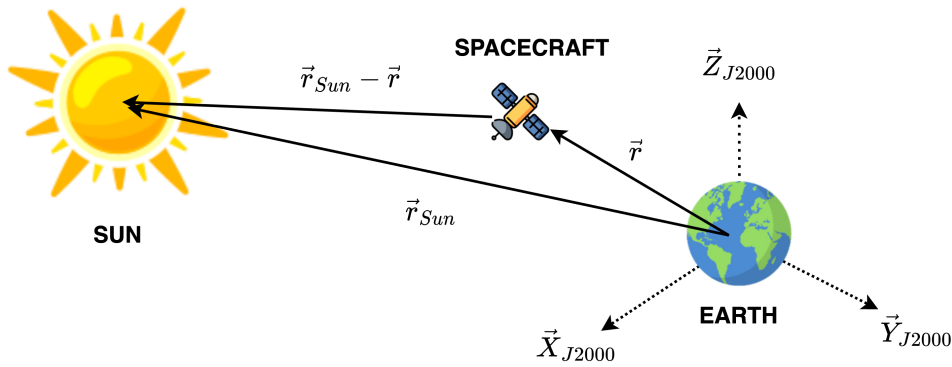


Figure 3.8: Position vectors for visualisation of a satellite's perturbation due to the Sun as a third body.

Similar to the lunar position, the geocentric position of the Sun w.r.t. the Earth or  $\vec{r}_{Sun}$  is epoch-dependent. The ephemerides of the Sun can also be downloaded from the Horizons website provided by JPL given an epoch [32]. However, like the Moon ephemerides, the position vector of the Sun at a given epoch is analytically computed by the algorithm specified in Curtis [30].

### 3.1.3.4 Aerodynamic drag

The Earth's atmosphere affects a satellite's trajectory by exerting a drag force. This perturbing force is dependent on several factors such as the drag coefficient of the object  $C_D$ , the atmospheric density  $\rho_{atm}$  which is altitude dependent, the area-to-mass ratio of the object ( $A/m$ ) and the velocity of the satellite relative to the rotating Earth atmosphere  $\vec{v}$ . The acceleration due to atmospheric drag can be computed from Equation 3.11 [27].

$$\vec{f}_{drag} = -\frac{1}{2} C_D \rho_{atm} \left( \frac{A}{m} \right) |\vec{v}| \vec{v} \quad (3.11)$$

The GEO regime is the orbital domain of interest for this thesis, which is at a high altitude of 35,786 km with a very low atmospheric density. As a consequence, the effect of aerodynamic drag is considered negligible in the simulation, which also simplifies the model to a great extent.

### 3.1.3.5 Solar radiation pressure

Apart from acting as a third body in an Earth-satellite environment, the Sun's radiation exerts a force on the satellite by emitting photons, which are absorbed and reflected by the spacecraft. This force exerted by the exchange of momenta between sunlight and the satellite surface is known as solar radiation pressure or SRP. There are many complex radiation pressure models depending on the shape of the satellite. A simple cannonball model has been assumed here, which assumes the body to be a homogeneous ball capable of fully reflecting or absorbing solar radiation. The overall force is opposite to the Sun vector and is calculated as given in Equation 3.12 [27].

$$\vec{f}_{SRP} = -C_r \left( \frac{S_r}{c} \right) \left( \frac{A}{m} \right) \frac{\vec{r}_{Sun} - \vec{r}}{||\vec{r}_{Sun} - \vec{r}||^3} \quad (3.12)$$

The magnitude and direction of SRP will depend on the satellite reflectivity properties and its orientation w.r.t. the Sun-satellite line. In the above equation,  $C_r$  is the radiation pressure coefficient,  $(A/m)$  is the reference area-to-mass ratio,  $(\vec{r}_{Sun} - \vec{r})$  is the vector pointing from the spacecraft to the Sun,  $c$  is the speed of light in vacuum equal to  $3 \times 10^8$  m/s, and  $S_r$  is the total amount of solar energy flux on Earth equal to  $1365$  W/m<sup>2</sup> [33]. In this thesis, the objects modeled have been assumed to be perfectly reflecting, which translates to a solar radiation coefficient value of 2. The solar radiation pressure is an important perturbation for large area-to-mass objects in higher orbits.

### 3.1.3.6 Summary of perturbations

To conduct a feasibility study, it is important to have a high-fidelity model yet simple to interpret. Due to this, the most relevant perturbations acting in the GEO regime were discussed and will be implemented in the model. The behaviour of perturbations discussed earlier as a function of orbital radius can be visualised in Figure 3.9 [27].

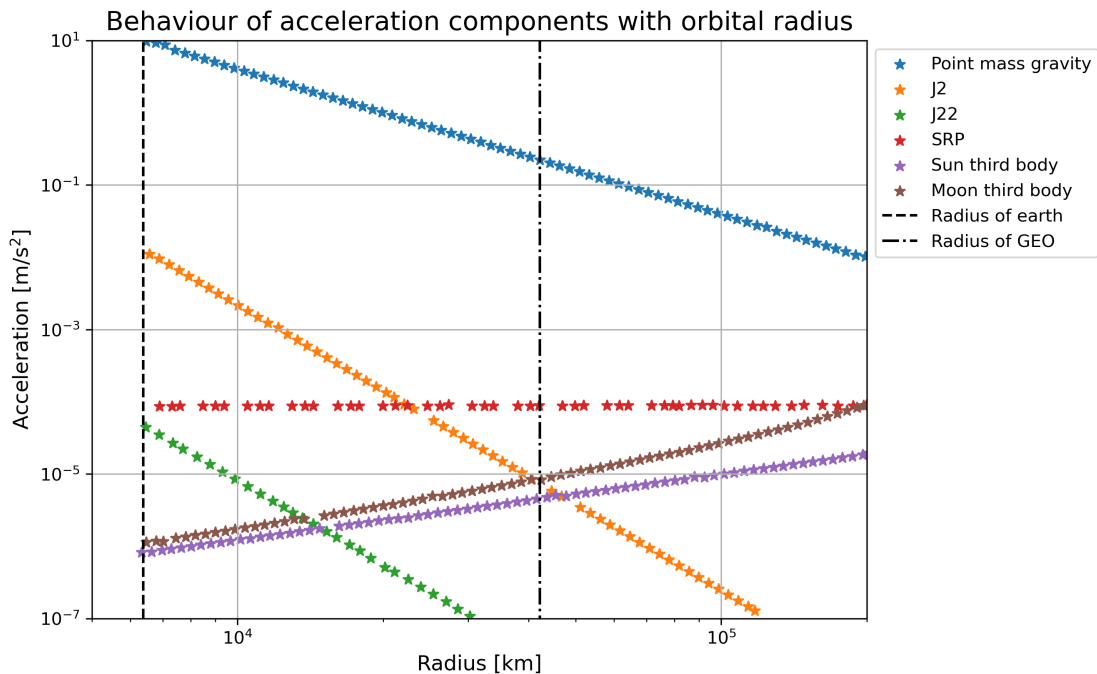


**Figure 3.9:** Variation of orbital perturbations on a satellite as a function of orbital radius, as adapted from Wakker [27]. The black dashed lines show the radius of the Earth and the GEO altitudes.

At the GEO altitude regime, the point-mass gravity acceleration shown in blue is the dominant acceleration throughout, with an order of magnitude close to  $0.2 \text{ m/s}^2$ . The green stars show the least affecting perturbation due to the  $J_{2,2}$  sectorial harmonics term. The straight red line, independent of orbital altitude, denotes the SRP. The exact magnitude depends on the satellite's surface properties and orientation with the Sun. The three perturbations at similar magnitudes are the  $J_2$  zonal harmonics term and the third-body perturbations due to the Sun and Moon, which lie in the order of magnitude of about  $10^{-5} \text{ m/s}^2$ .

The orbital dynamics of the problem was described in this section. The dominant accelerations discussed, such as the  $J_2$  and  $J_{2,2}$  terms, lunar and solar third-body perturbations, and SRP will be included in the orbital simulation model. This leads to the next aspect of the research i.e. the space-based observation system on which the feasibility study is based, discussed in Section 3.2.

## 3.2. Radar system theory

This section provides an overview of the theoretical aspects of a general radar and its various functionalities and parameters. Since this thesis is focused on the feasibility evaluation of a space-based radar, first, the motivation to choose a space-based radar is revisited by listing some of its major advantages and limitations in Section 3.2.1. Thereafter, the radar system parameters are made familiar to the reader by introducing the Radar link budget equation in Section 3.2.2, which is followed by explaining the different modes in which a radar can operate in Section 3.2.3. The rationale behind selecting radar waveforms and configurations is presented simply for the reader in Section 3.2.4. The section ends with Section 3.2.5, which explains how the measurement quality collected by the radar system can be quantified.

### 3.2.1. Motivation for space-based radar

A brief introduction to Radio Detection And Ranging (RADAR) was provided in Section 2.2, which defines the underlying working principle of a radar to detect and locate objects based on the echoes they reflect. Apart from enhancing the perception of an environment, the greatest application of radar lies in remote sensing due to its capability to scan large angular regions in a short amount of time. Moreover, the radar signals penetrate the atmosphere in any weather conditions to effectively provide better detection and measurements [34]. Due to limitations such as atmospheric losses, signal attenuation, and noise in the collected measurements, this thesis explores and reviews the performance of INDIGO, a conceptual space-based radar system. The advantages of using such a system motivate exploring it in the thesis. They are provided below.

- A better detection performance for the radar is expected due to the reduced distance between the target and the observer. Moreover, the reflected signal is expected to contain fewer sources of errors, facilitating better detection.
- As discussed earlier in Chapter 2, small-sized debris is critical for the safe operations of active satellites in GEO. An overview of different sources and their sizes can be seen in Figure 3.10 [35].

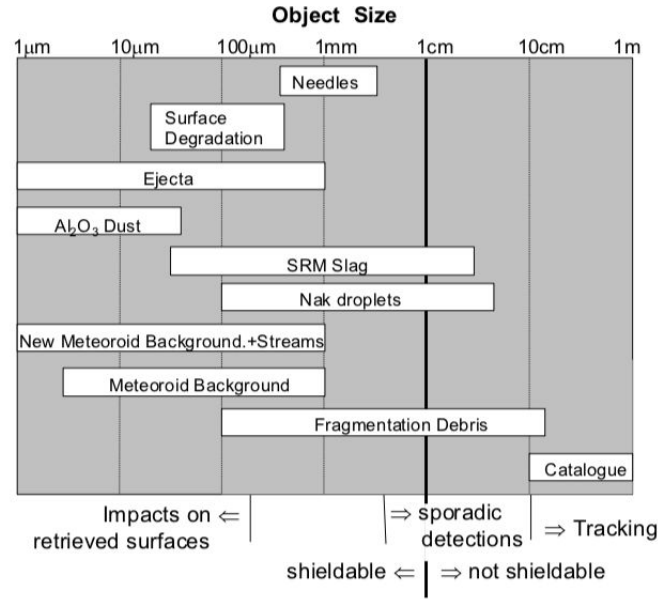


**Figure 3.10:** Size range of different debris particles. Objects in the range of 10 cm (for LEO) and 1 m (for GEO) are tracked from the ground. Impacts from mm-sized debris are possible to shield against. Sizes between 1 and 10 cm are crucial since they can neither be shielded against nor tracked from the ground [35].

The target of the thesis will be objects in the size range of 1 cm to 10 cm, which are either not shieldable or trackable. In the GEO regime, the study will focus on the debris caused by fragmentation from explosions of inactive satellites. The general expectation is that in-situ detection, surveillance, and tracking of such small-sized debris will be easier.

- Due to an observation platform close to the target object, debris is expected to be observed longer than ground observation time, allowing more frequent measurement opportunities.

Now that the motivation behind selecting a space-based radar has been presented, the details of the design and performance of a radar system can be understood in more detail.

### 3.2.2. Radar link budget

In general, a typical radar consists of a **transmitter** that sends out a radio signal i.e. a burst of energy, an **antenna** that receives the reflected signal, a **receiver** that amplifies the received signal, and a **signal processor** which distinguishes echoes from background noise or clutter, therefore, de-noising the signal. The act of radar designing depends on design and performance domains. The variables which affect the performance of a system are known as design parameters, while those which contribute to the evaluation of how well the radar functions are known as performance parameters [36].

The selection of a radar system to achieve a specific task or function starts with an optimal balance between the system design and performance parameters. This is done through a general **Radar range equation** or **Radar Link Budget analysis** which encapsulates target properties, radar characteristics, and distance between the target and observer for a given transmitting medium. This is presented in Equation 3.13 [37], followed by a brief explanation of the equation parameters.

$$SNR = \frac{P_t G_t G_r \lambda^2 \sigma L}{(4\pi)^3 R^4 k T_s B} \quad (3.13)$$

The **Signal-to-Noise Ratio** or **SNR** provided by any radar is its key performance measure. It is the

standard measure of a radar's ability to detect a target at a given range and is usually measured in decibel units. It is inversely proportional to the fourth power of the target **range**  $R$ .

The **peak power** at which the radar transmits a signal is given by  $P_t$ . The TIRA space observation radar in Germany operates at a peak power of 2 MW [34]. The higher the peak power, the better the SNR achieved. Having said so, limited power is available for space-based radars, which needs to be selected appropriately.

The **radar cross-section** or RCS of the target is given by  $\sigma$  in the radar range equation and is the measure of energy that is intercepted and scattered off the target back to the radar. The RCS is not simply related to the physical area of the target but mainly depends on the frequency and polarisation of the radio wave. The RCS of a target is determined by solving Maxwell's equations, which makes values for complex geometries very difficult to estimate [38]. For a simple spherical target, the RCS normalised with the surface area of a sphere of radius  $r$  is seen to vary as a function of the inverse of the radar wavelength  $\lambda$  in Figure 3.11.

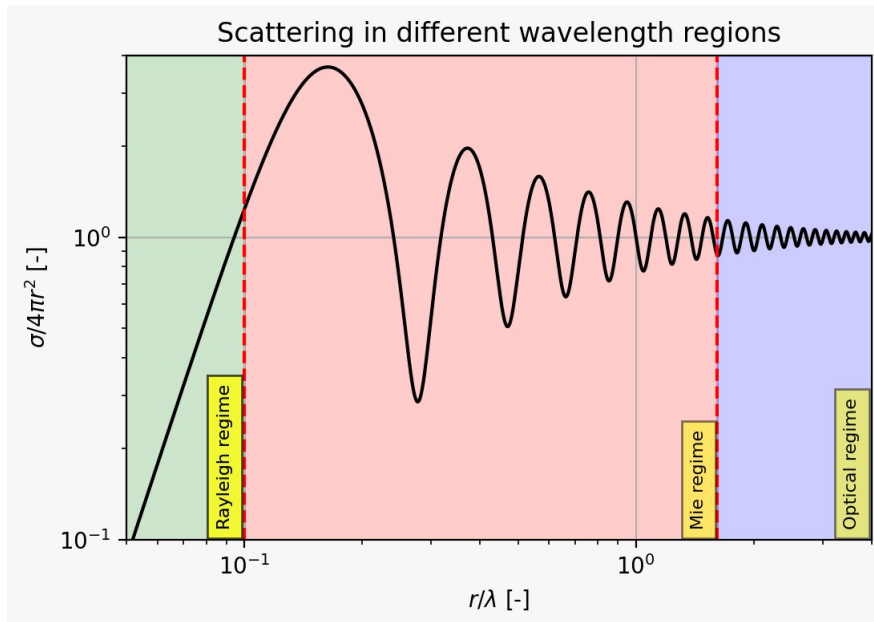


**Figure 3.11:** Normalised RCS as a function of object radius and wavelength. Three scattering regimes: Rayleigh, Mie, and optical are highlighted in green, red, and blue, respectively. This affects the computation of RCS of a simple conducting sphere. This plot is adapted from Li et. al [39].

The three scattering regimes, Rayleigh, Mie, and optical, are visible in the above plot. The spherical object's size is very small in the Rayleigh region (shown in green) compared to the wavelength ( $r \ll \lambda$ ), which causes the RCS to vary inversely with  $\lambda^4$ . In the optical region (shown in blue), the sphere's dimensions are larger than the wavelength ( $r \gg \lambda$ ), which leads to a constant RCS value of  $4\pi r^2$  (surface area of a sphere). In this research, a cross sectional scattering is considered instead of surface scattering, leading to an assumed RCS value of  $\pi r^2$ . The Mie or resonance region (shown in red) is the intermediate region between the Rayleigh and the optical region, which shows RCS value oscillations depending on the frequency selected. It can reach a maximum of 4 times the constant optical RCS value and a minimum of 0.26 the same optical RCS value [39].

A suitable **wavelength**  $\lambda$  is chosen for object detection depending on the target RCS. This is designed or selected based on **radar carrier frequency**  $f_c$  at which the signals are transmitted and

received. Radio-frequency bands vary in a wide range depending on system application and the requirements of the operation. The dependency of the carrier frequency with wavelength is given by the simple expression in Equation 3.14.

$$\lambda = \frac{c}{f_c} \quad (3.14)$$

where  $c$  is the speed of light in vacuum equal to a value of  $3 \times 10^8$  m/s. The carrier-wave frequency should be high if the object's RCS is modeled in the optical regime. This also ensures that to target objects of sizes between 1 and 10 cm, the wave's frequency should be between 30 GHz and 3 GHz, respectively. Choosing a higher frequency value ensures a reduction in overall system mass and size but increases the overall system power requirement. An optimal choice for the frequency band is needed, such that the target size objects can be detected with low power consumption.

The wavelength selection affects the **antenna beamwidth**  $\theta_{BW}$  of a radar which is defined at the level of half the power of the beam peak (a 3-dB beamwidth). Although it is not directly present in Equation 4.3, it is an important design parameter affecting the radiated power of the signal. A typical radar beam is shown in Figure 3.12 illustrating its beamwidth. Most of the power is represented by its beamwidth generated by the main lobe, followed by small minor lobes showing a fluctuation in signal behaviour [40].

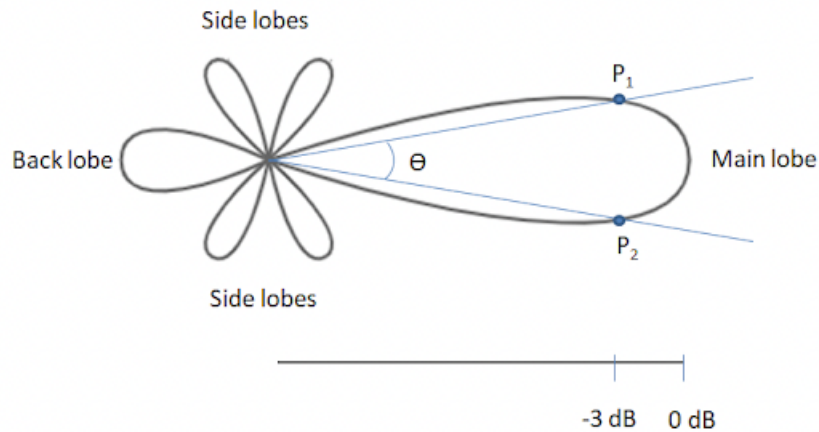


**Figure 3.12:** Geometry of a radar antenna beam (shown with a beamwidth  $\theta$ ). The main lobe and side lobes originating from the beam are depicted [40]

A standard metric for measuring the power of the signal's peak is the Half Power Beam Width (HPBW), whose power is given by the figure points  $P_1$  and  $P_2$ . Here,  $\theta$  corresponds to  $\theta_{BW}$ , whose signal strength decreases on moving towards the beam's centre of origin. The beamwidth represents the direction and distance of the signal strength, which gets narrower with high frequencies and wider with low frequencies. In general, the HPBW (in radians) for a lobe with diameter  $D_{lobe}$  and signal wavelength  $\lambda$  can be expressed by Equation 3.15.

$$HPBW = \frac{70\lambda}{D_{lobe}} \quad (3.15)$$

For surveillance radars, the beamwidth is large to detect targets at an angular offset with the axis of the beam, while tracking them requires a higher gain with a more focused beam. For a multi-function radar capable of both surveillance and tracking, the carrier frequency is adjusted based

on the functionality of the radar. For surveillance, more power is needed for better detection, but the pulses can be emitted with a lower carrier frequency. When the object is detected, the radar moves to a low power mode but emits waves at a higher frequency to accurately follow the object from an estimate based on prior measurements [41]. Subsequent discussion on the changing beamwidth of the selected radar configuration for this thesis is provided in Section 4.1.1.

$G_t$  and  $G_r$  are the **gains** for the transmitting and receiving antenna respectively, which is defined as the radiation intensity of the antenna in a given direction over that of an isotropic antenna which uniformly radiates in all directions [36]. If the transmitting and receiving antennae are the same (as in the case of pulsed Doppler radars), the gain value is taken as  $G$ . To ensure maximal signal return, the receiving antenna must have a high gain, which can be calculated by Equation 3.16.

$$G = \frac{4\pi\eta A_e}{\lambda^2} \quad (3.16)$$

Here,  $\eta$  refers to the **antenna efficiency** typically with values between 0.6 to 0.7 for ground-based systems [37].  $A_e$  denotes the **effective radiative area of the antenna**, which depends on the shape, size, and type of antenna used.

Among the remaining parameters in Equation 3.13,  $R$  is the **target range** i.e. the distance to a target from the observing system, which highly influences the SNR achieved and forming the measurement acquisition strategy for INDIGO of this study (more will be discussed in Section 4.1.2). Many sources of noise in a radar system affect its performance and accuracy. Some sources are solar, galactic, atmospheric, and human-made instrument noise, which gives rise to **total system losses** or  $L$  [36]. Free-space losses mainly dominate this term.  $T_s$  is the total **system noise temperature**, typically equal to 290 K for ground-based systems.  $B$  is the **signal noise bandwidth** of the receiver and  $k$  is the **Boltzmann constant** with a value of  $1.38 \times 10^{-23} \text{ J deg}^{-1}\text{K}^{-1}$ .

Knowledge of each link budget parameter is crucial for selecting the configuration and parameters for the space-based radar, which will be done in Section 4.1. However, a radar's different modes and functions can serve multiple purposes. They will be discussed in Section 3.2.3.

### 3.2.3. Radar functions

This section will briefly mention two main radar working modes. A radar can either operate in search mode or in track mode. It can also function in a Track-While-Scan (TWS) mode, having the possibility of switching between search and track modes.

While a surveillance radar is dedicated to detecting objects in its field of view, a tracking radar focuses on continuous measurements of the coordinates of a moving target to determine its path and predict its trajectory. Tracking can be done with range, range rate, and angular information collected by a surveillance radar. The angle at which the target is aligned w.r.t. the beam axis is an important property for tracking radars since they try to keep the beam pointed in the direction of the target, thereby maximising the SNR. A surveillance radar can receive signals from any direction if it is above its detection threshold.

Here, the space-based radar is expected to detect and collect measurements on small-sized debris objects, which are unknown due to limitations by ground-based sensors. It must be capable of scanning a wide area to detect new objects and derive information about their range, range rate, and angles. A TWS radar is suited to collect the in-situ measurements, which are processed

to generate an orbit estimation. With multiple measurement opportunities, the orbit prediction behaviour is expected to improve, which can be used for precise object tracking.

### 3.2.4. Selection of waveform and configuration

Several factors significantly affect the overall radar design. The waveform type must be chosen depending on the operating environment and intended use. There are broadly two types of waveforms that are presently used in most radars. This classifies radars into two types depending on the type of waveform used: **Continuous Wave (CW)** radars and **pulsed Doppler radars**.

**Continuous Wave (CW) radars** constantly emit in the radio-frequency spectrum, with a low power requirement. Their waveform is visualised with an example of a CW waveform shown in Figure 3.13. They are limited in their transmission power, which allows continuous operation. They are good for short-range targets since they are simple to design and implement with lower power and cost requirements, such as in a police speed measurement radar. Moreover, they are widely used in measuring target Doppler shift, which is used to estimate radial velocity by applying frequency modulation to the signal, which is then known as an FMCW waveform [38]. However, since the antenna must operate continuously, two separate antennae are required to transmit and accept the radar signals to avoid interference of signals. This limits their sensitivity and range, making them not an attractive choice for the study. Moreover, placing multiple antennae on a satellite is an extra challenge, which does not theoretically outperform the challenges a CW radar faces. Hence, CW radar waveforms are not considered in this thesis.

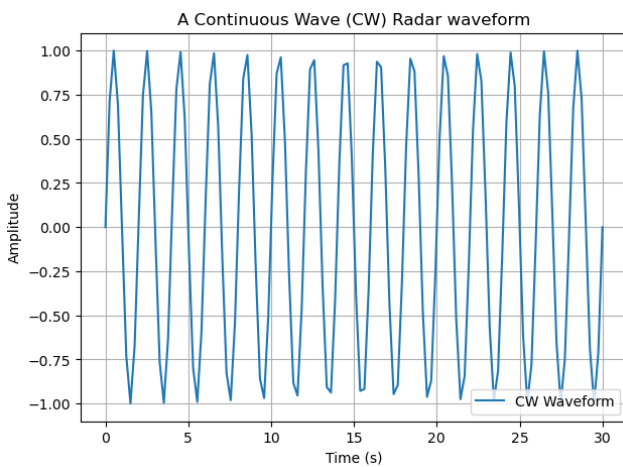


**Figure 3.13:** Visualisation of a CW radar waveform. The waves are emitted continuously and can operate at a lower power. The emission does not stop, and the radar detects a target by measuring the shift in the frequency spectrum. The waveform here is repeated every 2 seconds for a total duration of 30 seconds.

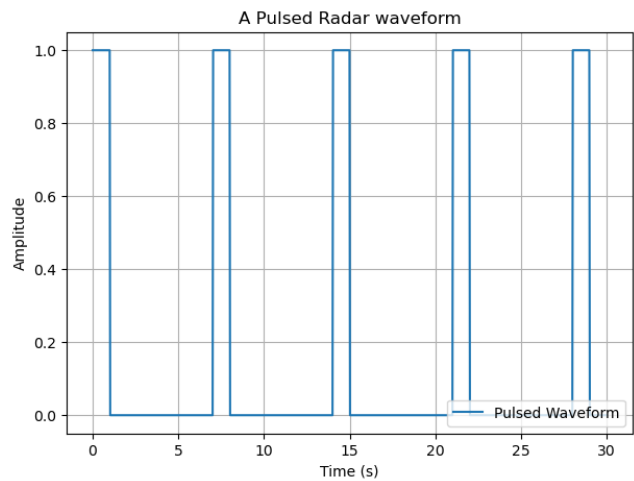


**Figure 3.14:** Visualisation of a pulsed waveform. The waves are emitted as high bursts of energy, after which the radar waits for a reflection. This waveform has a pulse duration of 1 second and a pulse repetition time of 7 seconds, out of which 6 seconds is reserved for listening for the echo that it transmitted previously.

A **pulsed Doppler radar wave** is based on the simple fundamental of sending a high burst of energy with a pulse duration  $\tau$  and waiting to receive its echo. The silence between pulses prevents signal interference while preserving the radar's operational power. A single antenna transmits and receives signals with the same gains. It measures the range to a target object using Equation 3.17.

$$R = \frac{c\Delta T}{2} \quad (3.17)$$

where  $\Delta T$  is the time trip time of the radar signal to and from the target, which then travels at the speed of light in vacuum  $c$  to a target at range  $R$ . It can also measure the target radial velocity along the Line-of-sight (LOS) vector  $v_r$  by measuring the Doppler shift in the transmitted and received frequencies. An increase in frequency is seen when the target comes closer to the radar, while a drop is seen as it moves away. A pulsed Doppler radar can measure the **Doppler frequency**  $f_d$  using Equation 3.18.

$$f_d = \frac{2v_r}{\lambda} \quad (3.18)$$

Pulsed Doppler radars come with functionalities such as pulse compression, which can vary the frequency during the pulse emission to allow the receiver to amplify the magnitude of the pulse, thus resulting in a higher SNR. All these characteristics are suited for the research conditions, making pulsed Doppler radars an attractive choice for selection.

Depending on the number of transmitters and receivers, there are different configurations of radars. In a broader sense, if one antenna transmits and receives the signal, the radar is called monostatic. On the other hand, if there are two antennae for transmitting and receiving signals separated by a certain distance, the radar is called bistatic. Since pulsed Doppler radars are the better waveform choice, choosing a monostatic radar configuration is sufficient for the thesis.

Apart from the waveform selection, the characteristics of a radar antenna influence the radar's ability to detect targets and precisely determine their position and other characteristics. Antennae can be a dish or a planar array depending on the functionalities needed. For tracking, narrow 'pencil' beams are preferred since they can concentrate the signal within the beam and receive a higher gain from the target, thus accurately knowing its trajectory before losing contact with it. However, a **phased array** radar with a planar surface is preferred if a broad area has to be surveyed. It can either have multiple pencil beams (originating from its multiple antenna elements) or a large 'fan-shaped' beam, which can be electronically steered in a desired direction, to measure the range, range rate and DOA (direction of arrival) of an object [41]. Phased-array radar configurations also have the advantage of efficiently switching from surveillance to a tracking mode by changing its dwell time and carrier frequency or adjusting the signal phase at the receiver [38]. This makes a phased array antenna with a pulsed waveform an appropriate choice for INDIGO, based on which parameters must be selected.

The general properties of a radar system are crucial for the operation and performance of any radar system and must be fully addressed while trading off between different possible configurations. This will be addressed in Section 4.1.

### 3.2.5. Measurement accuracy

The accuracy with which a radar can collect measurements depends on several factors. Accuracy refers to how close a measurement is to its true value [37]. Two of the most important contributors to the error sources of radar measurements are mentioned as follows:

- A threshold **SNR-dependent measurement error**, having a fixed standard deviation, is derived from the internal noise of the radar.

- Errors and uncertainties due to **system radar calibration** and **measurement process** lead to a constant bias in the measurements collected.

Accuracy is calculated as the root-mean-square (RMS) value of the difference between an estimated quantity and its true value. The standard deviations for range, range-rate, and angular observations can be derived using the **Cramer-Rao Lower bound** [42]. The standard deviation of range measurements  $\sigma_\rho$  can be calculated by Equation 3.19, and that of the range-rate measurements can be calculated by Equation 3.20.

$$\sigma_\rho = \frac{c}{2} \sqrt{\frac{3}{\pi^2 B^2 (2SNR)}} \quad (3.19)$$

$$\sigma_{\dot{\rho}} = \frac{\lambda}{2} \sqrt{\frac{3}{\pi^2 \tau^2 (2SNR)}} \quad (3.20)$$

The parameters in the above equations were previously introduced in Section 3.2.2. The Cramer-Rao lower bound for angular measurement accuracy is given by Equation 3.21. The identical standard deviation error value is taken for azimuth and elevation measurements.

$$\sigma_{az} = \sigma_{el} = \frac{\theta_{BW}}{k_M \sqrt{2(SNR)}} \quad (3.21)$$

Here,  $k_M$  is the monopulse pattern difference slope usually equal to 1.6. These equations will be useful to determine the standard deviations of the Gaussian white noise, which will be added to each of the true measurements in Section 4.2.2.2.

Having covered the two important aspects of the theoretical framework of the research, this section will describe the theory of the final pillar of this study: orbit determination of the debris object, based on the results of which the feasibility of the concept will be provided.

### 3.3. Orbit Determination theory

Determining the orbits of debris objects is a fundamental aspect of STM. The equations of motion are integrated w.r.t. time, which determines the debris's state at a given time during the simulation. However, the initial position and velocity of the debris are not known exactly, which introduces errors in the predicted motion.

In the work of Pocha [43], orbit determination has been defined as the process wherein the tracking observations are used to determine an object's orbital characteristics and **its position and velocity** in space. Tapley et. al [44] define orbit determination (OD) as follows:

#### Orbit determination

**Orbit determination** or **state estimation** is referred to as "the process of determining the best estimate of the state of an object (e.g. a satellite or debris) from collected observations, which are influenced by random and systematic errors" [44].

It was seen earlier in the literature study of this thesis that orbit determination could be performed using batch or sequential estimation techniques. The common **batch estimation** technique for orbit determination is the **Weighted Batch Least Squares (WLS)** method, while the

**Kalman Filter (KF)** is the **sequential estimator** for orbits. WLS is used for post-processing measurement data in a batch, while KF has more applications in real-time applications [42]. This thesis will focus on estimating the orbit of the debris object using a batch WLS method since continuous real-time updates are not required to prove the feasibility of a concept at this stage.

This section has two parts. The first part (Section 3.3.1) explains the basics and concept of the method of least squares used in orbit determination of satellites, which will also be used to determine the debris object's state. The second part (Section 3.3.2) explains the differential equation used to propagate a special set of equations known as the variational equations, which use observations and the force model behaviour to estimate the orbit.

### 3.3.1. Fundamentals of Least squares (LSQ)

The LSQ is essentially a simple optimisation formulation, which fits collected measurements to a mathematical model and minimizes the sum of the squares of the difference between the modeled observations and actual measurements (known as residuals) [45].

The vector containing the set of parameters to be estimated by the least squares technique is denoted by  $\vec{x}$ , which has the object's initial position  $\vec{r}_0$  and velocity vector  $\vec{v}_0$  and certain force parameters  $\vec{p}$  such as solar radiation pressure coefficient and drag coefficient, which influence the dynamical and observation model. The general formulation is given by Equation 3.22.

$$\vec{x} = \begin{bmatrix} \vec{r}_0 \\ \vec{v}_0 \\ \vec{p} \end{bmatrix} \quad (3.22)$$

In this thesis, no additional force parameters are estimated, which leaves the observed parameter set to contain only the state vector of the debris. Assuming there to be  $n_{meas}$  number of measurements, the vector of the measured observations  $\vec{z}$  can be given by Equation 3.23.

$$\vec{z} = \begin{bmatrix} z_1 \\ z_2 \\ \vdots \\ z_{n_{meas}} \end{bmatrix} \quad (3.23)$$

The estimation vector  $x$  with dimension  $6 \times 1$ , is integrated w.r.t. time, with an initial guess value of  $\vec{x}(t_0) = \vec{x}_0$ , and can be expressed in the following form as seen in Equation 3.24 [45].

$$\frac{d\vec{x}}{dt} = \vec{f}(t, \vec{x}) \quad (3.24)$$

where  $\vec{f}$  represents the ordinary differential equation function described by Equation 3.3 for the idealised case with no perturbations, and by Equation 4.9 for a fully perturbed model. The observations are described by the observation equation described by Equation 3.25.

$$\vec{z} = \vec{h}(\vec{x}_0) + \vec{\epsilon} \quad (3.25)$$

where  $\vec{h}$  represents the model value of the observations as a function of the state  $\vec{x}_0$  at the reference epoch  $t_0$ , and  $\vec{\epsilon}$  is the residual vector containing the difference between computed and

observed observations (residuals). The cost function  $J$  can thus be formulated as the minimising function for the LSQ problem. The expression is stated in Equation 3.26.

$$J(\vec{x}_0) = \vec{\epsilon}^T \vec{\epsilon} = (\vec{z} - \vec{h}(\vec{x}_0))^T (\vec{z} - \vec{h}(\vec{x}_0)) \quad (3.26)$$

However, a key challenge lies in the fact that the observation function  $\vec{h}$  is highly non-linear. It is attributed to how they are modeled (seen in Section 4.1.2). Hence, a linearisation must be performed before solving the least-squares problem. The solution obtained from the linearisation is an approximate solution to the non-linear problem. When Equation 3.25 is linearised around a reference state  $\vec{x}_0^{ref}$ , which is obtained after iterations from a starting initial approximate guess of  $\vec{x}_0^{appr}$ , the residual vector can now be expressed as given in Equation 3.27. An illustration from Montenbruck et. al [45] is provided in Figure 3.15, which shows the correction of the reference trajectory parameters to find the best fit for the observations.

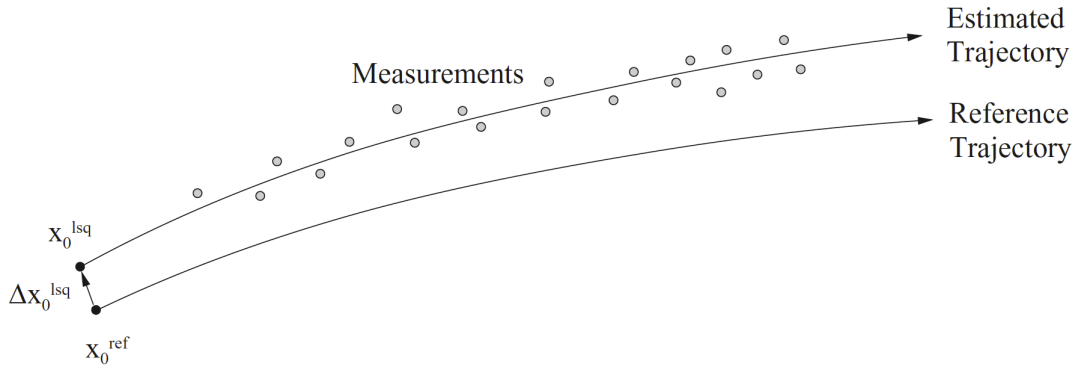


**Figure 3.15:** Schematic of the Least Squares method for orbit determination, from Montenbruck et. al [45]. A reference trajectory  $\vec{x}_0^{ref}$  is assumed as a starting point, which is corrected with each iteration to obtain an LSQ estimate  $\Delta \vec{x}_0^{lsq}$ , which is added to the reference guess, to obtain the initial state of the LSQ orbit  $\vec{x}_0^{lsq}$ , which fits through the measurements (shown as dots).

$$\vec{\epsilon} = \vec{z} - \vec{h}(\vec{x}_0) \approx \vec{z} - \vec{h}(\vec{x}_0^{ref}) - \frac{\partial \vec{h}}{\partial \vec{x}_0} (\vec{x}_0 - \vec{x}_0^{ref}) = \Delta \vec{z} - \mathbf{H} \Delta \vec{x}_0 \quad (3.27)$$

where  $\Delta z$  is the difference between the actual observations and the observations predicted by the dynamic model.  $\Delta \vec{x}_0$  represents the difference between the guessed value  $\vec{x}_0$  and the reference state  $\vec{x}_0^{ref}$ .  $\mathbf{H}$  is the Jacobian matrix, whose computation will be described in Section 3.3.2.

The cost function of the linearised LSQ problem is now re-formulated, which is given by Equation 3.28

$$J(\Delta \vec{x}_0) = (\Delta \vec{z} - \mathbf{H} \Delta \vec{x}_0)^T (\Delta \vec{z} - \mathbf{H} \Delta \vec{x}_0) \quad (3.28)$$

The least squares solution is estimated by solving the condition for a minimum  $\partial J / \partial \Delta \vec{x}_0 = 0$ . The general least squares solution, which assumes all measurements to be weighted the same, is given by Equation 3.29.

$$\Delta \vec{x}_0^{lsq} = (\mathbf{H}^T \mathbf{H})^{-1} (\mathbf{H}^T \Delta \vec{z}) \quad (3.29)$$

The matrix  $\mathbf{H}^T\mathbf{H}$  represents the normal equations matrix. Since the solution obtained from the linearisation process differs from the exact solution from the non-linear equation, the solution is made closer to the actual value by iterating through the process till the relative change in the cost function between the current and the previous iteration is below a threshold  $\epsilon_{conv}$  [44].

However, when the different types and quality of measurements are used to estimate an orbit, the assumption of them being equally important is not credible. Some measurements may not be accurate enough and may lead to poorer estimation if given equal importance to an accurate type of measurement. Since different observations have different levels of accuracy, a **weighting factor** is assigned to each of the observations, which gives an idea about the 'importance' of including a measurement in the estimation process.

The general practice is to assign weights to each observation with the inverse of its statistical measurement error. It was seen earlier that the accuracy of each type of measurement is computed from the Cramer-Rao lower bound, as discussed in Section 3.2.5. The observations with higher errors in acquisition are given a lower weight or importance to obtain a fair estimate. The weighting matrix for  $m'$  measurements is given by Equation 3.30.

$$\mathbf{W} = \begin{bmatrix} \sigma_1^{-2} & \dots & 0 \\ 0 & \ddots & 0 \\ 0 & 0 & \sigma_{m'}^{-2} \end{bmatrix} \quad (3.30)$$

The solution to the weighted least squares problem (WLS) can be expressed by Equation 3.31 [45].

$$\overrightarrow{\Delta x_0^{lsq}} = (\mathbf{H}^T\mathbf{W}\mathbf{H})^{-1}(\mathbf{H}^T\mathbf{W}\Delta\vec{z}) \quad (3.31)$$

### 3.3.2. Variational Equations

As mentioned above, the relation between the observables and the parameters to estimate requires linearisation to make the expressions simplified for ease of computation. A large number of partial derivatives are taken in the process, which generally are of four types [45]. For this study, only two of them will be considered, which are stated below.

- **State transition matrix**

The changes in the initial values of the state vector  $\vec{x}(t_0)$  can result in the change of the state vector at a later epoch  $t$ , which can be quantified by the State Transition Matrix (STM) as described by Equation 3.32.

$$\phi(t, t_0) = \left( \frac{\partial \vec{y}(t)}{\partial \vec{y}(t_0)} \right)_{6 \times 6} \quad (3.32)$$

- **Partial derivative matrix of measurements w.r.t. state vector**

Assuming the state vector at epoch  $t$  to be  $\vec{y}(t) = [x(t) \ y(t) \ z(t) \ v_x(t) \ v_y(t) \ v_z(t)]$ , and the measurement vector  $\vec{z}(t) = [\rho(t) \ \dot{\rho}(t) \ \theta_{az}(t) \ \theta_{el}(t)]$ , the partial derivative matrix of the measurements w.r.t. the state vector at an epoch  $t$  is given by Equation 3.33.

$$\frac{\partial \vec{z}(t)}{\partial \vec{y}(t)} = \begin{bmatrix} \frac{\partial \rho(t)}{\partial x(t)} & \frac{\partial \rho(t)}{\partial y(t)} & \frac{\partial \rho(t)}{\partial z(t)} & \frac{\partial \rho(t)}{\partial v_x(t)} & \frac{\partial \rho(t)}{\partial v_y(t)} & \frac{\partial \rho(t)}{\partial v_z(t)} \\ \frac{\partial \dot{\rho}(t)}{\partial x(t)} & \frac{\partial \dot{\rho}(t)}{\partial y(t)} & \frac{\partial \dot{\rho}(t)}{\partial z(t)} & \frac{\partial \dot{\rho}(t)}{\partial v_x(t)} & \frac{\partial \dot{\rho}(t)}{\partial v_y(t)} & \frac{\partial \dot{\rho}(t)}{\partial v_z(t)} \\ \frac{\partial \theta_{az}(t)}{\partial x(t)} & \frac{\partial \theta_{az}(t)}{\partial y(t)} & \frac{\partial \theta_{az}(t)}{\partial z(t)} & \frac{\partial \theta_{az}(t)}{\partial v_x(t)} & \frac{\partial \theta_{az}(t)}{\partial v_y(t)} & \frac{\partial \theta_{az}(t)}{\partial v_z(t)} \\ \frac{\partial \theta_{el}(t)}{\partial x(t)} & \frac{\partial \theta_{el}(t)}{\partial y(t)} & \frac{\partial \theta_{el}(t)}{\partial z(t)} & \frac{\partial \theta_{el}(t)}{\partial v_x(t)} & \frac{\partial \theta_{el}(t)}{\partial v_y(t)} & \frac{\partial \theta_{el}(t)}{\partial v_z(t)} \end{bmatrix}_{4 \times 6} \quad (3.33)$$

When the system dynamics are included along with the kinematics (only measurements), the set of differential equations needs to be solved in the computation of the STM, which needs to be propagated over the epochs. This consists of the STM and the sensitivity matrix (the partial derivative of the state vector w.r.t. estimated model parameters). Since this study does not investigate the estimation of model parameters, the variational equations will only involve the propagation of the STM.

Assuming that the state vector  $\vec{y}(t) = [\vec{r}(t) \quad \vec{v}(t)]^T$ , to obey the first-order differential equation given by Equation 3.34.

$$\frac{d}{dt} \vec{y}(t) = \vec{f}(t, \vec{y}) = [\vec{v}(t) \quad \vec{a}(t, \vec{r}, \vec{v})]^T \quad (3.34)$$

Then the derivative of this differential equation at epoch  $t$  w.r.t. the initial state at epoch  $t_0$  is given by Equation 3.35.

$$\frac{\partial}{\partial \vec{y}(t_0)} \frac{d\vec{y}(t)}{dt} = \frac{\partial \vec{f}(t, \vec{y}(t))}{\partial \vec{y}(t)} \left( \frac{\partial \vec{y}(t)}{\partial \vec{y}(t_0)} \right) \quad (3.35)$$

As seen earlier, the STM is defined by Equation 3.32. Therefore, the variational equation for the problem is given by Equation 3.36.

$$\frac{d\phi(t, t_0)}{dt} = \mathbf{A}(t) = \begin{bmatrix} \mathbf{0}_{3 \times 3} & \mathbf{1}_{3 \times 3} \\ \frac{\partial \vec{a}(\vec{r}, \vec{v}, t)}{\partial \vec{r}(t)} & \frac{\partial \vec{a}(\vec{r}, \vec{v}, t)}{\partial \vec{v}(t)} \end{bmatrix}_{6 \times 6} \phi(t, t_0) \quad (3.36)$$

where the initial starting value of the state transition matrix is assumed to be an identity matrix of dimensions  $6 \times 6$ . Considering the magnitude of the position vector to be  $|\vec{r}| = \sqrt{x^2 + y^2 + z^2}$ , the partial derivative of the acceleration w.r.t. the position  $\vec{r}$  is given by Equation 3.37.

$$\frac{\partial \vec{a}}{\partial \vec{r}} = \frac{\mu}{|\vec{r}|^5} \begin{bmatrix} 3x^2 - |\vec{r}|^2 & 3xy & 3xz \\ 3xy & 3y^2 - |\vec{r}|^2 & 3yz \\ 3xz & 3yz & 3z^2 - |\vec{r}|^2 \end{bmatrix} \quad (3.37)$$

All these equations will be applied in an algorithm described in Section 4.2.3, demonstrating the methodology for precise orbit determination using the measurements collected by the space-based radar system.

This chapter laid the foundation for the theoretical knowledge learned and applied during the thesis. The next chapter on research methodology will explain how this knowledge is applied in practice to obtain results on this study.

# 4

## Methodology

---

The objective of this chapter is to present the research methodology used in this thesis. It follows the theoretical basis described earlier in Chapter 3 and explains the approach to developing a simulation model. The key points in this chapter are important to understand the application of the literature in a practical framework.

The research approach or steps are presented in the following way. Developing from the theory of radar systems in Section 3.2, a link budget analysis is performed in Section 4.1. It defines the parameters and configurations of the space-based radar system and explains its measurement collection algorithm. This is followed by Section 4.2, which describes the setup, tools, and procedure followed to develop a numerical model which performs orbit propagation, data collection, and orbit estimation of a debris object through the space-based radar satellite. The chapter ends with Section 4.3, which presents the plan for analysing and interpreting results from the orbit determination method and defines metrics and cases that will be eventually studied to comment on INDIGO's feasibility.

### 4.1. INDIGO system design

The fundamentals of a radar system in Section 3.2 provided an overview to familiarise the reader with its working principle, link budget parameters, measurement types and different configurations. Selecting these characteristics is crucial to demonstrate that it is feasible to utilise such a radar with similar or better configurations in the long run. Moreover, the parameters must be defined prior to developing the simulation software, which will propagate the orbits of the debris object and observation satellite, to collect synthetic instantaneous measurements.

This section will revisit the theoretical aspects and address the design and performance constraints in Section 4.1.1, retrospectively examining the expected outcome of the conceptual system (previously described in Section 3.2.1). This will establish the design and working of a conceptual space-based radar system named INDIGO, which is a key element in the feasibility research. The strategy for collecting measurements and the method used to model the data collection function of INDIGO will be discussed in Section 4.1.2, which will be followed by Section 4.1.3 which will summarise the configuration and parameters for the selected radar system.

### 4.1.1. Parameters and Link Budget Analysis

Among the different metrics of a radar, the probability of detection of a target is the most crucial. The link budget equation described earlier in Equation 3.13 defines the SNR of a radar to be a crucial parameter to evaluate the feasibility. For radar to detect small-sized objects at a large distance, it must be sensitive to detections with a certain signal return value. This value is the **signal detection threshold** below which any signal obtained by the radar is automatically rejected, assuming it to be unwanted background noise or clutter. To obtain this value, it is important to set some statistical parameters. One such parameter is characterised by the probability with which the radar is expected to detect targets (**probability of detection**  $P_d$ ). The other describes the probability of the radar claiming to detect an object when in reality it is just amplified clutter (**probability of false alarms**  $P_{fa}$ ). Assuming the target signal to be a Case II Swerling model, which fluctuates from pulse to pulse, the detection SNR threshold or  $SNR_{ref}$  can be determined from Equation 4.1 [34].

$$SNR_{ref} = \frac{\log(n_{fa})}{n_i^{2/3} n_c \log\left(\frac{1}{P_d}\right)^\beta} \quad (4.1)$$

where  $n_c$  represents the number of coherent pulses,  $n_i$  refers to the number of incoherent pulses,  $\beta$  is a radar metric parameter and the false alarm number  $n_{fa}$  are defined by Equation 4.2.

$$\begin{aligned} n_{fa} &= \frac{\ln 0.5}{\ln(1 - P_{fa})} \\ \beta &= \frac{1}{6} + e^{-n_i/3} \end{aligned} \quad (4.2)$$

For 10 coherent and 1 non-coherent pulses, it is assumed that the radar shall detect targets with a probability of 0.9 and is allowed to have a false alarm probability of  $10^{-7}$ . These numbers are close to other radar integrity metrics in the work of Mahafza [37], which are substituted in Equations 4.1 and 4.2 to calculate a **threshold**  $SNR_{ref}$  of 10.182 dB. This value is rounded off as **10 dB** for the rest of the study.

A reasonable approximation is made by assuming the peak power of the space-based radar to be not more than **1 kW** or 1000 W. It is assumed that the radar's range resolution is **150 m**. It means the system can distinguish between two objects only if they are at least 150 m apart. Following the radar range resolution formula  $\Delta R = c/2B$ , the noise bandwidth of the receiver can be estimated. Using a 10 m  $\Delta R$  value, the noise equivalent bandwidth for the system  $B$  is estimated to be **15 MHz**.

As discussed in Section 3.2.2, to detect and track objects as small as 1 to 10 cm, the frequency of the radar must be in the range of 3 to 30 GHz. Selecting a higher frequency opens up the possibility of detecting even smaller objects but is power-expensive. Hence, owing to the power constraint set to 1 kW, a reasonable assumption of the radar carrier frequency  $f_c$  is made to be **18 GHz**.

Similarly, the radar's velocity resolution requirement can be approximately **0.4 m/s**. This is a similar requirement set in the work of Mahafza [37], a measure of distinction between two objects if they have the same range and angular resolutions. The target wavelength  $\lambda$  is set to 10 cm, and following the expression for velocity accuracy, the duration of the pulse  $\tau$  emitted by the radar can be computed by  $\Delta V = \lambda/(2\tau)$ . The pulse duration is computed as  $20 \times 10^{-3}$  s using the speci-

fied velocity accuracy value.

Since the system noise temperature  $T_s$  of space-based radars is unknown, it is assumed to be inherently equal to the ground-based sensor value of **290 K**. The overall system losses  $L$  highly depend on free space losses due to transmission, which diminish with the square of the signal propagation distance. The value of the total system losses has been assumed to be **2 dB**. A noise figure  $N_f$  value is assumed to be equal to **3 dB**. Both these parameters are assumed equal to the parameters studied in the work of Maori et.al [4].

A pulsed Doppler radar will be used for the study, assuming that a matched filter will maximise the SNR from a signal return [38]. Although the exact matched filter modeling is out of the scope of this current study, it is estimated that the radar can have a pulse compression (PC) typically equal to the product of noise bandwidth  $B$  and pulse duration  $\tau$ . A maximum PC factor of 20,000 can be applied to the assumed values. However, assuming the worst-case scenario of the radar having to emit every 1 ms instead of 20 ms, the PC ratio of **1000** has been chosen. This safety factor keeps the worst-case SNR above the reference threshold value.

The shape and area of the antenna are still unknown but are significant for estimating the possible two-way antenna gain. Since a pulsed radar is used, the transmitting and receiving antennae are the same, which assumes identical gains  $G$  for both. Studying the works of Maori et.al [4], Livingstone [46], and Hacker [34], two antenna configurations (A and B) have been chosen for the radar.

**Configuration A** is a 2D **planar rectangular antenna radar** of size 50 cm in length and 40 cm in width, capable of electronic steering with a high scan rate. At the same time, **configuration B** is a **parabolic dish antenna** of diameter 40 cm (same as the width of the rectangular antenna). The advantage of the parabolic dish is that it is simple for production and integration but has to be mechanically controlled. The parameters discussed earlier are assumed for both radar antenna configurations except the gain, which is used in a Link Budget equation to calculate the SNR for a reference range. Both configuration gains are calculated using Equation 3.16, where the area computation differs due to different geometries. The link budget for the SNR is calculated using Equation 4.3 [38], with a detailed analysis given in Table 4.1.

$$SNR[dB] = P_t[dB] + 2G[dB] + PC[dB] - 4R[dB] - kT_s B[dbW] - N_f[dB] - 32.97 \\ + 2\lambda[dB] + \sigma[dBsm] - L[dB] + n_{el}[dB] \quad (4.3)$$

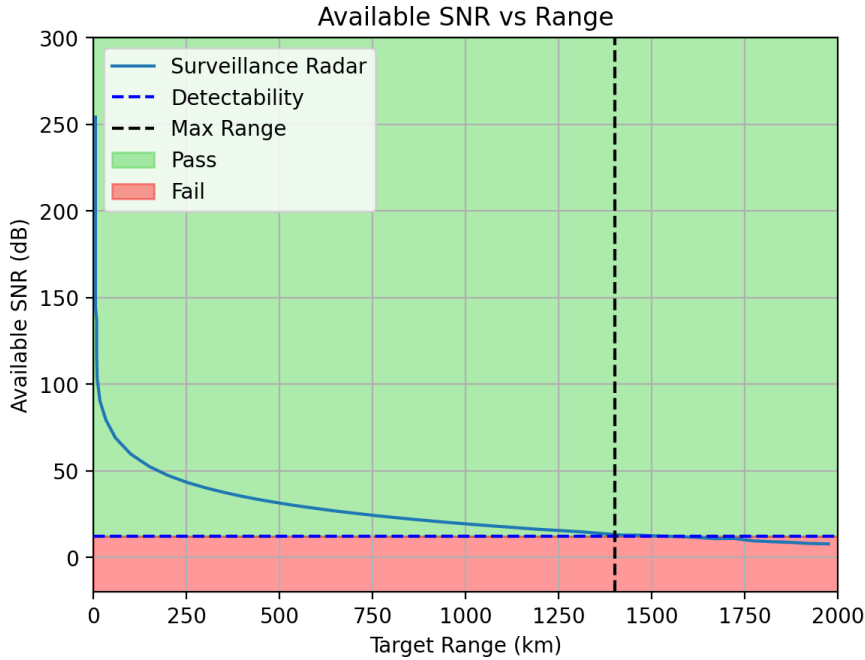
A reference range value  $R$  of 1000 km for both configurations is assumed. Here  $n_{el}$  is the number of individual array elements integrated into both configurations. An assumed value of 10 elements is chosen for the link budget analysis, which can be changed depending on the SNR achieved [38].

Analysing the SNR received for both configurations in Table 4.1, it is seen that **configuration A with the planar array performs better in terms of detection than configuration B** with the parabolic antenna. The parameters of radar configuration A are used in a MATLAB radar toolbox following the documentation in [47]. The plot of SNR achieved w.r.t. the range is shown in Figure 4.1.

The trend in Figure 4.1 shows the SNR (blue curve) to vary with  $R^4$  based on the values given in Table 4.2 for ranges starting from 100 to 2000 km. It can be seen that the SNR starts at a very high value and gradually decreases as the range increases. The blue horizontal dashed line refers to

**Table 4.1:** Link budget analysis in terms of achieved SNR for Configuration A (planar rectangular antenna) and Configuration B (a parabolic dish antenna).

Parameter	Configuration A	Configuration B
Peak transmitter power ( $P_T$ ) [dBW]	30	30
Antenna gain ( $G$ ) <sup>2</sup> [dB]	76.032	71.996
$(4\pi)^3$ [dB]	32.97	32.97
Range $R^4$ [dBm <sup>4</sup> ]	138.155	138.155
Radar wavelength ( $\lambda$ ) <sup>2</sup> [dBsm]	-81.886	-81.886
Receiver noise figure $N_f$ [dB]	3	3
Pulse compression ratio $PC$ [dB]	30	30
Receiver antenna area $A_e$ [dB]	3	3
Target RCS $\sigma$ [dBsm]	-21.049	-21.049
Losses $L$ [dB]	2	2
Thermal noise power $kT_s B$ [dBW]	-132.216	-132.216
Number of array elements $n_{el}$ [dB]	23.025	23.025
<b>Achieved SNR [dB]</b>	<b>12.211</b>	<b>8.177</b>

**Figure 4.1:** Link budget analysis for the same set of Configuration A parameters in the MATLAB Radar Toolbox.

the reference threshold  $\text{SNR}_{\text{ref}}$  value of 10 dB, below which the radar is insensitive due to the growing large distance, rejecting any signal as unwanted noise. The maximum range limit for the set of radar parameters is 1400 km, which shows an exact 10 dB value for the given set of parameters. The red-shaded box enclosed by these lines is the region at short distances between 0 and 1400 km, where no surveillance is possible because the radar incoming signals are below the minimum detectable threshold. Beyond 1400 km, even for the given power of 1 kW, the signals are too weak to reach the threshold level, and the radar does not listen to any more incoming echoes. The green section above the blue curve is the region where surveillance is possible due to SNR values higher than  $\text{SNR}_{\text{ref}}$ , where the radar shows good detection and surveillance behaviour.

As discussed in Chapter 3, **Phased-array radars** offer the advantage of agile electronic steering, wide-area surveillance, and the capacity to switch efficiently between different modes of searching and tracking objects. Moreover, the gain is increased because of multiple elements, which can electronically point their beam in any direction using the phase difference of the reflected signals at the faces of the array element. Due to these phase differences, an interference pattern is formed, creating a beam direction. This effect can be visualised in the schematic shown in Figure 4.2 [48].

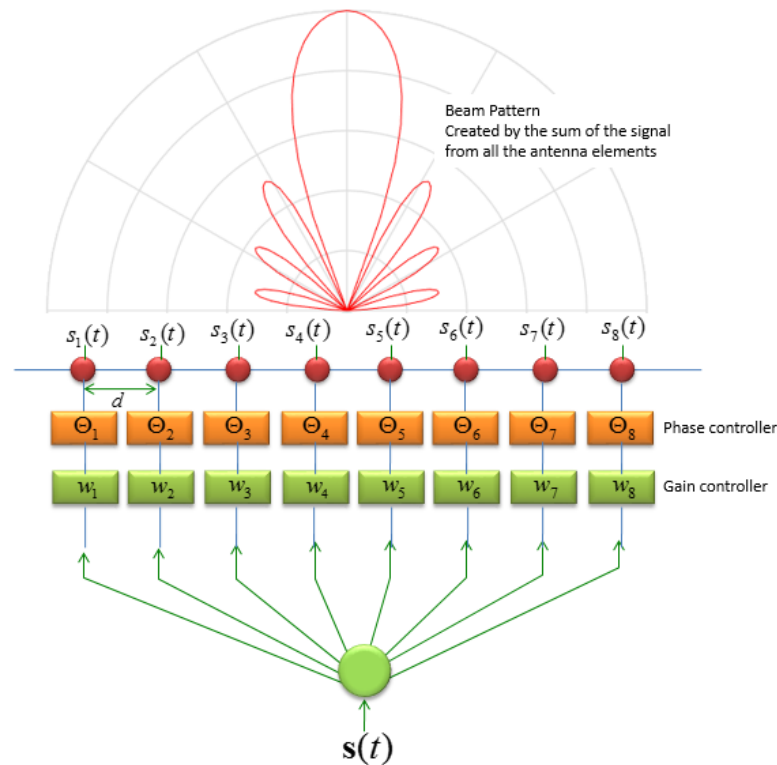


**Figure 4.2:** The effect of interference between received signals on a linear phased array system with 8 elements separated by a distance of  $d = \lambda/2$ . The beam is steered in a particular direction depending on the phase difference of the received signals. The beam pattern originates from the sum of the signals from individual antenna elements each adapted with a designated phase and gain controller [48].

On a deeper level, the interference creates a lobe that points toward the target and sweeps the surveillance area. The higher the peak of the lobe, the higher the radar signal gain. However, apart from the main lobe, due to the spacing of the antenna elements, there is the creation of side lobes which also pick up signals from objects in other directions, therefore producing ambiguity in the direction of arrival estimation.

The gain of a phased array radar is the sum of the individual gains of its array elements. Moreover, this gain results in the directivity of the array, which is affected by the positioning of the antenna elements. This is known as the **array factor** of a phased-array radar. By appropriately defining the array factor, the gain value can be amplified while also narrowing the beamwidth. This creates more sidelobes in the process, but the effect is diminished. The result of adding more antenna elements to the phased array radar is visualised in Figure 4.3 using MATLAB's phased array toolbox, with documentation found in [49].

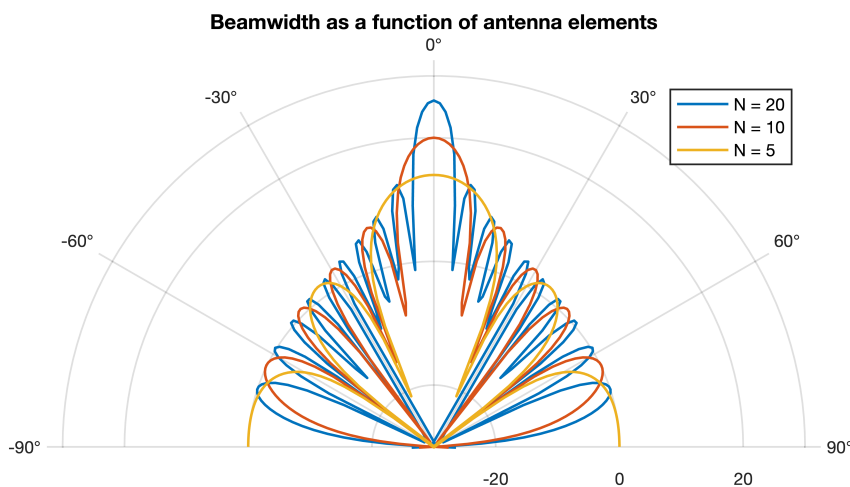


**Figure 4.3:** The decreasing beamwidth and increasing main lobe gain by adding more array elements to the phased array is visualised with MATLAB's phased array toolbox. For  $n_{el} = 20$  elements, sidelobes are created, but each one has a directivity and gain. This is used to amplify the overall gain and steer the beam toward the target.

Three cases for the different number of elements:  $n_{el} = 5$  (yellow),  $n_{el} = 10$  (red), and  $n_{el} = 20$  (blue) are analysed Figure 4.3, which shows the beam to get 'pointier' with the increase in the number of elements. As a result, the main lobe gain increases, and the beamwidth decreases, allowing for precise tracking functionality of the radar. Although the side lobes for 20 elements are higher than for 5 elements, they each have gains, which cumulatively resolve the directional ambiguity by electronically steering towards a target. With only five antenna elements, this was difficult, resulting in one main lobe and round continuous edges instead of side lobes.

Earlier in Chapter 3, it was stated that the effect of changing carrier frequency or wavelength would be analysed in this chapter, which would show the different modes of working of the radar in a scan and a track mode for the chosen configuration. This has been illustrated by the radar beamwidth polar plots in Figure 4.4 and Figure 4.5. The same MATLAB Radar toolbox used earlier generates these plots.

The first case shown by Figure 4.4 is for a lower frequency value of 9 GHz (i.e. half that of the so far assumed maximum operating frequency of 18 GHz). The 3-dB HPBW has been marked by the points  $C_1$  and  $C_2$ . The main lobe shows an azimuth beamwidth of  $22.68^\circ$  from the beam axis on either side. Four side lobes are seen along with the main lobe, which has reduced gain. This configuration is effective for the searching mode, which has a larger FOV for object detection. When the frequency is doubled to 18 GHz, the azimuth beamwidth decreases to  $11.3^\circ$ , increasing the number of side lobes to 8. The antenna gain pattern has increased directivity i.e. it can focus the energy on the object it wants to follow or track. INDIGO simultaneously performs search and track, switching conveniently between high and low-frequency modes. A similar effect of changing frequencies is expected for the elevation beamwidth too. The combined effect from azimuth and elevation beamwidths can be visualised in three dimensions but is not demonstrated as a

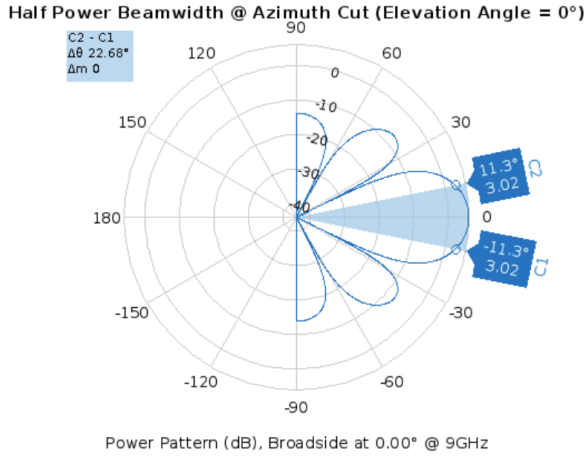


**Figure 4.4:** Illustration of azimuth beamwidth for a phased array with frequency 9 GHz, used in search mode. Increasing carrier frequency switches it to a track mode.

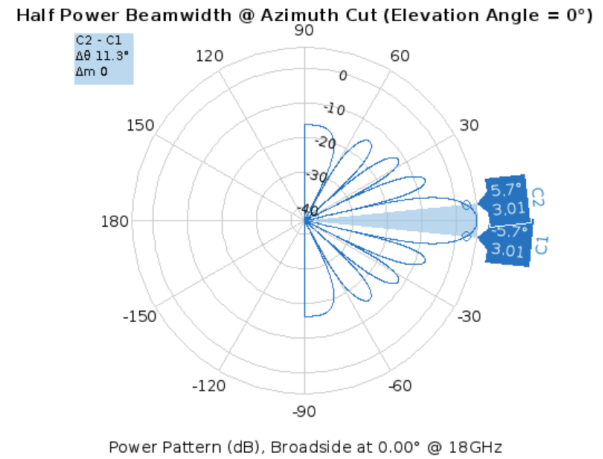


**Figure 4.5:** Illustration of azimuth beamwidth for a phased array with frequency 18 GHz, used in track mode. Decreasing carrier frequency switches it to a search mode.

part of this study.

Now, with the parameters defined, the measurement acquisition technique will be elaborated in the following subsection.

#### 4.1.2. Measurement acquisition strategy

The objective of collecting measurements is to get as many detections as possible with the best possible quality. The simulation duration, the SNR at each pulse, is calculated at every integration time step  $t_{int}$  and is coherently integrated by multiplying the individual SNR by the number of coherent pulses generated during the integration time  $n_c$ . For the sake of simplicity, coherent integration has been assumed instead of a non-coherent integration, which can be referred to in [38] for more explanation. The equation for coherent integration used in this study to integrate  $n_c$  number of pulses is presented in Equation 4.4.

$$SNR_{int} = n_c \cdot SNR \quad (4.4)$$

In this study, it is assumed that for a fixed integration time of 25 seconds, the radar generates 10 pulses each of length 20 ms, which results in a pulse generation time of 0.2 s. To cover a maximum distance of 1400 km, the wave takes 9.33 ms to travel to and back from the object. Due to their orbital velocities, the debris object moves around 28.7 m forward in orbit, while the satellite (1000 km lower) moves faster to about 29.04 m simultaneously. Due to their small relative position error, light-time effects have been neglected in the measurement module, which assumes the satellite is at the same position at reception as during the transmission.

Given the states of the debris object and the user satellite, the instantaneous true range can be computed at every time step of the simulation, propagated with a step size. The range computation is presented in Equation 4.5.

$$\rho = \sqrt{(x_D - x_S)^2 + (y_D - y_S)^2 + (z_D - z_S)^2} \quad (4.5)$$

where the position coordinates of the observing satellite are given by  $(x_S, y_S, z_S)$  and that of the

debris by  $(x_D, y_D, z_D)$ . This is the range that is inputted in Equation 4.3 to compute the SNR in dB. If the value of SNR is above 10 dB, it is assumed that the radar successfully detects the object and can collect corresponding measurements. The different types of measurements collected then are the range (given by Equation 4.5), the range rate or the measure of the radial velocity of the debris along the line-of-sight vector, and angular measurements, which give the directional information in the x-y plane (azimuth) and the x-z or y-z plane (elevation). The range rate, azimuth, and elevation equations are presented in Equations 4.6, 4.7 and 4.8 respectively.

$$\dot{\rho} = \frac{1}{\rho} [(\dot{x}_D - \dot{x}_S)(x_D - x_S) + (\dot{y}_D - \dot{y}_S)(y_D - y_S) + (\dot{z}_D - \dot{z}_S)(z_D - z_S)] \quad (4.6)$$

$$\theta_{az} = \text{atan2}(y_D - y_S, x_D - x_S) \quad (4.7)$$

$$\theta_{el} = \arcsin\left(\frac{z_D - z_S}{\rho}\right) \quad (4.8)$$

where the Cartesian velocity coordinates of the observing satellite are given by  $(\dot{x}_S, \dot{y}_S, \dot{z}_S)$  and that of the debris by  $(\dot{x}_D, \dot{y}_D, \dot{z}_D)$ .

In reality, the measurement data collected by an instrument has a large amount of random fluctuations, uncertainties, and error sources. To simulate the conditions of real measurements, **Gaussian white noise** (GWN) is added to a data set. It is one of the most commonly added types of noise in most stochastic engineering processes, which helps to make the data more realistic. The errors collected during measurements and inaccuracies during the data collection are conveniently represented by adding this. A Gaussian curve represents a normal distribution with a zero mean ( $\mu_n = 0$ ) and a standard deviation  $\sigma_{dev}$ , represented by  $N(\mu_n, \sigma_{dev})$ . GWN was chosen for several reasons [50].

- According to the **Central Limit Theorem**, the sum of a large number of independent random variables tends to follow a Gaussian or normal distribution, regardless of their underlying distribution [50]. Since collected measurements would be sampled, which is expected to follow a Gaussian distribution by virtue of this theorem, the noise modeling choice was also made for GWN.
- It is **unbiased** or **symmetric** about its mean, which makes it suitable for situations where noise is assumed unbiased. Moreover, in case of systematic errors or biases, adding random GWN can sometimes help in providing an **unbiased data representation**.
- It is **mathematically simple** to use and understand and has a **wide application** in real-life signal processing techniques.

However, there can be cases where systematic errors are present, which adds 'bias' to the data set. To account for this phenomenon, a constant value of bias with the same standard deviation as the GWN will be added to the data set to facilitate the orbit fitting process under more realistic conditions.

The intermediate results of measurement acquisition and noise addition will be shown in the coming section of the chapter, which will be integrated with the working of the orbit propagation module.

### 4.1.3. Selected configuration

After carefully studying the radar parameters and the expected conditions, the values for the INDIGO parameters are now fixed for the remainder of the study. It is considered that for these parameters, INDIGO can collect measurements, which will be used to estimate and predict the orbit of debris. The orbit quality will be assessed for several test cases using sensitivity analysis to demonstrate its feasibility. The final parameter values are stated in Table 4.2.

**Table 4.2:** Parameters of INDIGO pulsed Doppler radar parameters used in the thesis.

Parameter	Symbol	Value
Peak transmitter power	$P_t$	1000 W
Antenna area	$A_e$	0.2 m <sup>2</sup>
Transmitting antenna gain	$G_t$	38.016 dB
Receiving antenna gain	$G_r$	38.016 dB
Antenna efficiency	$\eta$	70 %
Pulse duration	$\tau$	$20 \times 10^{-3}$ s
Noise bandwidth	$B$	15 MHz
Wavelength	$\lambda$	16.67 mm
Losses	$L$	-2 dB
Noise figure	$N_f$	3 dB
System noise temperature	$T_s$	290 K
Pulse compression ratio	$PC$	1000
Number of elements in array	$n_{el}$	20
Number of coherently integrated pulses	$n_{int}$	10
Integration time	$t_{int}$	25 s

## 4.2. Simulation setup

The software developed and the framework adopted is the main focus of this section. It has three sub-parts, which explain the methodology corresponding to the three pillars in the theoretical background in Chapter 3. The methodology followed for the orbit propagation module is described in Section 4.2.1 along with intermediate results obtained. This is succeeded by Section 4.2.2 showing the collection of synthetic measurements and making them realistic by adding noise and bias. The section ends with an explanation of the precise orbit determination process in Section 4.2.3, which explains the application of Weighted Least Squares to this research and provides a first look at the POD results.

### 4.2.1. Propagating orbital model

The first step in the study is to generate a reference ephemeris for the objects of study. For the proof-of-concept, only one debris object of diameter 10 cm is assumed to be in the GEO belt, which is modeled using the theoretical knowledge gathered in Section 3.1. An observation satellite with the radar instrument is simulated in a sub-GEO orbit, which collects artificial measurements based on the true generated ephemeris, of the simulation of both objects.

### 4.2.1.1 Problem initialisation and assumptions

Before starting the simulation, the first assumption is that both the debris and the satellite are assumed to be point masses and are simulated in the J2000 reference frame. No aspect of rotational dynamics and hence satellite attitude control is considered in this thesis to simplify the problem. Secondly, no other perturbations are considered apart from those mentioned in Section 3.1.3. The updated equation of motion accounts for the perturbations in the GEO regime. It represents the orbital dynamics of the debris object and the observation satellite used in the simulation model. The equation is given in Equation 4.9.

$$\ddot{\vec{r}} = -\frac{\mu}{r^3} \vec{r} + \vec{f}_{J_2} + \vec{f}_{J_{2,2}} + \vec{f}_{Moon} + \vec{f}_{Sun} + \vec{f}_{SRP} \quad (4.9)$$

Thirdly, the body properties in terms of reflection of the solar radiation are assumed equal for both objects, although they have their area-to-mass ratios. The debris object is modeled as a 10 cm spherical aluminium object with a density of 2.7 g/cm<sup>3</sup>, with a mass of 1.413 kg and an area of  $7.85 \times 10^{-3}$  m<sup>2</sup>. The satellite is assumed to have a mass of 500 kg, with a reference area of solar panels equal to 5 m<sup>2</sup>. Lastly, an integration step size equal to 25 seconds has been chosen for the RK4 integrator to start with for consistency with the radar integration time step. More studies on choosing an optimal time step will be explained further in the report in Chapter 7.

The initial starting point of the simulation for both objects is presented in the form of Kepler orbital elements. They are then transformed to Cartesian coordinates using the transformations listed in Appendix A. The initial starting parameters are defined in Table 4.3, which are used to simulate the orbits of the debris object and the observation satellite in the GEO environment under the effect of perturbations. The simulation is initially executed for a small period of 5 days in the J2000 frame, which assumes the initial epoch to be on 1st January 2000, at 12:00:00 (12 hours since midnight).

**Table 4.3:** The initial conditions inputted to the Rk4 integrator to simulate the orbits of the debris object and satellite in the GEO regime under the effect of perturbations for 5 days since 1st January 2000, 12:00:00 UTC.

Initial conditions	Parameter	Satellite	Debris
Semi-major axis	$a$ [km]	41164	42164
Eccentricity	$e$ [-]	0.0	0.0
Inclination	$i$ [°]	0.0	0.0
Argument of perigee	$\omega$ [°]	0.0	0.0
Right Ascension of ascending node (RAAN)	$\Omega$ [°]	0.0	0.0
True anomaly	$\theta$ [°]	0.0	9.5
SRP coefficient	$C_r$ [-]	2.0	2.0
Mass	$m$ [kg]	500	1.413
Reference surface area	$A$ [m <sup>2</sup> ]	5	$7.85 \times 10^{-3}$
Initial epoch	$t_{start}$ [JD]	2451545.0	2451545.0
Ending epoch	$t_{end}$ [JD]	2451550.0	2451550.0
Integration step-size	$dt$ [s]	25	25

The measurement acquisition is also performed in the initial part of the model, which checks if the received SNR (computed by using Equation 4.3, depending on the range at that instant) is higher than the threshold value of 10 dB. In case of a positive outcome, it is stored in a list before propagating to the next epoch (which anyways, happens for a no-measurement case). The

flowchart that explains the orbit propagation methodology and measurement acquisition is presented in Figure 4.6.

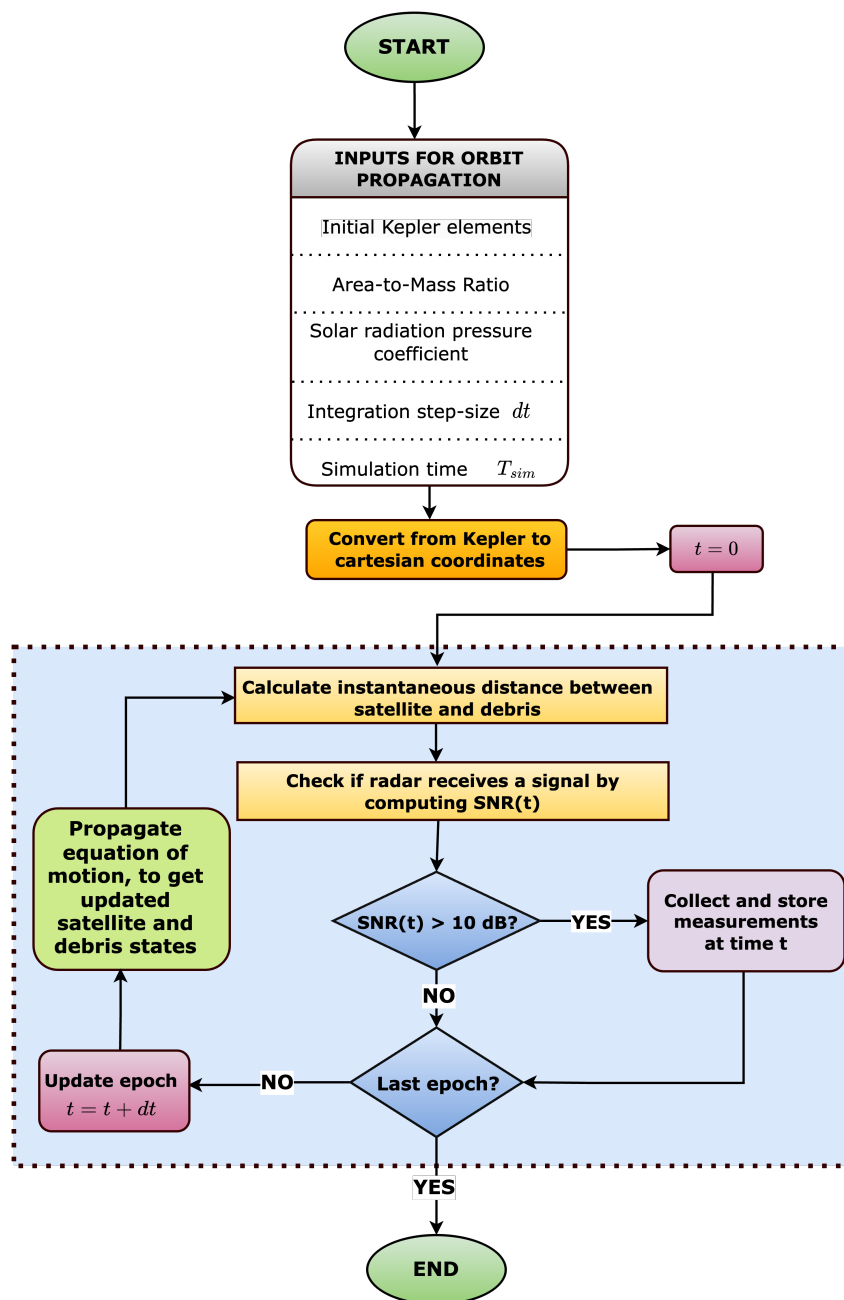


**Figure 4.6:** The methodology of orbit propagation and measurement acquisition is explained in the form of a flowchart, which is implemented in the developed Python software.

It should be noted that all orbital simulations and estimations for the developed model are done in **Python** using standard libraries like **NumPy**, and **SciPy** for computations. For visualisation of the obtained results, the libraries **Matplotlib** and **Seaborn** have been used.

#### 4.2.1.2 Integrator selection

The integrator chosen for the simulation is the **Runge-Kutta 4 (RK4) fixed-step integrator**. It is one of the most commonly used integrators, which solves an initialised value problem. Given a

step size  $h = t_{i+1} - t_i$ , where  $t_i$  represents epoch  $i$  and  $t_{i+1}$  represents the subsequent epoch. The integration scheme for RK4 is described by Equation 4.10.

$$\vec{y}_{i+1} = \vec{y}_i + \frac{1}{6} [\vec{K}_1 + 2\vec{K}_2 + 2\vec{K}_3 + \vec{K}_4] h \quad (4.10)$$

where  $\vec{y}_i$  is the evaluation of a function  $\mathbf{f}$  at epoch  $t_i$ , and  $\vec{y}_{i+1}$  is the evaluation after one integration time step at  $t_{i+1}$ . The individual vectors  $\vec{K}_1$ ,  $\vec{K}_2$ ,  $\vec{K}_3$  and  $\vec{K}_4$  are evaluated as seen in Equation 4.11.

$$\begin{aligned} \vec{K}_1 &= \mathbf{f}(t_i, \vec{y}_i) \\ \vec{K}_2 &= \mathbf{f}\left(t_i + \frac{h}{2}, \vec{y}_i + \frac{h}{2}\vec{K}_1\right) \\ \vec{K}_3 &= \mathbf{f}\left(t_i + \frac{h}{2}, \vec{y}_i + \frac{h}{2}\vec{K}_2\right) \\ \vec{K}_4 &= \mathbf{f}(t_i + h, \vec{y}_i + h\vec{K}_3) \end{aligned} \quad (4.11)$$

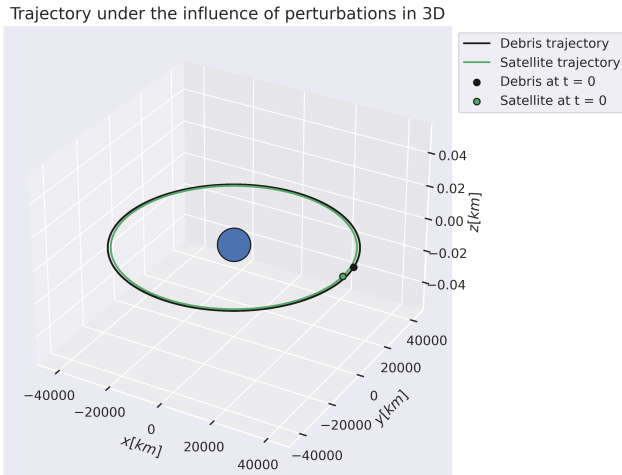
As discussed in the literature study, this method is chosen due to the combination of simplicity and accuracy. It is a stable method compared to the Euler method which is not very suited for orbit integration. The Runge-Kutta 4 method has a local truncation error of order  $O(h^5)$ , making it a fourth-order method. It should be noted that although other integration methods, such as a variable step-size RK4 integrator is possible for implementation, the accuracy in orbit computation using a fixed-step RK4 integrator suffices. Easy to implement in standard programming languages like Python or MATLAB, it has the advantage of producing accurate results. In summary, the RK4 fixed-step integrator exhibits good characteristics in terms of accuracy, stability, speed, and storage requirements [43]. 3

#### 4.2.1.3 Reference ephemeris generation

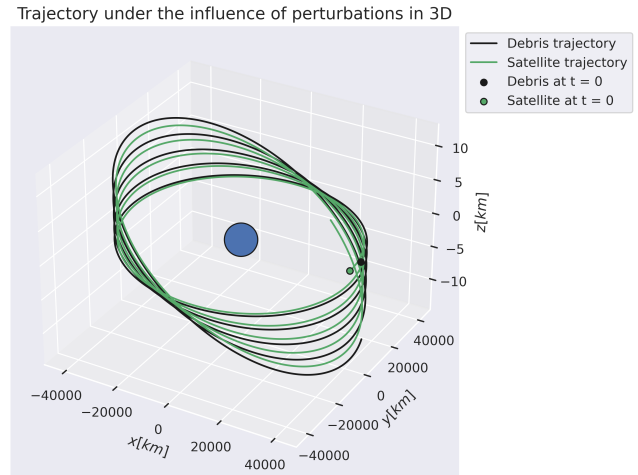
The initial conditions stated in Table 4.3 are used to begin the simulation as per the algorithm shown in Figure 4.6. The ephemerides of the objects are generated every 25 seconds for a total duration of 5 sidereal days, for two orbital models. The first case or model is without the influence of any orbital perturbations, corresponding with Equation 3.3, while the second case or model incorporates all the perturbations (which will also act on reality) while performing the integration, as per Equation 4.9. The three-dimensional trajectories of both cases are visualised, where Figure 4.7 shows the Kepler orbit case (no perturbations) and Figure 4.8 shows the trajectory when all perturbations are acting on the orbit.

Figure 4.7 shows a perfect GEO for both objects. Since the debris and satellite are 1000 km apart, the small distance difference is not easily plotted on the 3D plot scale. The satellite trajectory is seen by the green curve, while the black curve depicts the orbit of the debris object. Without perturbations, the Kepler orbits remain constant throughout the simulation as expected.

The more interesting case is for Figure 4.8, where the perturbation effects are visually also spotted by the deviating orbits of the satellite and debris object. The initial conditions are marked as dots to show that the two models have the same conditions. For deeper interpretation of the change over time, the Cartesian state vectors are transformed to Kepler elements and plotted for the satellite in Figure 4.9 and for the debris object in Figure 4.10.



**Figure 4.7:** Visualisation of the orbits of the debris object and the observation satellite in a Kepler state (i.e. with no orbital perturbations except Earth's point-mass gravity). The simulation is done for 5 days since JD epoch 2451545.0



**Figure 4.8:** Visualisation of the orbits of the debris object and the observation satellite, with all orbital perturbations active. The simulation is done for 5 days since JD epoch 2451545.0

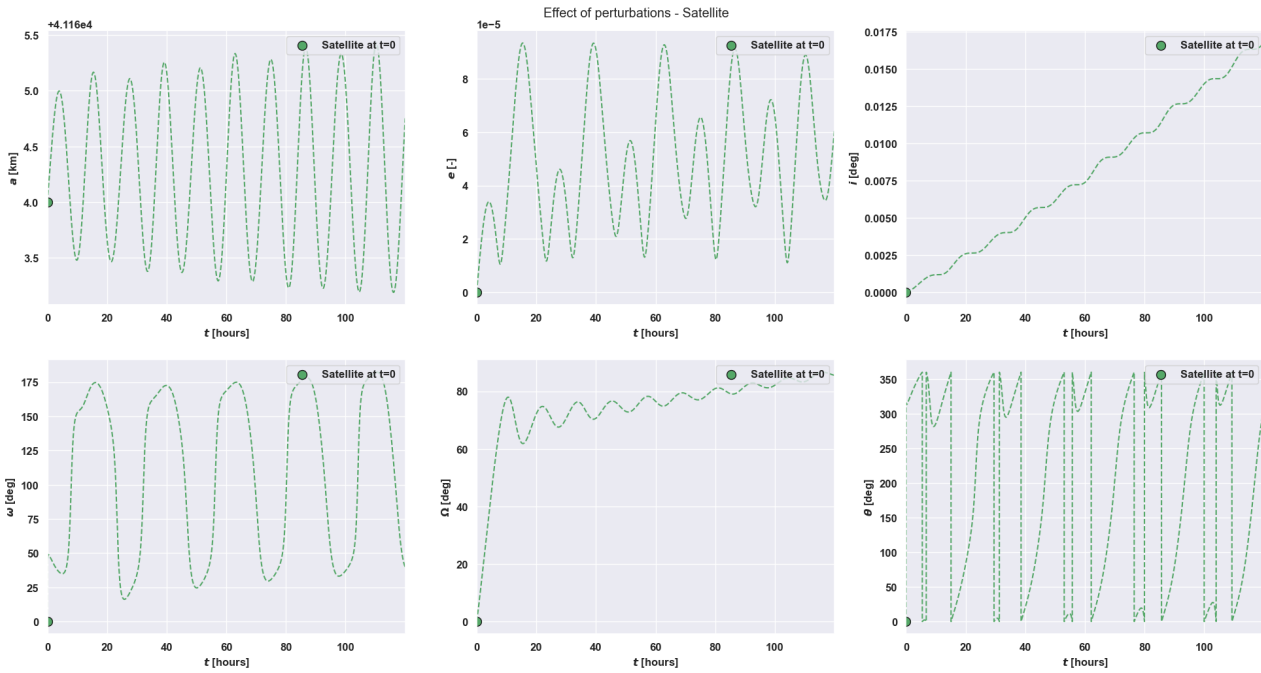


**Figure 4.9:** Temporal behaviour of the observation satellite's Kepler elements for 5 days.

Both plots show the individual Kepler elements, representing the orbit's shape, size, and orientation. The first element, or the semi-major axis, shows the orbit's size going through periodic variations but maintains a constant behaviour overall. This is as expected since the semi-major axis is a measure of the total orbital energy given by  $-\mu/2a$ , and is expected to be constant throughout time when the orbit is under the influence of Earth's point-mass gravity. Since other perturbations are acting on the satellite and debris, it can be seen that the amplitude of oscillations in  $a$  increases over time. The difference in the magnitude of the semi-major axis is also spotted in both plots. The initial circular orbit shown by Figure 4.7, is now eccentric due to the perturbations also seen in the eccentricity plot, which shows the eccentricity of both objects to be slowly rising,

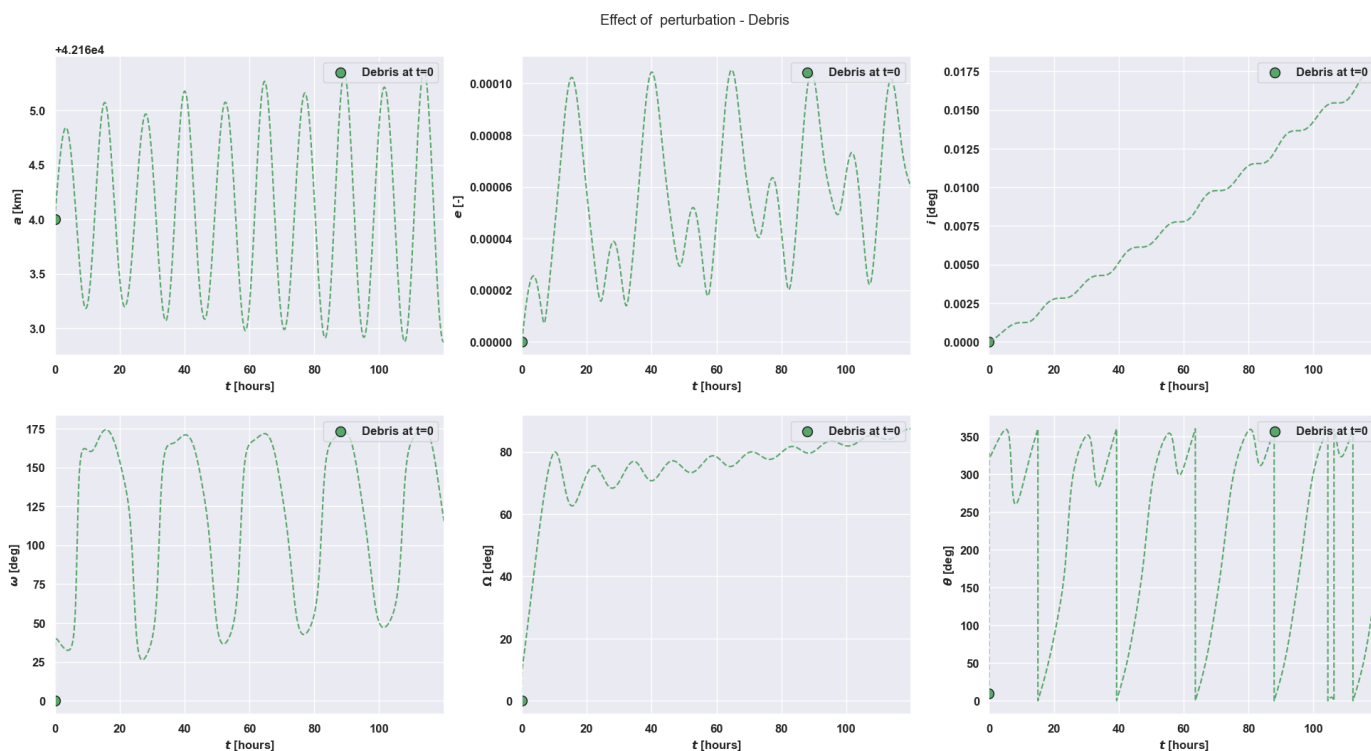


Figure 4.10: Temporal behaviour of the debris object's Kepler elements for 5 days.

still maintaining a periodic trend. The inclination is also seen to increase in the 3-dimensional trajectories, which is reflected by the secular trend of the inclination, causing an increase in the z-axis in the order of 10 km. The argument of perigee also shows gradual oscillations with 5 peaks corresponding to the 5 simulation days. The RAAN ( $\Omega$ ) shows a sharp rise on the first day of propagation, after which it shows a gradual secular trend. The true anomaly also shows periodic variations for 5 days, which shows the angular position of the object in orbit during the propagation time. It can be seen that the behaviour of the true anomaly is related to the behaviour of argument of perigee.

The credibility of these results will be discussed in Chapter 5, where the individual effects of the perturbations will be compared with the output of another verified numerical model.

#### 4.2.2. Generation of observations

To this point in the methodology, the reference or true orbits of both objects have been simulated with an appropriate force model, to replicate the effects of reality. Referring back to Figure 4.6, the measurement acquisition strategy (explained in Section 4.1.2), which depends on instantaneous SNR is now executed. In other words, the execution of the blue shaded box in the algorithm is now demonstrated as follows, which collects the artificial measurements.

##### 4.2.2.1 Ideal pseudo-measurements

The instantaneous SNR is computed for every time step of the propagation, to check if the radar gets a signal return from the debris object in its vicinity. An illustration of the behaviour of SNR received by INDIGO is presented in Figure 4.11.

It can be seen that the SNR reaches a value above 10, for only a short duration of time, which

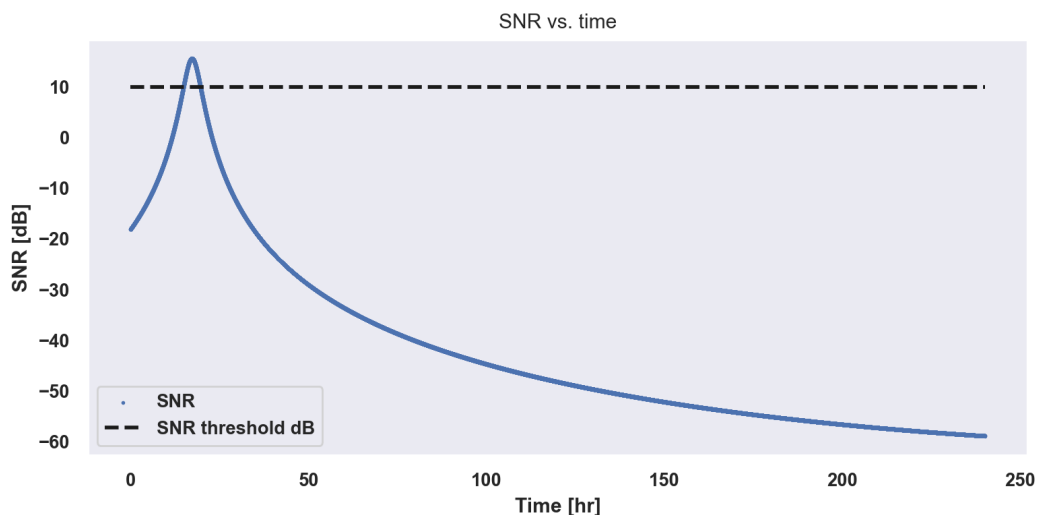


**Figure 4.11:** The instantaneous SNR from the reflection of radar waves off the debris object, collected by the observation satellite over the period of 5 sidereal days. It can be seen that compared to the total simulation time, only a small part of it is above the 10 dB threshold limit.

is not properly visible in this plot. The region where measurements are collected can be better visualised by looking at Figure 4.12.

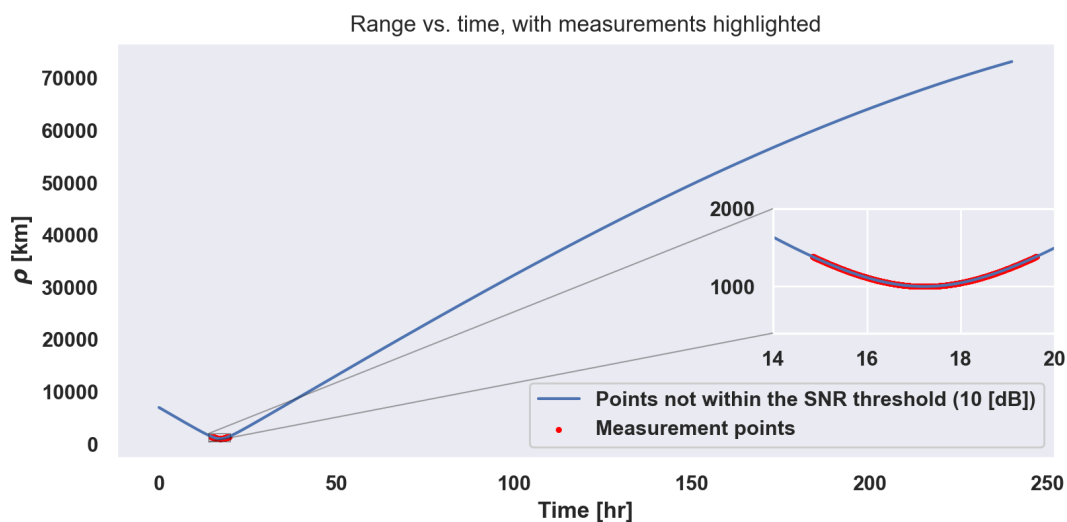
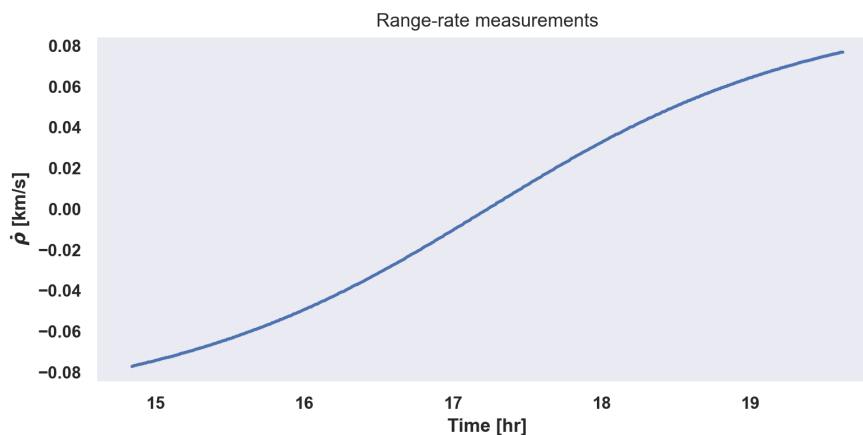


**Figure 4.12:** Visualising the region of measurement collection throughout the simulation time. The small red region marked in the range plot is highlighted to show the range measurement plot.

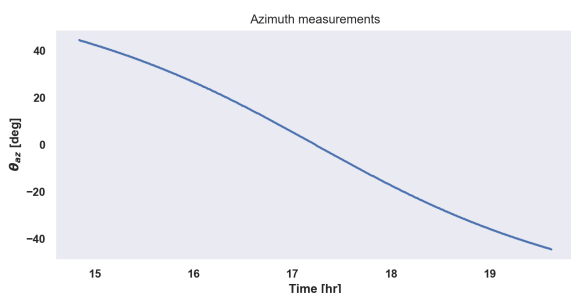
The measurements are collected w.r.t. the satellite, which requires a transformation of frame from J2000 to the local LVLH or RTN frame (discussed earlier in Section 3.1.1), The exact transformation process is shown in Appendix A.

Figure 4.12 shows the range measurements collected by INDIGO for 5 days using Equation 4.5. The measurement period is almost 5 hours, for which the object remains in view of the observation satellite. The rest of the blue curve corresponds to the range measurements that are not recorded, since they are outside the threshold SNR limit. The peak in the SNR curve in Figure 4.11 is now explained by the red curve that highlights the range measurements.

Not only is the range collected during this time, but the range-rate, azimuth, and elevation measurements are collected too. They are done so for only the five hours of measurements, which are shown by Figures 4.13, 4.14 and 4.15 representing the true range-rate, azimuth and elevation measurements, respectively.



**Figure 4.13:** True instantaneous range-rate measurements collected by INDIGO during the 5 hours of contact with the debris object, shown by the blue curve.



**Figure 4.14:** True instantaneous azimuth measurements collected by INDIGO during the 5 hours of contact with the debris object, shown by the blue curve.

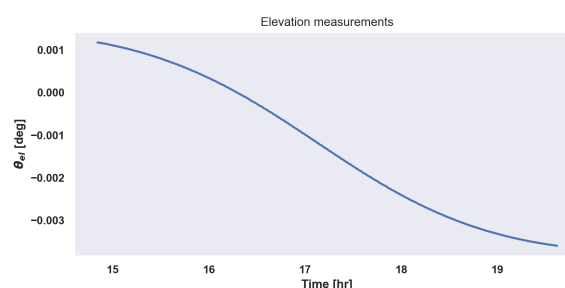


**Figure 4.15:** True instantaneous elevation measurements collected by INDIGO during the 5 hours of contact with the debris object, shown by the blue curve.

However, these measurements are the ‘ideal’ measurements, which is not what is collected in reality. As mentioned earlier, a Gaussian white noise with a certain standard deviation will be added, along with a constant bias representing systematic errors. Addition of their effects is described in Section 4.2.2.2.

#### 4.2.2.2 Simulating reality: addition of radar noise and bias

The algorithm of the addition of noise depends on the specific measurement which will be used to determine the orbit of the debris object. This means that different magnitudes and types of noise and bias will be added to the measurements, depending on the combinations of measurement types selected for post-processing. The algorithm for adding noise is depicted by Figure 4.16, which individually traverses all possibilities of measurement types that will be used for orbit determination and adds Gaussian noise and bias to it.

The amount of noise added to the measurements comes from the **Cramer-Rao lower bound rule**, discussed earlier in Section 3.2.5. Post the selection of radar parameters, the value of the stan-

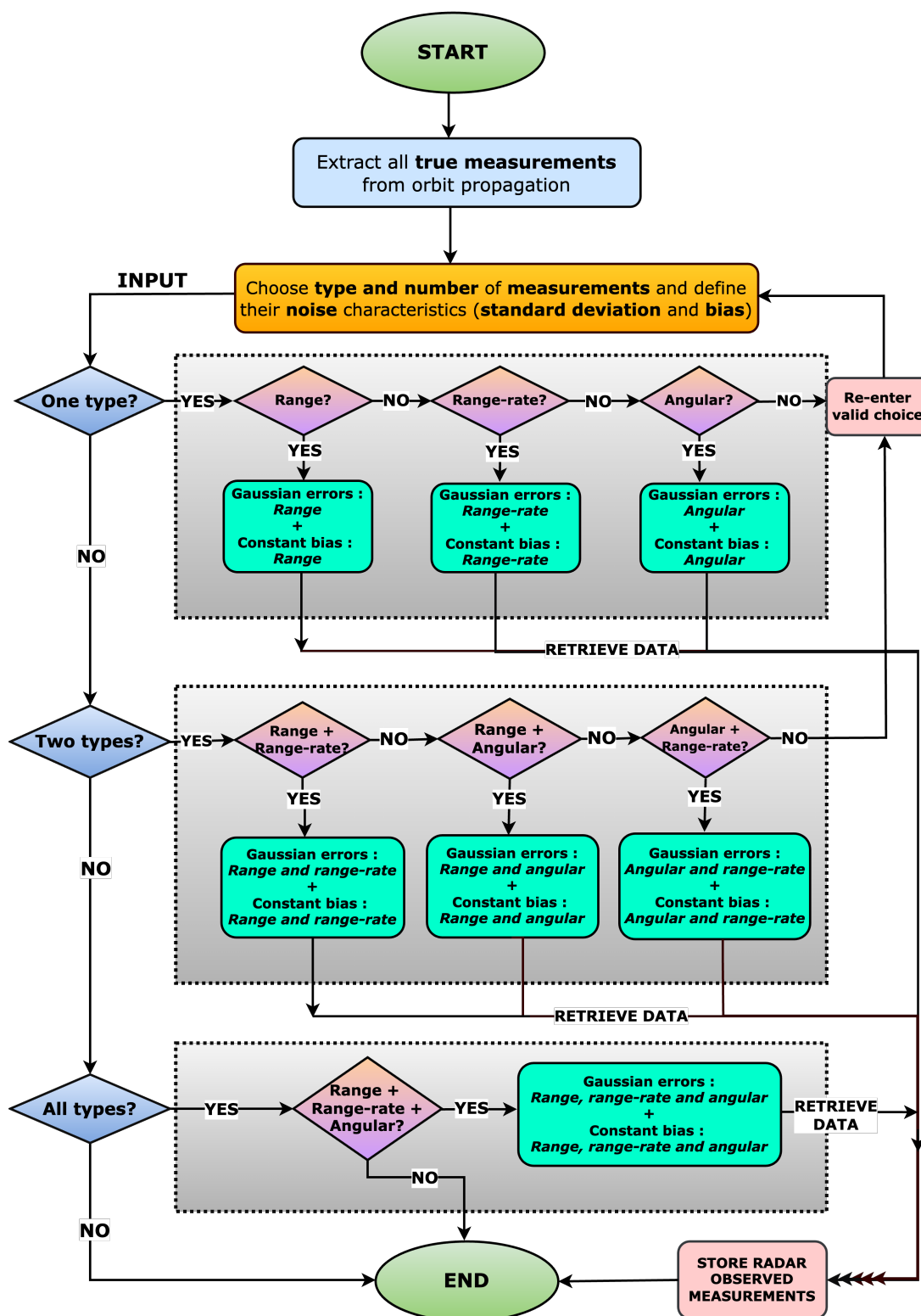


Figure 4.16: The methodology of the addition of noise and biases to the different measurements which is implemented in the developed Python software.

standard deviation of the added GWN per measurement can be computed for each of the measurement types using Equations 3.19, 3.20 and 3.21 for range, range-rate and angular measurements respectively. The value of the bias has been assumed to be of the same order of magnitude, of the noise standard deviation, respectively for all measurements. The noise and bias standard deviation values used in the study are presented in Table 4.4.

**Table 4.4:** Computed standard deviation values for radar measurements using the Cramer-Rao lower bound rule and value of estimated biases for individual measurements.

Noise Type	Range [m]	Range rate [cm/s]	Azimuth [°]	Elevation [°]
Gaussian noise $\sigma_{std}$	18.49	5.136	0.24	0.24
Systematic bias $\sigma_{bias}$	20	50	0.1	0.1

This is implemented in the developed model, but the effect of the addition of noise is not easily visible to check its correctness. Hence, for ease of verification, higher values of standard deviation for noise and bias (values present individually in the captions) are added to the true measurements, just for the purpose of visualisation of its effects. In each of the cases, the true measurements, measurements with only noise and measurements with both bias and noise are overlapped for visualisation. They are each shown by the red, blue and green lines in Figure 4.17 for range, Figure 4.18 for range rate, Figure 4.19 for azimuth and Figure 4.20 for elevation, respectively. It should be noted that the real standard deviation values added in the model are presented in Table 4.4, which is not what these graphs show.

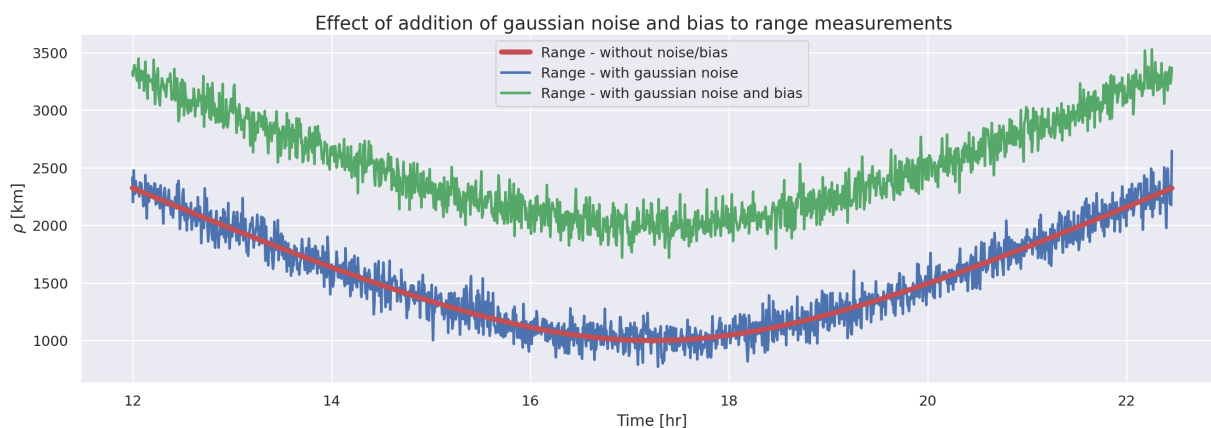


**Figure 4.17:** Visualising the three cases: no noise range measurements, addition of range noise with standard deviation 100 km, and then addition of range bias of 1000 km to the range measurements.

In each plot, the red line depicting true measurements is shown to fit through the mean of the blue points which show the addition of radar Gaussian noise. The green lines are shifted to the top of the blue curve due to the individual positive bias values added to the noisy measurements, which show the mean to be shifted by the amount of bias added.

These noisy measurements are used for the orbit determination process, whose methodology is described in Section 4.2.3.

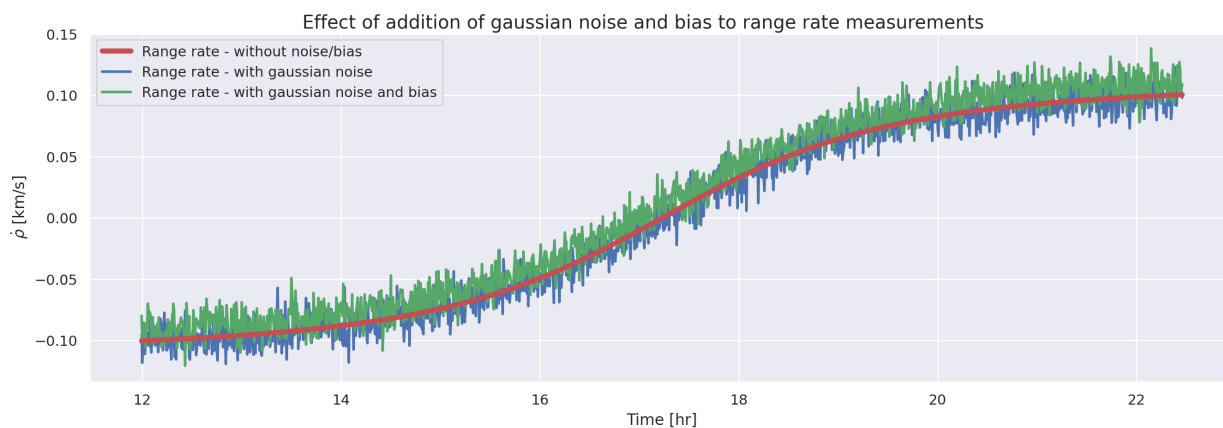


**Figure 4.18:** Visualising the three cases: no noise range-rate measurements, addition of range-rate noise of standard deviation 0.005 km/s, and then addition of range-rate bias of standard deviation 0.005 km/s to the range-rate measurements.

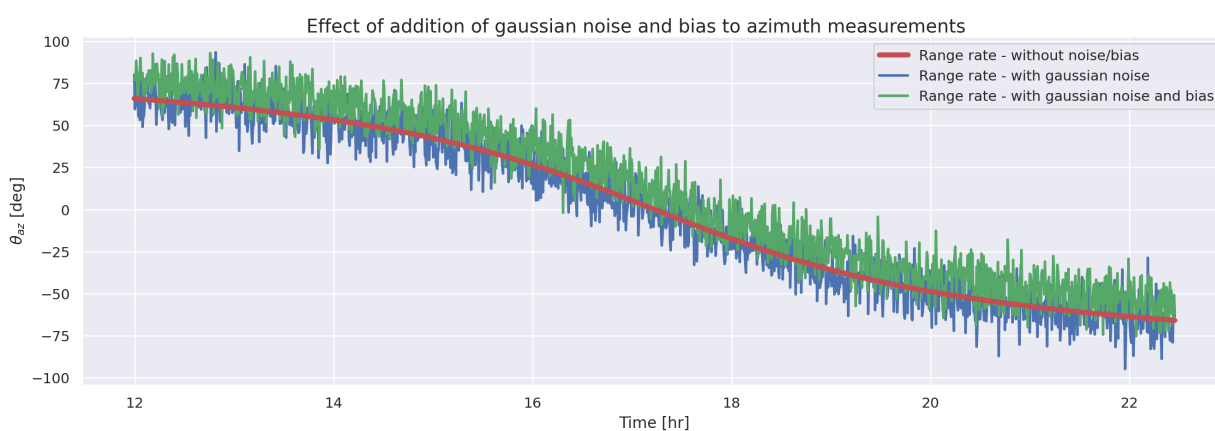


**Figure 4.19:** Visualising the three cases: no noise azimuth measurements, addition of azimuth noise of standard deviation  $10^\circ$ , and then addition of azimuth bias of standard deviation  $10^\circ$  to the azimuth measurements (green curve).

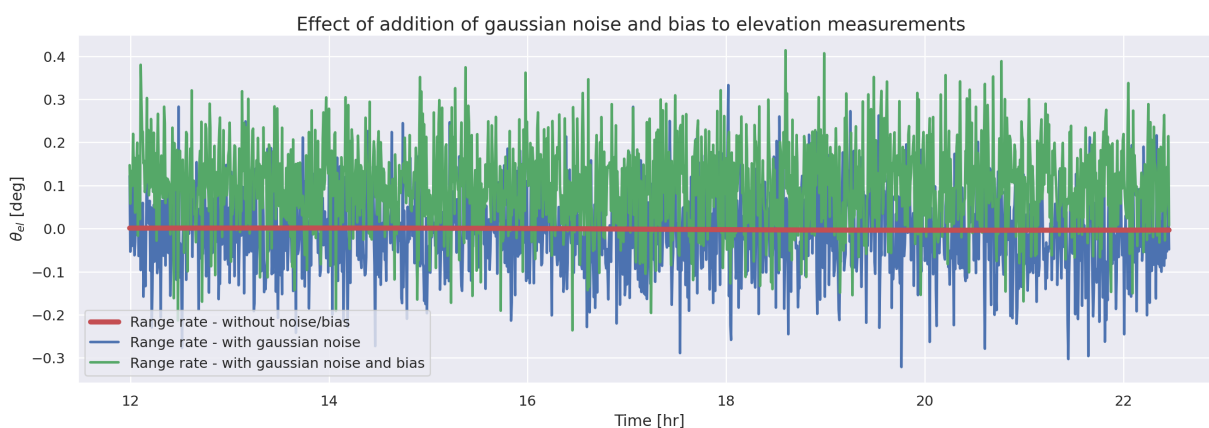


**Figure 4.20:** Visualising the three cases: no noise elevation measurements (red curve), addition of elevation noise of standard deviation  $0.1^\circ$  (blue curve), and then addition of elevation bias of standard deviation  $0.1^\circ$  to the elevation measurements (green curve).

### 4.2.3. Precise orbit determination (POD) process

The theory of orbit determination was explained in Section 3.3, where the basic equations that estimate the state vector of an object are explained. The same theoretical fundamentals will be

applied to estimate the orbit of the debris object, which will be explained in this section of the simulation framework setup.

After the measurements are collected, they are grouped in batches. For ease of computation, they have been collected in range, range rate, azimuth and elevation in this order and stored per measurement epoch. The initial state of the debris object is what is to be estimated, for which a reference trajectory is selected. The starting guess of the initial state of this trajectory is selected whose parameters are provided in Table 4.6. Beginning the OD from the true initial state with ideal measurements is expected to yield the exact solution, which does not demonstrate the functionality of the OD process. Hence, the true values of the initial debris state are also listed in Table 4.6 to show the offset in the chosen values. The theoretical aspect is converted into an algorithm that is implemented in the developed software. This is presented in Figure 4.21.

**Table 4.5:** Actual initial state value for the debris before the WLS process  $\vec{x}_0^{act}$ .

$x_0^{act}$ [km]	$y_0^{act}$ [km]	$z_0^{act}$ [km]	$v_{x0}^{act}$ [km/s]	$v_{y0}^{act}$ [km/s]	$v_{z0}^{act}$ [km/s]
41585.746	6959.067	0.000	-0.507	3.032	0.000

**Table 4.6:** Chosen initial state value for the debris before the WLS process  $\vec{x}_0^{appr}$ .

$x_0^{appr}$ [km]	$y_0^{appr}$ [km]	$z_0^{appr}$ [km]	$v_{x0}^{appr}$ [km/s]	$v_{y0}^{appr}$ [km/s]	$v_{z0}^{appr}$ [km/s]
41582.786	6957.524	-0.946	-0.546	3.011	1.019e-04

Starting with this guess, the least squares parameters are initialized. The derivatives of each of the measurements with respect to the state vectors are estimated, forming the elements of the matrix  $\mathbf{H}_k$ , whose elements are listed in Equation 4.12. The rows correspond to the measurements collected and the columns to the state vectors.

$$\mathbf{H}_k = \begin{bmatrix} \frac{\Delta x}{\rho} & \frac{\Delta y}{\rho} & \frac{\Delta z}{\rho} & 0 & 0 & 0 \\ \frac{\Delta v_x}{\rho} - \frac{\dot{\rho}\Delta x}{\rho^2} & \frac{\Delta v_y}{\rho} - \frac{\dot{\rho}\Delta y}{\rho^2} & \frac{\Delta v_z}{\rho} - \frac{\dot{\rho}\Delta z}{\rho^2} & \frac{\Delta x}{\rho} & \frac{\Delta y}{\rho} & \frac{\Delta z}{\rho} \\ \frac{-\Delta y}{\Delta x^2 + \Delta y^2} & \frac{-\Delta x}{\Delta x^2 + \Delta y^2} & 0 & 0 & 0 & 0 \\ \frac{-\Delta x \Delta z}{\rho^2 \sqrt{\Delta x^2 + \Delta y^2}} & \frac{-\Delta y \Delta z}{\rho^2 \sqrt{\Delta x^2 + \Delta y^2}} & \frac{-\Delta z \sqrt{\Delta x^2 + \Delta y^2}}{\rho^3} & 0 & 0 & 0 \end{bmatrix} \quad (4.12)$$

where  $\Delta x$ ,  $\Delta y$  and  $\Delta z$  represent the difference between Cartesian position coordinates of the debris (starting with the guessed  $\vec{x}_0^{appr}$  at a general epoch number  $k$ , and the position vector components of the satellite at the same epoch, previously generated during the orbit propagation phase. Similarly,  $\Delta v_x$ ,  $\Delta v_y$  and  $\Delta v_z$  hold for the velocity differences between debris and the satellite at the specified epoch.  $\rho$  represents the range,  $\dot{\rho}$  the range-rate. Everything is expressed in Cartesian coordinates which makes it easy to implement.

The state vector is propagated with the same acceleration settings used during orbit propagation to obtain the reference states. The variational equations (comprising the STM only) are propagated with an RK4 integrator with the same step size of 25 seconds using Equation 3.36. A reasonable assumption of not including the perturbations while propagating the variational equations has been made in the process, compared to the propagation of the state vector which has all perturbations included. This has been done for mathematical simplicity, which only affects the convergence time (expected to take one or two iterations more), without affecting the overall

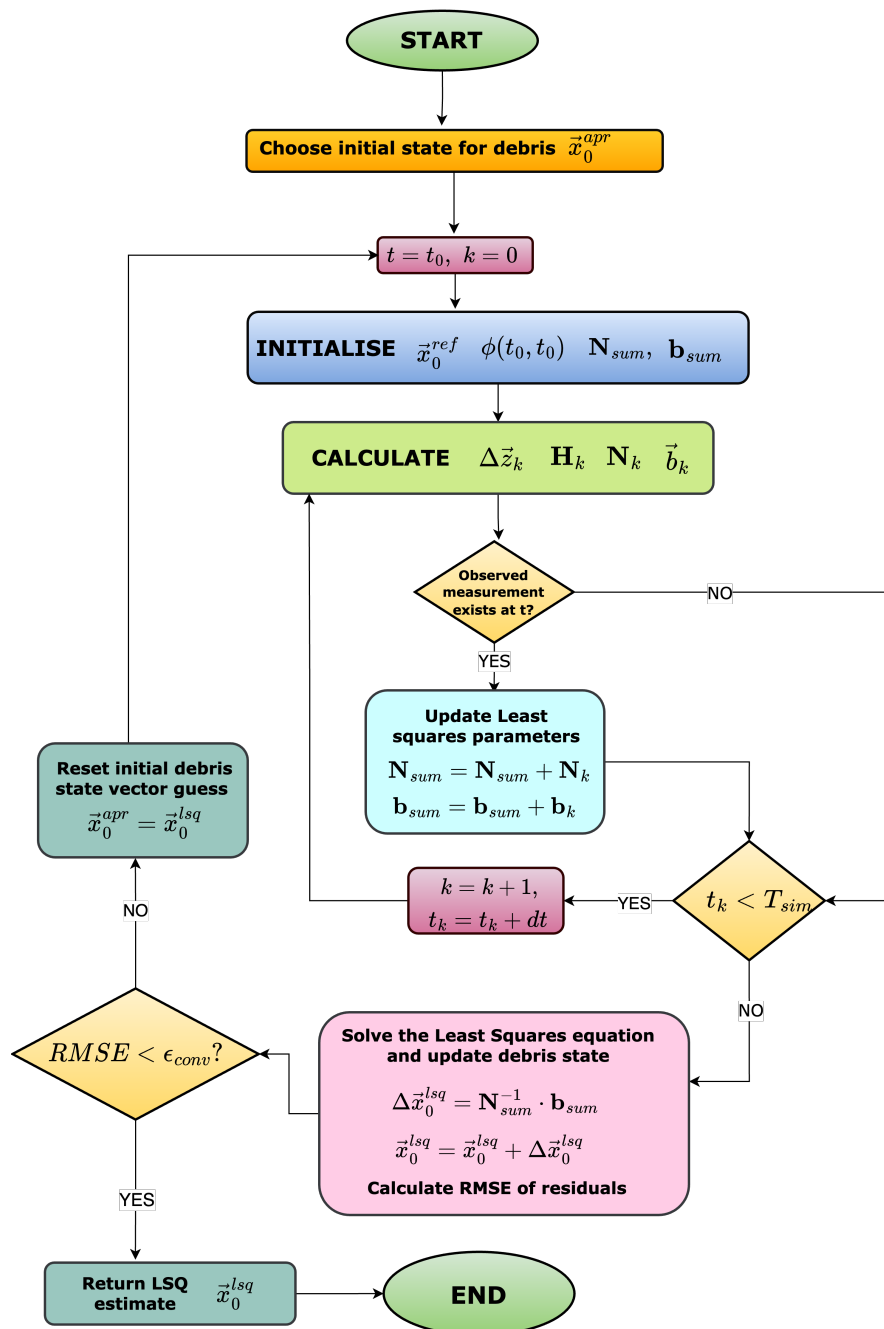


**Figure 4.21:** The methodology of initial state estimation using the Least squares (LSQ) method, which is also implemented in Python. It should be noted that in the software, the individual values of  $\mathbf{N}_k$  and  $\mathbf{b}_k$  computed in the process are appended to as big matrices  $\mathbf{N}_{sum}$  and  $\mathbf{b}_{sum}$ .

OD behaviour [45].

$\mathbf{N}_{sum}$  and  $\mathbf{b}_{sum}$  are computed at every epoch, for which there is a measurement residual computed. For epochs with no observations, no measurements are computed with the chosen debris guess and the epoch is simply propagated to the next.  $\mathbf{N}_{sum}$  and  $\mathbf{b}_{sum}$  remain unaltered. The matrices for an epoch number  $k$  are defined in Equation 4.13.

$$\begin{aligned}\mathbf{N}_k &= \mathbf{H}_k^T \mathbf{W} \mathbf{H}_k \\ \mathbf{b}_k &= \mathbf{H}_k^T \mathbf{W} \Delta \vec{z}_k\end{aligned}\quad (4.13)$$

where  $\mathbf{W}$  is the weighting matrix with the definition in the form of Equation 3.30. For the four types of measurements, the weighting matrix is defined as Equation 4.14. It assumes that the measurements are uncorrelated.

$$\mathbf{W} = \begin{bmatrix} \frac{1}{\sigma_\rho^2} & 0 & 0 & 0 \\ 0 & \frac{1}{\sigma_\rho^2} & 0 & 0 \\ 0 & 0 & \frac{1}{\sigma_{\theta_{az}}^2} & 0 \\ 0 & 0 & 0 & \frac{1}{\sigma_{\theta_{el}}^2} \end{bmatrix}\quad (4.14)$$

During the propagation,  $\mathbf{N}_{sum}$  and  $\mathbf{b}_{sum}$  are calculated by appending the individual matrices one after the other. For instance, if there are three measurement epochs, an initial  $\mathbf{N}_{sum}$  matrix with dimensions  $6 \times 6$  becomes  $18 \times 6$ , and an initial  $\mathbf{b}_{sum}$  vector of dimensions  $6 \times 1$  becomes  $18 \times 1$ . The solution of the least squares solution is a  $6 \times 1$  vector containing the state vectors.

The WLS is an iterative process that updates the initial state of the debris, with which the observations are computed. Till the residuals are minimised, the process goes on. However, a stopping condition needs to be imposed for the iteration to stop at a point where the square root of the mean of the errors is minimum. This is known as the **RMS error** or **RMSE**, an important metric determining the performance of the LSQ process. For a case where the observations are weighted, the weighted RMSE of the residuals is calculated by Equation 4.15.

$$RMSE = \sqrt{\frac{\sum_{i=1}^{n_{comb}} \vec{\epsilon}^T \mathbf{W} \vec{\epsilon}}{n_{meas}}}\quad (4.15)$$

where  $\vec{\epsilon}$  can be computed from Equation 3.27,  $n_{meas}$  is the total number of observations made, and  $n_{comb}$  is the number of epochs, for which the measurements have been collected.

In this study, a convergence criterion has been imposed, which checks the relative difference between the RMSE of the current iteration  $RMSE_j$  and the previous iteration  $RMSE_{j-1}$ , for  $j$  iterations of updated guesses for debris state vector in the WLS process. The procedure is considered converged if their relative difference is below a certain threshold  $\epsilon_{conv}$ . The RMSE condition for convergence (i.e. stopping the iterative process) is given in Equation 4.16. The tolerance value has been set to  $10^{-6}$  for expecting a good convergence behaviour i.e. a small final value of the RMSE.

$$\left| \frac{RMSE_j - RMSE_{j-1}}{RMSE_{j-1}} \right| < 10^{-6}\quad (4.16)$$

When this is followed for the measurements collected in Section 4.2.2, the orbit determination procedure is performed using all types of measurements, for utilising the maximum information available, to fit an orbit through the measurements used.

The estimated measurements through observed values during the propagation 5 days are shown in Figure 4.22 for range, Figure 4.23 for range rate, Figure 4.24 for azimuth and Figure 4.25 for elevation.

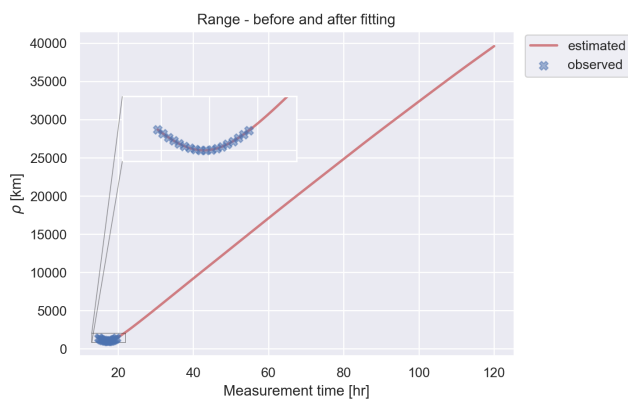


**Figure 4.22:** Estimated range observations, which fit through observed range measurements collected over 5 days since JD epoch 2451545.0

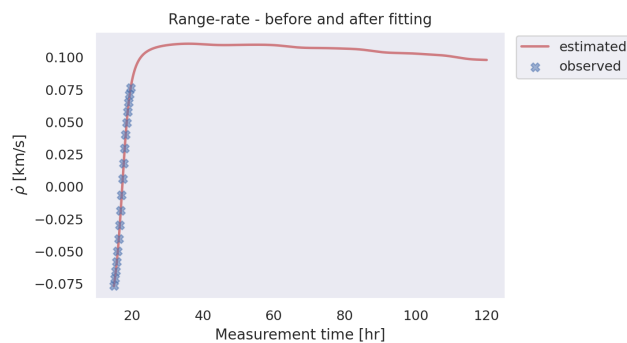


**Figure 4.23:** Estimated range-rate observations, which fit through observed range-rate measurements collected over 5 days since JD epoch 2451545.0

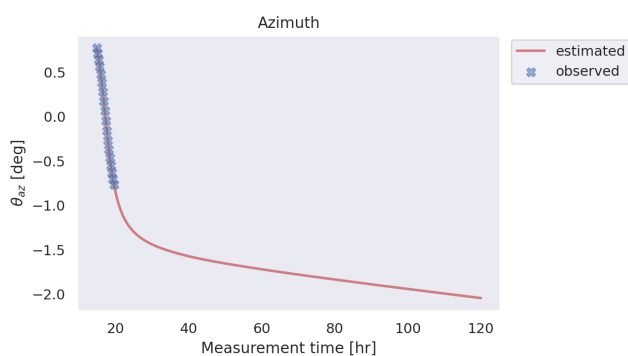


**Figure 4.24:** Estimated azimuth observations, which fit through observed elevation measurements collected over 5 days since JD epoch 2451545.0

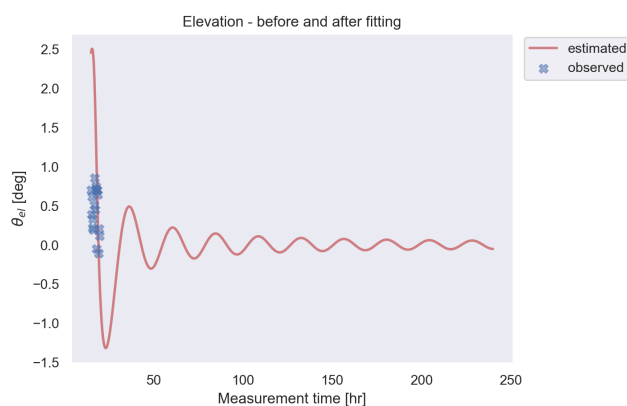


**Figure 4.25:** Estimated elevation observations, which fit through observed elevation measurements collected over 5 days since JD epoch 2451545.0

The blue dots show the observed values corresponding to the observations with the noise and bias added per the values given in Table 4.4. The red line shows the estimated measurements from the linearised model, which fits through the observed values nicely, after an iterative process of minimising the residuals between them. This red line also extends for the period even after 5 hours of measurements, to anticipate the trend of these observations for longer periods. This divides the propagation time into two regions: the estimation phase (corresponding to when there are measurements available) and the prediction phase (which commences after estimation phase, with no more new measurements).

This marks the end of the simulation setup discussion, which was focused on explanation of how the model was developed, showing its intermediate outcomes on the way. The following section will focus on explaining the procedure/methodology that is followed to investigate the results obtained to evaluate their significance.

### 4.3. Framework for analysis of results

The simulation framework was described in Section 4.2, which demonstrated the setup of the orbit propagation, measurement collection and estimation algorithm using weighted least squares. Once the model is setup, there is a wide variety of performance and statistical analyses that can be conducted to evaluate the performance of the orbit determination achieved by the chosen space-based radar for different conditions.

Dedicated to explaining the methodology for addressing method of analysis of the results, this section first explains the metrics which determine the performance of the orbit determination process in Section 4.3.1. It then defines the different cases that will be studied in Section 4.3.2. The section ends with Section 4.3.3, which presents a strategy to optimise the OD performance, by combining the POD metrics and sensitivity cases in one, which will be used to evaluate the feasibility of the study later.

#### 4.3.1. POD performance metrics

As seen in Section 4.2.3, orbit determination is an iterative process which aims to estimate the trajectory of an object by minimising the observation residuals. The computed observations originate from an initial debris state guess, which is improved by minimising the RMSE. To know how well the OD process performs, the thesis will introduce performance metrics to analyse this behaviour for different cases. The metrics that are of interest in this study are explained as follows.

##### Convergence

The first metric is related to the **RMSE** of the convergence. It is a measure of how well the residuals are minimised and the **LSQ algorithm converges**. The lower the value of RMSE, the better. This behaviour depends on the number of measurements available primarily, which makes it crucial to study different cases, to see for which RMSE is better, and to identify the better-performing cases. Hence, the final RMSE value after convergence will be analysed for the different cases studied as part of this thesis.

##### Initial position and velocity estimation accuracy

Since the initial state is not known, it is important to see the deviation of the estimated initial state from the real one. The accuracy of the initial state can be calculated from the **covariance matrix**  $\mathbf{P}_0$ , which gives a measure of how much deviation in position and velocity can be expected for the initial state calculated, based on the number, geometry and time distribution of measurements [44]. This study considers the noise-only covariance matrix, the inverse of the normal equations matrix ( $6 \times 6$  in dimensions). The expression for the covariance matrix is given by Equation 4.17.

$$\mathbf{P}_0 = (\mathbf{H}^T \mathbf{W} \mathbf{H})^{-1} = \begin{bmatrix} \sigma_x^2 & \sigma_x \sigma_y \rho_{xy} & \sigma_x \sigma_z \rho_{xz} & \sigma_x \sigma_{v_x} \rho_{xv_x} & \sigma_x \sigma_{v_y} \rho_{xv_y} & \sigma_x \sigma_{v_z} \rho_{xv_z} \\ \sigma_x \sigma_y \rho_{xy} & \sigma_y^2 & \sigma_y \sigma_z \rho_{yz} & \sigma_y \sigma_{v_x} \rho_{yv_x} & \sigma_y \sigma_{v_y} \rho_{yv_y} & \sigma_y \sigma_{v_z} \rho_{yv_z} \\ \sigma_z \sigma_x \rho_{xz} & \sigma_z \sigma_y \rho_{yz} & \sigma_z^2 & \sigma_z \sigma_{v_x} \rho_{zv_x} & \sigma_z \sigma_{v_y} \rho_{zv_y} & \sigma_z \sigma_{v_z} \rho_{zv_z} \\ \sigma_{v_x} \sigma_x \rho_{v_x} & \sigma_{v_x} \sigma_y & \sigma_{v_x} \sigma_z & \sigma_{v_x}^2 & \sigma_{v_x} \sigma_{v_y} \rho_{v_x v_y} & \sigma_{v_x} \sigma_{v_z} \rho_{v_x v_z} \\ \sigma_{v_y} \sigma_x \rho_{xv_y} & \sigma_{v_y} \sigma_y \rho_{yv_y} & \sigma_{v_y} \sigma_z \rho_{zv_y} & \sigma_{v_y} \sigma_{v_x} \rho_{v_y v_x} & \sigma_{v_y}^2 & \sigma_{v_y} \sigma_{v_z} \rho_{v_y v_z} \\ \sigma_{v_z} \sigma_x \rho_{xv_z} & \sigma_{v_z} \sigma_y \rho_{yv_z} & \sigma_{v_z} \sigma_z \rho_{zv_z} & \sigma_{v_z} \sigma_{v_x} \rho_{v_z v_x} & \sigma_{v_z} \sigma_{v_y} \rho_{v_z v_y} & \sigma_{v_z}^2 \end{bmatrix} \quad (4.17)$$

The elements of the diagonal matrix give an estimate of the initial state vector accuracy, which is

also known as the **formal uncertainty**. The total position and velocity uncertainties are expressed by Equation 4.18, assuming the errors in x,y and z are not correlated.

$$\begin{aligned}\sigma_{pos} &= \sqrt{\sigma_x^2 + \sigma_y^2 + \sigma_z^2} \\ \sigma_{vel} &= \sqrt{\sigma_{v_x}^2 + \sigma_{v_y}^2 + \sigma_{v_z}^2}\end{aligned}\quad (4.18)$$

The off-diagonal terms are the covariances between all possible pairs of variables. For example, the correlation coefficient of x and y positions is given by Equation 4.19, which holds for the rest of the variables in the covariance matrix.

$$\rho_{xy} = \frac{\sigma_{xy}}{\sigma_x \sigma_y} \quad (4.19)$$

### Evolution of errors in position and velocity over time

The last metric is straightforward. After orbit determination i.e. fitting an orbit by starting with a reasonable guess of the initial state, the states are propagated further from the final state vector solution for future epochs. This is where prediction commences. The computed trajectory is then compared to the reference trajectory generated using the methodology presented earlier in Section 4.2.1.3. This gives the behaviour of the errors in the Cartesian coordinates for position and velocity and shows their overall trend for long periods of time when there is no measurement available. This is also categorised as **error analysis** or **prediction performance analysis**.

These explained performance metrics will be applied to several study cases for this thesis, to determine the quality of orbit determination using in-situ measurements, hence determining the feasibility of the concept.

### 4.3.2. Parametric study cases

Determining the feasibility of a design concept does not stop at one parametric study. Design parameters sensitive to the simulation model need to be studied before evaluating a 'working' outcome. Many sets of parameters and their combinations can be considered for this process, which studies the quality of OD by evaluating the performance metrics listed earlier in Section 4.3.1. Five analysis parameters listed below will be varied to study the effect on OD performance compared to a nominal case.

- **Case 1: Noise parameters**

Each measurement comes with some noise and bias, which is determined by the Cramer-Rao lower bound explained in Section 3.2. Cases with and without noise and bias will be studied to test the effect of adding noise and bias to the accuracy with which the orbit is determined.

- **Case 2: Integration time of the radar or orbit integration step-size**

The radar is designed assuming it collects measurements every 25 seconds. This is equal to the nominal time step of propagation. The frequency of measurements collected is less due to lesser detection instances in the model. Having an integration time step of 1 second will give more measurements, which could improve the overall OD quality. However, decreasing the step-size is expected to increase the computation time. Thus, it is important to study this parameter to ensure good OD quality but not at the expense of very high computing time.

- **Case 3: Satellite orbit geometry**

The altitude (Case 3a) and inclination (Case 3b) of the satellite orbit are expected to play a big role in the collection of measurements and the quality of the orbit determination. Hence, the altitude and inclination of the observing satellite will be varied to sense the change in the number of measurements and errors over time.

- **Case 4: Measurement types**

Typically, ground-based telescopes derive data on GEO objects using only angular measurements. Using only one type of measurement will perform the OD with a certain accuracy, which is expected to be different when other (combinations of) measurements are used. This difference will be quantified and studied to identify the best and worst measurements collected by the space-based radar.

- **Case 5: Number of satellites**

One satellite will cover a particular section of the debris GEO orbit while gathering measurements. This may not be enough to predict the trajectory with a small measurement time for longer periods. Employing multiple satellites in different geometries for gathering measurements is expected to perform better in a constellation. In principle, there can be many satellites covering the entire GEO ring but that requires extra resources for operation and maintenance (not absolutely feasible for a real mission). Hence, keeping a realistic perspective, a maximum of three satellites in the observation network will be first-hand studied in this thesis.

These parameters will be varied and analysed in detail in Chapter 6. It will be then possible to obtain insights on their individual performances on the overall OD quality.

### 4.3.3. Approach for optimisation

As discussed earlier in Section 4.3.1 and Section 4.3.2, there can be endless cases originating from permutations and combinations of performance metrics and analysis parameters. For a preliminary feasibility study, it is important to be realistic and restrict our analysis to limited cases. A finite short range of values for each of the parameters will be studied, to narrow the search for an optimal configuration. Optimisation is the numerical method by which the best possible solution to a problem is obtained [51]. Although there are numerous optimisation algorithms widely used in astrodynamics, a simple **Grid Search** method will suffice for this study, which will search through a design space, with the selected parameters, and present the range of optimal solutions. Since advanced and rigorous optimisation is not the main focus of this thesis, only a simple analysis of the problem by varying a few key parameters will be performed in Chapter 7, which will also provide some inference on the research questions.

Having explained the methodology adopted in this thesis, the results can now be analysed to understand the behaviour of various parameters. However, before that can be done, it must be ensured that the software is credible enough to trust its outcome, which also aligns with the underlying physics of the problem. Hence, a small section on verification and validation is provided in Chapter 5 before encountering the results.

# 5

## Verification and Validation

The framework for simulation of the numerical model was presented in Chapter 4, which described the model of the physical problem. The model is expected to generate results which will be used to assess the system's feasibility. However, before one can do that, it is crucial to check the correctness of the model and interpret if the results obtained are reliable. This leads to the verification and validation aspect of any scientific or engineering endeavor such that the accuracy, reliability, and credibility of models, simulations, or experiments are ensured.

This chapter covers both these aspects by first exploring the verification process and assessing the correctness of the orbital model in Section 5.1. Thereafter, the working of the space-based radar model is tested for a different radar parameter set defined in Maori et. al [4]. The chapter ends with reflecting on the model's validity using Two-Line-Element (TLE) data of a debris object in the GEO regime to see how well the numerical model corresponds to real measurement data, particularly the trajectory solutions.

### 5.1. Verification with TUDATPy

**Verification** implies confirming a model implementation to check if it accurately represents the intended theoretical concepts or physical model [52]. Verification can be performed by either comparing the results obtained from a numerical model to analytical model outcomes, or comparing the results with that of another verified numerical model. This thesis verifies the developed model by comparing the obtained orbital simulation results to those of verified software. The verification software chosen for this purpose is **TUDAT**, which is **TU Delft's Astrodynamics Toolbox**. It contains several useful libraries for orbital propagation, written in C++ and Python. Detailed Application Programming Interface (API) documentation on TUDAT can be found in [53]. The Python version of this software is chosen for verification, whose testing results are discussed in this section.

All the individual perturbing forces applied to the orbital dynamics problem are analysed. The variations in the orbits of the debris object and the user satellite are analysed in the form of Kepler elements, which are generated for a set of given initial conditions. The same conditions are used to visualise the behaviour of the objects when computed with the TUDATPy software. The ephemerides are then compared to verify the working of the developed numerical orbit propagation model.

Since the debris object and the user satellite are assumed to be in the GEO regime with the same dynamics model, only the results of the debris object are presented in this report for conciseness. The initial conditions of the debris orbit provided are defined in Table 5.1

**Table 5.1:** The initial propagation conditions provided for the simulation of the debris object in both the developed numerical model and TUDATPy.

Initial epoch [JD]	Final epoch [JD]	dt [s]	$a$ [km]	$e$ [-]; $i$ [°]; $\Omega$ [°]	$\omega$ [°]	$\theta$ [°]	
2451545.0	2451555.0	25.0	42164	0.0	0.0	0.0	9.5

### 5.1.1. $J_2$

The spherical harmonics coefficients were discussed in Section 3.1.3.1, which showed that the  $J_2$  term was the most dominant term. To better understand its behaviour on the orbits, the Kepler elements have been extracted to show their variation with the  $J_2$  harmonics coefficient. The debris orbit was simulated using the initial conditions stated in Table 5.1, with only the  $J_2$  perturbation acting throughout the simulation. The effect on the six Kepler elements for 10 days is seen in the propagation model output for this case in Figure 5.1.

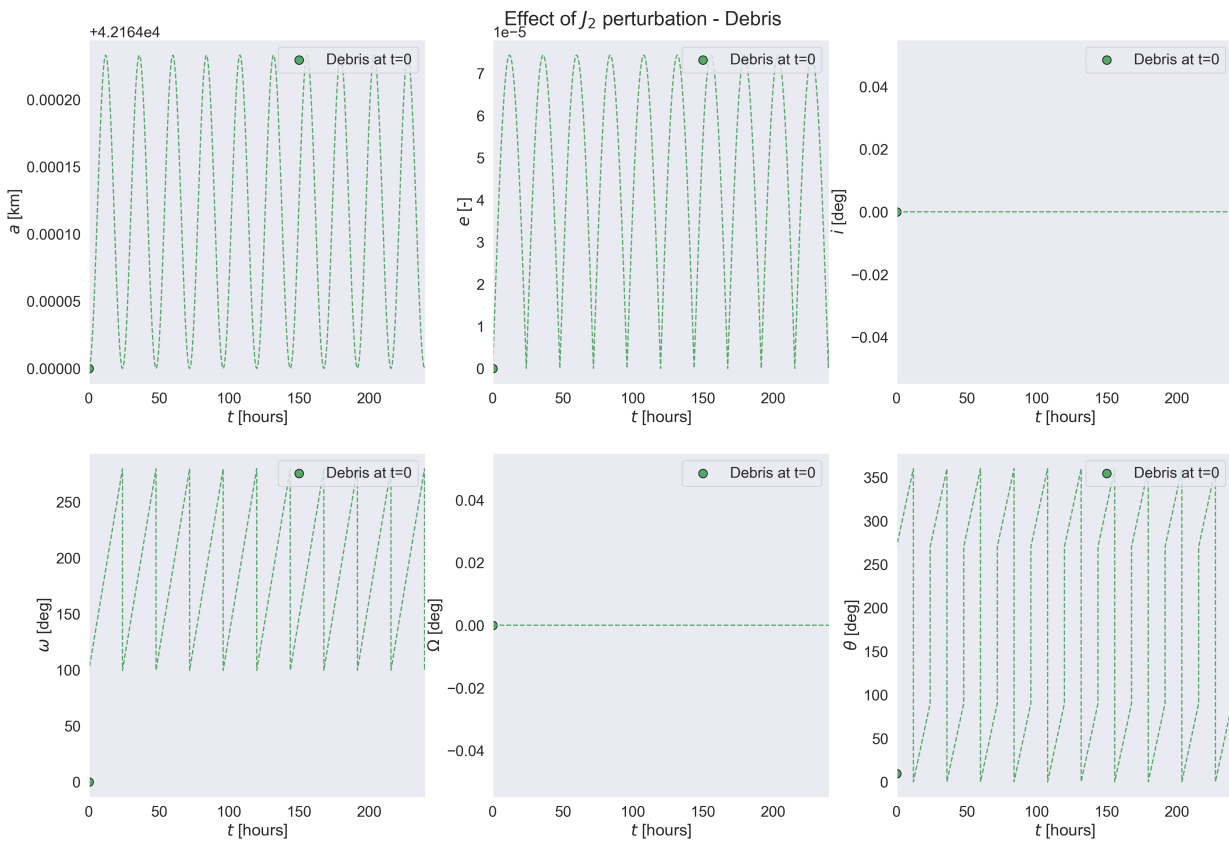


**Figure 5.1:** The individual effect of  $J_2$  on the debris object for 10 days, using the developed numerical propagation model.

This simulation is repeated with the same initial conditions in TUDATPy, to analyse the differences in the magnitude and behaviour of the Kepler elements. The simulation output from TUDATPy is presented in Figure 5.2.

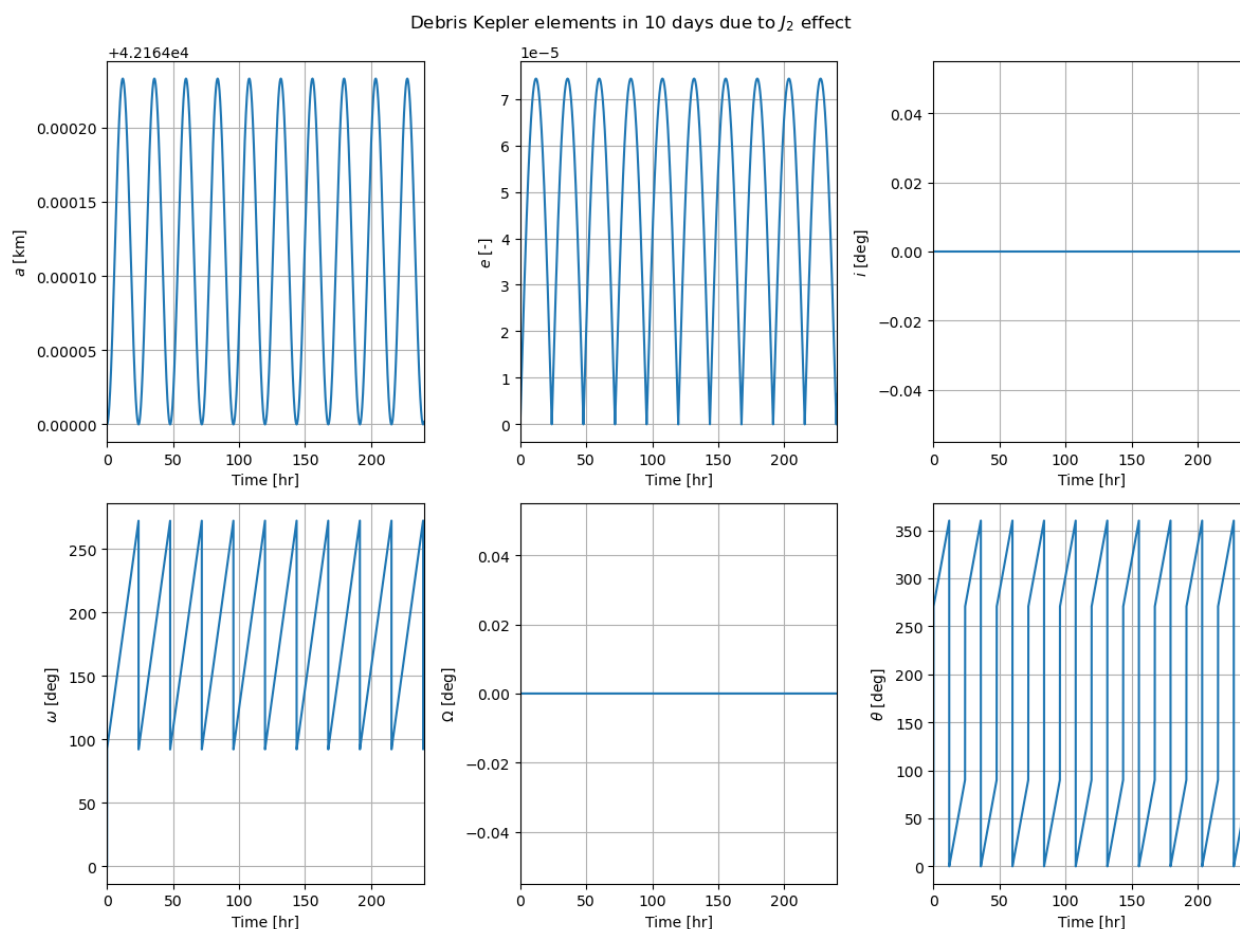


**Figure 5.2:** Visualising the individual effect of  $J_2$  on the debris object for 10 days, using the available numerical propagation TUDAT model.

It can be seen that the two plots are the same in magnitude and behaviour. From a physical point of view, the inclination of an object in a geostationary orbit above the equator is not affected. The same effect can be interpreted for both Figure 5.1 and Figure 5.2 which show the inclination  $i$  to be at a constant value of  $0^\circ$ . At the start of the simulation, the ascending node is assumed to be at a  $90^\circ$  with the vernal equinox or the x-axis of the J2000 frame. The argument of perigee is the angle between the ascending node and the perigee (the point where the orbit is closest to the Earth). Since the orbit was initially circular, the perigee and the ascending node were assumed to coincide. With changing eccentricity, under the effect of  $J_2$ , the perigee moves by  $\pi$  [rad] in one rotation around the Earth, which explains why the value of  $\omega$  is between  $\pi/2$  [rad] and  $3\pi/2$  [rad]. The rest of the elements show consistent behaviour throughout the propagation period. This verifies the implementation of  $J_2$  perturbation in the orbital model.

### 5.1.2. $J_{2,2}$

Similar to the  $J_2$  perturbation, the effect of  $J_{2,2}$  was considered in the orbit propagation model due to its long-term effects on an object in GEO. The debris orbit was simulated using the initial conditions stated in Table 5.1, this time with just the  $J_{2,2}$  perturbation acting throughout the simulation. The effect on the six Kepler elements for 10 days is seen in the propagation model output for this case in Figure 5.3.

TUDATPy is efficiently equipped with calculating the cumulative perturbation effects of spherical harmonics to a certain degree and order. It starts by assuming the point mass gravity (which is assumed to be degree 0 and order 0). In this case, when the order and degree of 2 each were provided, the effect of  $J_2$  was also considered in the simulation, thus overshadowing the individual effect of  $J_{2,2}$ . Moreover, the simulation also considered additional terms such as  $J_{2,1}$ , which were not included in the developed model. This posed a challenge for comparing Kepler elements for this particular perturbation with TUDATPy.

For studying the individual effect of  $J_{2,2}$  on the orbital elements of the debris, the open-source Python Library **Poliastro** is used instead of TUDATPy. It is an interactive astrodynamics and orbital mechanics Python library provided by the Massachusetts Institute of Technology. It is easy and efficient to use and comes with concise API documentation [54]. Modifying gravity coefficients in function database in TUDATPy would require extensive modification in the original C++ code, which can be done much simpler in Poliastro since it is fully based on Python. Hence, the debris orbit was re-simulated in Poliastro only using the  $J_{2,2}$  perturbation. The effects on the Kepler elements can be seen in Figure 5.4.

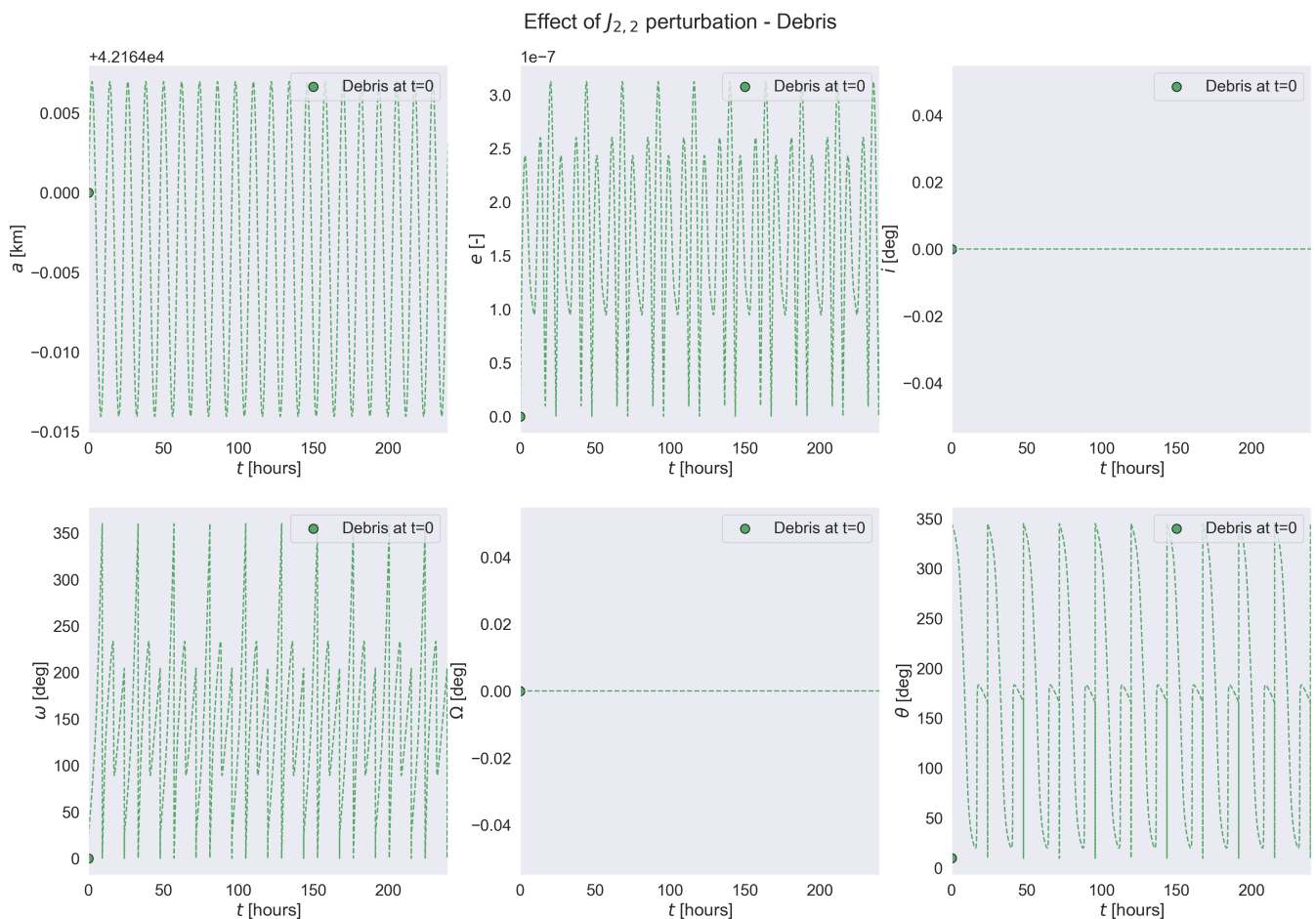


**Figure 5.3:** The individual effect of  $J_{2,2}$  on the debris object for 10 days, using the developed numerical propagation model.

The two plots again correspond with each other. It can be seen that the semi-major axis, eccentricity, argument of perigee and true anomaly show periodic variations, which show consistent

trends. Interestingly, the semi-major axis shows twice the number of oscillations for the simulation time compared to only  $J_2$  perturbations. As per the work of Martin et. al [55], this behaviour is anticipated since the  $J_{2,2}$  perturbation induces an oscillation with higher magnitude in the semi-major axis component. Due to the higher-order spherical harmonics of  $J_{2,2}$  ( $m = 2$ ), there are 20 oscillations for 10 simulation days. The RAAN and the inclination are unaffected, similar to the  $J_2$  effect. The true anomaly is consistent and shows ten peaks resembling the ten orbital revolutions around the Earth, with longitudinal drifts in the orbit for each of the revolutions. The change in eccentricity is in the order of  $10^{-7}$ , which is smaller than the order of magnitude of eccentricity change for  $J_2$  alone.

Since the output of the numerical model matches in magnitude and behaviour with that of the Poliastro module, the implementation of the  $J_{2,2}$  perturbation in the orbital model is considered to be verified.

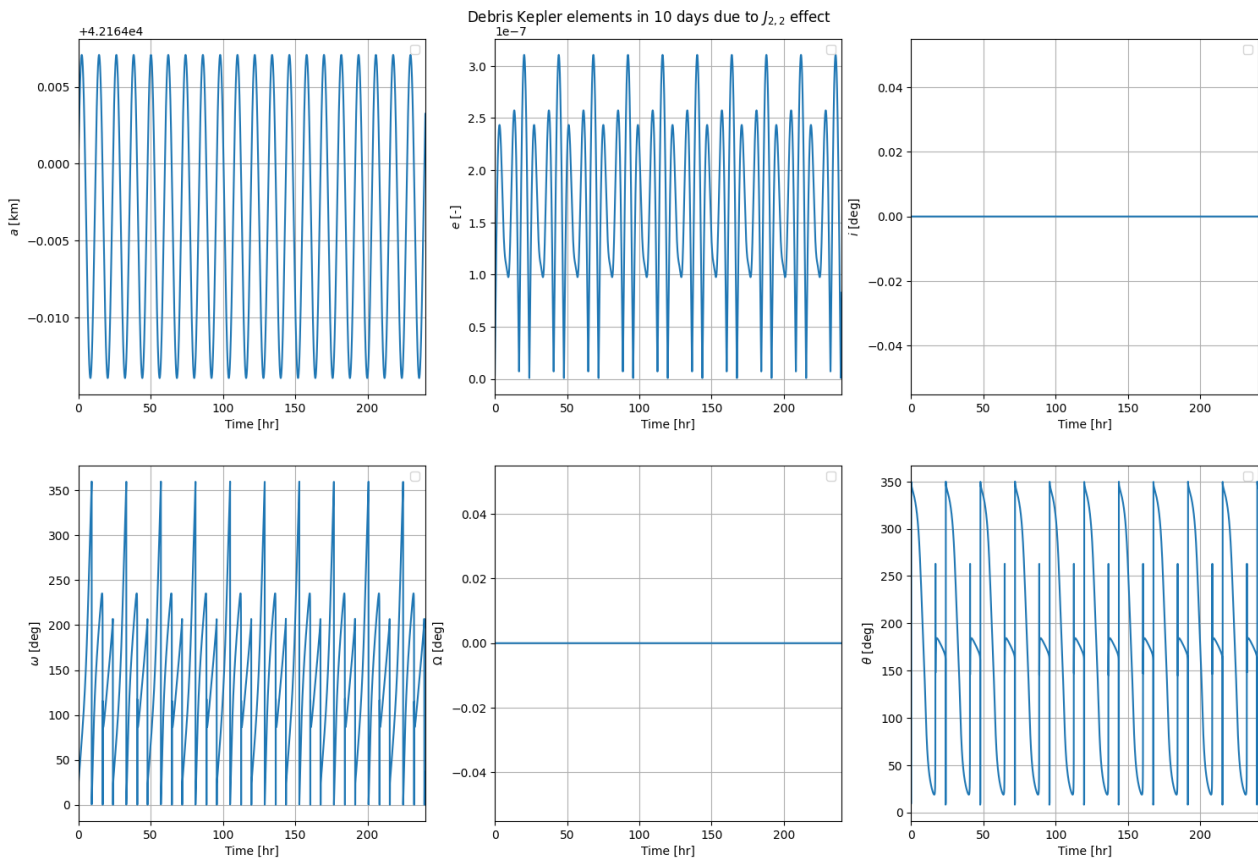


**Figure 5.4:** Visualising the individual effect of the  $J_{2,2}$  on debris object for 10 days, using the available numerical propagation Poliastro model.

### 5.1.3. Third-body Moon perturbation

The effect of adding third-body perturbations due to the Moon to the debris dynamics is visualized next. The Kepler elements for 10 days under the influence of lunar and Earth point mass gravity are visualised in Figure 5.5. The same simulation conditions are applied to TUDATPy to test the working of the developed numerical model, whose outputs are shown in Figure 5.6.

The major difference between the two software is how the position vector of the Moon w.r.t. the

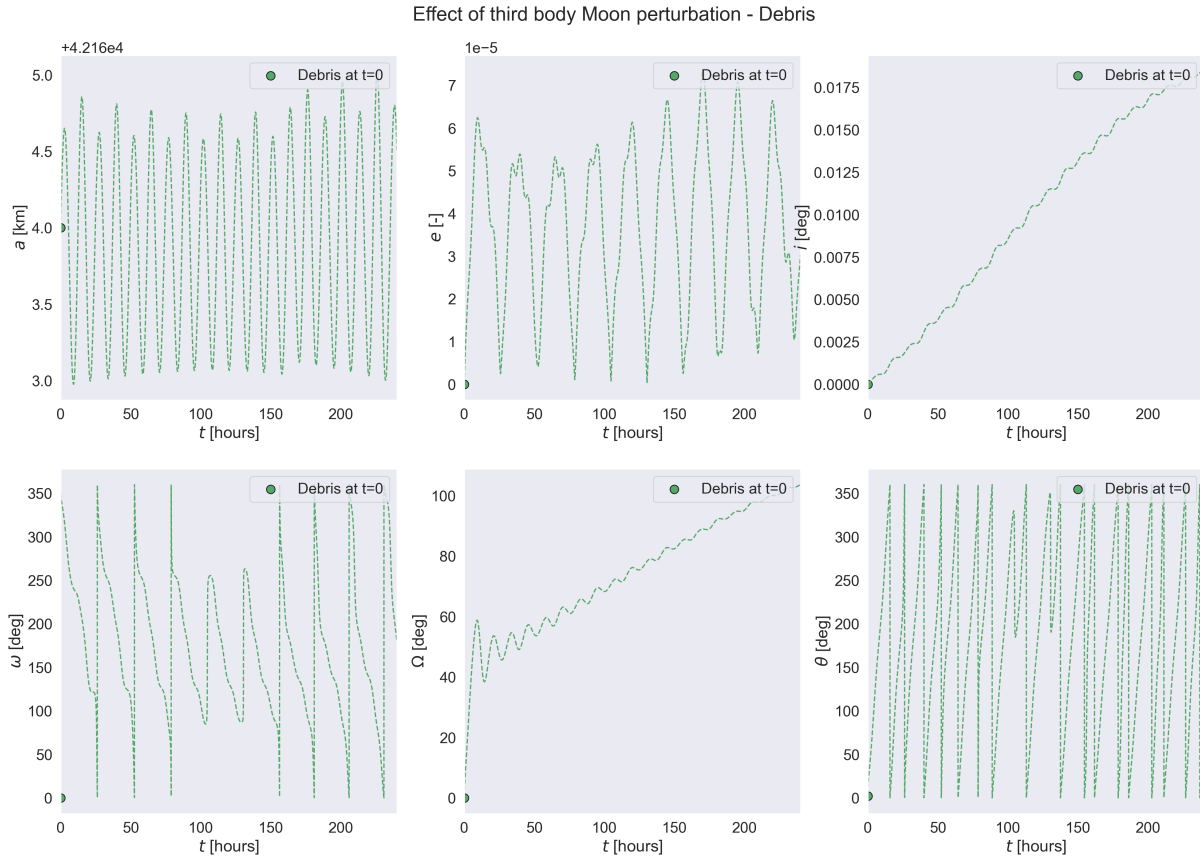


**Figure 5.5:** The individual effect of lunar third-body perturbations on the debris object for 10 days, using the developed numerical propagation model.

Earth is extracted. In TUDATPy, the ephemerides can be loaded directly from NASA Spice files, from which the data can be used for any epoch. For our own model, the position vectors are calculated analytically from the algorithm specified in Curtis [30], making the software adapt to any epoch specified without downloading the data frequently.

The results are highly dependent on the position of the Moon at that epoch. The initial epoch Cartesian positions of the Moon w.r.t. the Earth are provided in Table 5.2. This covers the values for our own model and also for TUDATPy, so see how close the values are.

**Table 5.2:** Comparison between developed software and TUDATPy on the position coordinates of the Moon w.r.t the Earth for the initial epoch.

Software	Initial epoch [JD]	Final epoch [JD]	$x_0$ [km]	$y_0$ [km]	$z_0$ [km]
Own model	2451545.0	2451555.0	291619.330	265518.870	75219.976
TUDATPy	2451545.0	2451555.0	291608.4	266716.8	76102.5

The position error of the Moon ephemeris at the first epoch generated by both models is 0.37%. Due to the small magnitude of relative errors, the working of the analytical method for Moon third-body perturbations is verified.

The changes in position are very small between the starting and ending epochs, which keeps the

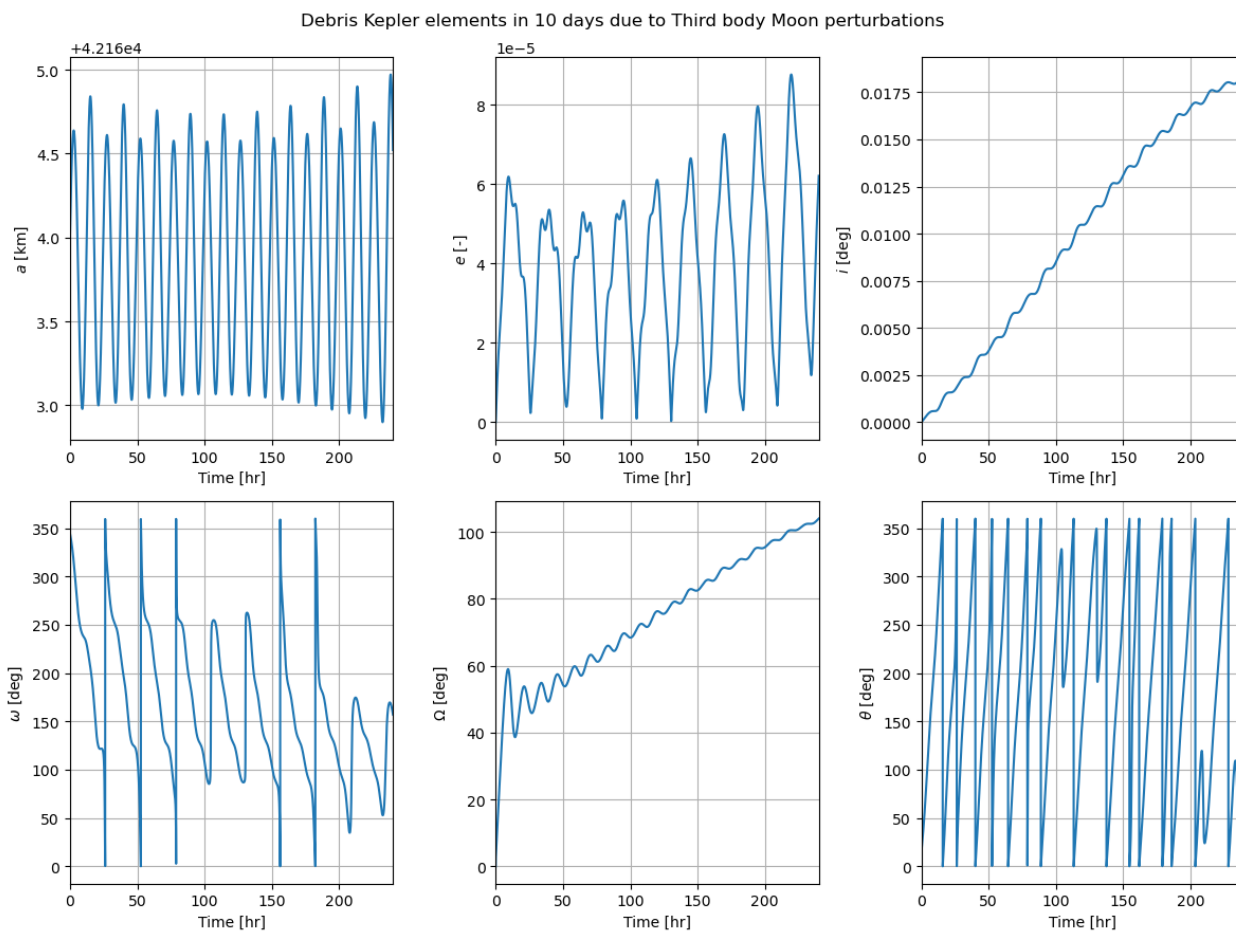


**Figure 5.6:** The individual effect of lunar third-body perturbations on the debris object for 10 days, using the available numerical propagation TUDAT model.

semi-major axis constant (hence preserving the total orbital energy). The eccentricity rises and falls for each day, showing a periodic variation with a slightly increasing trend for the time propagated. The inclination and RAAN show a secular trend which increases for the time propagated.

Since the behaviour, magnitude, and trend of the developed model and TUDATPy are the same, implementing third-body Moon perturbations is verified.

#### 5.1.4. Third-body Sun perturbation

The effect of adding third-body perturbations to the debris dynamics due to the Sun is also visualised. The Kepler elements for 10 days under the influence of the Sun and Earth point mass gravity is visualised in Figure 5.7. The same simulation conditions are applied to TUDATPy to test the working of the developed numerical model, whose outputs are shown in Figure 5.8.

Similarly to what was analysed for the Moon, the third-body accelerations are highly dependent on the position of the Sun at the epoch of computation. The initial Cartesian positions of the Sun w.r.t. the Earth at the starting epoch of propagation are provided in Table 5.3. This covers the values for our own model and also for TUDATPy, to see how close the values are.

The relative position error at the first epoch computed by both models is about 1.59%. Similar to

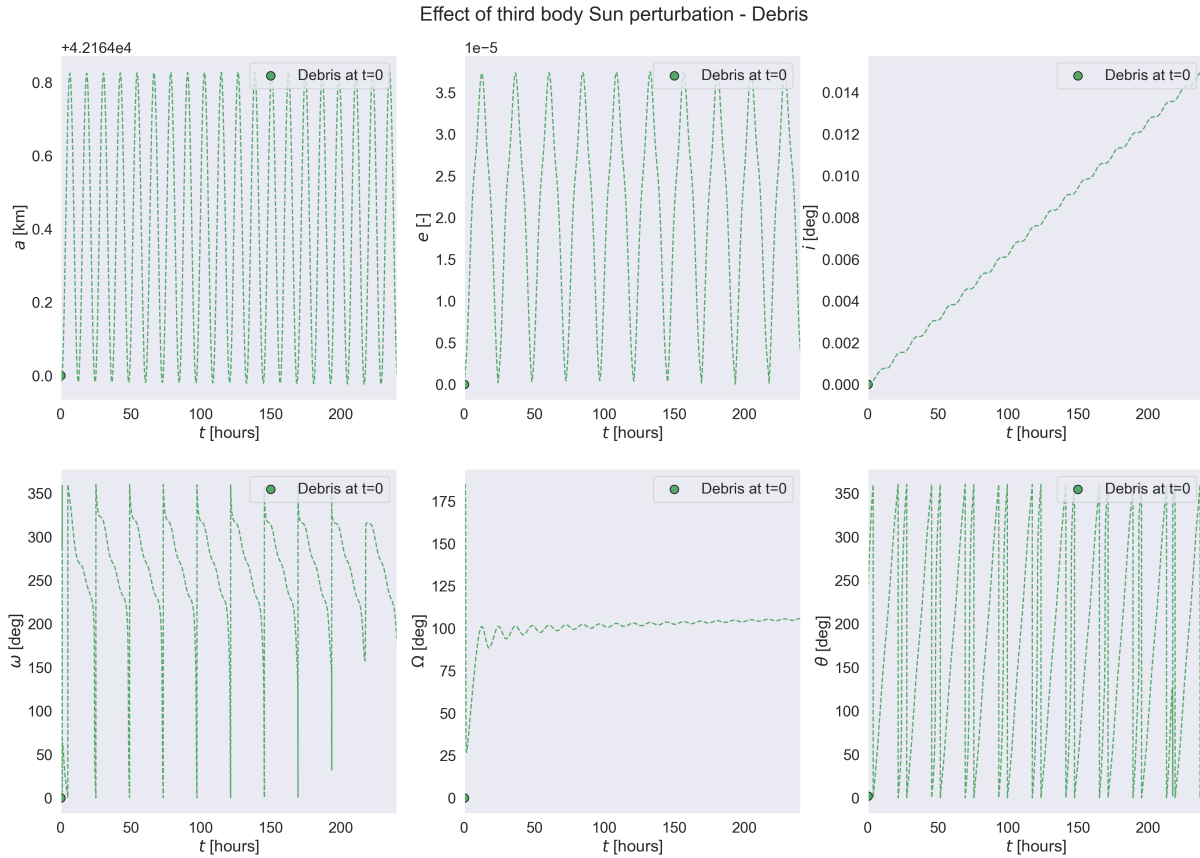


**Figure 5.7:** The individual effect of solar third-body perturbations on the debris object for 10 days, using the developed numerical propagation model.

**Table 5.3:** Comparison between developed software and TUDATPy on the position coordinates of the Sun w.r.t. the Earth for the initial epoch of propagation.

Software	Initial epoch [JD]	Final epoch [JD]	$x_0$ [km]	$y_0$ [km]	$z_0$ [km]
Own model	2451545.0	2451555.0	24183536.7	-133127600.4	-57717879.1
TUDATPy	2451545.0	2451555.0	26499033.6	-132757417.4	-57556718.5

the Moon, the error in ephemeris computation of the Sun is very small, which verifies the working of the analytical method extracting third-body positions in a geocentric reference frame.

The changes in position are very small between the starting and ending epochs, which keeps the semi-major axis constant (hence preserving the total orbital energy). The eccentricity for the solar perturbation remains constant compared to the lunar perturbation since the relative position change of the Sun is even smaller than that of the Moon owing to a faster revolution of the Moon around the Earth than the revolution of Earth around the Sun. The inclination shows a secular trend which increases the time propagated. The RAAN becomes constant after a decrease in the initial propagation stages. The argument of perigee and true anomaly, respectively, show periodic variations which are constant in trend for 10 days.

Since the behaviour, magnitude, and trend of the developed model and TUDATPy are the same, implementing third-body Sun perturbations is verified.

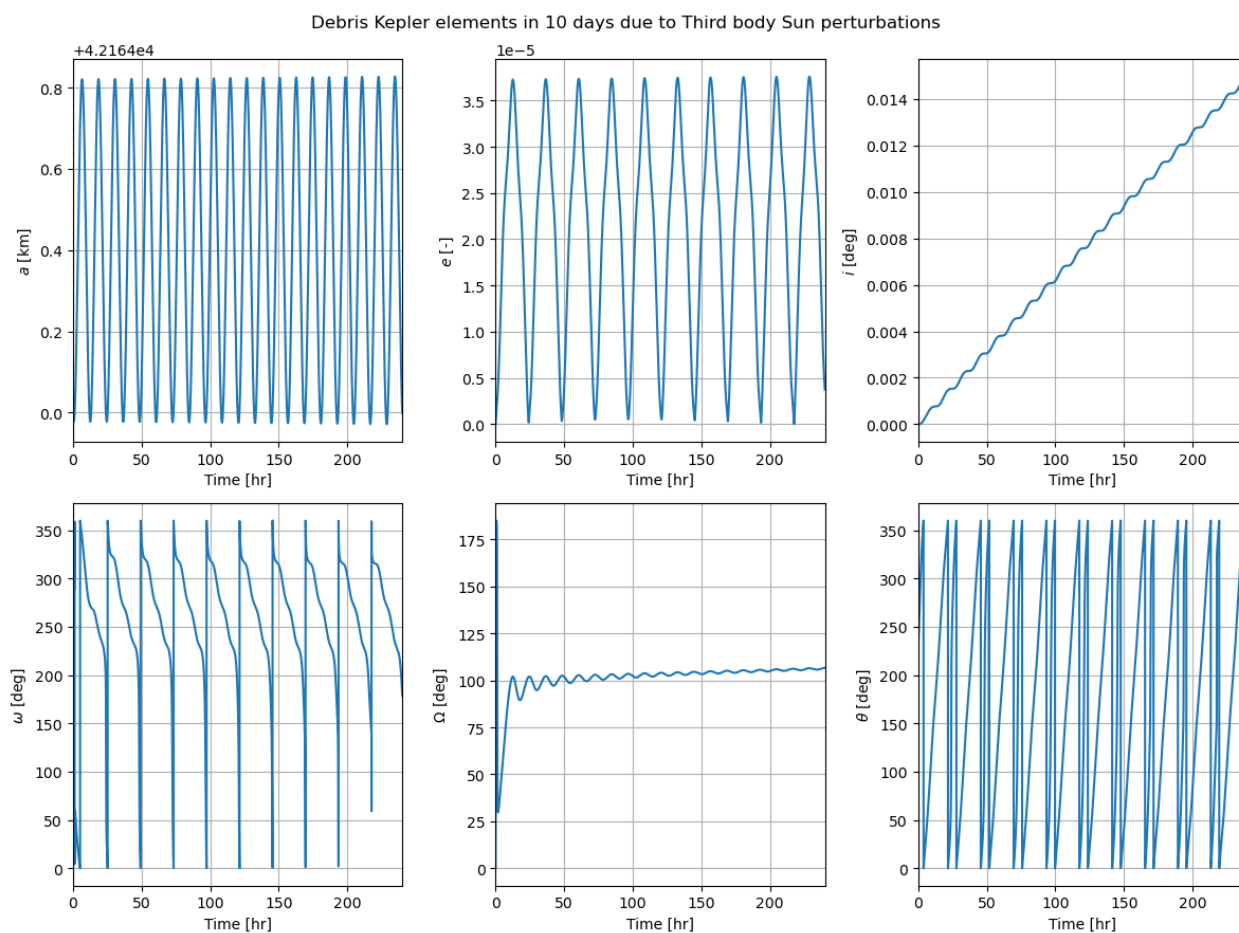


**Figure 5.8:** The individual effect of solar third-body perturbations on the debris object for 10 days, using the available numerical propagation TUDAT model.

### 5.1.5. SRP perturbation

The final perturbation implemented in the model is the solar radiation pressure, verified in this section. It is unique from the rest of the perturbations since it does not depend on the orbital altitude around the Earth but rather depends on the surface properties of the object on which it acts and on its relative Sun position vector. The direct incoming solar radiation contributes to this force, and the albedo solar radiation from the Earth also acts on the debris. However, the solar radiation force model developed in this study does not include albedo solar radiation. Objects with a higher area-to-mass ratio are subjected to higher SRP perturbations. Moreover, it also depends on whether the surface is absorptive or reflective. A reflecting body would be subjected to a higher SRP.

In this case, a spherical aluminum debris object was taken, which is assumed to be completely reflective. As mentioned earlier in Chapter 4, the area-to-mass ratio for the debris is  $5.556 \times 10^{-6} \text{ m}^2/\text{kg}$ . The position of the Sun computed for the case of third-body Sun perturbations is re-used to compute the accelerations for SRP alone. The variations in Kepler elements for the developed code are visible in Figure 5.9, while the same for TUDATPy is visible in Figure 5.10.

The semi-major axis and the argument of perigee show the same constant periodic trends for both models. The eccentricity shows a different trend compared to what was seen for the solar

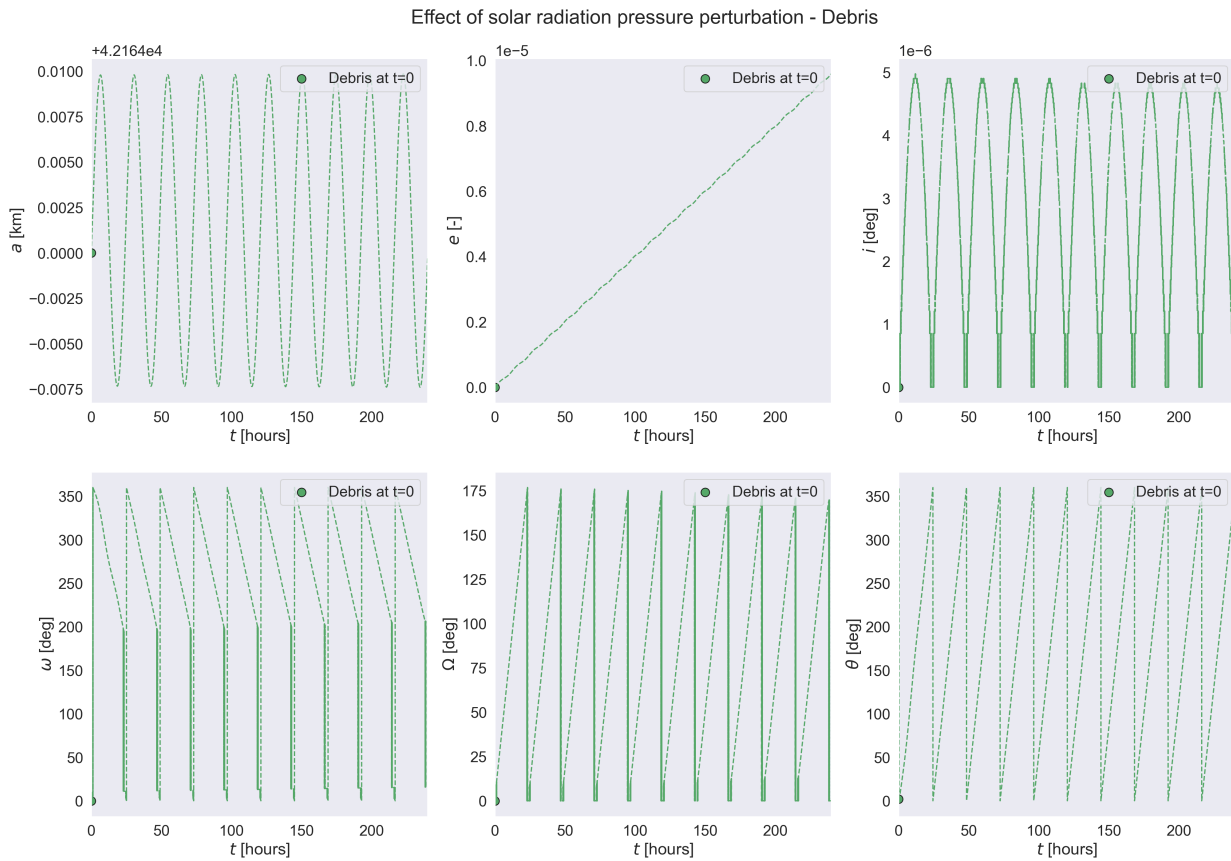


**Figure 5.9:** The individual effect of solar radiation pressure on the debris object for 10 days, using the developed numerical propagation model.

third-body perturbations. This shows the cumulative effect of SRP for higher orbits, where the satellite faces a continuous outward force in the direction away from the Sun, which increases its eccentricity in small amounts. However, the effects are smaller due to the small  $A/m$  value, which otherwise would have been higher. The inclination is more or less maintained at a constant value. The remaining orbital elements show a constant periodic variation over 10 days.

Since the behaviour, magnitude, and trend of the developed model and TUDATPy are the same, implementing solar radiation pressure perturbations is also verified.

### 5.1.6. Other orbital regimes

The overall effect of perturbations is also tested outside the GEO regime, for different altitudes. This is done to verify the overall behaviour and magnitudes of the perturbations similar to the work of Wakker [27], which was seen earlier in Figure 3.9. The model was run for those altitude regimes to check the magnitudes of each acceleration. The comparison results can be seen in Figure 5.11.

The points shown as stars refer to the values from Wakker [27], while the lines in the same color correspond to the acceleration computed by our numerical model. The point-mass gravity,  $J_2$ , and  $J_{2,2}$  accelerations show a perfect overlap. The third bodies Moon and Sun, also show a decent fit. They are not perfectly aligned since the epochs at which Wakker calculated the Sun and

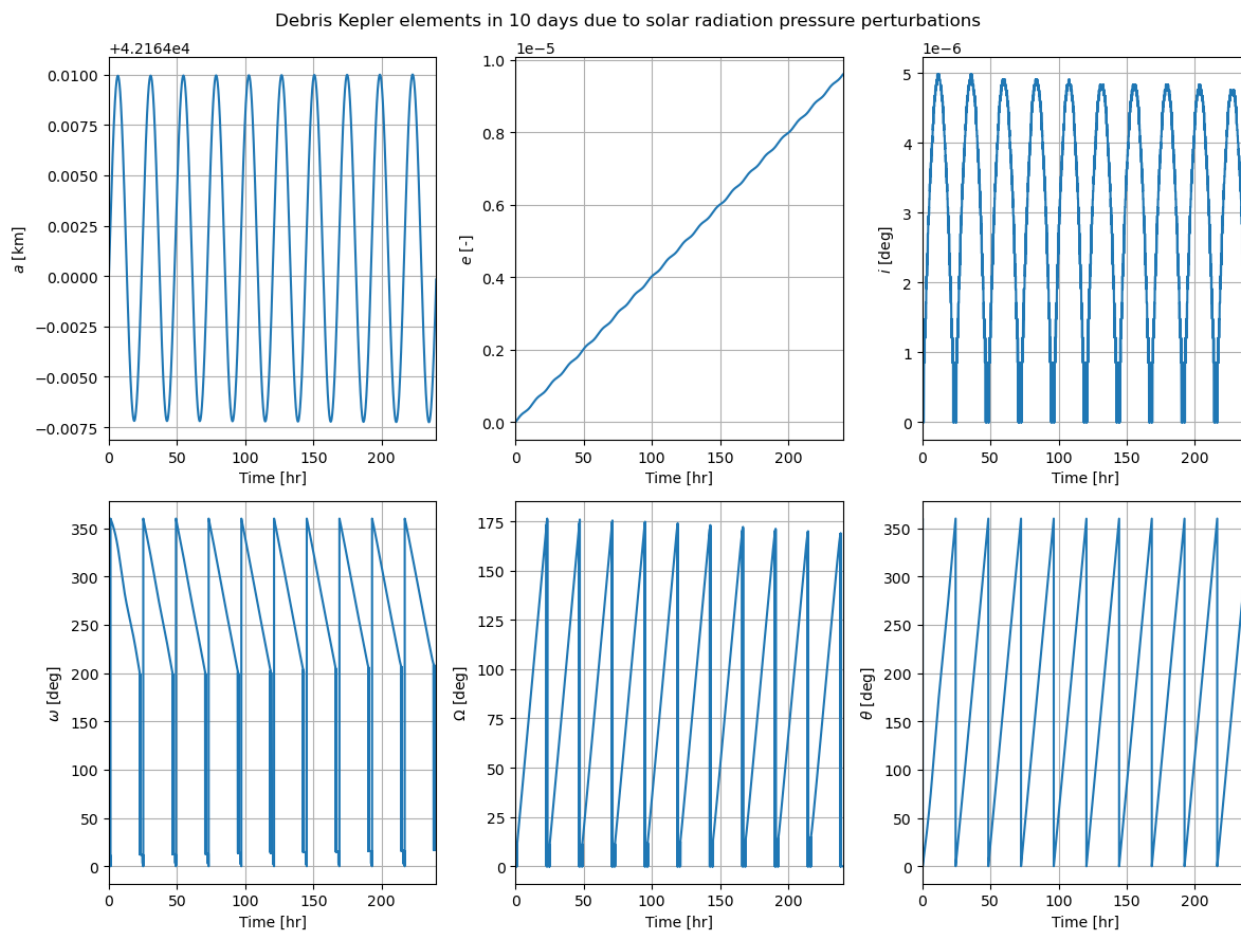


**Figure 5.10:** The individual effect of solar radiation pressure on the debris object for 10 days, using the available numerical propagation TUDAT model.

Moon geocentric positions were not explicitly mentioned. The same was analysed for solar radiation pressure, where the surface properties were taken for the satellite Echo I ( $A/m = 12 \text{ m}^2/\text{kg}$ ,  $C_R = 1.9$ ) for September 1960. The variation of acceleration for SRP is at a constant value of  $10^{-4} \text{ m/s}^2$ , which is slightly shifted to the right, owing to the lack of knowledge of the exact orbital simulation period. However, the approximated position computation for September 1960 shows a decent fit through the endpoints and is considered valid enough for this study.

With this analysis, the orbit propagation model implemented in the developed model is verified completely using TUDATPy and literature, resulting in a high-confidence model. Accurate modeling of the perturbations in the orbital model of the debris object and the satellite is essential for simulating the pseudo-measurements since they highly depend on the state vectors of the bodies. Moreover, the propagation results need to be accurate in the case of state estimation, which is then used to predict the evolution of the orbital errors over time.

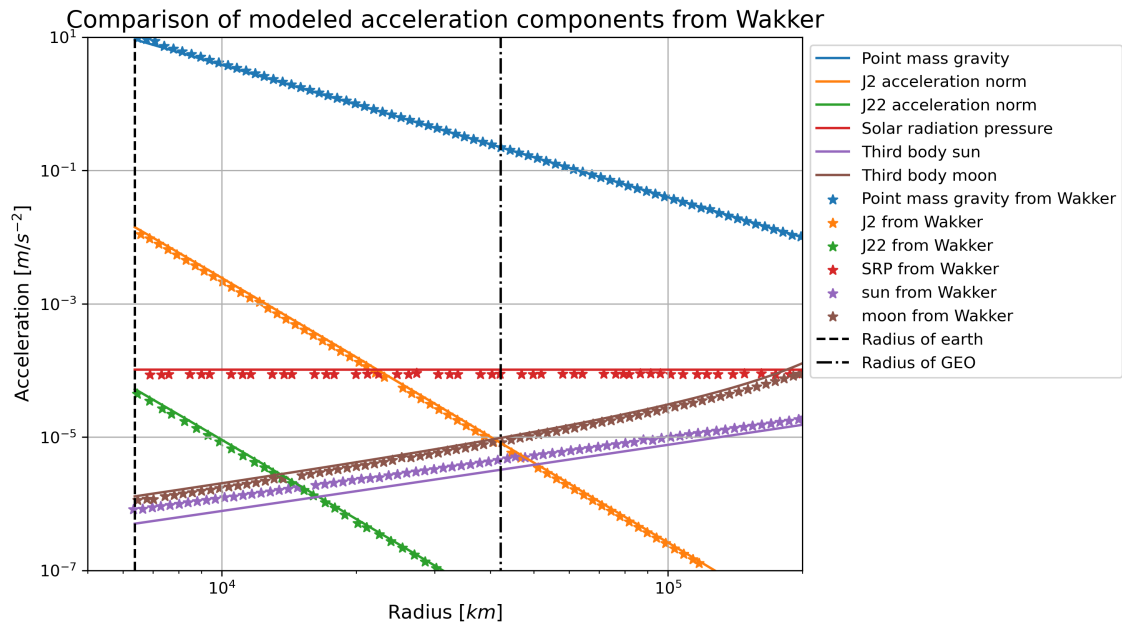


**Figure 5.11:** Overview of the magnitudes of acting perturbations in the developed model for all orbital altitudes. This is simulated to show the comparison with the acceleration magnitudes specified in Figure 3.9, which was adapted from Wakker [27].

## 5.2. Radar design verification

The instrument parameters with which the pseudo-measurements are collected also need to be tested such that the measurements can be considered reliable and can be reproduced in the future. For this purpose, the work of Maori et. al [4] has been used as a valid reference, a preliminary investigation of space-based radars to detect milli-meter-sized debris objects by ESA performed in 2017. Although this paper studies the performance of a continuous-wave radar in particular, it also analyses the performance of a pulsed Doppler radar at a small distance of less than 1 km, which is used as a reference for comparison with the INDIGO radar selected in this study.

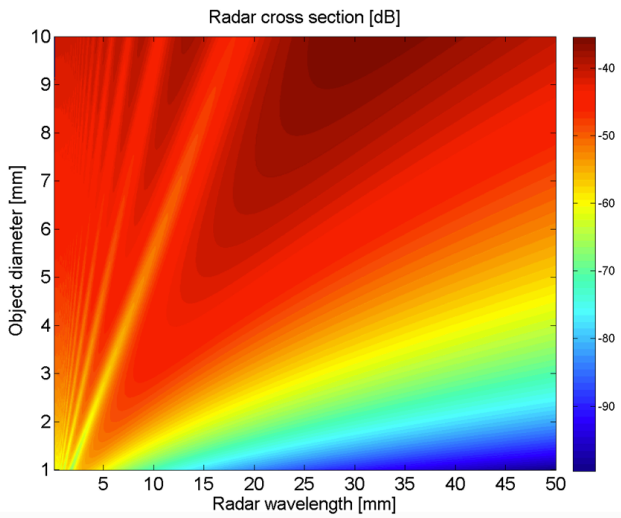
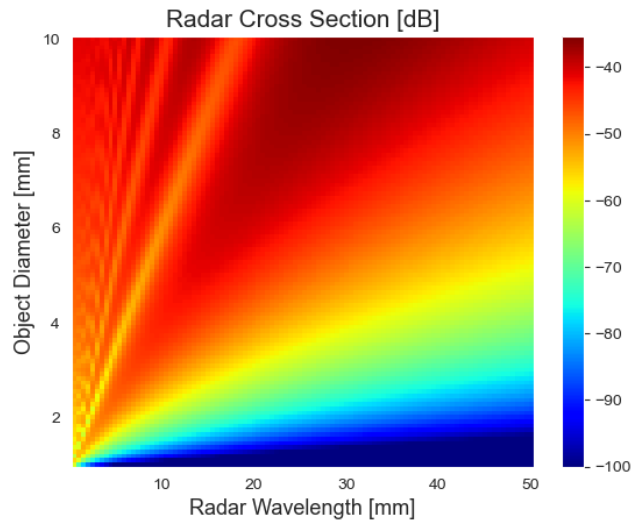
In the research by ESA, the measurements were simulated with their verified PROOF tool, which stands for Program for Radar and Optical Observations Forecasting. It was used to simulate the performance of a radar with the parameters specified in Table 5.4. Further, to validate the space debris model and the outputs from the PROOF tool, they were compared to measurements collected by a separately developed radar simulator, which showed similar detection and sensitivity results [4].

As seen in Table 5.4, the radar's wavelength is 8 mm, comparable to the target size (millimeter level). The spherical metal object is subjected to Mie and Rayleigh scattering, whose RCS variation was studied by ESA as seen in Figure 5.12 [4]. In the developed model for radar, the different scattering regimes (as visualised earlier in Figure 3.11) are considered for the same mm-sized object. The same plot was recreated with a color map to show the RCS variations. It can be seen in Figure 5.13.

Figure 5.13 is a close recreation of Figure 5.12 with similar magnitudes and behaviour showing the different scattering regimes. When the radar wavelength is much larger than the object di-

**Table 5.4:** Parameters of the coherent pulse radar parameters simulated with ESA's PROOF tool in the work of Maori et. al [4].

Parameter	Symbol	Value
Peak transmitter power	$P_t$	50 W
Antenna diameter	$D_{ant}$	80 cm
Transmitting antenna gain	$G_t$	38.39 dB
Receiving antenna gain	$G_r$	38.39 dB
Antenna efficiency	$\eta$	70 %
Pulse duration	$\tau$	$66 \times 10^{-9}$ s
Noise bandwidth	$B$	15 MHz
Wavelength	$\lambda$	8 mm
Losses	$L$	-2 dB
Noise figure	$N_f$	3 dB
System noise temperature	$T_s$	297K

**Figure 5.12:** Original plot from Maori et. al [4], showing the variation of RCS as a function of object diameter and radar wavelength.**Figure 5.13:** Recreated plot for RCS variation, using the same pulsed radar parameters used in Table 5.4 [4].

ameter, the behaviour of the RCS is seen to be varying with  $\lambda^{-4}$  in the lower right region of the plots. The Mie region is the upper right region, where contour lines oscillate between -40 dB and -60 dB. The left corner corresponds to the optical region with an almost constant value of almost -45 dB.

After the RCS values have been verified, the SNR of the pulse Doppler radar is studied. The SNR is the main performance parameter on which the measurement acquisition for INDIGO is based. Hence, it is crucial to verify the SNR to consider the collected measurements credible for orbit determination. The available SNR of the debris using the radar parameters in Table 5.4 is simulated using the developed software in an attempt to recreate the original plot shown in Figure 5.14 [4]. The resulting recreation is visualised in Figure 5.15.

The recreated plot is very close to the original plot in values and matching in behaviour. There are slight differences in the resolution and SNR values for the radar wavelength. This is due to

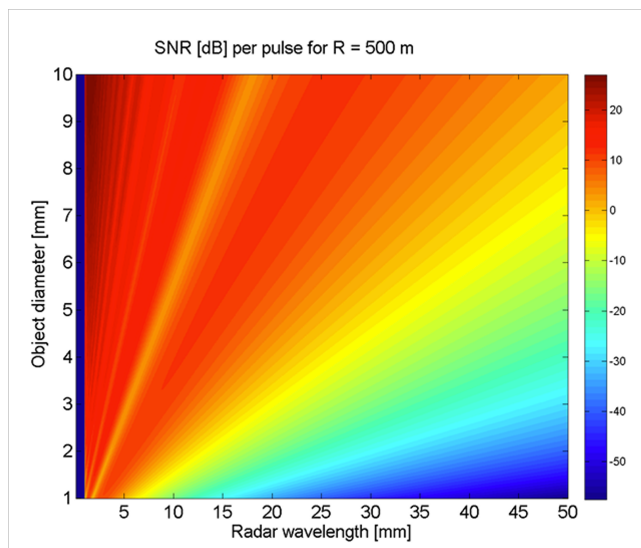


**Figure 5.14:** Original plot from Maori et. al [4], showing the SNR as a function of object diameter and radar wavelength at an object distance of 500 m.

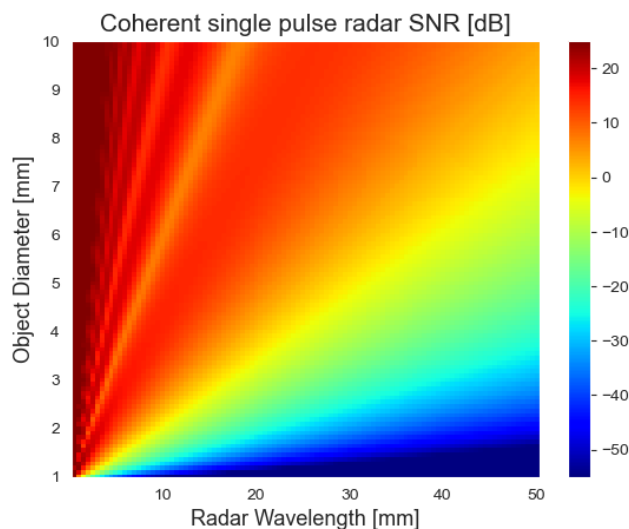


**Figure 5.15:** Recreated plot for SNR variation at a distance of 500 m, using the same pulsed radar parameters used in Table 5.4 [4].

the inclusion of a matched filter in the work of Maori et. al [4], which improves the SNR and accounts for Doppler variation and Fast Fourier Transform (FFT) losses. The model developed in the thesis is a simplified version, which does not include the filtering facilities used in the ESA study.

Despite its simplicity, the developed radar measurement model is capable of reproducing similar results as [4]. This verifies the correctness of the radar module's measurement modeling, thus validating its measurement acquisition methodology in the process. The pseudo-measurements can hence be considered a simple and good approximation of complex radar physics.

### 5.3. Validation with TLE orbital data

While the essence of verification is to test the working or mathematics behind a model, **validation** is performed to determine if the simulation results accurately represent the actual physical problem as a confrontation with reality [52]. The predictions by a model are compared to either experimental data or observed behaviour in practice. Since there has not been a physical mission that collects in-situ radar measurement data for debris, it is not possible to directly validate from real-life measurement data.

However, the working and accuracy of the orbit propagation model can be tested to see how the simplified developed model compares to a well-known high-fidelity propagator such as the general **Simplified General Perturbation (SGP4)** propagator used by NASA and NORAD to propagate the orbits using Two-Line-Element (TLE) data sets tracked by ground-based sensors; a clear link to "physical truth".

Since the debris object in this study is in the GEO regime, the TLE of real GEO debris is used for a validation study. One of the fragments of the **Ekran 2** satellite which the US SSN tracks, is used. The data for this object with a **NORAD catalogue number 12996** is downloaded from the NORAD satellite catalogue [56] from 9th January 2023 to 9th July 2023. An example of the TLE data of this object on the latter date is given below.

```

1 EKRA 2 DEB
2 1 12996U 77092J 23190.49945449 -.00000272 00000+0 00000+0 0 9995
3 2 12996 7.0509 288.9576 0019691 231.3997 48.0273 1.00031440 73754

```

The Kepler elements are extracted following the instructions on the NORAD documentation website [57]. They are set as initial conditions for simulation in the orbit propagation model developed in this research for 10 days. The actual TLE state vectors and the propagated orbit are overlapped and plotted in Figure 5.16.

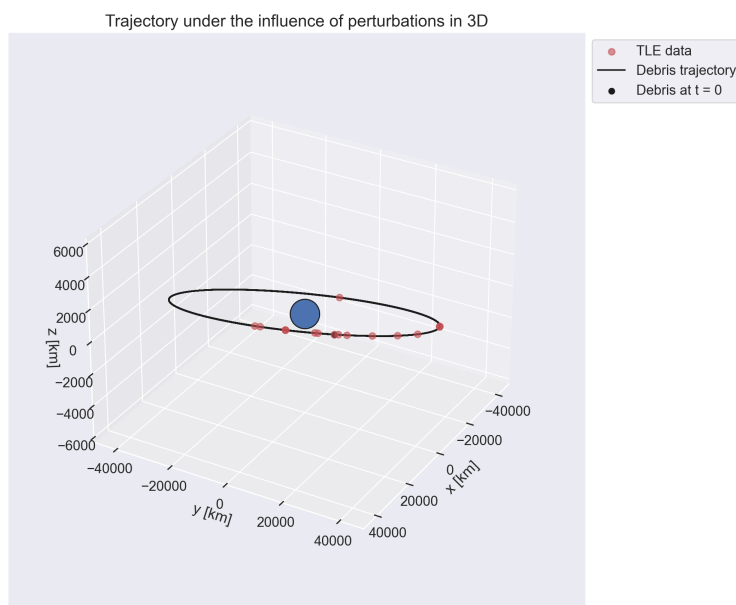


**Figure 5.16:** The TLE orbital data for the Ekran 2 debris (NORAD ID: 12996 [56]) overlapping with the orbital propagation model developed in this thesis. The plot validates the working of the orbital model.

The simulation was started, and the INDIGO system was made to collect measurements for the object. In 10 days, using the original INDIGO radar parameters, only three TLE measurements were seen to coincide with the simulated INDIGO pseudo-measurements. With only three measurements, the orbit determination process developed in the research diverges and does not yield credible results. Hence, instead of the measurements collected by the INDIGO system, the orbit is estimated and predicted for 10 days. The results showing the behaviour of the x, y, and z-coordinates in position are seen in Figures 5.17, 5.19 and 5.21. Similarly, the behaviour of the x, y, and z coordinates in velocity are seen in Figures 5.18, 5.20 and 5.22.

The state vectors estimated and predicted for the same period, using the developed model are presented for each state vector in the above figures. The yellow curves show the state vector elements for each Cartesian position and velocity vector component. The estimation and the prediction zone are separated by the dashed line marked as the 'prediction start' in each figure. The red dots represent the collected TLE data Cartesian state vector components, which are seen to fit well through the yellow curve. The initial state and last measurement points are marked by the dark and light blue dots respectively, in the estimation phase of the simulation. This is also where the black dots are seen, which correspond to the in-situ measurements collected when the debris is within the detection threshold of INDIGO. This exercise establishes that the orbit propagation, measurement model, and orbit estimation and prediction modules for the developed

software are credible and are capable of representing a real-life situation.

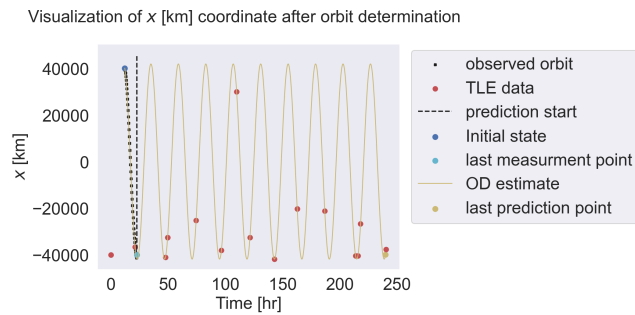


**Figure 5.17:** The behaviour of position in the x-coordinate of the orbit obtained for an Ekran 2 debris object (NORAD ID: 12996) between 9th January 2023 to 20th January 2023.

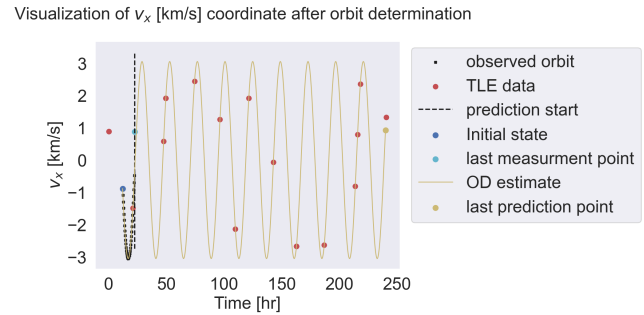


**Figure 5.18:** The behaviour of velocity in the x-coordinate of the orbit obtained for an Ekran 2 debris object (NORAD ID: 12996) between 9th January 2023 to 20th January 2023.

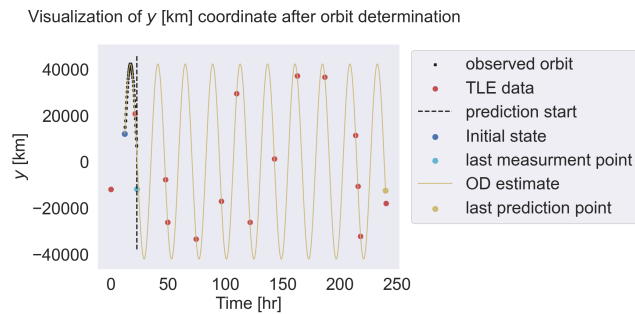


**Figure 5.19:** The behaviour of position in the y-coordinate of the orbit obtained for an Ekran 2 debris object (NORAD ID: 12996) between 9th January 2023 to 20th January 2023.

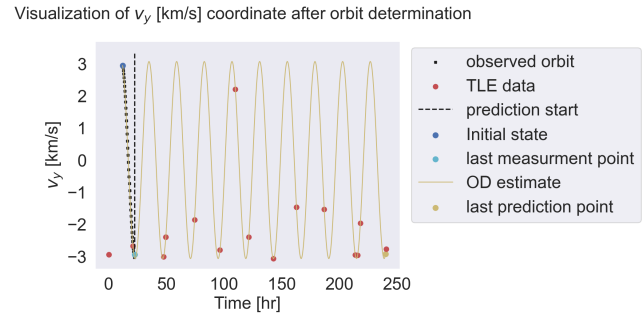


**Figure 5.20:** The behaviour of velocity in the y-coordinate of the orbit obtained for an Ekran 2 debris object (NORAD ID: 12996) between 9th January 2023 to 20th January 2023.

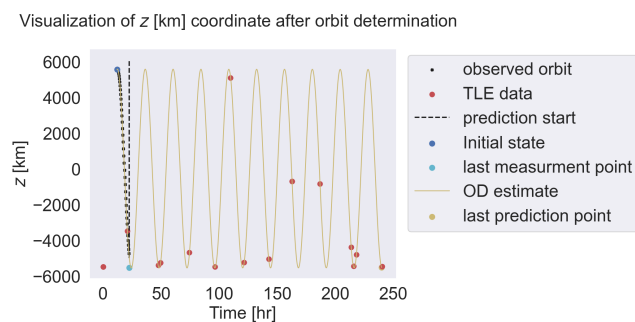


**Figure 5.21:** The behaviour of position in the z-coordinate of the orbit obtained for an Ekran 2 debris object (NORAD ID: 12996) between 9th January 2023 to 20th January 2023.

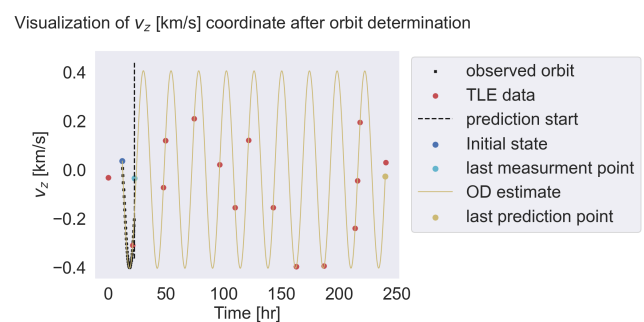


**Figure 5.22:** The behaviour of velocity in the z-coordinate of the orbit obtained for an Ekran 2 debris object (NORAD ID: 12996) between 9th January 2023 to 9th January 2023.

Having completed the verification of the software and validation with a real debris object, the results can be considered to be out of a **"black box"**, which will be applied for different cases and parameters. These results are discussed in the following chapter, which contains the results obtained from this study, and provides an interpretation of the same.

# 6

## Results and Discussion

The developed software was tested in Chapter 5, where the orbit propagation results were verified with the TUDATPy software and the orbit determination was verified from state estimation of an actual GEO debris object using its TLE data. Hence, after establishing the credibility of the results and software, a more detailed analysis can now be performed, which can be interpreted to draw conclusions on the research questions.

This chapter studies the study cases mentioned earlier in Section 4.3.2. First, the results of the nominal case are presented in Section 6.1 where the effect of the addition of noise and bias is interpreted. The effect of changing the integration step-size is studied in Section 6.2, followed by the orbital geometry analysis. Different altitudes and inclinations for the observation satellite geometry are studied in Sections 6.3 and 6.4 respectively. The effect of using different measurement types is discussed Section 6.5 followed by studying the effect of adding more satellites to the observation network in Section 6.6. The chapter ends with a sensitivity analysis in Section 6.7 for assessing the influence of uncertainties in the model.

### 6.1. Case 1: Nominal case

The nominal case refers to the first chosen case, which uses the initial propagation conditions of the orbit as stated in Table 4.3 to collect in-situ radar measurements using the radar parameters as stated in Table 4.2. The measurements are post-processed by the addition of noise and bias, after which the orbit determination is carried out using the initial debris state guess as provided in Table 4.6.

This section is dedicated to get a primary understanding of interpretation of the OD performance metrics for three different cases, defined below. It must be noted that the nominal case considers the orbital dynamics model and estimation model to include all orbital perturbations.

- **All ideal measurements:**

This reference measurement case is generated simply by following the measurement acquisition strategy stated earlier in Section 4.1.2. This consists of fitting the orbit using all measurements: range, range-rate, azimuth and elevation. It is free of any error sources and depends on the relative positions and velocities of the modeled debris object and the observation satellite at an altitude of 1000 km below the GEO ring. Both objects have an inclination of  $0^\circ$ .

- **Addition of Gaussian noise only:**

Gradually, Gaussian noise will be added to all radar measurements, worsening the OD performance. The standard deviation values for each measurement are obtained from Table 4.4.

- **Addition of both noise and bias:**

Finally, bias values stated in Table 4.4 are added to the radar measurements to account for systematic errors. This is expected to simulate reality, worsening the OD performance compared to the no-noise or noise-only case.

### 6.1.1. Ideal measurements case

The measurement residuals computed are first analysed for all noise-free cases. Figure 6.1 shows the true range residuals, Figure 6.2 shows the true range-rate residuals, Figure 6.3 shows the true azimuth residuals and Figure 6.4 shows the true elevation residuals.

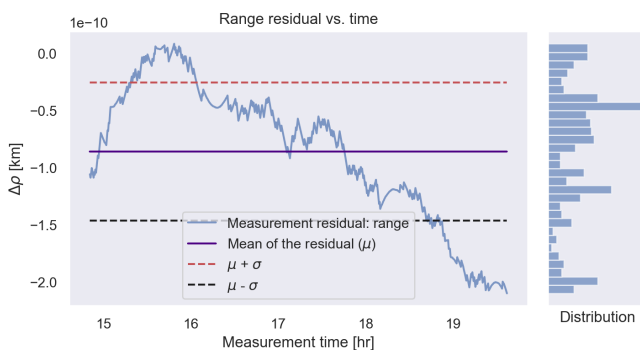


**Figure 6.1:** Residuals in range measurements for the nominal case of a single satellite ( $\Delta h = 1000$  km,  $\Delta i = 0^\circ$ , all measurements) for a case with no noise added to the measurements.

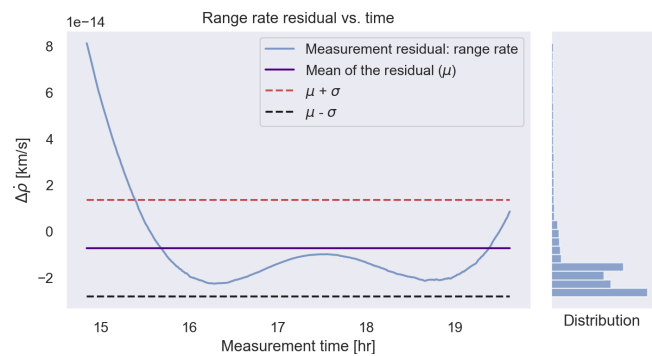


**Figure 6.2:** Residuals in range-rate measurements for the nominal case of a single satellite ( $\Delta h = 1000$  km,  $\Delta i = 0^\circ$ , all measurements) for a case with no noise added to the measurements.

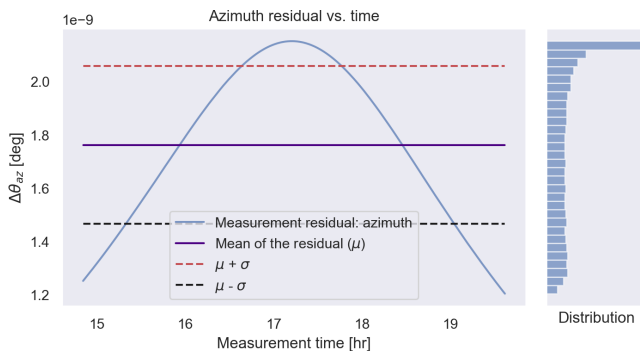


**Figure 6.3:** Residuals in azimuth measurements for the nominal case of a single satellite ( $\Delta h = 1000$  km,  $\Delta i = 0^\circ$ , all measurements) for a case with no noise added to the measurements.

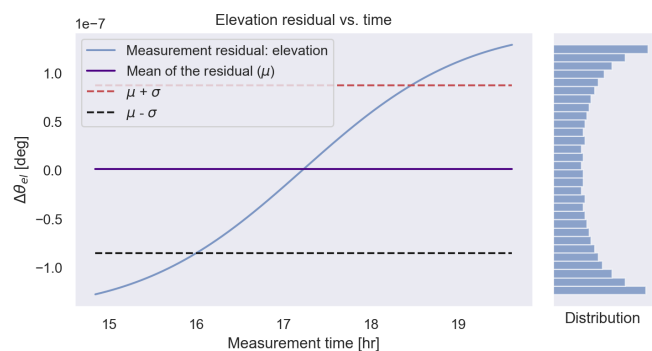


**Figure 6.4:** Residuals in elevation measurements for the nominal case of a single satellite ( $\Delta h = 1000$  km,  $\Delta i = 0^\circ$ , all measurements) for a case with no noise added to the measurements.

It can be seen that all the values are very small (in the order of  $10^{-10}$  km for the range,  $10^{-14}$  km/s for the range rate,  $10^{-9}$  for azimuth, and  $10^{-7}$  for elevation). The right-hand side of the plot shows the distribution of the residuals. The purple line marks the mean of the distribution, while the

dashed lines indicate the  $1\sigma$  upper and lower bounds from the mean. The residual curves show an overall smooth behaviour, which implies that measurements with no noise are supposed to fit perfectly through the observed measurements. This is visualised in Figure 6.5.

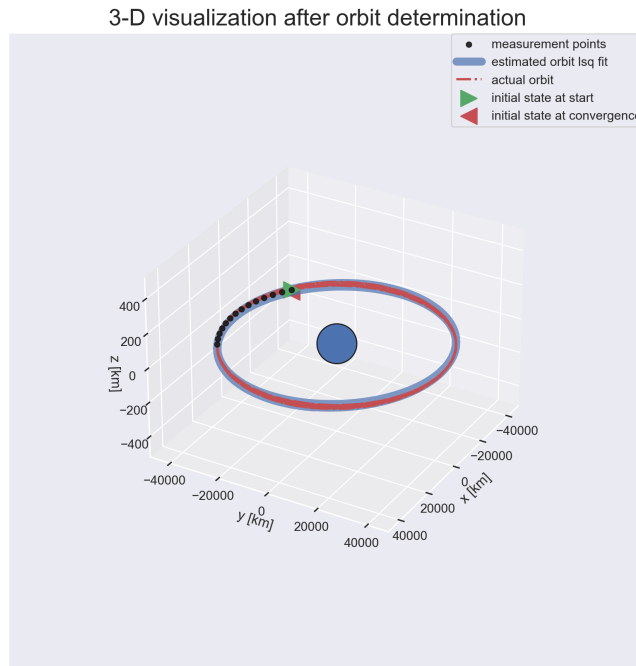


**Figure 6.5:** Three-dimensional orbit fitting visualisation of the debris, when only all ideal measurements are used. A perfect fit can be seen as expected.

### 6.1.2. Addition of Gaussian noise only

Now, the true measurements are perturbed by accounting for the noise present in measurements due to the properties of the radar. To reiterate, the standard deviation values taken are 18.49 m for range, 5.136 cm/s for the range rate and  $0.24^\circ$  for both angles.

Figure 6.6 shows the noise only range residuals, Figure 6.7 shows the noise only range-rate residuals, Figure 6.8 shows the noise only azimuth residuals and Figure 6.9 shows the noise only elevation residuals.

It can be seen in comparison to the previous case, that the oscillations in residuals have increased. The distribution of the measurements now demonstrates the effect of input Gaussian noise distribution, which is also conserved in the output of the measurement residuals. The mean value of the range, range rate and azimuth coincide with the peak of the distribution. For elevation, the residuals are not centred around the mean but still show a Gaussian distribution, as expected.

The residual values with noise only are no longer small. The range residuals show a  $1\sigma$  value of near 0.02 km or 20 m, which corresponds to the input noise value of 18.49 m added earlier. For range rate, the  $1\sigma$  value is about  $5 \times 10^{-5}$  km/s, which corresponds with the standard deviation noise of 5.136 km/s added to the range-rate measurements. The azimuth residuals too are centred around  $0^\circ$  showing a  $1\sigma$  value of about  $0.286^\circ$ . The elevation residuals are not centred around  $0^\circ$ , which does not make it a perfect Gaussian distribution. Hence, the  $1\sigma$  value is not represen-

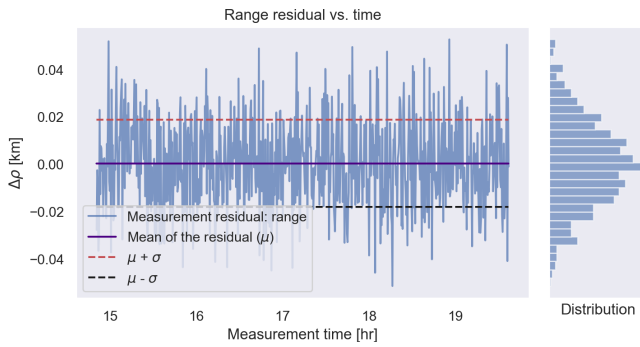


**Figure 6.6:** Residuals in range measurements for the nominal case of a single satellite ( $\Delta h = 1000$  km,  $\Delta i = 0^\circ$ , all measurements) for a case with only noise of standard deviation 18.49 m added to the true measurements.

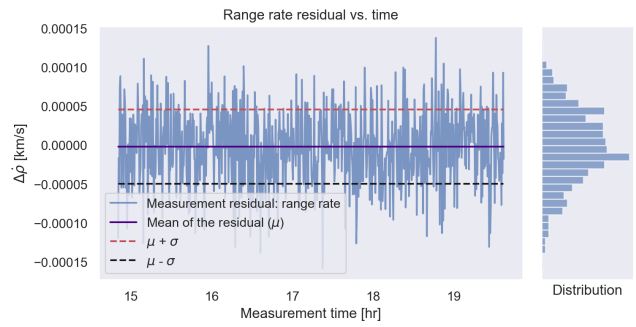


**Figure 6.7:** Residuals in range-rate measurements for the nominal case of a single satellite ( $\Delta h = 1000$  km,  $\Delta i = 0^\circ$ , all measurements) for a case with only noise of standard deviation 5.136 cm/s added to the true measurements.

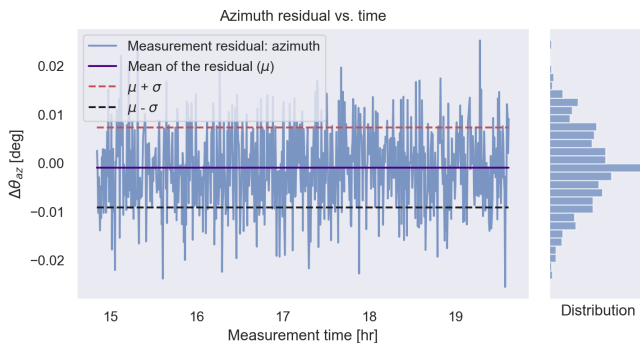


**Figure 6.8:** Residuals in azimuth measurements for the nominal case of a single satellite ( $\Delta h = 1000$  km,  $\Delta i = 0^\circ$ , all measurements) for a case with only noise of standard deviation  $0.24^\circ$  added to the true measurements.

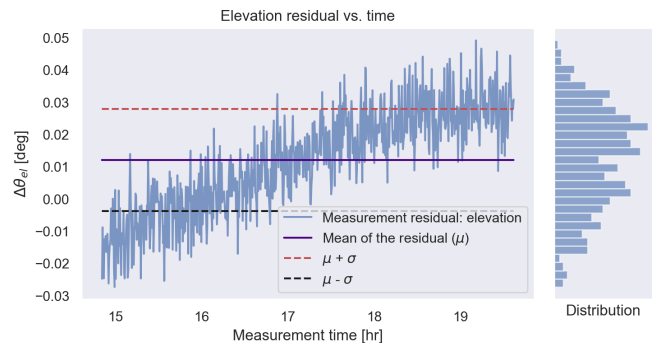


**Figure 6.9:** Residuals in elevation measurements for the nominal case of a single satellite ( $\Delta h = 1000$  km,  $\Delta i = 0^\circ$ , all measurements) for a case with only noise of standard deviation  $0.24^\circ$  added to the true measurements.

tative of the amount of standard deviation provided initially. This is an interesting case, which hints at poorly collected elevation measurements due to the debris object's planar orbits and the satellite. This can also be spotted in the 3D orbit visualisation where there is a deviation in the inclination of the estimated orbit (shown in blue) from the actual orbit (shown in red) in Figure 6.10.

The effect of addition of only Gaussian noise can be seen in Figure 6.10, where there is a slight deviation especially in the inclination estimated. The red scatter represents the actual orbit, while the blue curve represents the fitted orbit. The measurement points collected are marked by black dots. The starting and converging points during the WLS process is visualised by the green and the red arrowheads, marking the start and end of estimation.

### 6.1.3. Addition of noise and bias

After analysing the effect of noise, the systematic errors are also accounted for in the measurements, by adding individual biases to the noise-only measurements. To re-iterate, a bias value of 20 m is added for the range, 50 cm/s for the range rate, and  $0.1^\circ$  for both azimuth and elevation angles.

Figure 6.11 shows the range residuals, Figure 6.12 shows the range-rate residuals, Figure 6.13 shows the azimuth residuals and Figure 6.14 shows the elevation residuals.

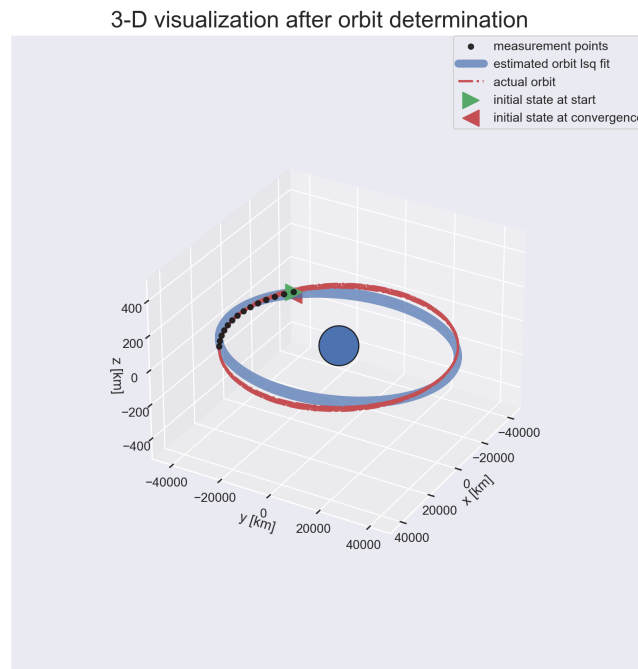


**Figure 6.10:** Three-dimensional orbit fitting visualisation of the debris, when only noise is added to all ideal measurements. The orbit now deviates (relatively 7.4 times higher RMS error than the case without noise and bias) from a perfect fit compared to what was seen in Figure 6.5.

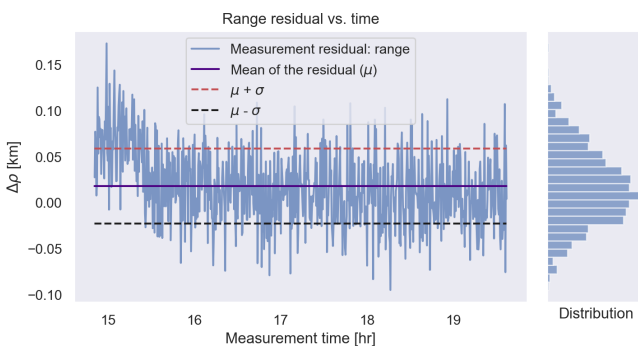


**Figure 6.11:** Residuals in range measurements for the nominal case of a single satellite ( $\Delta h = 1000$  km,  $\Delta i = 0^\circ$ , all measurements) for a case with both noise of standard deviation 18.49 m and bias 20 m of added to the true measurements.

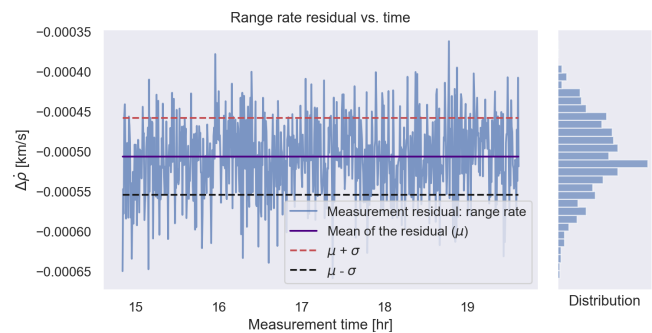


**Figure 6.12:** Residuals in range-rate measurements for the nominal case of a single satellite ( $\Delta h = 1000$  km,  $\Delta i = 0^\circ$ , all measurements) for a case with both noise of standard deviation 5.136 cm/s and bias 50 cm/s of added to the true measurements.

The effect of addition of bias to the noisy data can be observed by the change in residual distribution, which has its peak shifted by the amount of standard deviation added as bias. This is visible more or less for all measurements, with no significant change in the deviation values as observed in Section 6.1.2, apart from a slight shift of the mean value denoted by the purple line. The 3D visualisation for the orbit fitting is visualised again this time for both noisy and biased data. The results are seen in Figure 6.15.

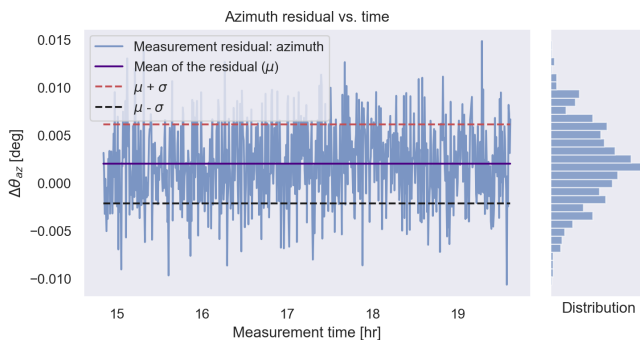


**Figure 6.13:** Residuals in azimuth measurements for the nominal case of a single satellite ( $\Delta h = 1000$  km,  $\Delta i = 0^\circ$ , all measurements) for a case with both noise of standard deviation  $0.24^\circ$  and bias  $0.1^\circ$  of added to the true measurements.

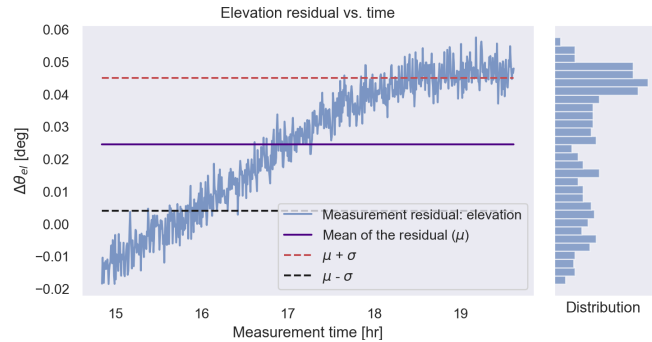


**Figure 6.14:** Residuals in elevation measurements for the nominal case of a single satellite ( $\Delta h = 1000$  km,  $\Delta i = 0^\circ$ , all measurements) for a case with both noise of standard deviation  $0.24^\circ$  and bias  $0.1^\circ$  of added to the true measurements.

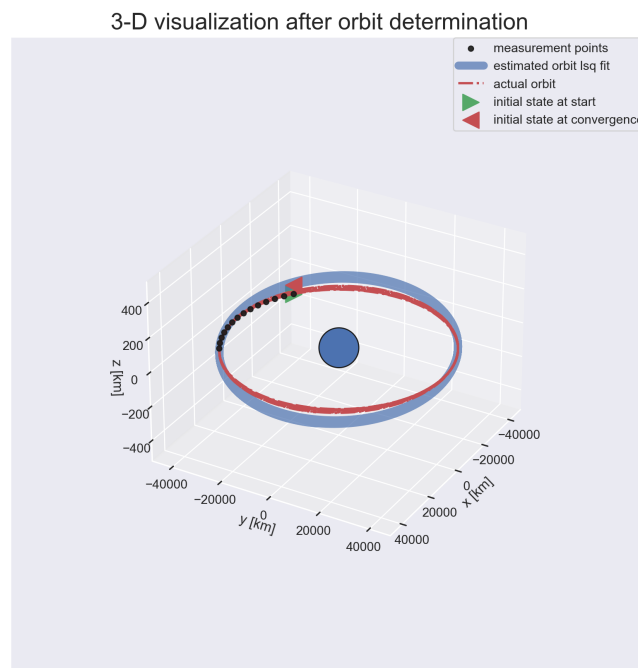


**Figure 6.15:** Three-dimensional orbit fitting visualisation of the debris, when both noise and bias is added to all ideal measurements. The orbit deviates more (relatively 9 times higher RMS error than the case without noise and bias) than what was seen in Figure 6.5 or Figure 6.10.

#### 6.1.4. Overall nominal case analysis

Now that the individual sub-cases of the nominal have been analysed, an overall conclusion can be drawn. The convergence behaviour of the three sub-cases can be understood from the RMSE values over the iterations. This is visualised in Figure 6.16.

It can be seen that the blue line has an RMSE of almost  $10^{-7}$ , which is a very small value, representing very good convergence behaviour. The RMSE of the noise-only case is expected to be about 1, while for the noise and bias case, it is expected to be higher. This exhibits that convergence behaviour is worse for an only noise case, compared to a no-noise case and is worsened with addition of a constant bias to the data set.

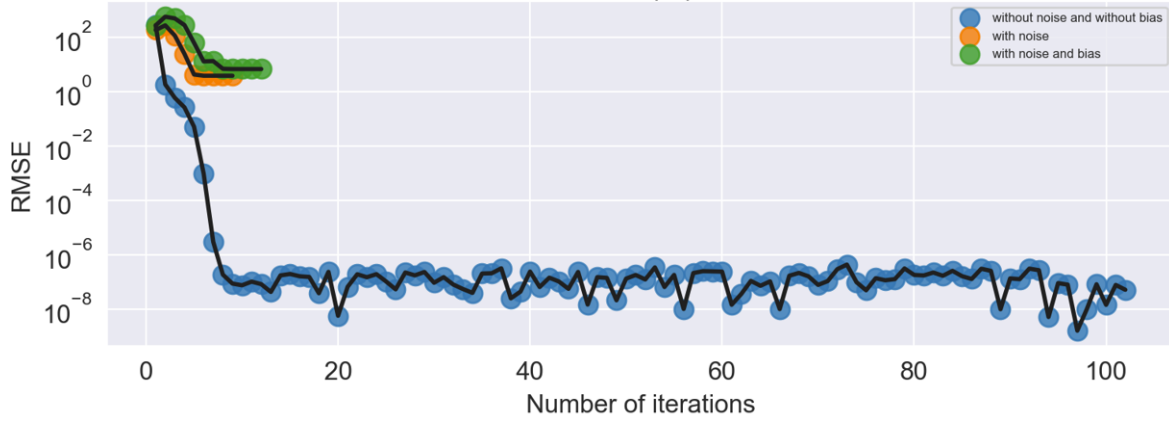


**Figure 6.16:** The RMSE convergence pattern for the three sub-cases of the Nominal case. The blue line represents the case with no noise, followed by the orange line representing only the noise-only case. The green line considers the noise and bias both incorporated into the measurements.

Then, the accuracy with which the initial position and velocity of the debris is derived can be computed from the noise-only covariance matrix. The formal uncertainty in position and velocity and the RMSE error for three cases are presented in Table 6.1.

**Table 6.1:** Formal uncertainties in position and velocity for a nominal case: with no error sources, only Gaussian noise, and both noise and bias.

Nominal case	Position accuracy [m]	Velocity accuracy [m/s]	RMSE
No noise	$2.83 \times 10^{-6}$	$4.97 \times 10^{-9}$	$1.05 \times 10^{-7}$
Only noise	1885.4	0.8034	1.905
Both noise and bias	3536.4	1.814	5.894

The accuracy is very small for the no-noise case, which increases with the addition of Gaussian noise in the order of  $10^3$  km for position and  $10^{-1}$  m/s for velocity. As bias is introduced, the accuracy worsens (i.e. its magnitude increases). The accuracy highly depends on the number of measurements provided, which were only 689 for the nominal case for 5 hours.

Lastly, the evolution of errors can be studied. The behaviour of the errors in Cartesian position and velocity components can be visualised from Figure 6.17.

Here too, the same behaviour is reflected, where the errors in  $x$ ,  $y$ ,  $v_x$  and  $v_y$  are seen to get worse for the case with both noise and bias (shown by the green line), which extends to maximum errors of 100 km in position and 0.008 km/s in velocity for these coordinates. It must be noted that the position and velocity in the  $z$ -coordinate do not exhibit the same behaviour, which is not unexpected, given the lack of information acquired in the  $z$ -plane.

The nominal case aimed to provide the reader with an understanding of the interpretation of relevant POD performance metrics. A more straightforward approach will be followed for the remaining cases to present the results concisely for the test cases listed.

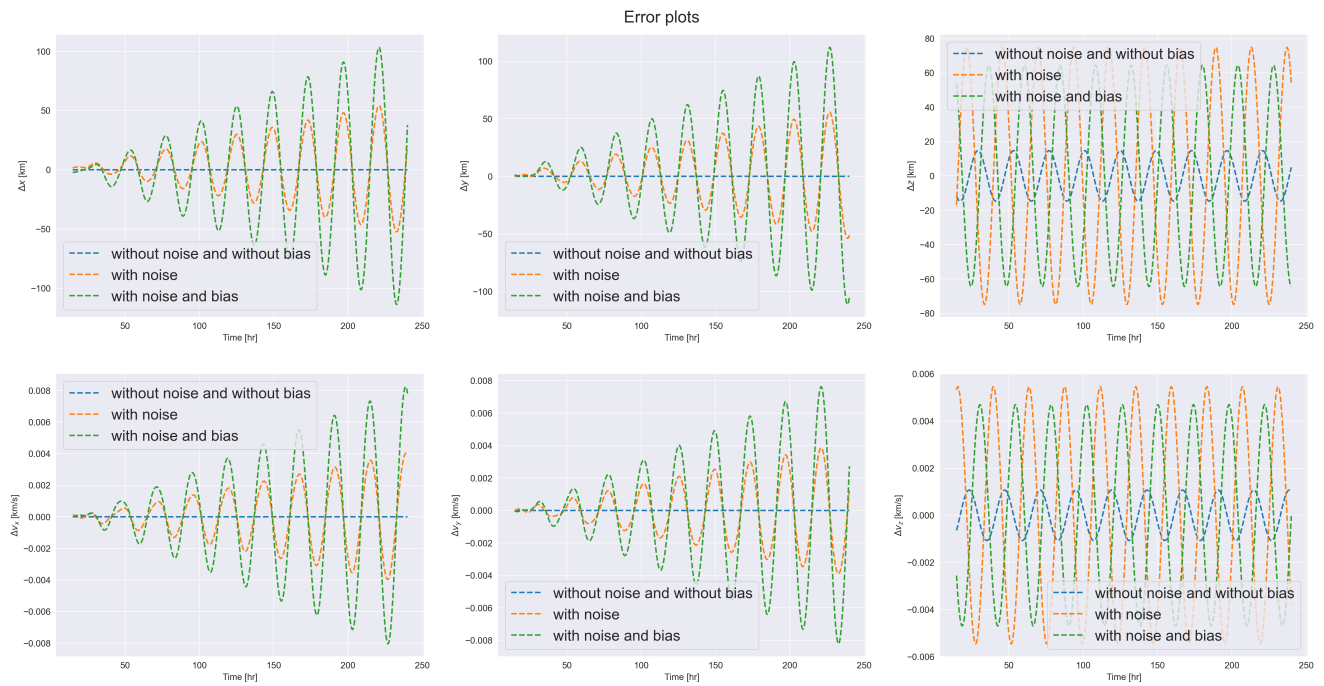


**Figure 6.17:** The growth of errors between actual and estimated state vectors over time for the three sub-cases of the nominal case. Like the RMSE plot, the blue line represents case with no noise, followed by the orange line representing only noise case. The green line considers the noise and bias both incorporated into the measurements.

## 6.2. Case 2: Different integration step sizes

The performance of the orbit determination process will also depend on how frequently the measurements are calculated. Choosing a larger step size will lead to less data, so a less accurate position and velocity determination. However, a smaller step size will result in a longer computation time. Moreover, the step size choice determines the numerical integration errors. Hence, an analysis has been carried out with  $\Delta h = 1000$  km, and  $\Delta i = 0^\circ$ , which analyses the effect of step size on OD performance. Based on this, the behaviour of changing step sizes on the OD quality can be inferred.

For model tuning, six step sizes have been chosen. They are equal to 1, 5, 10, 25, 50, and 100 s. The convergence behavior based on RMSE and the formal uncertainty in position and velocity for the initial state is studied. This is presented in Table 6.2.

**Table 6.2:** Formal uncertainties in position and velocity and RMSE for a case studying different step sizes for integrating the orbit for the nominal case. ( $\Delta h = 1000$  km,  $\Delta i = 0^\circ$ )

Step size [s]	Position accuracy [m]	Velocity accuracy [m/s]	RMSE	Computational time [s]
1	186.00	0.0107	1.646	938
5	448.13	0.0142	1.305	34
10	564.80	0.0186	1.192	26
25	1413.63	0.0450	1.788	5
50	2995.14	0.1303	2.732	3
100	26564.77	2.7919	93.225	7

It can be seen from Table 6.2 that increasing the step size from 1 to 100 seconds, decreases the

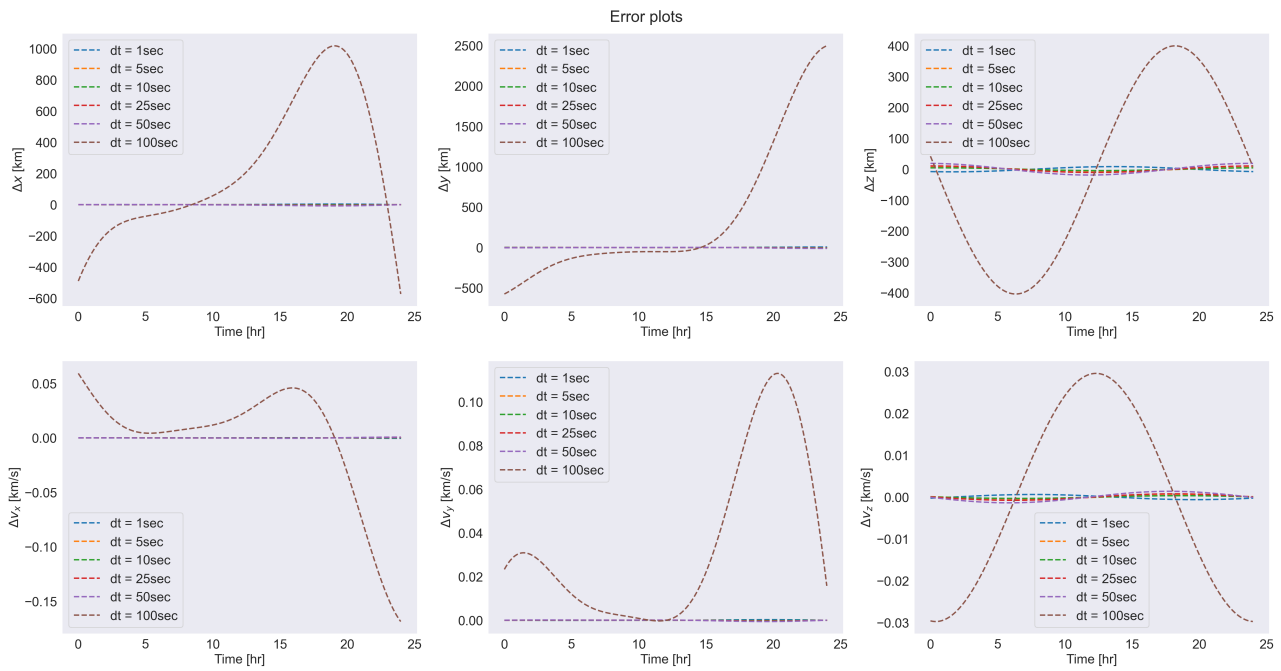


Figure 6.18: The evolution of errors in the Cartesian coordinates due to different step sizes chosen.

position and velocity accuracy. Since the radar integration time and the orbit integration step size are the same, increasing the step size means that there are fewer measurements per time step. As a result, the RMSE value can be seen to increase as we go down the table. The step sizes of  $dt = 5$  s,  $dt = 10$  s and  $dt = 25$  s, are of interest since they exhibit comparable position and velocity accuracies with good convergence. Looking at the computation time, it is better to select the step size of 25 seconds for the remainder of the study cases. Later in Chapter 7, a final answer on the step-size selection will be concluded, to answer one of the sub-research questions.

Finally, the errors in Cartesian coordinates are visualised in Figure 6.18. It is seen from the figure that the step size of 100 s has the largest error. Although the remaining step-size cases are not explicitly visible in this figure, the values in Table 6.2, support the expected outcome of improved accuracy and smaller errors.

### 6.3. Case 3a: Different satellite altitudes

The accuracy in position was found to be at the km level for the nominal case, which comes from the lack of sufficient measurements at 1000 km altitude difference, and the lack of information in the z-component of the state vector. Since a radar gets a higher SNR when closer to the target, this section evaluates the OD performance for three altitude cases. Additionally, the inclination of the satellite orbit was increased to  $2.5^\circ$  to obtain more information on debris in the z-direction. Three cases for different altitudes (250, 500 and 1000 km difference) at a fixed inclination have been studied in this research to evaluate the performance of state estimation when the satellite moves closer to the debris.

#### 6.3.1. Altitude difference 250 km

The measurement residuals for range, range rate, azimuth and elevation are shown in Figures 6.19, 6.20, 6.21 and 6.22, respectively. The measurement model includes the effect of Gaussian noise

and bias for each of the measurement types (similar as Section 6.1.3).

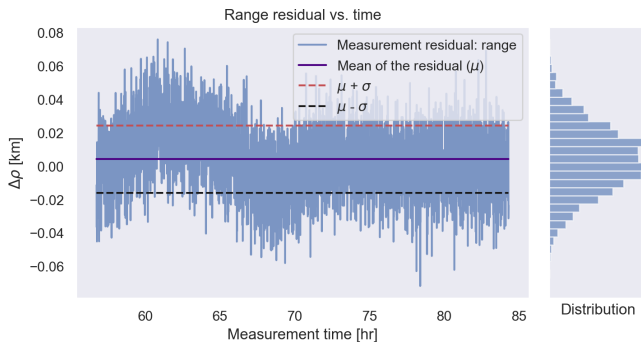


**Figure 6.19:** Residuals in range measurements for the change in altitude study case of a single satellite ( $\Delta h = 250$  km,  $\Delta i = 2.5^\circ$ , all measurements) for a case with both noise of standard deviation 18.49 m and bias 20 m of added to the true measurements.

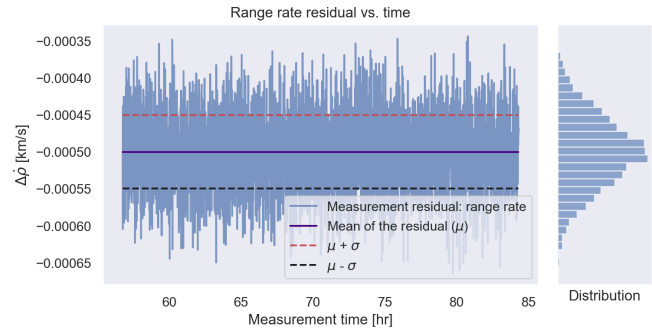


**Figure 6.20:** Residuals in range-rate measurements for the change in altitude study case of a single satellite ( $\Delta h = 250$  km,  $\Delta i = 2.5^\circ$ , all measurements) for a case with both noise of standard deviation 5.136 km/s and bias 50 cm/s of added to the true measurements.

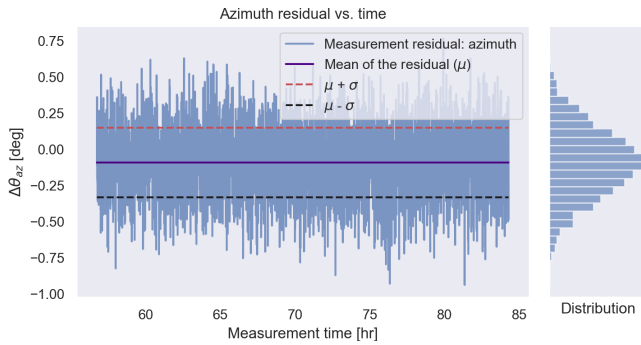


**Figure 6.21:** Residuals in azimuth measurements for the change in altitude study case of a single satellite ( $\Delta h = 250$  km,  $\Delta i = 2.5^\circ$ , all measurements) for a case with both noise of standard deviation  $0.24^\circ$  and bias  $0.1^\circ$  of added to the true measurements.

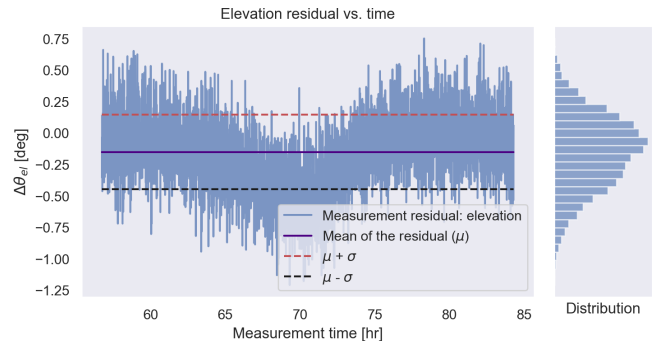


**Figure 6.22:** Residuals in elevation measurements for the change in altitude study case of a single satellite ( $\Delta h = 250$  km,  $\Delta i = 2.5^\circ$ , all measurements) for a case with both noise of standard deviation  $0.24^\circ$  and bias  $0.1^\circ$  of added to the true measurements.

The measurement residuals in all measurement types show a normal distribution, with the mean at the value of the bias provided to each measurement. The high density of the residuals arises from the fact that in this geometrical configuration, the radar can collect 3971 measurements in total, which cover close to 11% of the GEO debris ring since the difference in orbital velocity between the debris and the satellite is much less.

### 6.3.2. Altitude difference 500 km

The measurement residuals at an altitude difference of 500 km for range, range rate, azimuth and elevation are shown in Figures 6.23, 6.24, 6.25 and 6.26, respectively. The measurement model includes the effect of Gaussian noise and bias for each measurement type (similar to Section 6.1.3).

It is seen that the measurement residuals worsen as compared to the previous case of 250 km altitude difference. This is expected since the radar can collect 1873 measurements in this configuration. Although the density of the measurement residuals is less than that of  $\Delta h = 250$  km, they still follow a normal distribution.

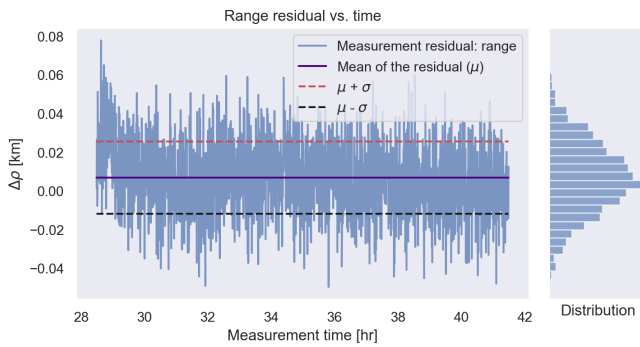


**Figure 6.23:** Residuals in range measurements for the change in altitude study case of a single satellite ( $\Delta h = 500$  km,  $\Delta i = 2.5^\circ$ , all measurements) for a case with both noise of standard deviation 18.49 m and bias 20 m of added to the true measurements.

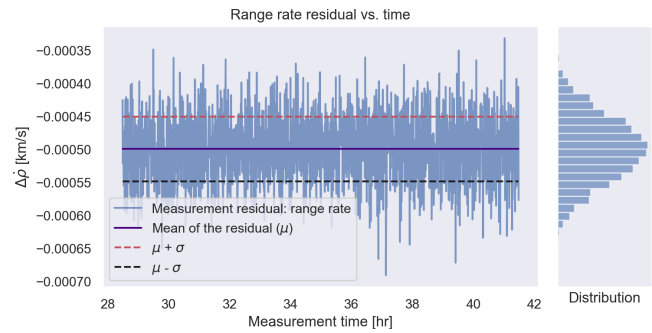


**Figure 6.24:** Residuals in range-rate measurements for the change in altitude study case of a single satellite ( $\Delta h = 500$  km,  $\Delta i = 2.5^\circ$ , all measurements) for a case with both noise of standard deviation 5.136 km/s and bias 50 cm/s of added to the true measurements.

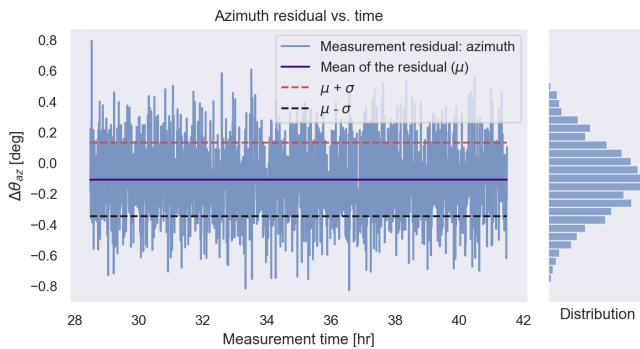


**Figure 6.25:** Residuals in azimuth measurements for the change in altitude study case of a single satellite ( $\Delta h = 500$  km,  $\Delta i = 2.5^\circ$ , all measurements) for a case with both noise of standard deviation 0.24° and bias 0.1° of added to the true measurements.

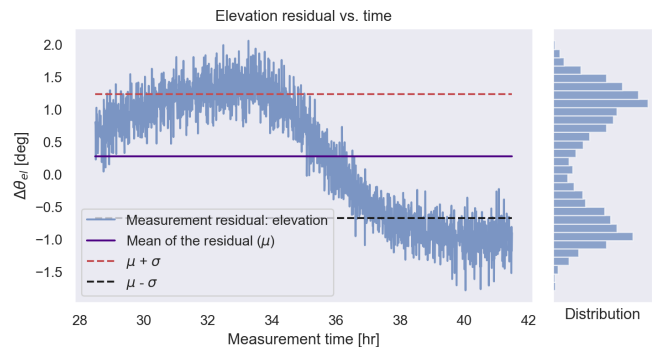


**Figure 6.26:** Residuals in elevation measurements for the change in altitude study case of a single satellite ( $\Delta h = 500$  km,  $\Delta i = 2.5^\circ$ , all measurements) for a case with both noise of standard deviation 0.24° and bias 0.1° of added to the true measurements.

### 6.3.3. Altitude difference 1000 km

Finally, the measurement residuals at an altitude difference of 1000 km for range, range rate, azimuth and elevation are shown in Figures 6.27, 6.28, 6.29 and 6.30, respectively. The measurement model includes the effect of Gaussian noise and bias for each measurement type.

The quality of measurement residuals is the worst compared to the previous cases of  $\Delta h = 250$  km and  $\Delta h = 500$  km. This is again expected since the radar can collect only 688 measurements in this configuration (similar to what was seen in the nominal case study at  $0^\circ$  too).

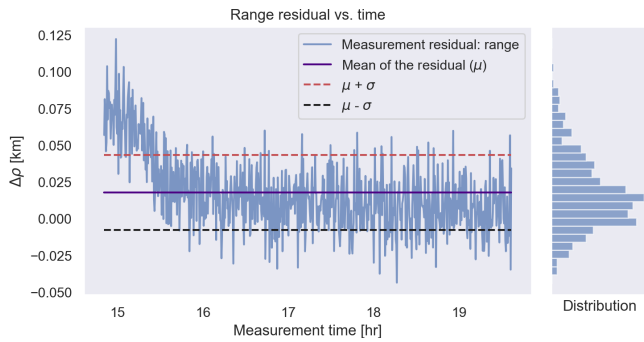


**Figure 6.27:** Residuals in range measurements for the change in altitude study case of a single satellite ( $\Delta h = 1000$  km,  $\Delta i = 2.5^\circ$ , all measurements) for a case with both noise of standard deviation 18.49 m and bias 20 m of added to the true measurements.

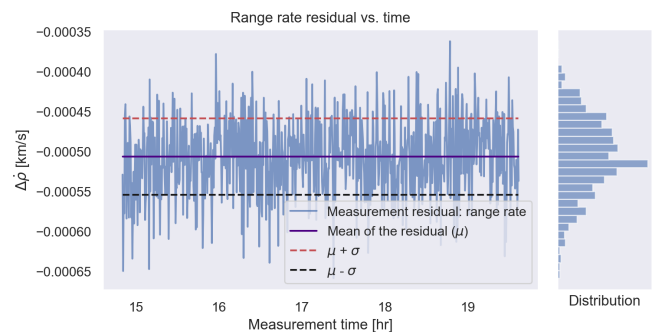


**Figure 6.28:** Residuals in range-rate measurements for the change in altitude study case of a single satellite ( $\Delta h = 1000$  km,  $\Delta i = 2.5^\circ$ , all measurements) for a case with both noise of standard deviation 5.136 km/s and bias 50 cm/s of added to the true measurements.

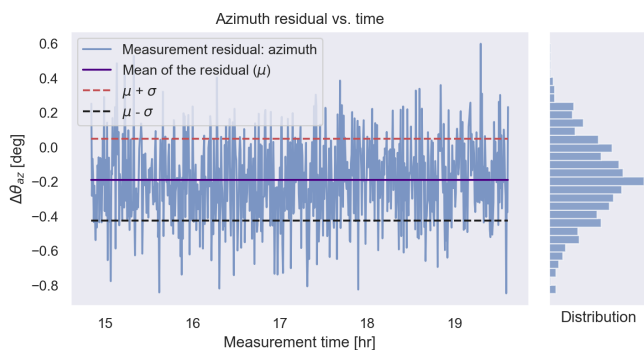


**Figure 6.29:** Residuals in azimuth measurements for the change in altitude study case of a single satellite ( $\Delta h = 1000$  km,  $\Delta i = 2.5^\circ$ , all measurements) for a case with both noise of standard deviation  $0.24^\circ$  and bias  $0.1^\circ$  of added to the true measurements.

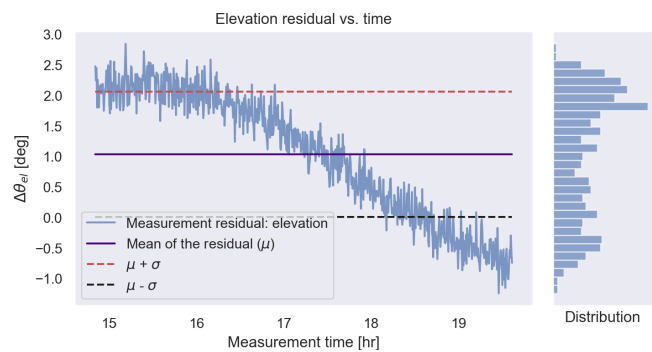


**Figure 6.30:** Residuals in elevation measurements for the change in altitude study case of a single satellite ( $\Delta h = 1000$  km,  $\Delta i = 2.5^\circ$ , all measurements) for a case with both noise of standard deviation  $0.24^\circ$  and bias  $0.1^\circ$  of added to the true measurements.

### 6.3.4. Overall altitude analysis

The convergence behaviour of all three cases can be visualised in Figure 6.31.

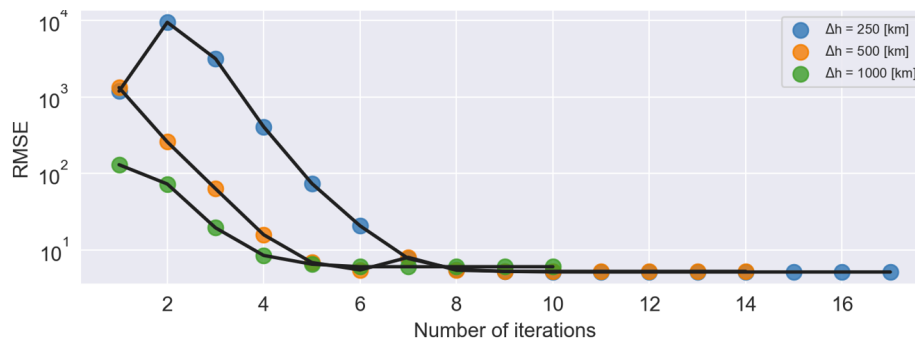


**Figure 6.31:** The RMSE convergence pattern for the three sub-cases of the altitude study case. The blue line represents the  $\Delta h = 250$  km case, followed by the orange line representing  $\Delta h = 500$  km. The green line considers the  $\Delta h = 1000$  km, all at an inclination of  $\Delta i = 2.5^\circ$

It is seen that the blue line depicting  $\Delta h = 250$  km starts with the highest RMSE initial value (due to more measurements to iterate through) and ends up at a value that is close to 5. This is again

expected since the noise includes the addition of bias to the measurements along with the noise. The orange line depicting  $\Delta h = 500$  km and the green line depicting  $\Delta h = 1000$  km follow next, which all converge at nearly similar values, but does take more iterations for convergence where there is more data.

The errors in the Cartesian coordinates can be found by taking the difference between the actual orbit and the estimated orbits using the above cases. The propagation of errors can then be visualised for a period of 10 days, to see how the prediction behaviour is by virtue of the collected measurements. The errors due to different altitude cases are shown in Figure 6.32.

For  $\Delta h = 1000$  km (shown by the green curves), the errors are highest with a magnitude of about 2 km in position and 0.3 m/s in velocity (norm of the individual Cartesian coordinates). For  $\Delta h = 500$  km (shown by the orange curves) and the  $\Delta h = 250$  km (shown by the blue curves), the errors are not distinctively visible in Figure 6.32. This requires a study into the accuracy of the initial state and RMSE value at convergence.

**Table 6.3:** Formal uncertainties in position and velocity for a case studying different altitudes of the satellite orbit for  $\Delta i = 2.5^\circ$ .

$\Delta h$ [km]	Position accuracy [m]	Velocity accuracy [m/s]	RMSE	No. of obs.
250	5.131	$4.97 \times 10^{-9}$	5.131	3971
500	19.06	0.0388	5.227	1873
1000	273.98	0.0789	6.013	688

Corresponding to the behaviour in prediction errors, the initial position and velocity accuracy values in Table 6.3 decrease as the values of  $\Delta h$  increases from 250 to 1000 km. The values of RMSE for the three cases are also summarised and are seen to concur with what was seen in Figure 6.31.

From the different altitude case studies, it is inferred that moving closer to the debris object gives the radar more opportunity to collect more measurements, thereby improving its quality. However, it also takes a longer time for convergence due to more measurements present, whose residual minimisation takes longer. Moreover, the revisit time is a big problem since for decreasing altitude, the synodic period increases. For  $\Delta h = 1000$  km, the synodic period is 27 days, while for  $\Delta h = 500$  km it is 55 days. For  $\Delta h = 250$  km, the synodic period is 113 days, which is a long time the satellite has to wait to be able to get a signal from the same debris object, which is not always suitable for the given simulation conditions. Hence, these aspects also need to be considered before choosing a suitable altitude regime for measurements.

## 6.4. Case 3b: Different satellite inclinations

The study into the effect of different inclinations is done to overcome the disadvantage of not obtaining much information on the z-component of the debris state vector, which remains ill-determined and difficult to predict due to the lack of proper measurements. To study this, specifically for this section, only the elevation measurements have been shown instead of all measurement residuals, since it is interesting to see what happens to them specifically for varying orbital inclinations. From the analysis of altitudes in Section 6.3, a  $\Delta h$  value of 500 km has been chosen for this study, where four values of satellite orbit inclination have been considered.

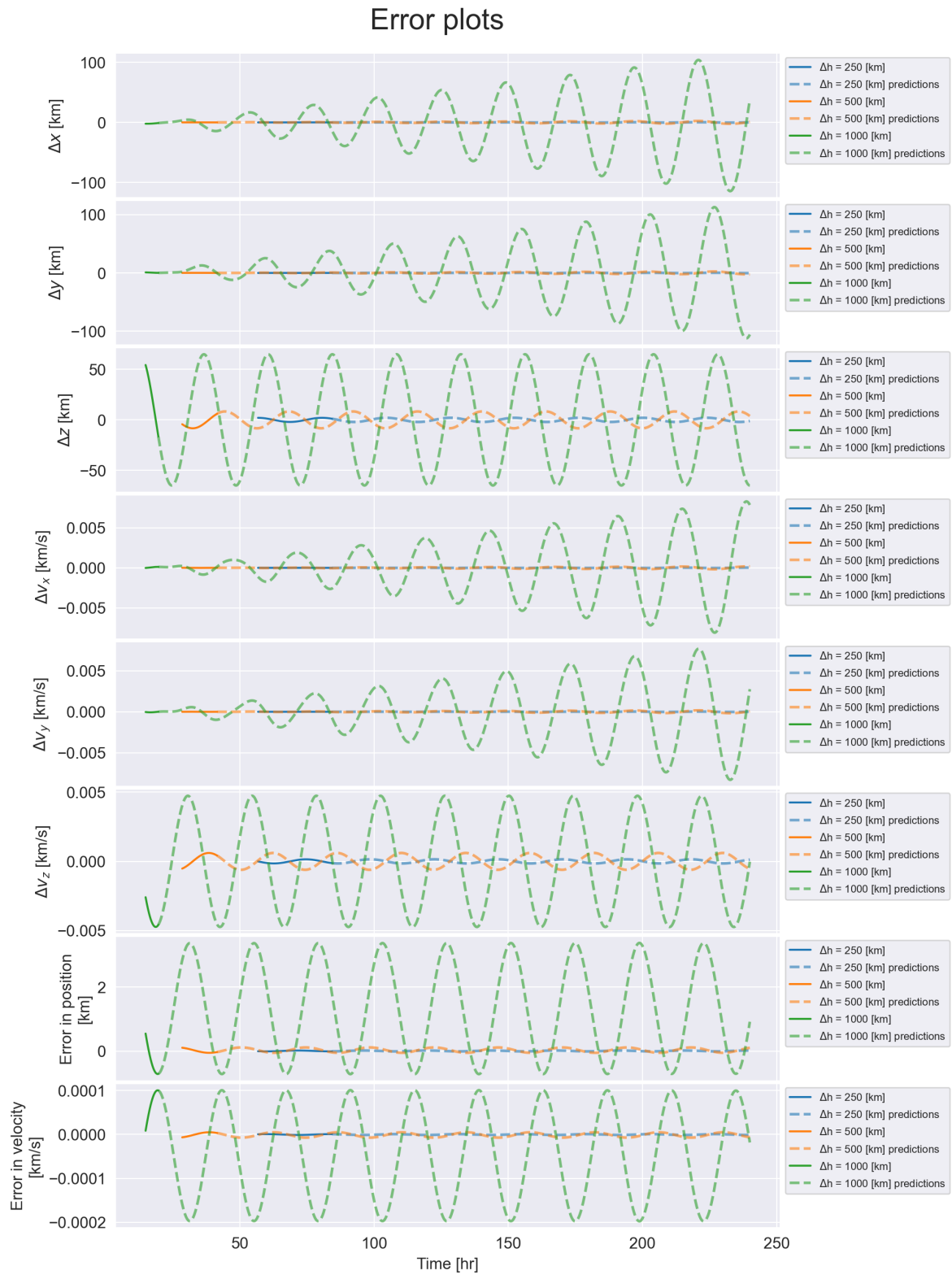


**Figure 6.32:** The error and prediction pattern for the three sub-cases of the altitude study case. The blue line represents the  $\Delta h = 250$  km case, followed by the orange line representing  $\Delta h = 500$  km. The green line considers the  $\Delta h = 1000$  km, all at an inclination of  $\Delta i = 2.5^\circ$

### 6.4.1. Inclination difference $0.1^\circ$

Directly taking an inclination of  $0^\circ$  leads to a poor estimation of the elevation measurements, which was seen in the nominal case and also in the altitude study case (for which it was rather done for  $\Delta i = 2.5^\circ$ ). By changing the relative inclination, the possibility of collecting information on the object's elevation is studied here.

Figure 6.33 shows the residuals of the elevation measurements for a relative inclination of  $0.1^\circ$ , while Figure 6.34 shows the estimated and observed elevation measurements for the same case.

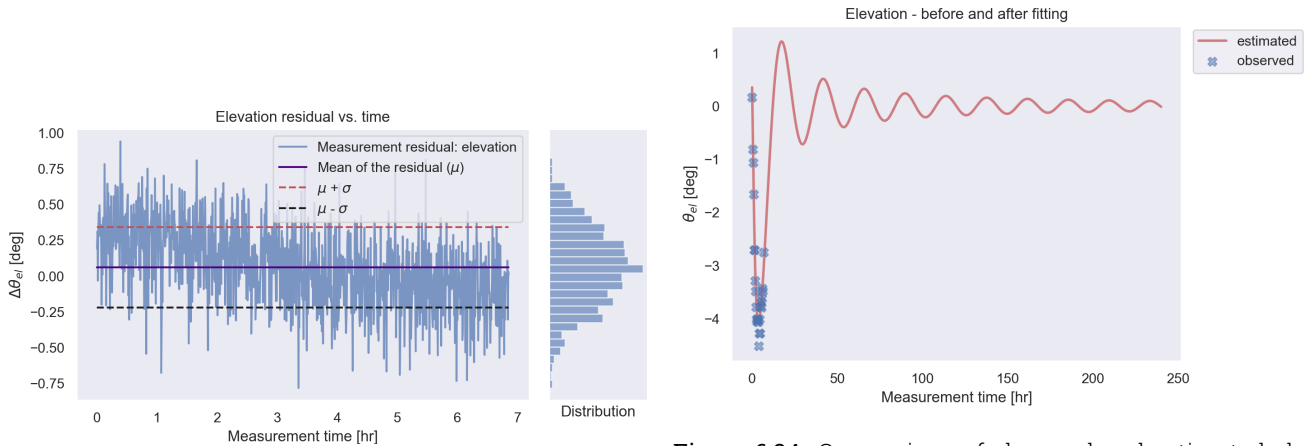


**Figure 6.33:** Residuals in elevation measurements for the change in inclination study case of a single satellite ( $\Delta h = 500$  km,  $\Delta i = 0.1^\circ$ , all measurements) for a case with both noise of standard deviation  $0.24^\circ$  and bias  $0.1^\circ$  of added to the true measurements.

**Figure 6.34:** Comparison of observed and estimated elevation measurements for Residuals in elevation measurements for the change in inclination study case of a single satellite ( $\Delta h = 500$  km,  $\Delta i = 0.1^\circ$ , all measurements) for a case with both noise of standard deviation  $0.24^\circ$  and bias  $0.1^\circ$  of added to the true measurements.

The distribution of elevation residuals is still a Gaussian distribution shifted up by the specified bias value of  $0.1^\circ$  or  $0.0018$  rad, well preserving its input noise characteristics. This configuration shows the collection of 988 measurements in 5 hours, shown by the blue dots in Figure 6.34, which shows the red line showing the elevation estimated by the WLS model to fit through the measurements. This configuration performs worse than the  $0^\circ$  inclination case with 1873 measurements, showing that a higher relative inclination value could be required.

### 6.4.2. Inclination difference $1^\circ$

Increasing the relative inclination to  $1^\circ$  produces a new set of elevation measurements and residual behaviour. Figure 6.35 shows the residuals of the elevation measurements for a relative inclination of  $1^\circ$ , while Figure 6.34 shows the estimated and observed elevation measurements for the same case.

For this configuration, the mean of the distribution lies around  $-0.015$  [rad] or  $1.317^\circ$ , which is close to the elevation residual values seen in the nominal case described in Section 6.1. The distribution on the right shows more samples within the  $1\sigma$  region, which is significantly more than in the previous case or the nominal elevation case. The measurements collected are more evenly spaced out in Figure 6.36, which spans 10 times the range of elevation values listed in Figure 6.34. The number of measurements collected is 825, less than in the previous case. However, since the samples are more concentrated toward the mean, it is expected to yield better state estimation

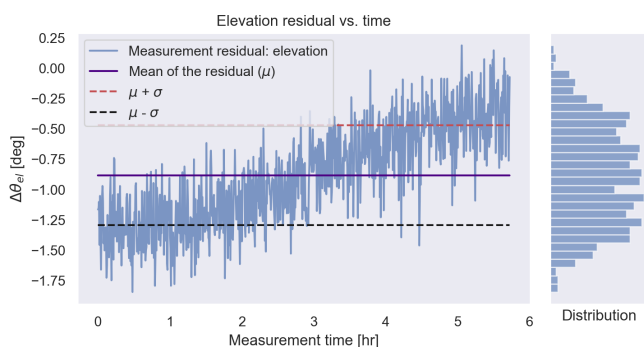


**Figure 6.35:** Residuals in elevation measurements for the change in inclination study case of a single satellite ( $\Delta h = 500$  km,  $\Delta i = 1^\circ$ , all measurements) for a case with both noise of standard deviation  $0.24^\circ$  and bias  $0.1^\circ$  of added to the true measurements.

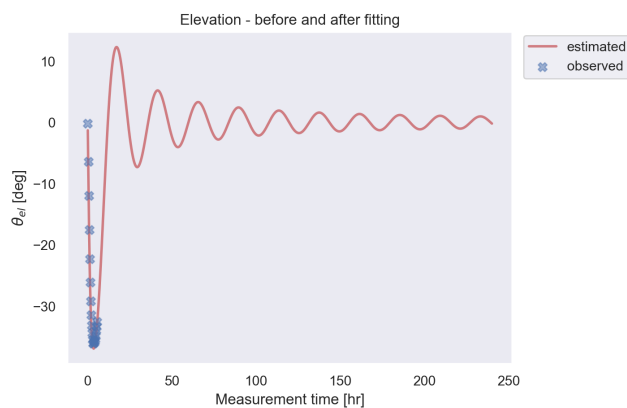


**Figure 6.36:** Comparison of observed and estimated elevation measurements for Residuals in elevation measurements for the change in inclination study case of a single satellite ( $\Delta h = 500$  km,  $\Delta i = 1^\circ$ , all measurements) for a case with both noise of standard deviation  $0.24^\circ$  and bias  $0.1^\circ$  of added to the true measurements.

accuracy.

### 6.4.3. Inclination difference $2.5^\circ$

The inclination of the satellite orbit is increased to  $2.5^\circ$  to see if more elevation measurement residual samples can be extracted. Figure 6.37 shows the residuals of the elevation measurements for a relative inclination of  $2.5^\circ$ , while Figure 6.38 shows the estimated and observed elevation measurements for the same case.

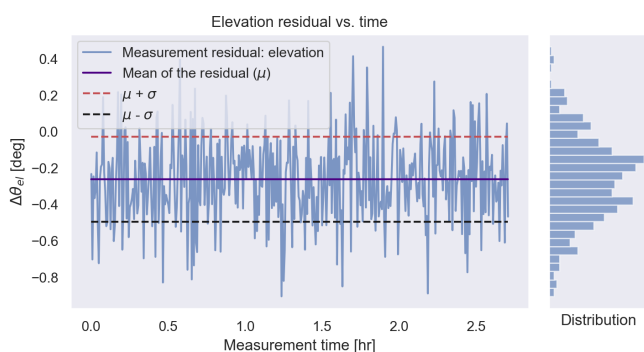


**Figure 6.37:** Residuals in elevation measurements for the change in inclination study case of a single satellite ( $\Delta h = 500$  km,  $\Delta i = 2.5^\circ$ , all measurements) for a case with both noise of standard deviation  $0.24^\circ$  and bias  $0.1^\circ$  of added to the true measurements.

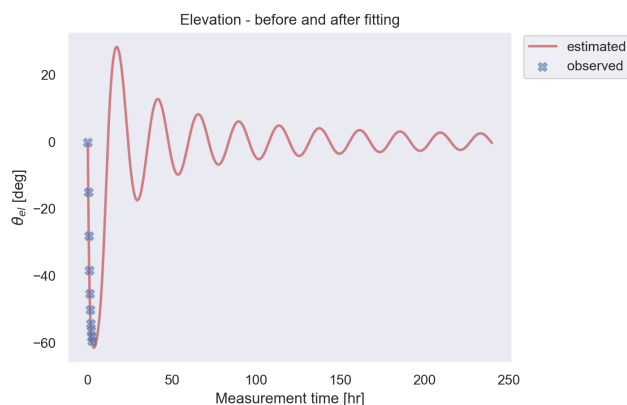


**Figure 6.38:** Comparison of observed and estimated elevation measurements for Residuals in elevation measurements for the change in inclination study case of a single satellite ( $\Delta h = 500$  km,  $\Delta i = 2.5^\circ$ , all measurements) for a case with both noise of standard deviation  $0.24^\circ$  and bias  $0.1^\circ$  of added to the true measurements.

The density of the oscillations is seen to decrease, leading to the acquisition of only 391 measurements. This is expected to cause a drop in accuracy and increase prediction errors. The scattered measurements are also not concentrated at the mean but are spread out following a normal distribution with gradually decreasing samples at the edges.

### 6.4.4. Inclination difference 5°

When the inclination of the satellite is further increased, the behaviour of the elevation residuals and fitting worsens. Figure 6.39 shows the residuals of the elevation measurements for a relative inclination of 5°, while Figure 6.40 shows the estimated and observed elevation measurements for the same case.

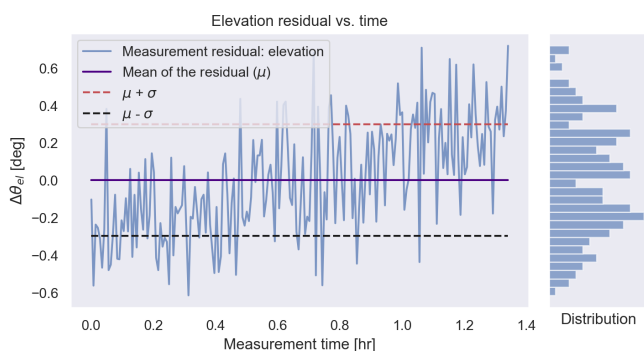


**Figure 6.39:** Residuals in elevation measurements for the change in inclination study case of a single satellite ( $\Delta h = 500$  km,  $\Delta i = 5^\circ$ , all measurements) for a case with both noise of standard deviation  $0.24^\circ$  and bias  $0.1^\circ$  of added to the true measurements.

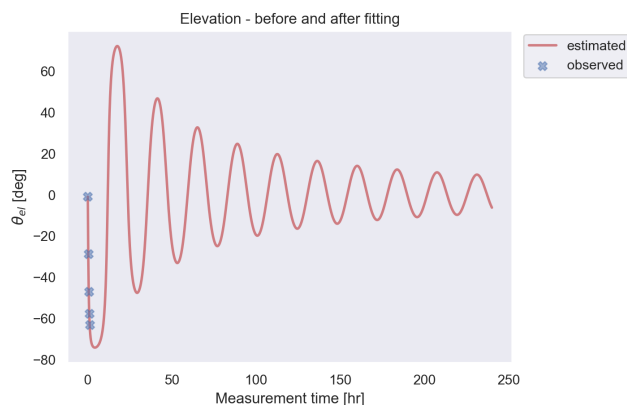


**Figure 6.40:** Comparison of observed and estimated elevation measurements for Residuals in elevation measurements for the change in inclination study case of a single satellite ( $\Delta h = 500$  km,  $\Delta i = 5^\circ$ , all measurements) for a case with both noise of standard deviation  $0.24^\circ$  and bias  $0.1^\circ$  of added to the true measurements.

It can be seen that increasing the satellite inclination gives the radar the liberty to scan in the z-plane, giving more elevation samples towards the end of the distribution. There is no distinct peak or mean visible for this configuration. The density of the distribution is also low compared to the previous inclination cases, which is seen by the fact that the satellite moves away from the debris faster therefore only collecting 194 measurements in 5 hours.

### 6.4.5. Overall inclination analysis

Compared to the altitude case study, the inclination case study shows that there were less measurements collected. This is because the satellite and the debris move apart due to the relative inclination change, contrary to a co-planar case, where the satellite simply follows the debris in a similar higher orbit, till it loses contact with it. Increasing the inclination gives directional information better than the nominal case but does not perform well in detection since it depends on the range solely (which increases). Therefore, a suitable inclination must be chosen such that it gives enough information on the elevation of the debris, and still collects ample measurements for accurately estimating the orbit and predicting its future trajectory.

The convergence behaviour of the different cases is seen in Figure 6.41. The blue line for  $0.1^\circ$  converges extremely steeply, which is expected to be the least accurate. The  $5^\circ$  case (red line) converges at a slightly higher value compared to the  $2.5^\circ$  case (green line), which was also expected from their residual distribution patterns. The orange line is the case for  $1^\circ$ , which shows the longest convergence duration in 30 iterations since it traverses through 825 measurements.

The behaviour of errors in the Cartesian coordinates in position and velocity are seen in Fig-

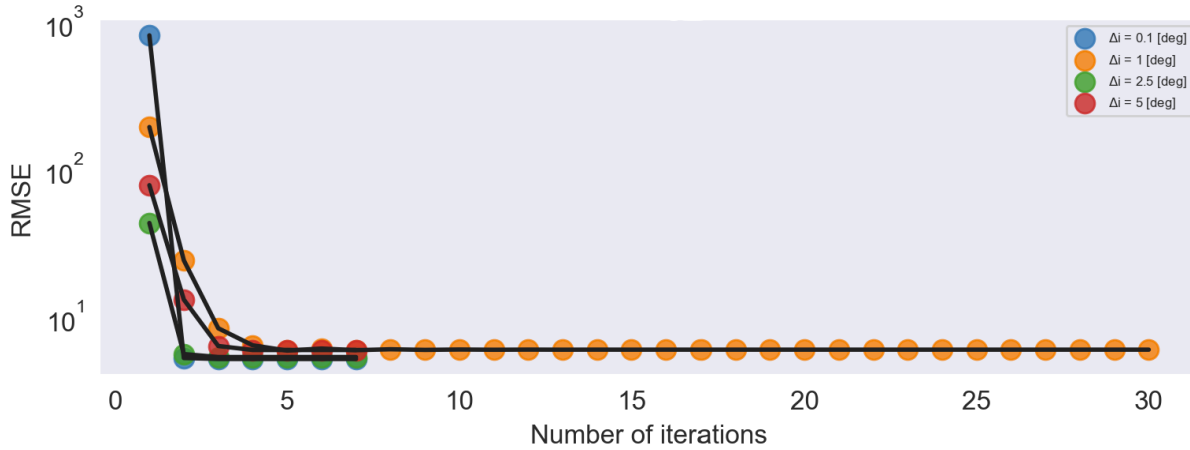


**Figure 6.41:** The RMSE convergence pattern for the four sub-cases of the inclination study case at an altitude difference of 500 km. The blue line represents the  $\Delta i = 0.1^\circ$  case, followed by the orange line representing  $\Delta i = 1^\circ$ . The green line considers the  $\Delta i = 2.5^\circ$ , and the red line considers the  $\Delta i = 5^\circ$ .

ure 6.42. The highest errors are seen for the  $5^\circ$  case, where the total position error grows to 400 km, and the total velocity error grows as large as 20 m/s in 10 days. Although it is difficult to describe the behaviour of the rest of the cases by this plot, it is seen that there is still not much information gathered for the z-coordinate position or velocity by the  $1^\circ$  case. The errors in the z-coordinate are minimum for  $\Delta i = 2.5^\circ$ , which makes it an interesting choice.

The covariance matrix for this configuration also yields the position and velocity accuracy as given by Table 6.4.

**Table 6.4:** Formal uncertainties in position and velocity for a case studying different inclinations of the satellite orbit.

$\Delta i [^\circ]$	Position accuracy [m]	Velocity accuracy [m/s]	RMSE	No. of obs.
0.1	3746.709	0.129	5.160	988
1	793.66	0.043	5.973	825
2.5	1104.73	0.218	5.319	391
5	1899.6	0.749	5.941	194

Although  $0.1^\circ$  has the highest number of measurements, leading to the lowest RMSE value, its formal errors are worse than those with higher inclination. The accuracy decreases to 793.66 m for the position with  $1^\circ$ , which again rises to 1104.73 m for  $2.5^\circ$ . Although the number of measurements for  $\Delta i = 5^\circ$  is less than that of  $\Delta i = 2.5^\circ$ , the order of magnitude of position and velocity accuracies is the same for both cases. This implies that an optimal solution for the relative inclination would be lying somewhere between  $1^\circ$  and  $5^\circ$ .

## 6.5. Case 4: Different measurement types

All the measurements do not perform equally in the OD process, which is why the Weighted Least Squares method is used to assign weights to the measurements. The more accurate measurement is given a higher weight for better state estimation. The performance of the previous cases depended largely on the number of measurements collected, assuming that they were all the same type. However, it is also important to study the effect of individual types of measurements, assuming the same number of measurement opportunities, to analyze the observation quality.

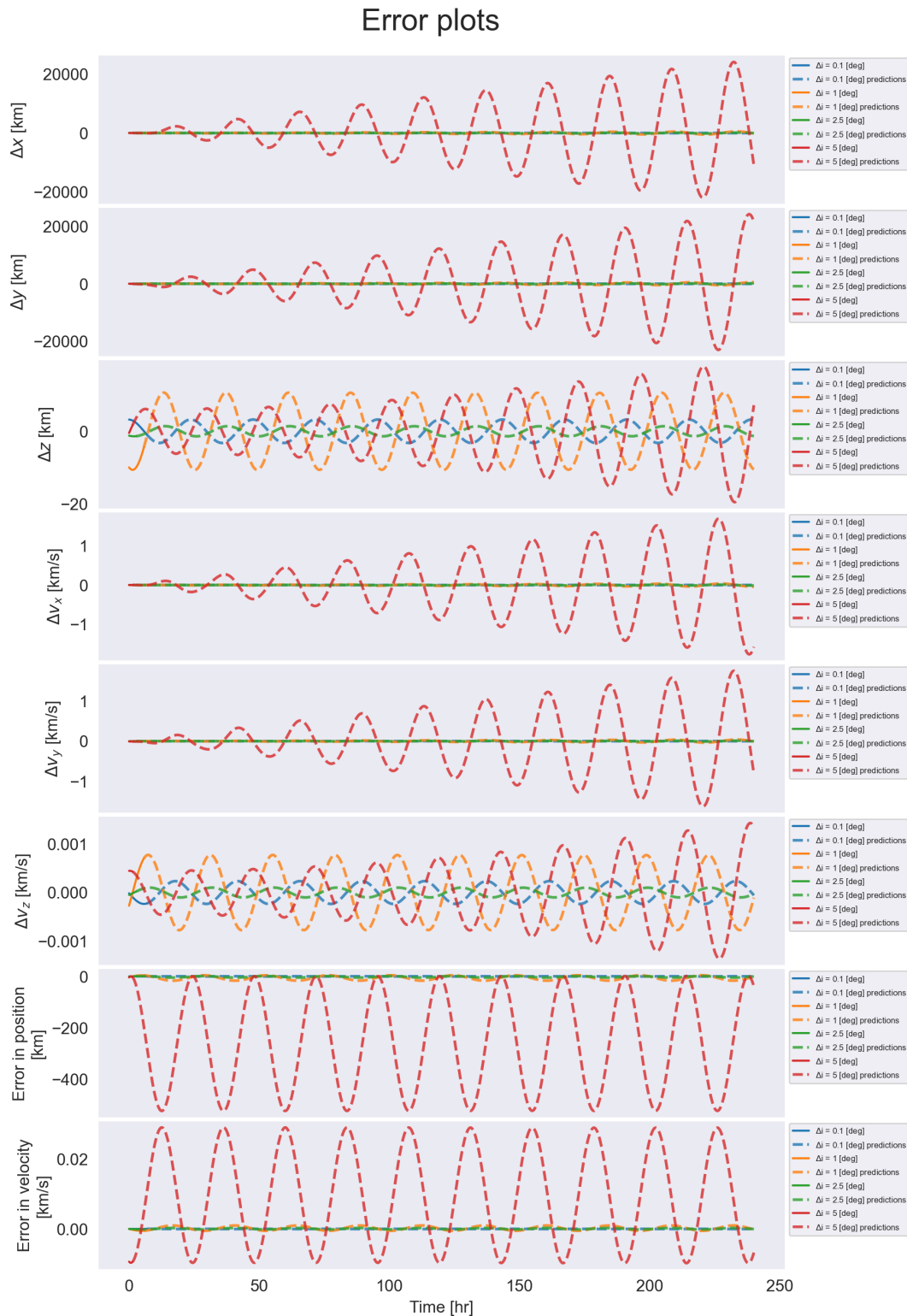


**Figure 6.42:** The error and prediction pattern for the three sub-cases of the inclination study case. The blue line represents the  $\Delta i = 0.1^\circ$  case, followed by the orange line representing  $\Delta i = 1^\circ$ . The green line considers the  $\Delta i = 2.5^\circ$ , and the red line considers the  $\Delta i = 5^\circ$ . The altitude difference at which the measurements have been collected is 500 km for this case.

In this case, first, an overall analysis of all measurement types is made in terms of convergence and formal uncertainty in position and velocity. This is done to eliminate the poor-performing combinations and reflect upon the better-performing cases to study the prediction error evolution over time.

### 6.5.1. Overall quality for all measurement types

First, the trends in RMSE of all the measurements used in this study is visualised to understand convergence behaviour. This is shown in Figure 6.43.

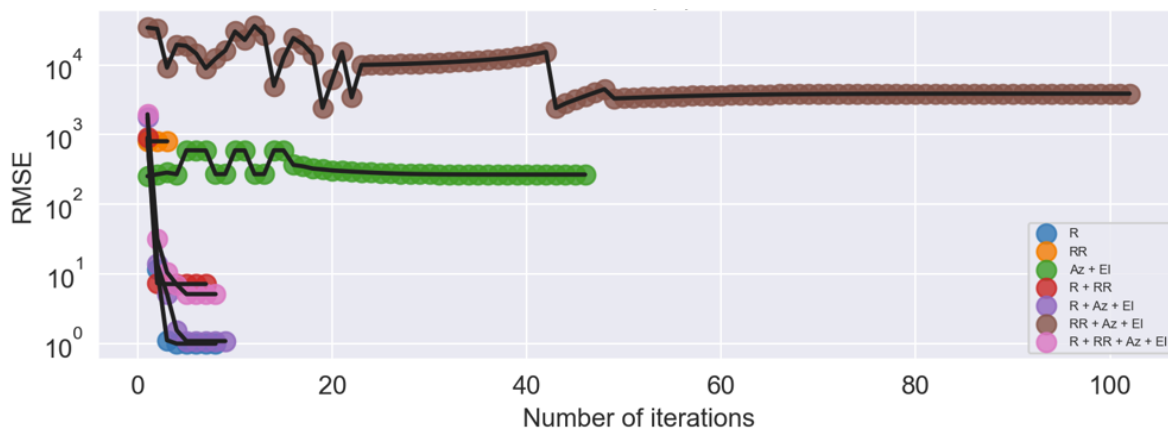


**Figure 6.43:** The RMSE convergence pattern for the seven combinations of measurement types, at an altitude difference of 1000 km and  $0^\circ$  inclination. The legend explains the measurement type, where, R represents the case with only range measurements, RR represents the case with only range-rate measurements, Az + El represents the case with only angular measurements, R + RR represents the case with both range and range-rate measurements, R + Az + El represents the case with range and angular measurements, RR + Az + El represents the case with range-rate and angular measurements, R + RR + Az + El represents the case with all types of measurements.

It can be seen that the case with range rate and angular measurements combined shows the worst convergence at a high value between  $10^3$  and  $10^4$ . The combination of angular measurements of azimuth and elevation exhibits the second-worst behaviour. This is expected since there were multiple instances in the previous case studies where the elevation was established as the poorly defined component. In the third position comes range rate only, which shows a very quick convergence even with strict convergence criteria. The range and range rate combined converge at more or less the same value of RMSE as the case with all measurement types. The best-performing measurement types in terms of RMSE are the range only (shown in blue) and the range combined with angular data (shown in purple).

To understand their behaviour better, the formal uncertainties are listed in Table 6.5, with the corresponding RMSE value at the end of convergence. They are arranged in their order of convergence, from best to worst.

It can be readily identified that the individual and combinations of range-rate and angular measurements perform the worst for the nominal case. The top-two candidates are the range alone and the range combined with angular measurements, which show comparable accuracies.

**Table 6.5:** Formal uncertainties in position and velocity for a case studying different measurement types and combinations used by the radar satellite in a nominal orbit.

Measurement type	Position accuracy [m]	Velocity accuracy [m/s]	RMSE
Range	50.08	0.0136	0.9947
Range + angular	53.33	0.0143	1.084
All	266.11	0.0667	5.123
Range + range-rate	380.19	0.0967	7.150
Range-rate	$12.32 \times 10^5$	61.524	807.622
Angular	$1.16 \times 10^{57}$	$2.15 \times 10^{52}$	266
Range-rate + angular	$62.87 \times 10^6$	$5.39 \times 10^6$	3874.49

### 6.5.2. Selective prediction performance for measurement types

It was seen in Table 6.5, that the top three measurement type performers were the range only, the range added with angular data and all measurement combinations. To introduce versatility in the type of measurements, the range-only measurement results are not shown for analysis here. The two interesting hybrid cases of combined range and angular data and the case with all measurements are shown in Figure 6.44, where the absolute errors in Cartesian position and velocity are shown. The convergence behaviour for the two selected measurement types is shown as well. This is done for the nominal case but with higher inclination ( $\Delta h = 1000$  km and  $\Delta i = 2.5^\circ$ ) to get better information in the z-plane.

It can be seen that the RMSE value when using all measurement types is the lowest. Moreover, the blue curve shows slightly more errors in all the coordinates. Although range measurement alone has exceptional accuracy, the effect of the combination of measurements is the advantage of space-based radar. This property will be further used to reduce prediction errors.

It must be noted that the radar will collect all types of measurements to evaluate its feasibility. This means that the performance in prediction errors or convergence can be better than what will be obtained with all measurements. However, the choice of measurements included for WLS is an act of post-processing and does not influence the radar parameters anymore. For the rest of the analysis, all the measurements will be considered, whose performance will be studied.

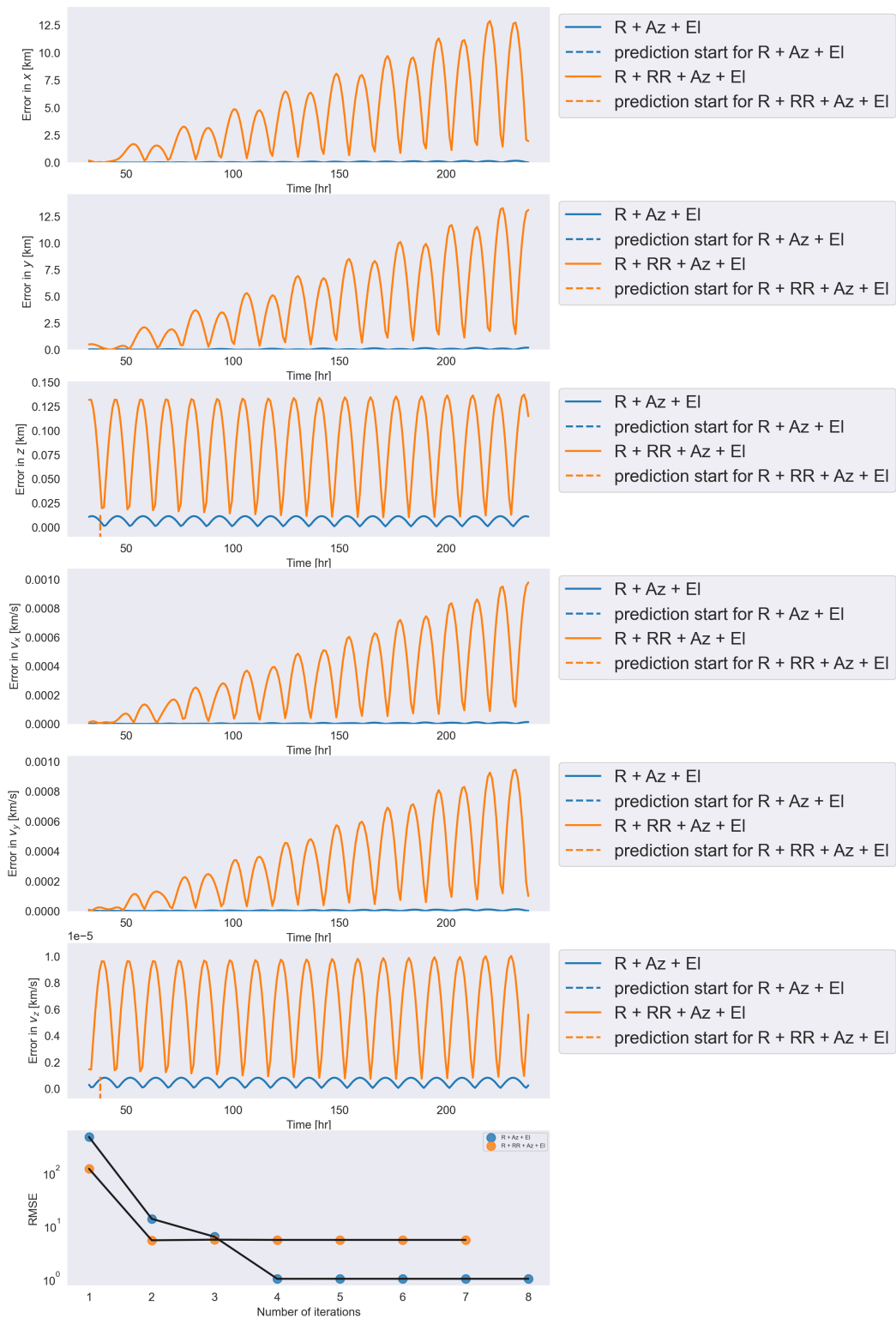


**Figure 6.44:** The absolute errors in Cartesian position and velocity components over time. The blue curve represents the range and angular measurements combined, while the orange curve also includes the range-rate measurements. The dotted line denotes the start of prediction, where the errors grow linearly with time for the x- and y-components and stay constant for the z-component.

## 6.6. Case 5: Different satellites and configurations

As seen earlier, measurements at 1000 km of relative altitude only allow 5 hours of continuous surveillance. However, for long-term feasibility, the entire debris orbit must be covered for obtaining measurements for any arc of the orbit. This is possible when multiple observation platforms are employed in orbit to survey an object. This is expected to improve the accuracy and reduce errors since combined measurements will be used to estimate the state.

In this study, a maximum of three satellites has been considered in the constellation for simplicity and cost constraints. The relative phasing of the satellite plays an important role in the measurement acquisition: where they could be in series one after the other or far apart on opposite sides of the orbit. Section 6.6.1 will describe the two-satellite framework results, while the Section 6.6.2 will describe the three-satellite configuration.

### 6.6.1. Two-satellite framework

Two configurations were studied for a twin-satellite framework.

- **Twin-Series configuration:**

Here the satellites are assumed to be in a nominal orbit with  $\Delta h = 1000$  km and  $\Delta i = 2.5^\circ$ . They are at a true anomaly of  $0^\circ$  and  $5^\circ$ , respectively. This is a case where Satellite 2 immediately follows behind Satellite 1, taking re-observations of the debris for a longer arc.

- **Twin-Apart configuration:**

Here the satellites are assumed to be in a nominal orbit with  $\Delta h = 1000$  km and relative inclination with the debris orbit of  $\Delta i = 2.5^\circ$  and  $\Delta i = 177.5^\circ$ . They are at a true anomaly of  $0^\circ$  and  $180^\circ$ , respectively. In this case, Satellite 1 covers one section of the orbit, while Satellite 2 sweeps through the other half.

Visualization of the orbits of the satellites can be seen in Figure 6.45.

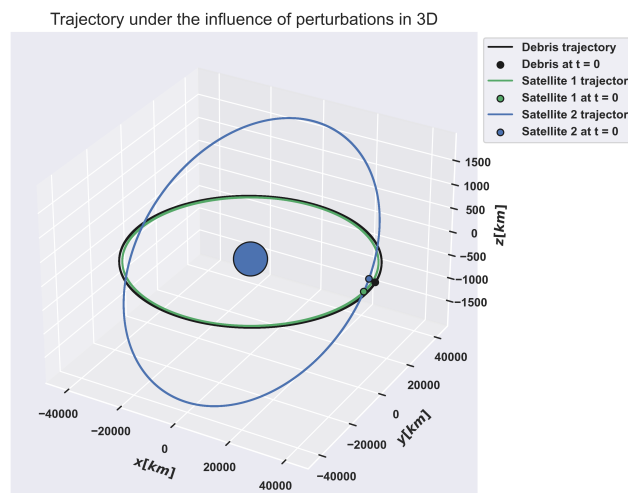


**Figure 6.45:** For visualisation purposes, the second satellite's inclination has been equal to  $5^\circ$ , while the first stays at  $0^\circ$  inclination. The satellites are at an altitude difference of  $\Delta h = 1000$  km.

The behaviour of the individual SNR from each of the satellites can be visualised in Figure 6.46 for the twin-series configuration and in Figure 6.47 for the twin-apart configuration. In a similar

fashion, the range measurements collected by the two satellites are shown by the orange and blue lines in Figure 6.48 for twin-apart and Figure 6.49 for the twin-apart configuration.

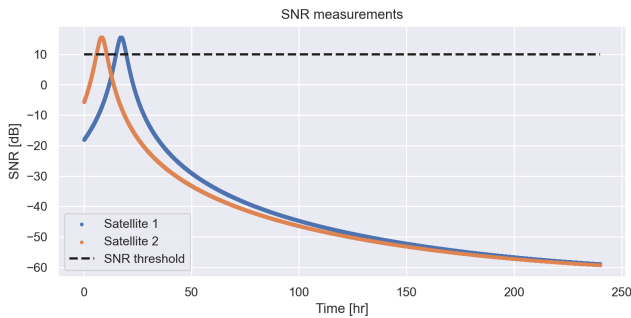


Figure 6.46: SNR collected by two satellites in the Twin-Series configuration for 10 days.

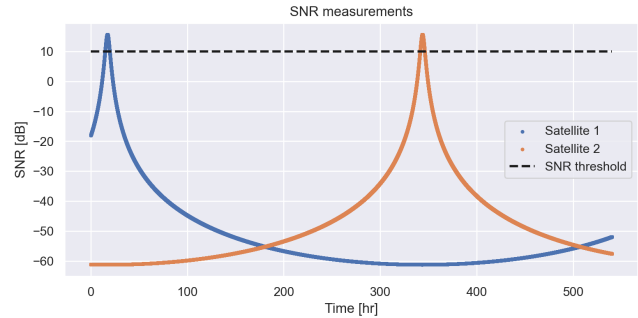


Figure 6.47: SNR collected by two satellites in the Twin-Apart configuration for 10 days.

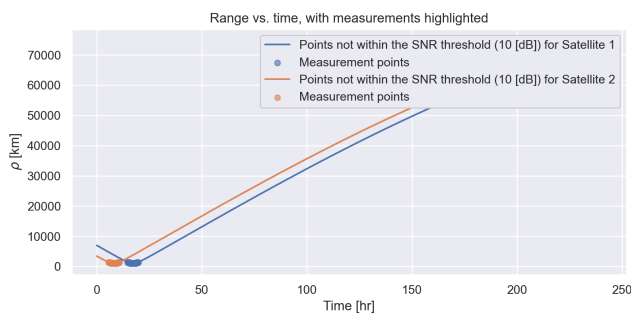


Figure 6.48: Range measurements collected by two satellites in the Twin-Series configuration for 10 days.

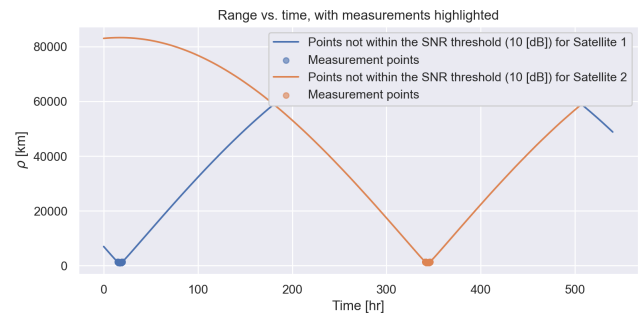


Figure 6.49: Range measurements collected by two satellites in the Twin-Apart configuration for 10 days.

The position and velocity accuracy along with the RMSE for both these configurations is studied in Table 6.6. The number of measurements collected by each of the satellites in both the configurations is seen in Table 6.7.

Table 6.6: Formal uncertainties in position, velocity and RMSE for a case studying a twin-observation system.

Two-satellite configuration	Position accuracy [m]	Velocity accuracy [m/s]	RMSE
Twin-series	127.96	0.006595	13.30
Twin-apart	18.71	0.03575	5.28

Table 6.7: Number of measurements collected by satellites in the twin-satellite observation system.

Two-satellite configuration	Satelite No.	No. of measurements
Twin-series	1	689
	2	687
Twin-apart	1	689
	2	689

It is also seen that the overall accuracy of two satellites in a twin-series configuration is worse than for a twin-apart configuration. The number of measurements seems almost comparable for both cases, but it must be noted that for the twin series configuration, the satellites collect measurements that overlap with each other in a short period of time. Hence, the RMSE is higher for the series configuration (which has to process more data together), while it is lower for the twin-apart configuration due to measurements being collected in a different location in the orbit.

When orbit determination is carried out using two satellites, the behavior of the Cartesian component errors can be visualised as seen in Figure 6.50. The maximum error magnitude is about 10 km in position and 75 cm/s in velocity for the configuration in series. For the triangulated configuration, it is even less. This is because of more orbit coverage, which takes measurements at different points in the orbit, than repeating the same arc.

Since the analysis can be extended to a maximum of three satellites, it is interesting to see the effect of one more satellite in the system on the initial position, velocity accuracy, and prediction errors. Moreover, it is expected that more measurements will be collected with one more satellite. This is explored in the next section.

### 6.6.2. Three-satellite framework

Similarly, the twin-satellite configuration has two configurations for three satellites. They are as follows :

- **Tri-Series configuration:**

Here the satellites are assumed to be in a nominal orbit with  $\Delta h = 1000$  km and  $\Delta i = 2.5^\circ$ . They are at a true anomaly of  $0^\circ$ ,  $5^\circ$  and  $355^\circ$ , respectively. This is a case where Satellite 2 immediately follows behind Satellite 1, taking re-observations of the debris for a longer arc.

- **Triangulated configuration:**

Here the satellites are assumed to be in orbits with common  $\Delta h = 1000$  km and  $\Delta i = 2.5^\circ$ . They are at a true anomaly of  $0^\circ$ ,  $120^\circ$  and  $240^\circ$ , respectively. In this case, Satellite 1 covers one section of the orbit while Satellite 2 sweeps through the other half.

The trajectory in general can be visualized by Figure 6.51. The SNR plots for the two configurations for three satellites can be seen in Figure 6.52 for the series configuration and Figure 6.53 for the triangulated configuration. Similarly, for the range using three satellites, the series range can be seen in Figure 6.54, while the triangulated range can be seen in Figure 6.55.

The position and velocity accuracy along with the RMSE for both these configurations is studied in Table 6.8. The number of measurements collected by each satellite in both configurations is seen in Table 6.9.

**Table 6.8:** Formal uncertainties in position, velocity and RMSE for a case studying a three satellite observation system.

Three satellite configuration	Position accuracy [m]	Velocity accuracy [m/s]	RMSE
Tri-series	296.061	0.010	37.393
Triangulated	266.116	0.097	5.123

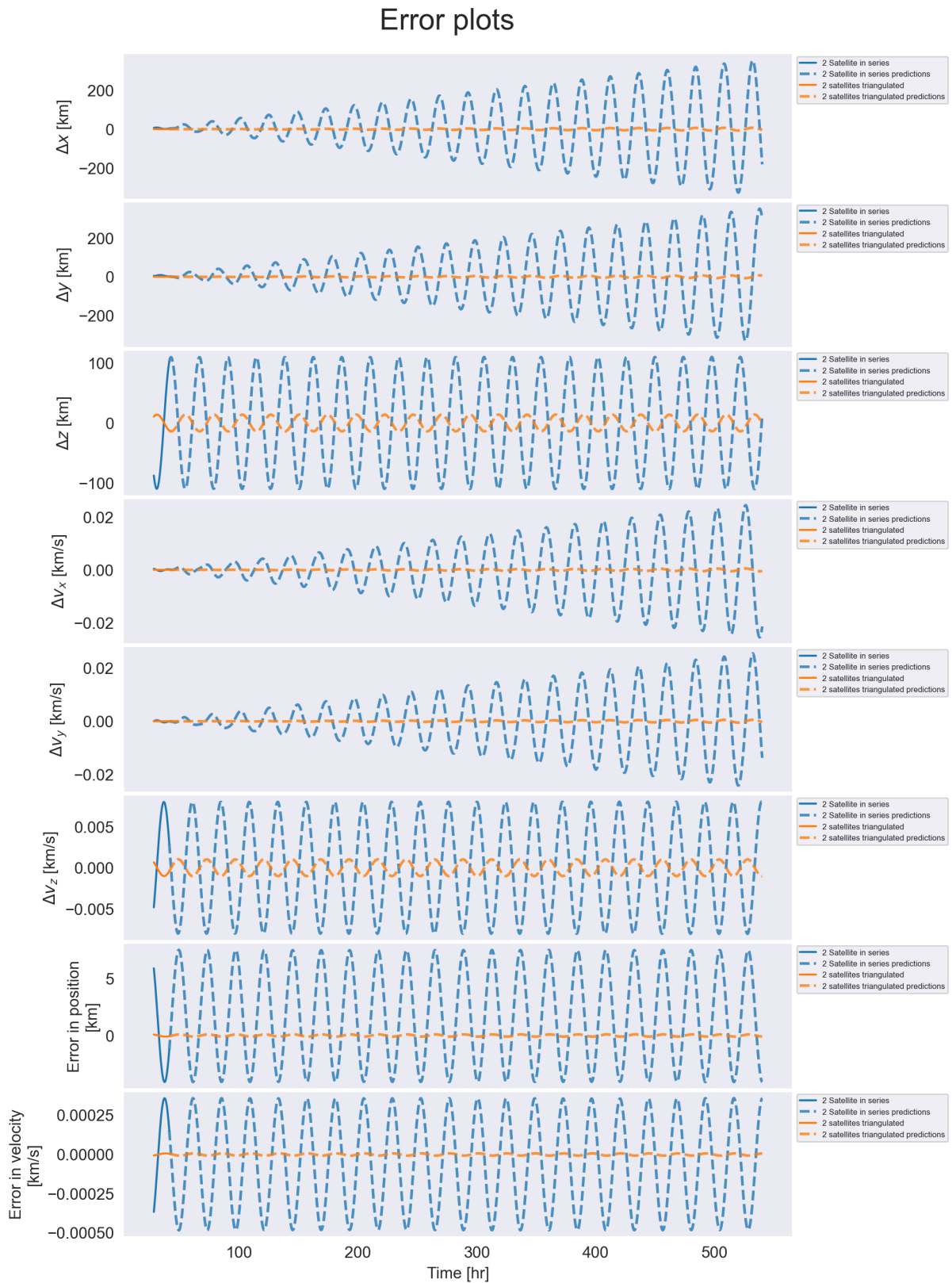


**Figure 6.50:** The errors in Cartesian coordinates are presented in blue curves for two satellites in series, while the orange curve examines the two satellites at opposite poles of the orbit ( $\theta_1 = 0^\circ$  and  $\theta_2 = 180^\circ$ )

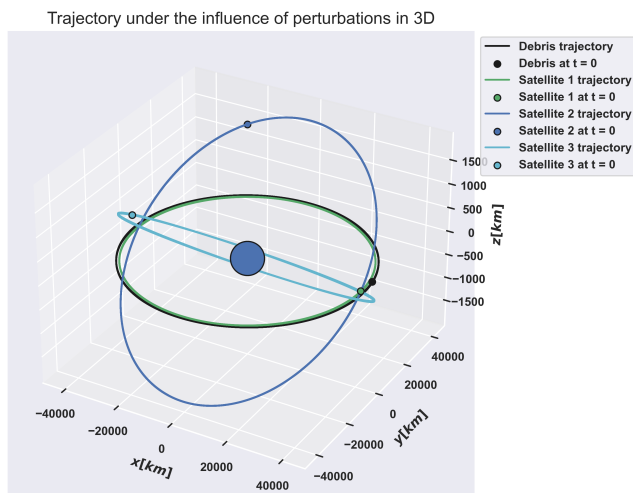


**Figure 6.51:** For visualisation purposes, the second satellite's inclination has been equal to 5°, while the first stays at 0° inclination. The third satellite is at 175° inclination

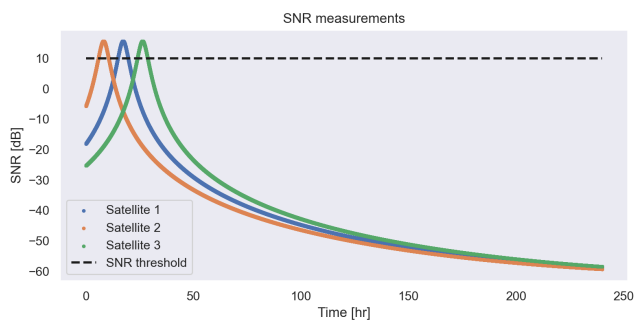


**Figure 6.52:** SNR collected by three satellites in the Tri-series configuration for 10 days.

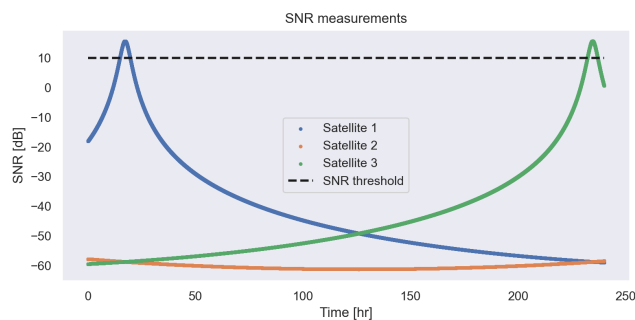


**Figure 6.53:** SNR collected by three satellites in the Triangulated configuration for 10 days.

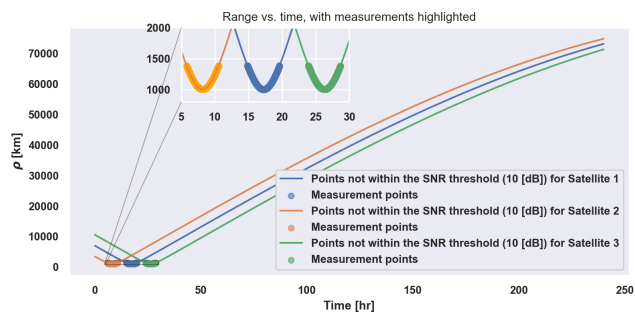


**Figure 6.54:** Range measurements collected by three satellites in the Tri-series configuration for 10 days.

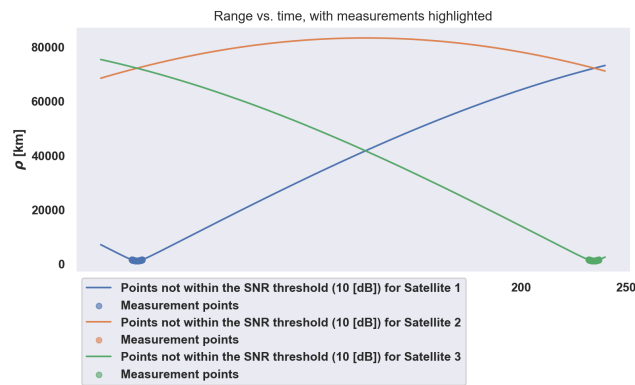


**Figure 6.55:** Range measurements collected by three satellites in the Triangulated configuration for 10 days.

Similar to what was seen in the 2-satellite case, the accuracy with 3 satellites can be studied for different configurations from the above tables. The tri-series and triangulated show comparable position accuracies, with an RMSE of almost 7.3 times larger for the series configuration. This arises similarly because many measurements are processed simultaneously for a series, in comparison to the triangulated configuration, where measurements from different locations in the orbit are collected.

**Table 6.9:** Number of measurements collected by satellites in three satellite observation system.

Three satellite configuration	Satellite No.	No. of measurements
Tri-series	1	689
	2	687
	3	687
Triangulated	1	689
	2	688
	3	688

The results of errors in the Cartesian coordinates of the three-satellite configuration are provided in Figure 6.56. The series configuration reaches a maximum position error of 6 km. and a maximum velocity error of 20 cm/s. This is much lower than what was obtained from a single satellite or two satellites.

It can be seen that the triangulated 3-satellite configuration performs very well in terms of lower prediction errors. A long-term feasibility outcome will be discussed in Chapter 7, where the prediction performance will be analysed for a longer simulation time with multiple measurement occurrences.

After going through the different parametric study cases, a sensitivity analysis for model parameters can be performed.

## 6.7. Sensitivity Analysis

A sensitivity analysis has been carried out to check the robustness of the solution to uncertainties in modeling. Of the different model parameters, some of the most sensitive ones are discussed, which are expected to have the greatest influence on the results. As discussed earlier, the nominal solution is generated using the high-fidelity model presented in Section 4.2, which will be tested for different model parameters to see its sensitivity to changes in those parameters.

In this section, the uncertainty in the initial guess of the debris state is shortly discussed in Section 6.7.1. Then, the effect of changing the standard deviation of Gaussian noise and bias in the range measurements is briefly discussed in Section 6.7.2. The properties of the debris are studied next. The effect of changing the debris mass, size and SRP coefficient are concisely analysed in Sections 6.7.3, 6.7.4 and 6.7.5 respectively.

### 6.7.1. Uncertainty in initial guess of debris state for WLS

The initial state of the debris is chosen and used for computing the measurements with that guess, which is the starter to minimize the residuals. The better the guess, the faster the convergence is expected. The software selects the initial state within a defining range of values within which the software assumes a certain value and begins the OD process. To assess the change in performance of the solution depending on the initial state, 20 random Monte Carlo samples are extracted within the same range. The confidence ellipse around the initial state is presented in Figure 6.57. This gives a measure of uncertainty in the model due to the initial state guess.

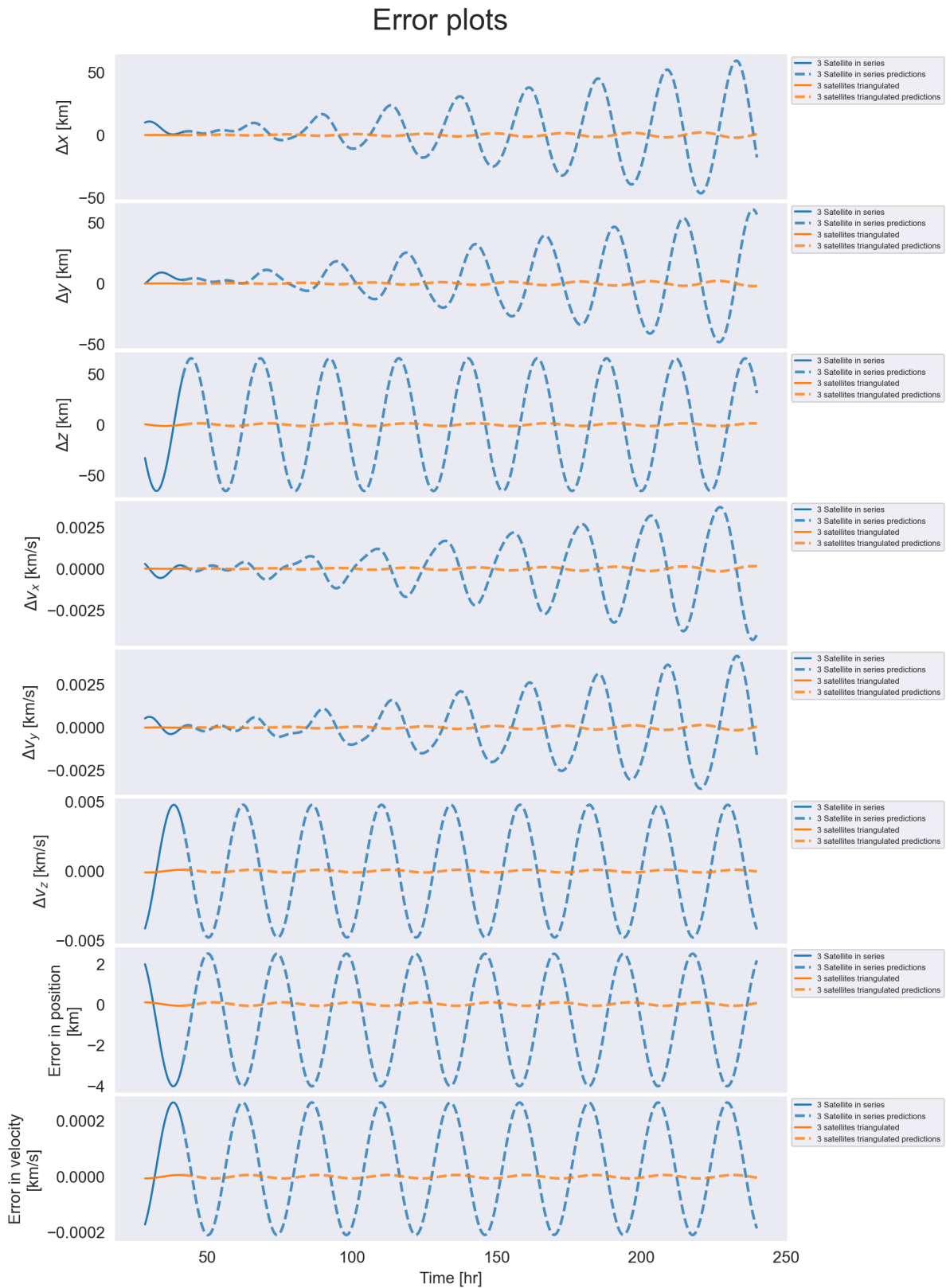


**Figure 6.56:** The errors in Cartesian coordinates are presented in blue curves for three satellites in series, while the orange curve examines the three satellites are equally distributed along the orbit ( $\theta_1 = 0^\circ$  and  $\theta_2 = 120^\circ$  and  $\theta_3 = 240^\circ$ )

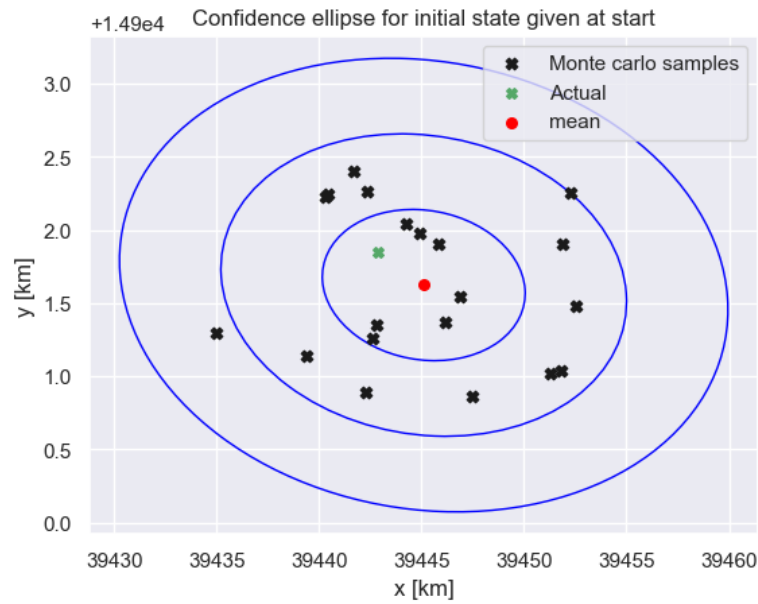


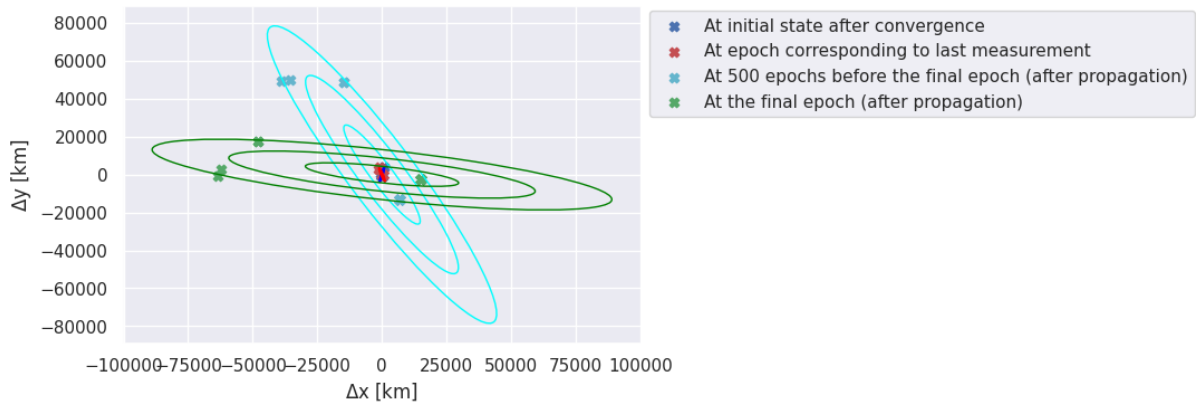
Figure 6.57: Confidence ellipse shown for estimating initial state in X and Y for 20 random Monte Carlo samples drawn.

Table 6.10: Monte Carlo initial state samples and RMSE corresponding to the samples.

Sample No.	x [km]	y [km]	z [km]	vx [km/s]	vy [km/s]	vz [km/s]	RMSE
1	-25481.001	-33593.530	0.307	2.450	-1.859	2.60E-05	5.723
2	-25478.779	-33593.503	0.012	2.450	-1.858	8.47E-05	5.723
3	-25485.694	-33593.237	0.468	2.449	-1.859	9.61E-05	5.723
4	-25485.529	-33593.049	-0.417	2.450	-1.857	2.96E-05	4.24E+11
5	-25482.204	-33593.917	-0.334	2.450	-1.858	5.07E-06	2.74E+12
6	-25480.387	-33593.662	0.043	2.450	-1.857	-6.99E-05	5.723
7	-25480.756	-33593.460	0.345	2.450	-1.859	1.17E-05	5.723
8	-25484.763	-33593.057	0.085	2.449	-1.858	2.19E-05	6.927
9	-25479.166	-33593.570	0.145	2.450	-1.858	-7.35E-05	6.927
10	-25478.120	-33593.900	-0.253	2.450	-1.859	-1.36E-06	5.723
11	-25485.119	-33593.584	-0.219	2.449	-1.858	-4.98E-05	1.47E+11
12	-25484.548	-33593.293	0.354	2.449	-1.859	-1.33E-05	5.723
13	-25480.461	-33593.724	-0.096	2.449	-1.858	2.43E-06	2.32E+11
14	-25477.409	-33593.668	-0.112	2.450	-1.858	3.76E-05	5.723
15	-25477.744	-33593.518	-0.423	2.450	-1.859	1.26E-05	6.927
16	-25476.614	-33593.274	-0.139	2.449	-1.859	2.09E-05	5.723
17	-25480.574	-33593.475	-0.093	2.451	-1.858	-8.46E-05	5.723
18	-25477.994	-33593.162	-0.360	2.449	-1.859	-9.23E-05	3.38E+14
19	-25476.531	-33593.913	-0.236	2.449	-1.857	7.27E-05	5.723
20	-25482.790	-33593.914	0.234	2.449	-1.858	8.62E-05	5.723

As seen in Figure 6.57, the center is marked by a red dot, which corresponds to the mean of the X and Y values. The green point refers to the point where the first measurement is collected. The black dots refer to the Monte Carlo samples, which are seen to lie within the  $2\sigma$  contour of the ellipse.

When plotted for different points in the orbit, the ellipse's size and orientation change from what was shown before. In Figure 6.58, the red dot in the center corresponds to the epoch at the last measurement. The small blue ellipse with 20 such blue dots refers to the point in orbit right after the convergence. The green ellipse corresponds to the point of 500 epochs before the start of the last measurement. Finally, the cyan ellipse reflects the ending epoch ellipse. It can be seen that the size of the ellipse increases from the orbit determination phase to the orbit prediction phase, therefore portraying the increase in uncertainty.



**Figure 6.58:** Confidence ellipse shown for estimating initial state in X and Y for 20 random Monte Carlo samples drawn at four points in the orbit.

The uncertainty can be visualised by analysing the growth of the confidence interval for the entire orbit simulation. The behaviour in x-coordinate can be visualised by Figures 6.59 and 6.60 for position and velocity. The same is visualised by Figures 6.61 and 6.62 for the position and velocity in the y-coordinate. Similarly, the position and velocity behavior in the z-coordinate can be represented by Figures 6.63 and 6.64. In each, the  $1\sigma$  region is shaded as red, followed by the  $2\sigma$  and  $3\sigma$  regions shaded as blue and green respectively.

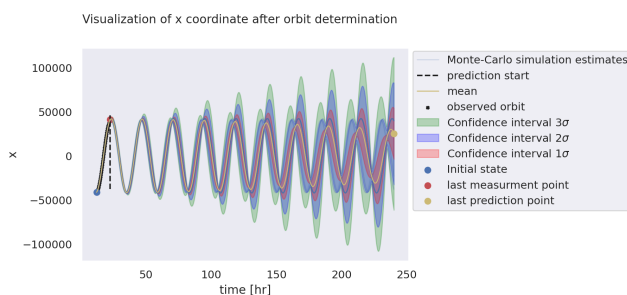


**Figure 6.59:** Behaviour of the position in x-coordinate over time, during orbit determination and prediction over 10 days, using 20 Monte Carlo samples.

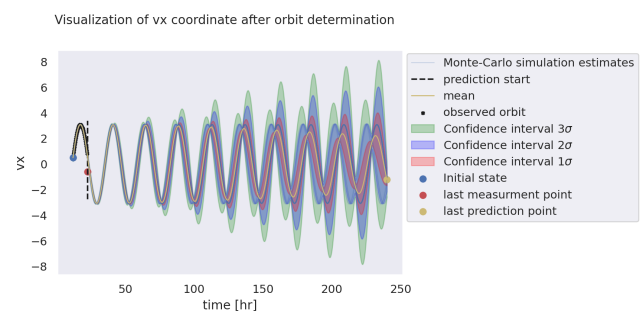


**Figure 6.60:** Behaviour of the velocity in x-coordinate over time, during orbit determination and prediction over 10 days, using 20 Monte Carlo samples.

The general trend is that as time of propagation increases, the uncertainty keeps increasing for the x and y Cartesian states, while it largely remains constant for z (which is ill-defined anyways).

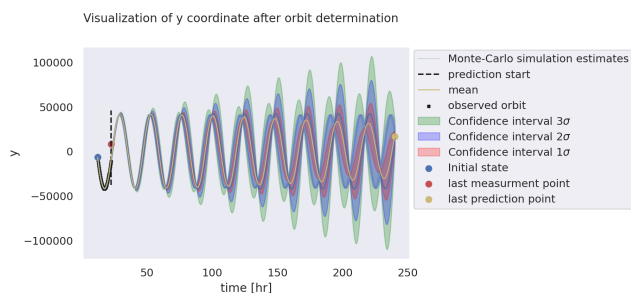


**Figure 6.61:** Behaviour of the position in y-coordinate over time, during orbit determination and prediction over 10 days, using 20 Monte Carlo samples.

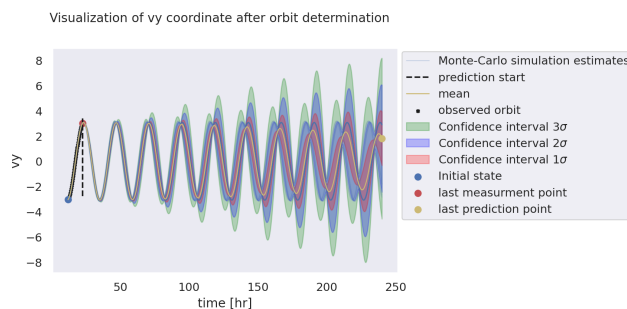


**Figure 6.62:** Behaviour of the velocity in y-coordinate over time, during orbit determination and prediction over 10 days, using 20 Monte Carlo samples.

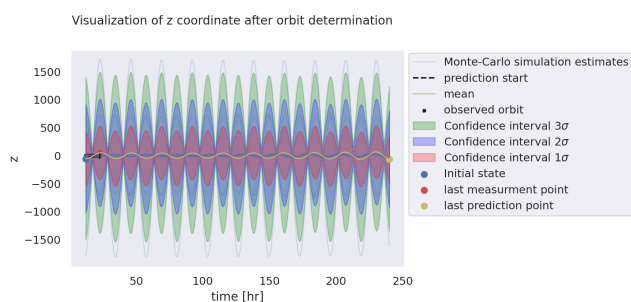


**Figure 6.63:** Behaviour of the position in z-coordinate over time, during orbit determination and prediction over 10 days, using 20 Monte Carlo samples.

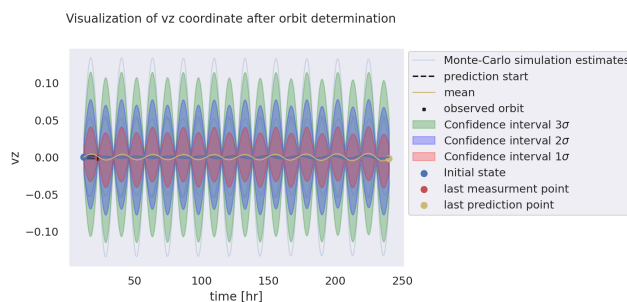


**Figure 6.64:** Behaviour of the velocity in z-coordinate over time, during orbit determination and prediction over 10 days, using 20 Monte Carlo samples.

### 6.7.2. Different noise and bias

The magnitude of the Gaussian noise was determined by the Cramer-Rao Lower bound rule while defining the radar parameters, and the bias was assumed to be of the same order of magnitude as that of the noise. In this subsection, the effect of changing the noise in radar measurements is studied.

First, the bias values are changed. The amount of bias that is added to each of the individual measurement types along with their RMSE and formal uncertainties is given in Table 6.11. The accuracies seem to get worse with higher bias and so does the RMSE. The errors in Cartesian coordinates due to changing bias is visualised in Figure 6.65 only for the range measurements. Here as well, it concurs with the behaviour in accuracy, where an increase in the magnitude of bias increases the errors over time.

Thereafter, keeping the biases constant, the values of standard deviation for Gaussian noise in all measurement types are presented in Table 6.12.

Table 6.11: Effect of variation of bias in measurements on orbit determination results.

Measurement type	Bias added	Position accuracy [m]	Velocity Accuracy [m/s]	RMSE
R	0.1 m	25.343	0.009	5.354
	1 m	25.449	0.008	5.485
	10 m	52.225	0.012	11.843
	100 m	10586.071	0.327	77.784
RR	0.0001 m/s	10.353	0.033	2.527
	0.001 m/s	44.986	0.205	10.192
	0.01 m/s	552.446	0.228	100.586
Az + El	0.0001 rad	22.511	0.082	5.424
	0.001 rad	22.479	0.082	5.418
	0.01 rad	24.032	0.087	5.793
	0.1 rad	74.761	0.272	18.071

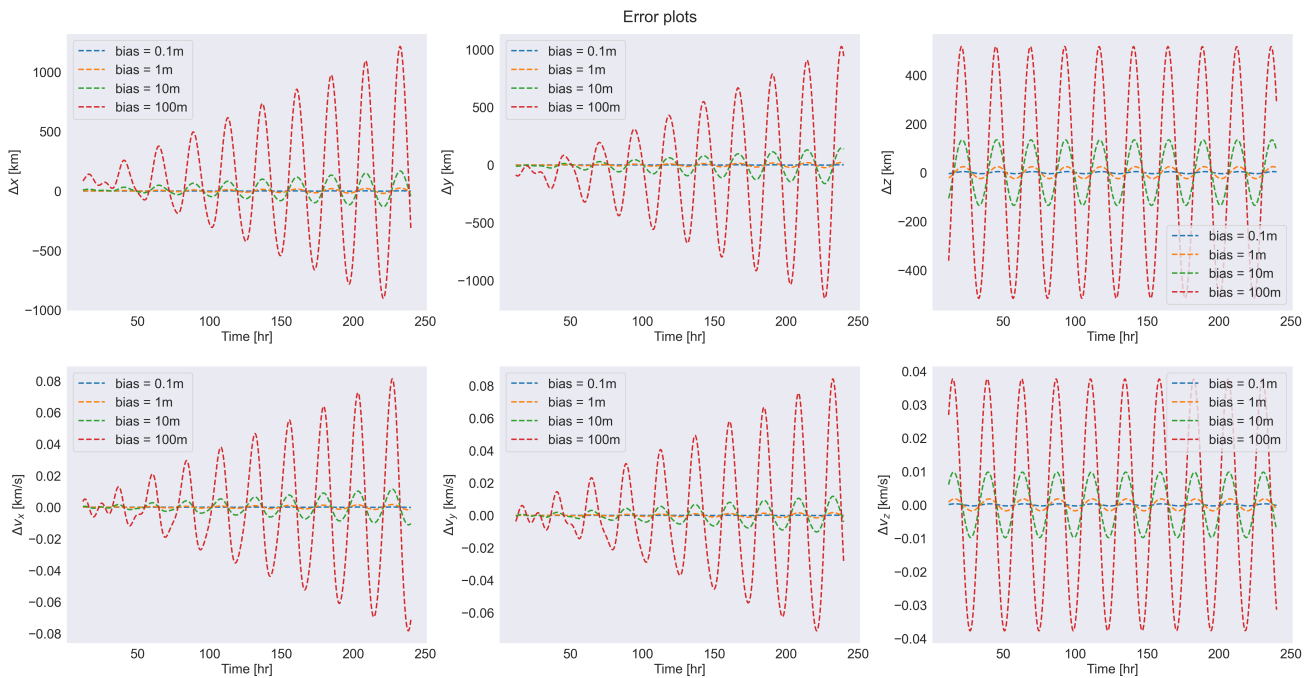
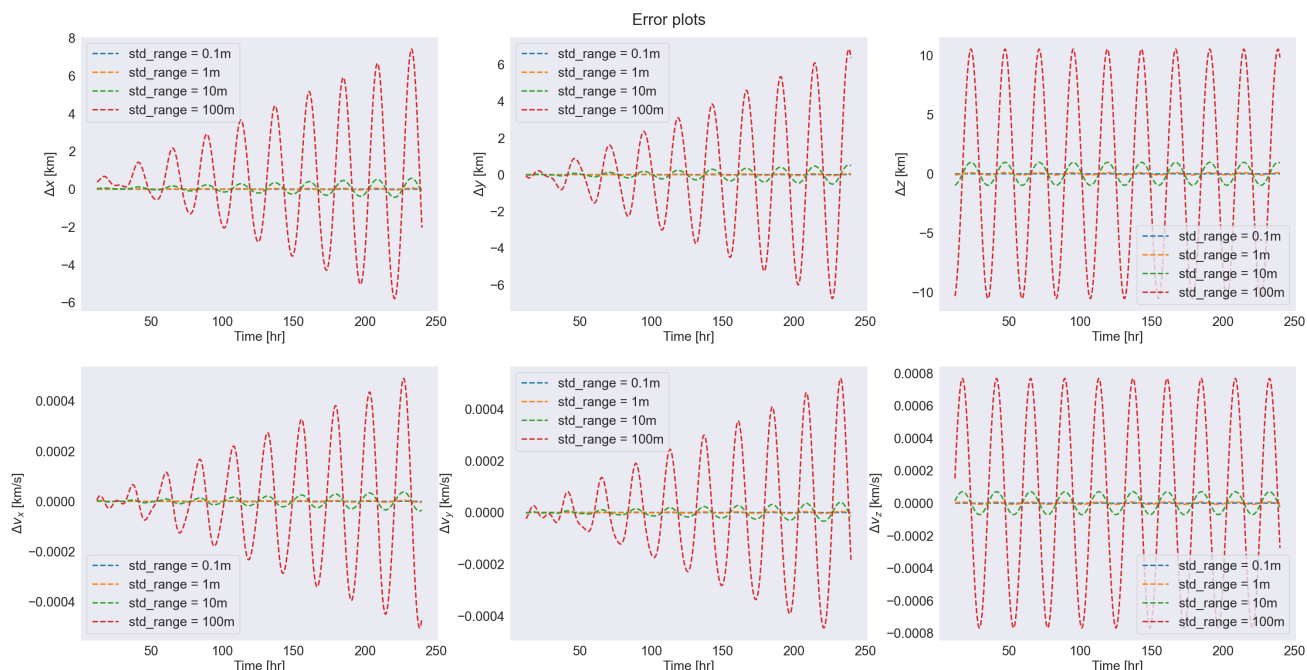


Figure 6.65: Behaviour of error vs. epochs when bias added to the range measurements is varied.

Table 6.12: Effect of variation of standard deviation in measurements on orbit determination results.

Measurement type	STDDEV added	Position accuracy [m]	Velocity Accuracy [m/s]	RMSE
R	0.1 m	0.025	9.00E-06	0.986
	1 m	0.256	9.00E-05	0.986
	10 m	2.556	9.00E-04	0.987
	100 m	22.473	0.009	1.104
RR	0.0001 m/s	0.395	0.083	0.985
	0.001 m/s	1.221	0.061	0.991
	0.01 m/s	6.18E+10	4.15E+06	1.38E+08
Az + El	0.0001 rad	73.383	0.485	19.819
	0.001 rad	13.643	0.069	3.385
	0.01 rad	4.171	0.021	1.033
	0.1 rad	5.38E+07	3.42E+05	5.48E+07

Here, the same behaviour as bias can be noticed. The position and velocity accuracies worsen with the addition of more noise than what the radar can handle. Also, the RMSE values increase with increasing amount of bias for all the measurements. The behaviour in prediction errors can be visualised in Figure 6.66.



**Figure 6.66:** Behaviour of error vs. epochs when standard deviation added to the range measurements is varied.

The errors grow linearly over time for increasing values of noise standard deviation. This concurs with our expectations.

### 6.7.3. Different debris masses

The mass of the debris was earlier assumed to be 1.413 kg assuming it to be an aluminium sphere with a 10 cm diameter. However, this is an uncertainty that we deal with in the model, since the mass is not entirely known. The effect of changes in debris mass is studied by keeping the diameter constant at 10 cm and varying the mass of the debris object for four values given in Table 6.13.

**Table 6.13:** Effect of variation of debris masses on orbit determination results. The diameter has been assumed to be constant at 10 cm, meaning that the material can be different.

Debris mass [kg]	Position accuracy [m]	Velocity Accuracy [m/s]	RMSE
0.1	4.934	0.016	1.352
1	5.117	0.015	1.408
3	4.987	0.015	1.374
10	5.112	0.015	1.406

The changes in position and velocity accuracy do not change much with changing masses. The same behaviour is seen for the RMSE, which oscillates around an average value of 1.4. So far not a lot has been inferred on the effect of varying debris mass, for which the prediction errors are also analysed in Figure 6.67.

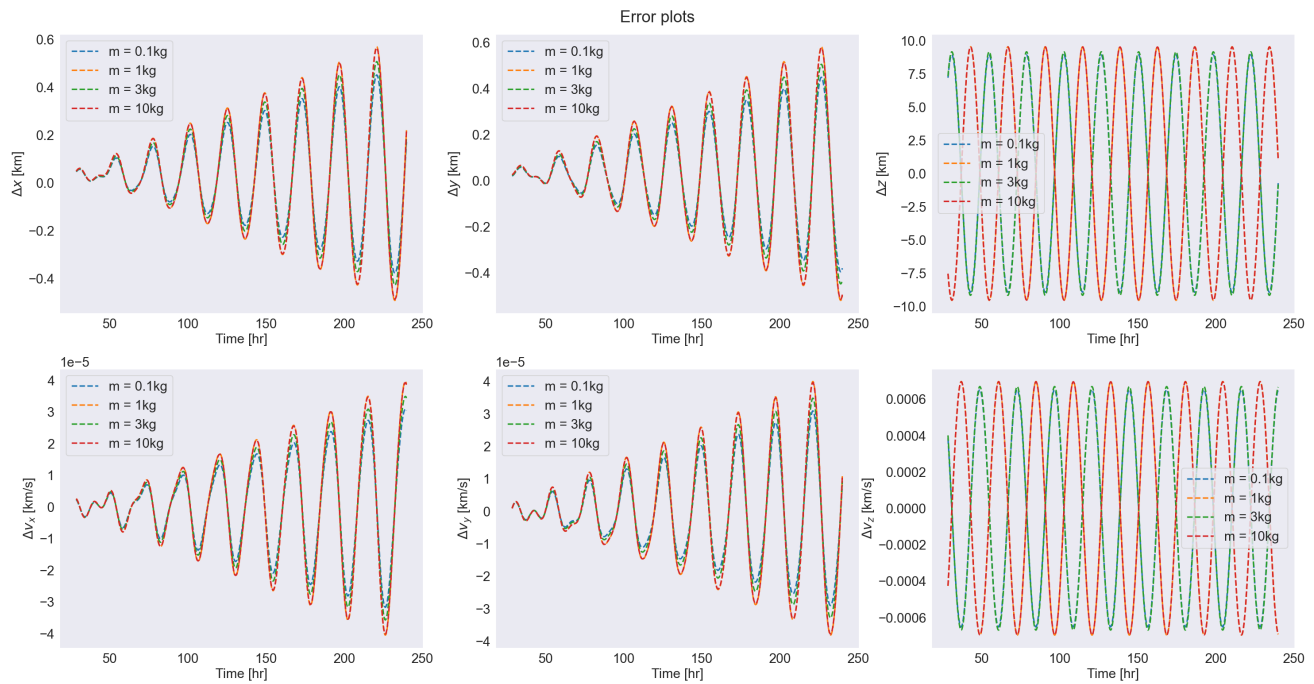


Figure 6.67: Behaviour of error vs. epochs when debris mass is varied for a 10 cm object.

It is hence seen that the errors are very close to each other for the four cases of varying masses with constant RCS. It is hence concluded that the position and velocity errors and accuracies do not significantly vary with the mass.

#### 6.7.4. Different debris sizes

Similar to the debris mass, the size of the debris was assumed to be 10 cm for the simulation. In reality, a wide range of small-sized debris in a debris cloud could be the target for INDIGO. Hence, it is important to study the effect of changing debris diameter (still assuming it to be circular in shape).

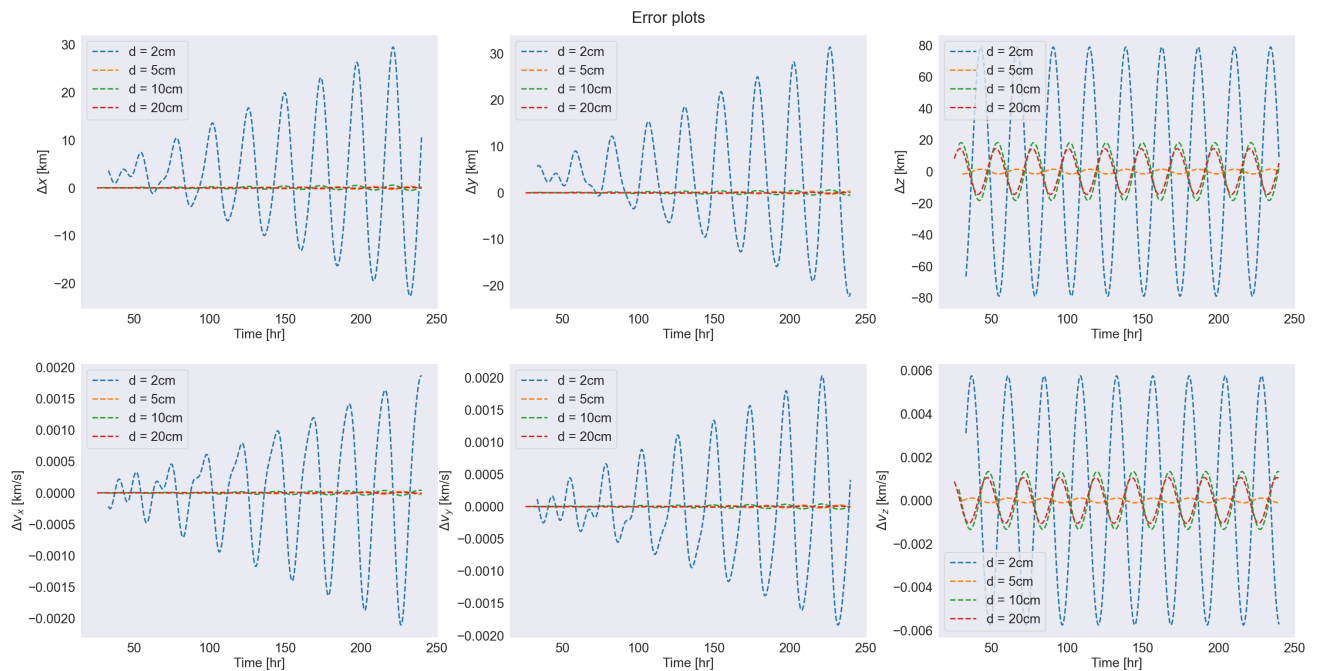
Four debris diameter sizes of 2 cm, 5 cm, 10 cm, and 20 cm have been studied. The values of position and velocity accuracies and the RMSE have been provided in Table 6.14.

Table 6.14: Effect of variation of debris sizes on orbit determination results. The mass of the debris has been considered to be 1.413 kg, similar to the original simulation conditions.

Debris diameter [cm]	Position accuracy [m]	Velocity Accuracy [m/s]	RMSE	No. of obs.
2	5747.452	0.361	9.382	531
5	10.365	0.031	0.995	1222
10	7.875	0.025	2.009	1873
20	3.148	0.043	1.589	2746

It is seen that for the debris of size 2 cm, the accuracy is the worst. However, this is mainly attributed to the lack of measurements for smaller sizes since the radar is sensitive to the SNR which depends directly on the target RCS. A smaller object reduces higher power for detection, which is not sufficient with the assumed power of 1 kW.

The evolution of errors over time is also analogously studied for the case with varying debris sizes. It is presented by Figure 6.68.



**Figure 6.68:** Behaviour of error vs. epochs when debris size is varied with a mass of 1.413 kg.

The blue curve depicts the 2 cm size debris object's error. The rest of the sizes are quite close to each other in the error plots, due to comparable position and velocity accuracies resulting as a result of their individual number of observations. It can be hence concluded that the position and velocity errors and accuracies vary with changes in debris diameter, which is a sensitive parameter of this study.

### 6.7.5. Different SRP coefficients

The surface property of the debris is another uncertainty in the model. The debris object in the simulation is assumed to be entirely reflective ( $C_r = 2$ ). However, there can be different sources and types of debris, which have different surface properties and hence variable SRP coefficients. Hence, this subsection studies the effect of varying SRP coefficients between 0.5 and 2 (ranging from fully absorbing to fully reflective debris surfaces).

The position and velocity accuracies along with the RMSE values for the different  $C_r$  values are presented in Table 6.15.

**Table 6.15:** Effect of variation of SRP coefficient on orbit determination results. The debris mass considered is 1.413 kg and the debris diameter is considered to be 10 cm.

$C_r$ [-]	Position accuracy [m]	Velocity Accuracy [m/s]	RMSE
0.5	4.528	0.014	1.157
1	4.527	0.013	1.155
1.5	4.528	0.014	1.157
2	4.528	0.014	1.157

The values in position and velocity accuracy are on average equal to 4.5 m and 0.0135 m/s for the different SRP coefficients. It means that regardless of the surface properties, the orbital formal errors and RMSE remain greatly unaffected.

The errors in Cartesian position and velocity evolving over time can be visualised in Figure 6.69. It can be seen that the error plots overlap with each other even for errors in the z-direction. This implies that the  $C_r$  has very little impact on the overall orbital accuracy and prediction errors in the debris orbit.

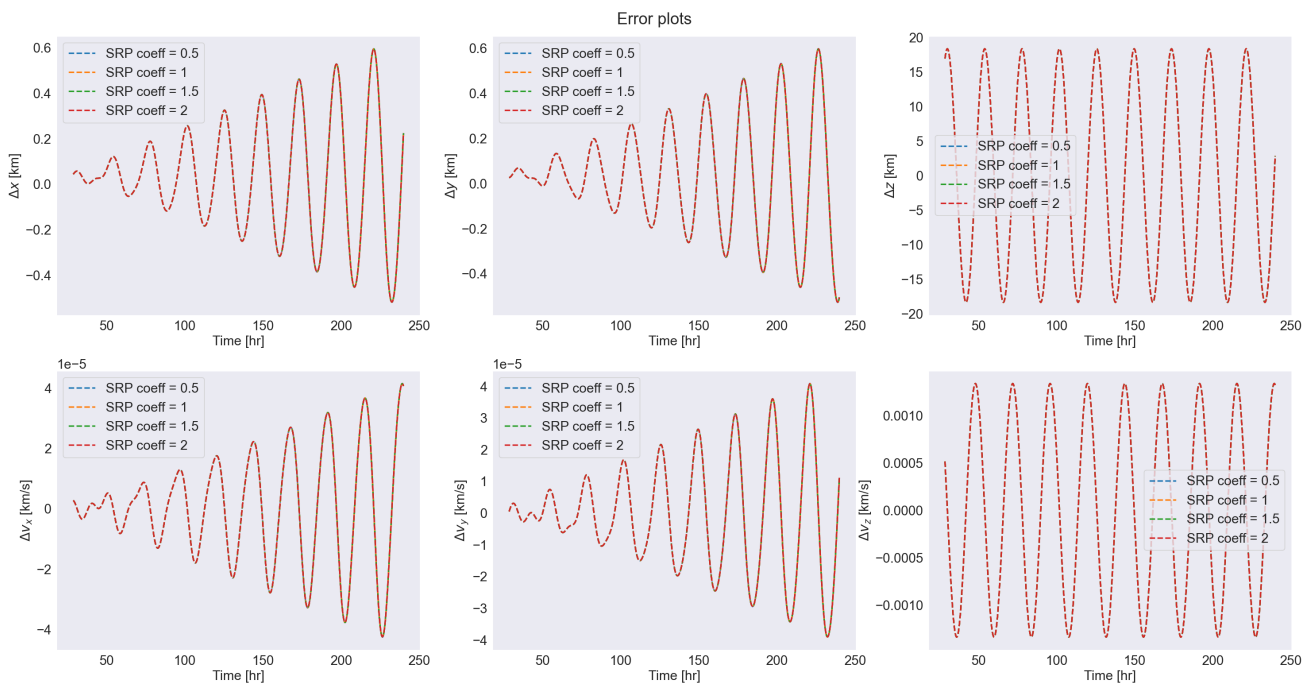


Figure 6.69: Behaviour of error vs. epochs when SRP coefficient is varied.

Now that the different cases have been studied, along with performing a sensitivity analysis for model parameters and initial debris guess, the next chapter will assess the feasibility of the solution and present optimal choices for the parameters studied. Research questions will be revisited and answered using the work done in the research, which was summarised in this chapter.



# 7

## Application of the study

Dedicated to reflecting on the results obtained throughout the study, this chapter aims to fulfill the overall research goal defined in Chapter 2. After determining the performance metrics for OD and analysing the trends of changing some critical parameters, a design space must be scanned to get the optimal values, which can suggest a feasible or non-feasible outcome for the study.

The feasibility will be evaluated on the orbit determination accuracy performance, which will be compared to the accuracy of TLE data for trackable GEO objects. As per the work of Früh et al. [58], the position accuracy of the TLE for a GEO object is claimed to be 25 km in the radial direction and 10 km in the along-track direction. Not much information about velocity accuracy is available in the literature, which gives priority to position accuracy for computation of accuracy. The accuracy for the most feasible configuration will be compared to this value from the ground to answer the question of space-based radar feasibility in terms of performance.

### 7.1. Revisit time

It was seen earlier in Section 6.3, that an altitude difference of 250 km was the best in terms of lower positions and velocity errors. However, it has a longer latency time due to a higher synodic period, before a revisit can occur. Hence, to study revisits, the observation satellite is modeled at an altitude difference of 500 km. This is propagated using the initial conditions as discussed in Table 4.6. The propagation is done for close to 4 months to evaluate its long-term feasibility. The collected measurements are shown by Figure 7.1 for range, Figure 7.2 for range rate, Figure 7.3 for azimuth and Figure 7.4 for elevation.

Three revisits are seen, occurring after intervals of close to 58 days. This is shown by the blue crosses denoting observations. The red curves show the estimated measurements from the measurements collected. This corresponds to the synodic period of the satellite and debris for that altitude difference.

It is important to know how much error is present for the period before a measurement is collected to demonstrate the impact of space-based measurements. By a rule of thumb, it can be considered a good observation system if the errors in each coordinate are not extremely large before the next measurement opportunity.

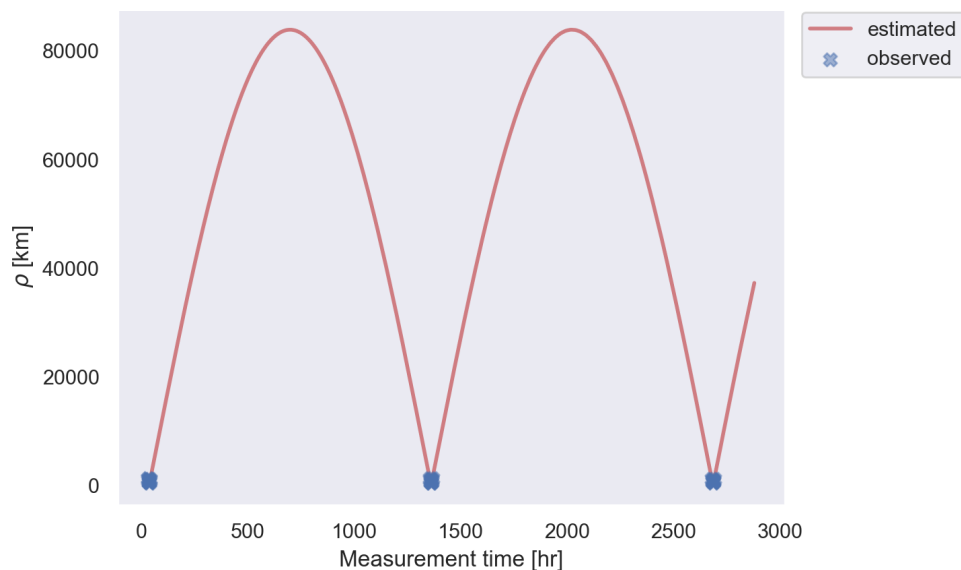


**Figure 7.1:** The revisiting contact seen after almost 58 days for  $\Delta h = 500$  km, which corresponds with the synodic period as predicted before. There are 3 revisit instances for almost 4 months.

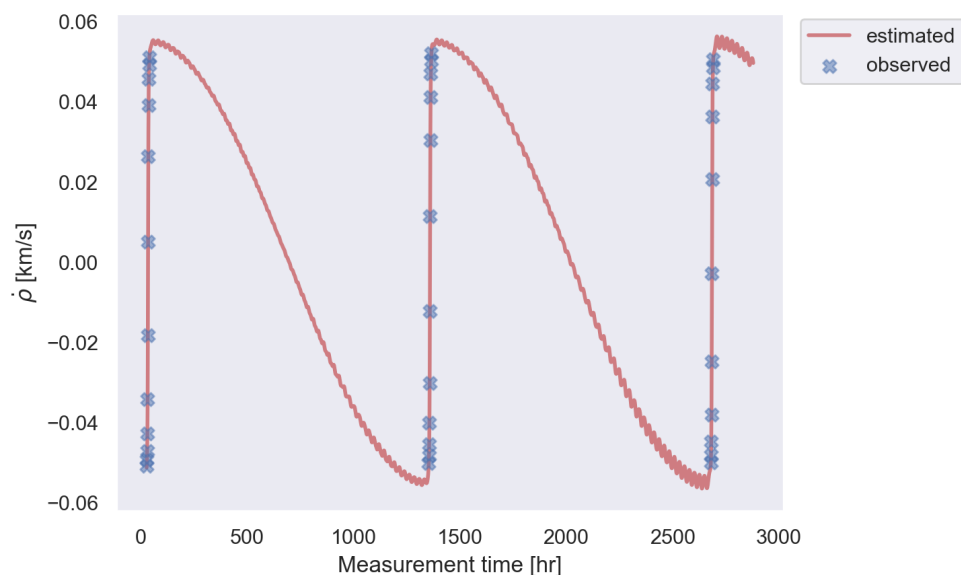


**Figure 7.2:** The range-rate measurements can be seen to fit through the estimated observables, showing the three instances of revisit

The behaviour of the errors in Cartesian position and velocity coordinates is seen in Figure 7.5.

The trend can be seen in this plot, where the errors keep increasing due to prediction with the measurement data set till a new measurement is obtained. The maximum position error in  $x$ ,  $y$  and  $z$  coordinates is almost 20 km. The error grows linearly over time for the  $x$  and  $y$  coordinates, while for  $z$  it is still ill-determined and maintains a constant behaviour of oscillations. The magnitude of errors in the  $z$  position and velocity decreases with the next observation opportunity, while the pattern is repeated for the  $x$  and  $y$  coordinate errors. The error is reduced with a revisit immediately since the satellite now has new information about the debris' state, which can be used in another OD process to update the position and velocity of the debris.

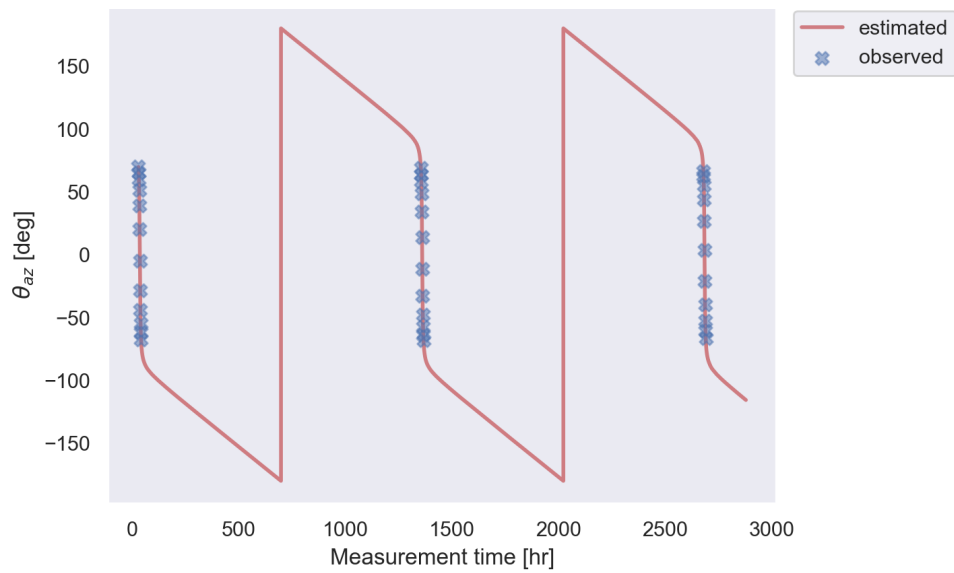


**Figure 7.3:** The revisiting contact seen after almost 58 days for  $\Delta h = 500$  km, which corresponds with the synodic period as predicted before. There are 3 revisit instances for almost 4 months.

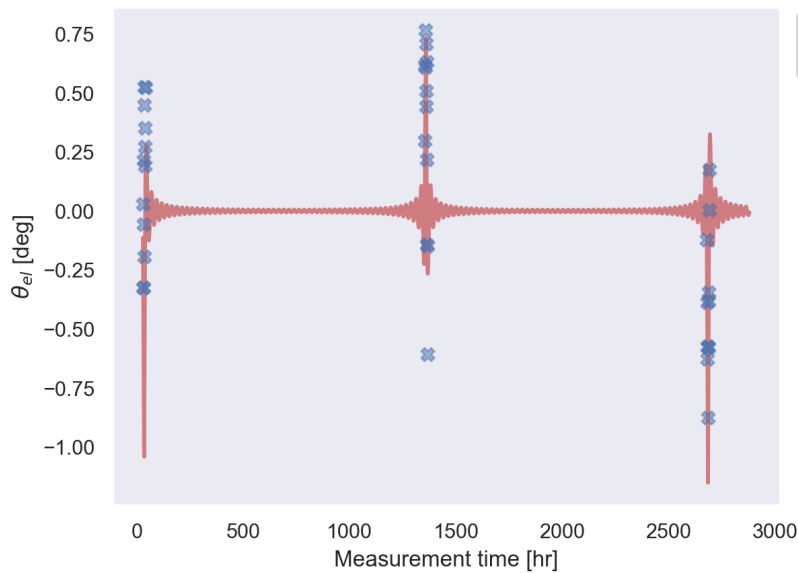


**Figure 7.4:** The revisiting contact seen after almost 58 days for  $\Delta h = 500$  km, which corresponds with the synodic period as predicted before. There are 3 revisit instances for almost 4 months.

By this exercise, it can be inferred that one satellite at a relative altitude difference of 500 km and relative inclination difference of  $2.5^\circ$  can have three revisits in four months, leading to maximum position errors in the magnitude of 20 km and maximum velocity errors in the magnitude of  $40 \mu\text{s}$ .

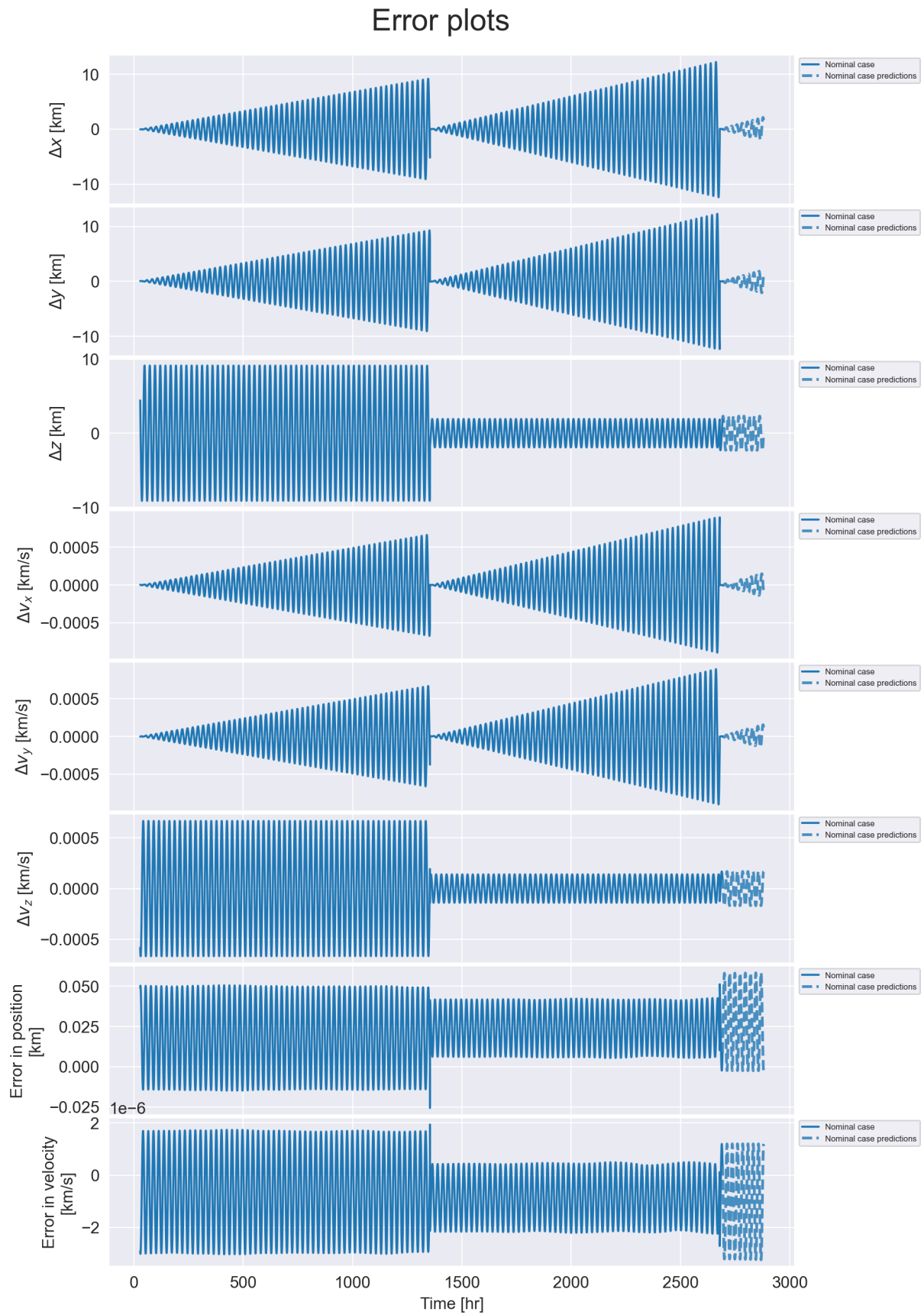


**Figure 7.5:** The behaviour of the prediction errors when the satellites at  $\Delta h = 500$  km and  $\Delta i = 2.5^\circ$  revisit the debris at GEO. The true values grow to about 20 km in  $x$ ,  $y$  and  $z$ , then decrease again since there are new sets of measurements to fit. The error in position is in the order of 75 m and for velocity is in the order of 40 cm/s

## 7.2. Optimisation of design space and parameters

It was seen that the parameters  $\Delta h$  and  $\Delta i$  have a significant role on the quality of measurements and hence the accuracy of orbit determination. It was also seen that a three-satellite configuration performed better in terms of predicted errors in position and velocity over time. Having identified the crucial parameters which affect OD quality, a simple grid is created, varying through different altitude and inclination values of three satellites in a triangulated configuration.

An infinite number of cases could be possible but would not be performed here. This study only considers a limited grid, keeping the first satellite at a constant  $\Delta h$  value of 500 km and  $\Delta i$  value of  $0^\circ$ . The remaining two satellites are varied in those values, resulting in 25 grid points to be studied. The cases are presented in Table 7.1.

**Table 7.1:** The grid points for different combinations of  $\Delta h$  and  $\Delta i$  for three satellites, that are studied to optimise the overall OD quality.

Case	$\Delta h$ [km]			$\Delta i$ [°]		
	Satellite 1	Satellite 2	Satellite 3	Satellite 1	Satellite 2	Satellite 3
1	500	500	500	0	1	179
2	500	600	400	0	1	179
3	500	700	300	0	1	179
4	500	800	200	0	1	179
5	500	900	100	0	1	179
6	500	500	500	0	2	178
7	500	600	400	0	2	178
8	500	700	300	0	2	178
9	500	800	200	0	2	178
10	500	900	100	0	2	178
11	500	500	500	0	3	177
12	500	600	400	0	3	177
13	500	700	300	0	3	177
14	500	800	200	0	3	177
15	500	900	100	0	3	177
16	500	500	500	0	4	176
17	500	600	400	0	4	176
18	500	700	300	0	4	176
19	500	800	200	0	4	176
20	500	900	100	0	4	176
21	500	500	500	0	5	175
22	500	600	400	0	5	175
23	500	700	300	0	5	175
24	500	800	200	0	5	175
25	500	900	100	0	5	175

For the cases mentioned in the above table, the OD exercise is performed for a duration of 1.5 months. Taking a longer simulation time would introduce revisits and make the process more complicated, over which a simplistic analysis was preferred. The performance metrics evaluated in this case are the average position and velocity errors in the prediction phase, the initial position and velocity accuracy or formal uncertainty, and the number of measurements collected in

that configuration. The overall results are presented in a bar plot with the cases on the x-axis and a log scale on the y-axis in Figure 7.6. The initial position accuracy is labeled in blue, followed by the initial velocity accuracy in orange. The number of measurements are labeled in green, followed by the average errors in position and velocity predictions labeled in red and purple respectively.

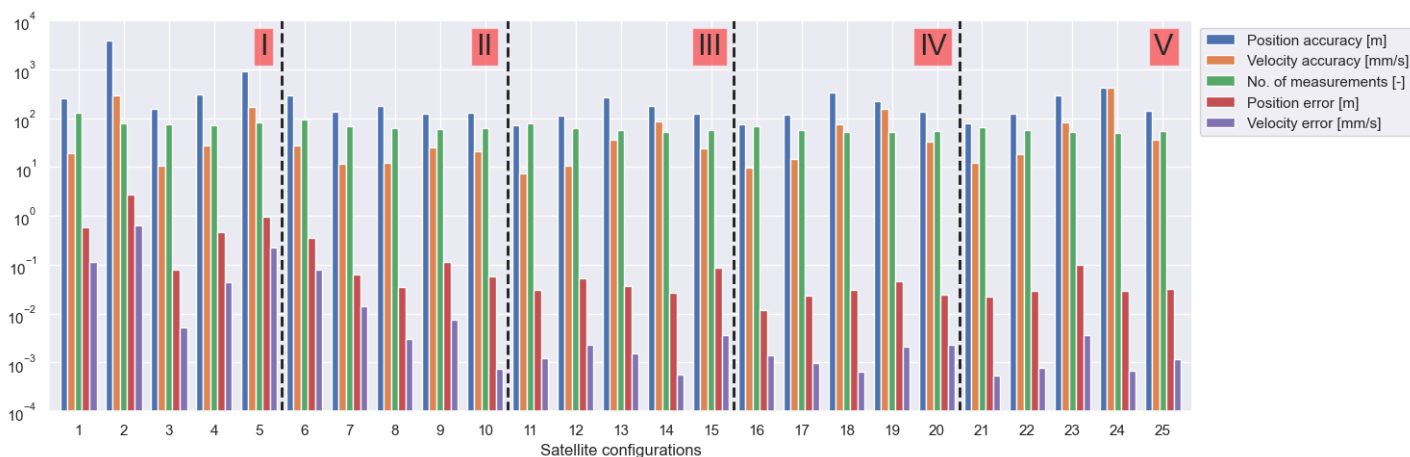


Figure 7.6: OD performance results obtained for the 25 cases listed in Table 7.1, by means of a simple Grid search.

At a single glance, it is difficult to draw conclusions on the optimal satellite configuration geometry. The error and accuracy must be minimal and the number of measurements maximum for an optimal OD quality. To analyse them closely, Figure 7.6 has been divided into five regions, which signify the changing inclinations. Inside each of these regions, the altitude difference is then varied. Each of the regions is considered individually, to highlight the most interesting case to analyse further.

**Region I:** The first five cases from the grid space are considered for analysis here. The metrics in Region I are plotted in a polar plot, also known as a 'radar' plot. This is seen in Figure 7.7.

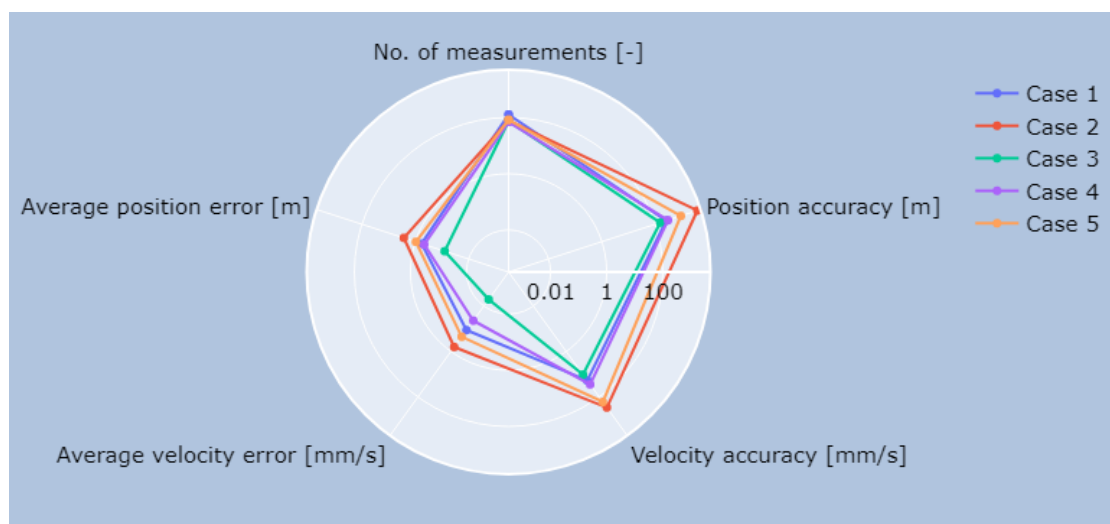
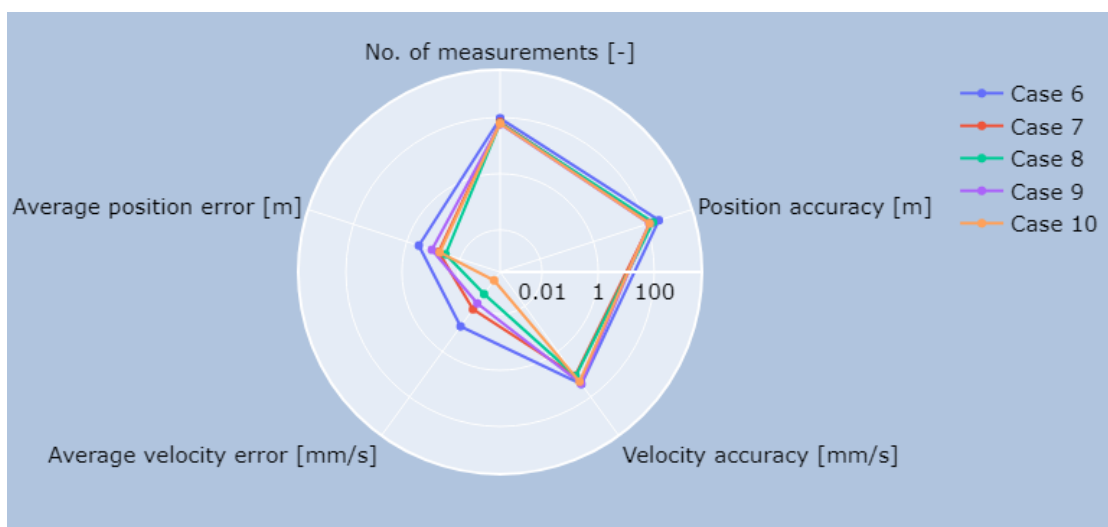


Figure 7.7: Radar plot on a log scale for Region I, demonstrating the OD quality metrics. The inclination values are  $\Delta i_1 = 0^\circ$ ,  $\Delta i_2 = 1^\circ$  and  $\Delta i_3 = 179^\circ$ . The logarithmic range of the polar plot is from  $10^{-4}$  to  $10^4$ .

The first vertex denoting the number of measurements is seen to be of the same order of magnitude for all the cases, due to their relative inclinations being equal. The red curve denoting Case 2 shows the highest position and velocity errors and the worst accuracy. The blue (Case 1), purple (Case 4) and yellow (Case 5) curves behave very closely, out of which Case 4 is relatively better. The green curve depicting Case 3 for relative inclinations  $\Delta i_1 = 0^\circ$ ,  $\Delta i_2 = 1^\circ$  and  $\Delta i_3 = 179^\circ$  and relative altitudes  $\Delta h_1 = 500$  km,  $\Delta h_2 = 700$  km and  $\Delta h_3 = 300$  km have comparable accuracies with the rest of the cases. However, it performs the best in terms of least average position and velocity errors, making it the top choice from Region I. Hence, **Case 3** will be carried forward to the second round of grid search.

**Region II:** Similarly, the next five cases from the grid space (Cases 6 - 10) are considered for analysis here. The metrics in Region II are plotted in a similar radar plot. This is seen in Figure 7.8.



**Figure 7.8:** Radar plot on a log scale for Region II, demonstrating the OD quality metrics. The inclination values are  $\Delta i_1 = 0^\circ$ ,  $\Delta i_2 = 2^\circ$  and  $\Delta i_3 = 178^\circ$ . The logarithmic range of the polar plot is from  $10^{-4}$  to  $10^4$ .

The first vertex again denotes the number of measurements for all the cases, which are almost the same for all cases in this region due to their equal relative inclinations. The blue curve denoting Case 6 shows the highest position and velocity errors and the worst accuracy. The red (Case 7), green (Case 8) and purple (Case 9) curves behave very closely, out of which Case 8 is relatively better by showing lower average velocity errors. The yellow curve depicting Case 10 for relative inclinations  $\Delta i_1 = 0^\circ$ ,  $\Delta i_2 = 2^\circ$  and  $\Delta i_3 = 178^\circ$  and relative altitudes  $\Delta h_1 = 500$  km,  $\Delta h_2 = 900$  km and  $\Delta h_3 = 100$  km have comparable accuracies with the rest of the cases. However, it performs the best in terms of least average velocity error and highest position accuracy making it the top choice from Region II. Hence, **Case 10** will be carried forward to the second round of grid search.

**Region III:** Similarly, the subsequent five cases from the big grid space (Cases 11 - 15) are considered for analysis here. The metrics in Region III are plotted in a similar radar plot. This is seen in Figure 7.9.

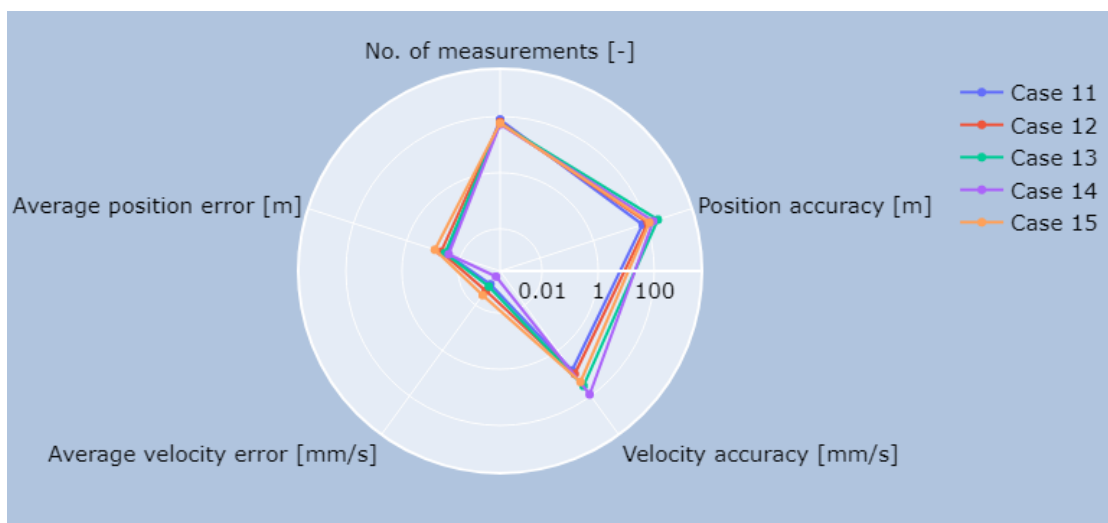


**Figure 7.9:** Radar plot on a log scale for Region III, demonstrating the OD quality metrics. The inclination values are  $\Delta i_1 = 0^\circ$ ,  $\Delta i_2 = 3^\circ$  and  $\Delta i_3 = 177^\circ$ . The logarithmic range of the polar plot is from  $10^{-4}$  to  $10^4$

In this plot, no good or bad case is easily visible. The first vertex again denotes the number of measurements for all the cases, which are almost the same for all cases in this region due to their equal relative inclinations. All the cases have comparable position errors, with the yellow curve (Case 15) having the highest value and the blue curve (Case 11) having the least value. The purple curve (Case 14) has a worse velocity accuracy but a lower overall error in velocity. The red (case 12) and green (Case 13) curves perform almost similarly except for the position accuracy, where Case 13 performs worse. Overall, the blue curve or Case 11 for relative inclinations  $\Delta i_1 = 0^\circ$ ,  $\Delta i_2 = 3^\circ$  and  $\Delta i_3 = 177^\circ$  and relative altitudes  $\Delta h_1 = 500$  km,  $\Delta h_2 = 500$  km and  $\Delta h_3 = 500$  km performs the best in all the metrics, making it the top choice from Region III. Hence, **Case 11** will be carried forward to the second round of grid search.

**Region IV:** Similarly, the subsequent five cases from the big grid space (Cases 16 - 20) are considered for analysis here. The metrics in Region IV are plotted in a similar radar plot. This is seen in Figure 7.10.

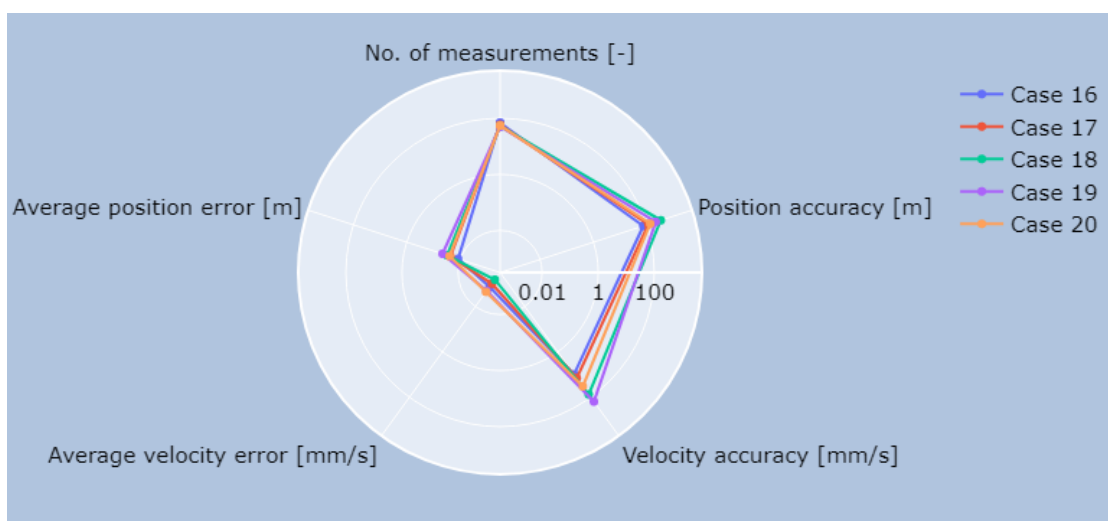


**Figure 7.10:** Radar plot on a log scale for Region IV, demonstrating the OD quality metrics. The inclination values are  $\Delta i_1 = 0^\circ$ ,  $\Delta i_2 = 4^\circ$  and  $\Delta i_3 = 176^\circ$ . The logarithmic range of the polar plot is from  $10^{-4}$  to  $10^4$ .

Similar to Region III, also in Region 4 no good or bad case is easily visible. The first vertex again denotes the number of measurements for all the cases, which are almost the same for all cases in this region due to their equal relative inclinations. All the cases have comparable position errors, with the purple curve (Case 19) having the highest value and the blue curve (Case 16) having the least value. Case 19 has a worse velocity accuracy, but the green curve (Case 18) has the highest average velocity error. The red (Case 17) and yellow (Case 20) curves perform almost similarly except for the average velocity error, where Case 20 performs worse. Overall, the blue curve or Case 16 for relative inclinations  $\Delta i_1 = 0^\circ$ ,  $\Delta i_2 = 4^\circ$  and  $\Delta i_3 = 176^\circ$  and relative altitudes  $\Delta h_1 = 500$  km,  $\Delta h_2 = 500$  km and  $\Delta h_3 = 500$  km performs the best in all the metrics, making it the top choice from Region III. Hence, **Case 16** will be carried forward to the second round of grid search.

**Region V:** Finally, the last five cases from the big grid space (Cases 21-25) are considered for analysis here. The metrics in Region V are plotted in a similar radar plot. This is seen in Figure 7.11

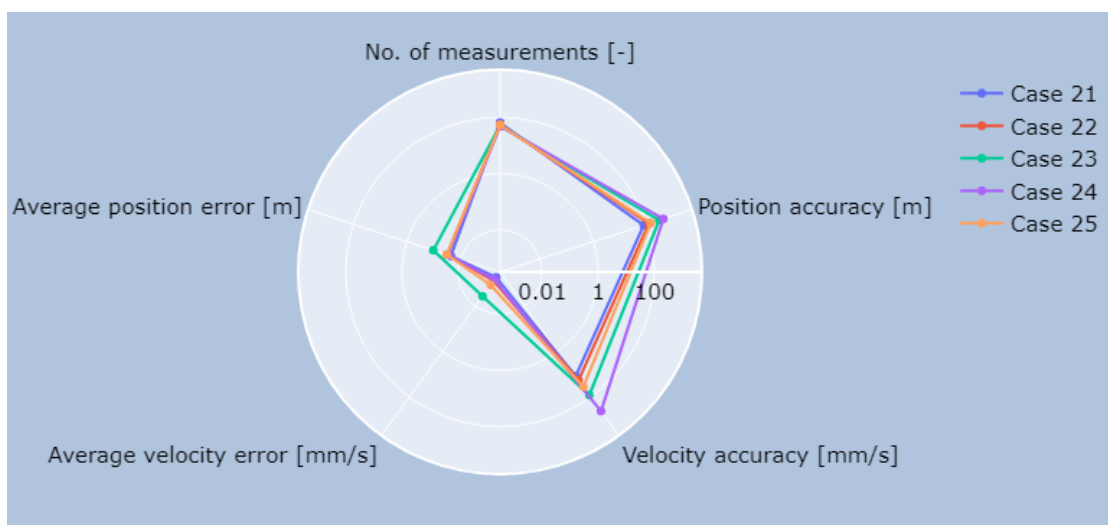


**Figure 7.11:** Radar plot on a log scale for Region V, demonstrating the OD quality metrics. The inclination values are  $\Delta i_1 = 0^\circ$ ,  $\Delta i_2 = 5^\circ$  and  $\Delta i_3 = 175^\circ$ . The logarithmic range of the polar plot is from  $10^{-4}$  to  $10^4$ .

The first vertex again denotes the number of measurements for all the cases, which are almost the same for all cases in this region due to their equal relative inclinations. The green curve (Case 23) shows the highest average position and velocity errors, followed by the purple curve (Case 24) which shows the worst accuracy in position and velocity. The red (Case 22), yellow (Case 25), and blue (Case 21) curves behave together, where Case 25 behaves worse than Case 22 in velocity accuracy and position accuracy. The blue curve depicting Case 21 for relative inclinations  $\Delta i_1 = 0^\circ$ ,  $\Delta i_2 = 5^\circ$  and  $\Delta i_3 = 175^\circ$  and relative altitudes  $\Delta h_1 = 500$  km,  $\Delta h_2 = 500$  km and  $\Delta h_3 = 500$  km is the most interesting case. It performs the best in terms of least average position and velocity errors as well as the highest position and velocity accuracies making it the top choice from Region V. Hence, **Case 21** will be carried forward to the second round of grid search.

### Overall Grid Search

After selecting each case from each region of the Grid space, Figure 7.6 now looks like Figure 7.12. The selected cases are highlighted whereas the remaining are kept blurred.

As discussed earlier, the best-performing cases are Case 3 from Region I, Case 10 from Region II, Case 11 from Region III, Case 16 from Region IV and Case 21 from Region V. The purpose of per-

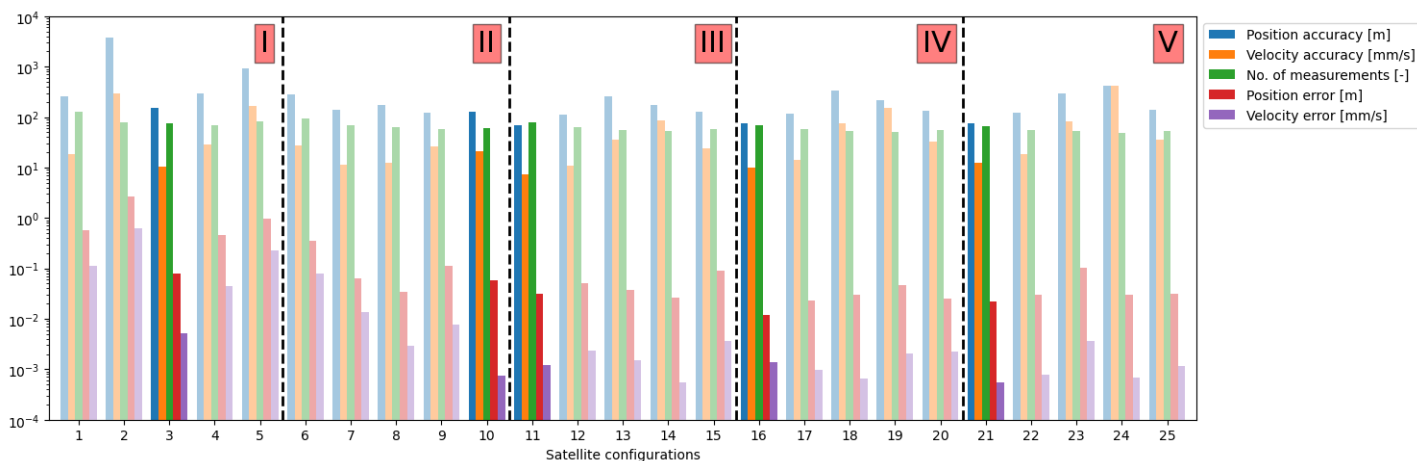


**Figure 7.12:** Overall bar plots in the total grid of 25 configurations, from which the best of each section is selected to create a smaller grid of 5 configurations.

forming the first-level grid search is to narrow down the optimum range of parameters for which an optimal quality orbit determination can be performed by INDIGO. When the five selected parameters are individually tested against the same performance metrics, Figure 7.13

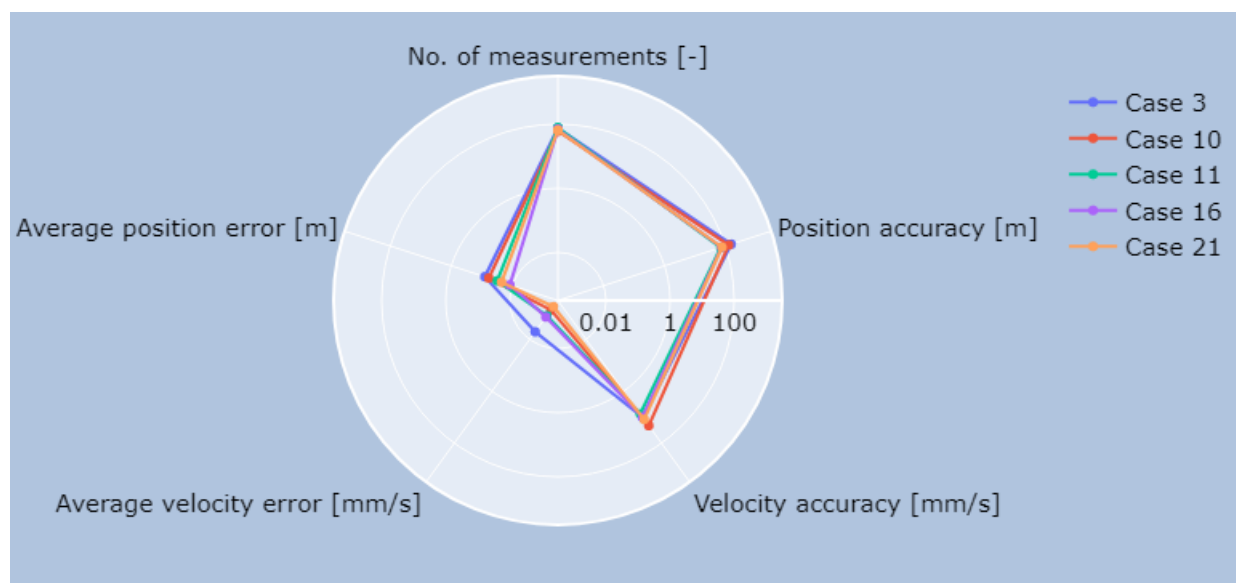


**Figure 7.13:** Radar plot on a log scale for the best-performing cases from each section for demonstrating the OD quality metrics. The best case is Case 16 for which the inclination difference values are  $\Delta i_1 = 0^\circ$ ,  $\Delta i_2 = 4^\circ$  and  $\Delta i_3 = 176^\circ$ , and the altitude difference values are  $\Delta h_1 = 500$  km,  $\Delta h_2 = 500$  km and  $\Delta h_3 = 500$  km. The logarithmic range of the polar plot is from  $10^{-4}$  to  $10^4$ .

Looking at the radar plot, it can be seen that all candidates perform almost equally in terms of the number of measurements, position and velocity accuracy. The decisive factors are hence the average errors in position and velocity. The blue curve (Case 3) performs the worst in velocity errors, but the red curve (Case 10) performs the worst in position errors. The yellow curve (Case 21) performs the best in terms of velocity errors, but not the best for position errors, whereas the purple curve (Case 16) performs the best. The green curve (Case 11) does not perform the best or worst in any of the criteria. Apart from the best position error performance, Case 16 has fewer

velocity errors, while Case 21 performs worse in velocity accuracy than Case 11. This implies that **Case 16** is the most optimal configuration determined from this particular Grid Search, which is recommended for further analysis for feasibility.

After researching on the aspects of orbit propagation, radar functionalities, and effects of changing model parameters on orbit determination quality, it is time to re-iterate the research goal and revisit the research questions.

### 7.3. Research Questions revisited

This section will discuss the three research questions defined at the end of Chapter 2. We will start with the first research question of the study.

#### Research question 1

Is using a space-based radar system **feasible** for space surveillance and tracking of small-sized debris objects in GEO?

- What are the **performance metrics** that determine the system's feasibility?
- How does the performance of the space-based system **compare** with conventional ground-based SSA systems?

#### Answer:

A space-based radar named INDIGO was explored for its design and detection performance to observe small-sized objects in GEO in the range of 1 to 10 cm. It was seen that the range at which the satellite must be placed in orbit is derived from the different object sizes targeted. From Figure 7.14, it can be seen that at 1000 km, it is possible to detect a spherical object of diameter 5.2 cm. For a 1 cm-sized object, though, for the reference SNR value selected for INDIGO, the target must be between 250 km to 500 km away for proper detection.

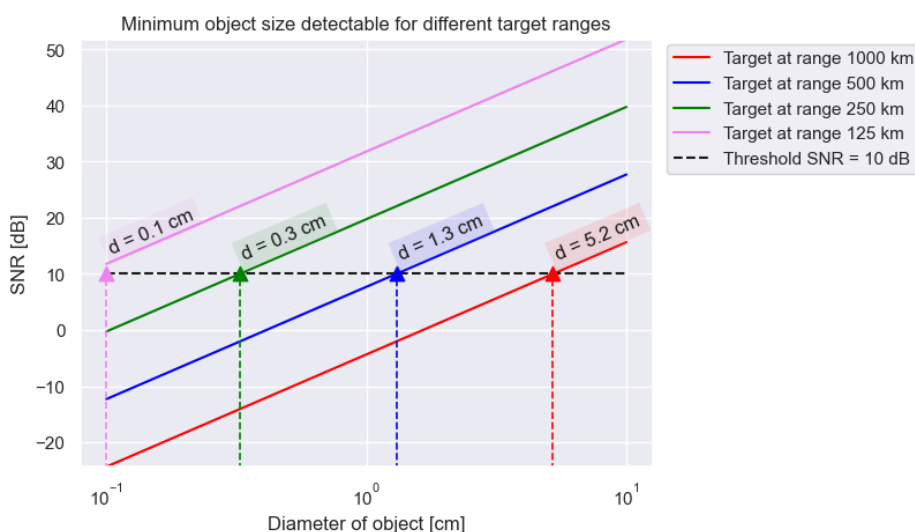


**Figure 7.14:** SNR varies with the fourth power of the range to the target, which is different for different objects. The labeled colors show the threshold value of SNR for different object sizes.

Similarly, as seen in Figure 7.15, a 1 mm object is not detected at 1000 km but is rather detected

only for distances less than 200 km, which was not a part of the study. A 10 cm object (as what was studied) can easily be detected by INDIGO even at a maximum distance of 1400 km.

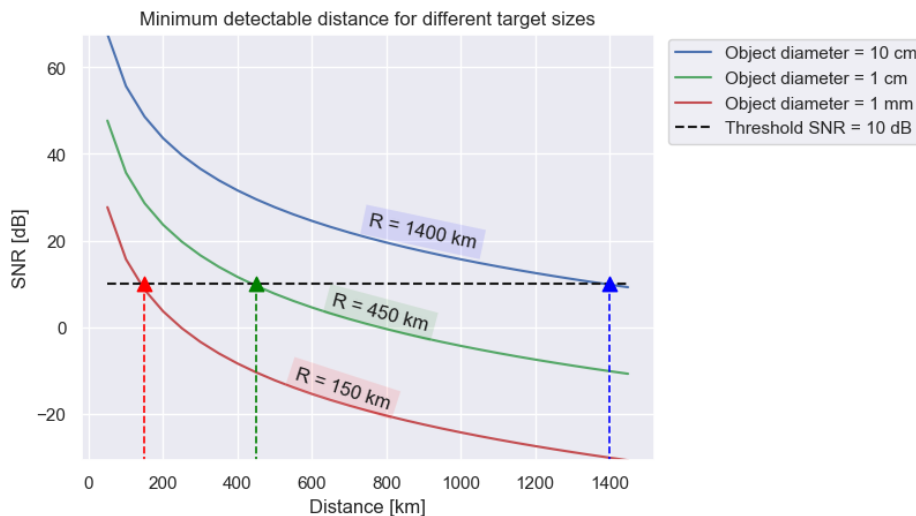


Figure 7.15: SNR varies with the RCS of an object, which is shown for different ranges.

The main aspect of Question 1, of the feasibility of INDIGO to detect small-sized objects can now be answered. For the given ranges of target sizes, the radar performance showed that **it was feasible** for detecting and surveillance of small objects.

#### Sub-question 1 :

The metrics that were used to define INDIGO's feasibility were its orbit determination quality and its performance in detecting and tracking small-sized objects. They are mentioned below:

- Its **measurement quality** is given by the weighted sum of squares of the residuals (**RMSE**). The smaller the RMSE, the better the measurements are for orbit fitting.
- **Measurement quantity**: the higher the number of measurements recorded, the better the orbit fitting performance is.
- The **absolute error behavior** of the system's orbit determination performance. This shows the trend of the errors w.r.t time, which gives an idea about its uncertainty in orbit prediction.
- The **accuracy** with which the initial state of the debris object is estimated. This is also known as the **formal position** and **velocity** uncertainties.
- **Revisit time and geometry**: The configuration of the satellite's orbit affects the number of measurements and hence the system performance.

#### Sub-question 2 :

The accuracy of TLE data for GEO was found to be almost 27 km in position [58]. So far, all the values found for the accuracy in position for any of the configurations or cases were better than this value. In fact, for the most optimal configuration, the position accuracy of 19 m was obtained, which is considerably smaller than 27 km. Since other metrics for ground-based systems could not be found in previous studies, only the position accuracy has been used for a fair comparison. Based on that assumption, compared to conventional ground-based systems, INDIGO achieves a

higher position accuracy value, thus proving that it is feasible in terms of performance.

The second research question can now be tackled.

### Research question 2

How do the dynamic model parameters, observation types, and trajectory prediction outcome contribute to the **feasibility assessment** of the system?

- For which **type** or **settings** of the **orbit propagation model** is the system's feasibility assessed, given a requirement on orbit accuracy?
- Which **category** or **combinations** of collected **in-situ measurements** lead to the optimal performance of the space-based system?
- How well is the orbit determination scheme capable of **predicting the debris orbit** when the system collects no measurements?

### Answer:

The dynamic model parameters and observation types that were studied are useful in answering this question.

### Sub-question 1:

The orbital model considered the perturbations of  $J_2$ ,  $J_{2,2}$  spherical harmonics, perturbations from the third body Sun and Moon, and solar radiation pressure. An analysis on step size tuning was performed in Chapter 6, where there was a trade-off that needed to be made between position accuracy obtained and computation time. A simple analysis is shown in Figure 7.16, which shows  $dt = 50$  s to be the balance between position accuracy and computation time. However, the errors in position and velocity are higher, for which it is not selected. Rather, the originally chosen time step  $dt$  of 25 seconds is established as the optimal choice for step-size selection.

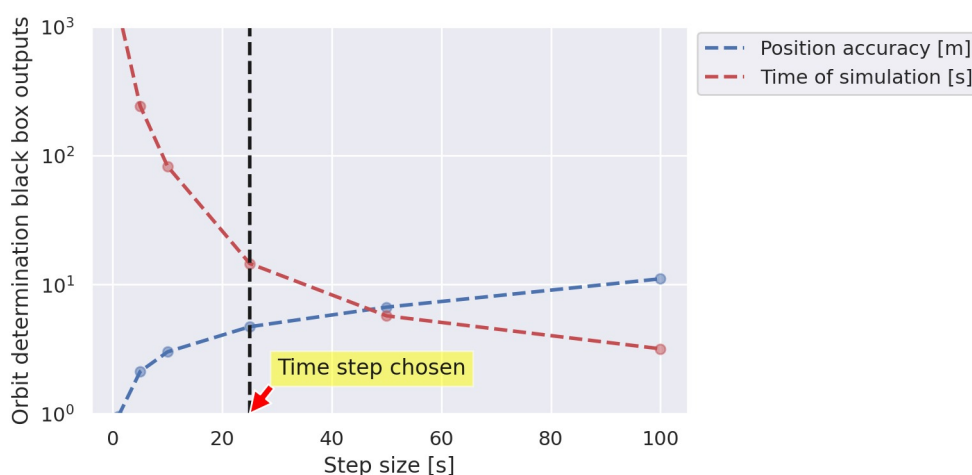


**Figure 7.16:** Choice of step-size depending on position accuracy and time of computation.

Hence, the step size for integration of orbital propagation and estimation is tuned to **25 seconds**,

which is also equal to INDIGO's integration time.

### Sub-question 2:

Range measurements performed the best in terms of initial state accuracy and convergence for cases with zero inclination between the orbits of the debris and the satellite. When a slight increase in inclination was observed, the **combination of range, range-rate, and angular measurements** was seen to perform optimally. This gives the freedom to use more types of measurements and acts as an advantage over typical optical systems, which take angular data for GEO objects. More variety of measurements makes the system capable of significantly improving the accuracy in position and velocity.

### Sub-question 3:

As seen in the revisit time errors in Figure 7.5, the maximum position error using all measurements was 75 m, and the maximum velocity error was 40 cm/s. After this, there was a new measurement opportunity, which reduced the errors again.

Now the final research question can be explored.

#### Research question 3

How **sensitive** is the orbit determination **accuracy** of small-sized debris objects in GEO to changes in uncertainties and satellite geometric configuration?

- How do changes in the **system noise** and **uncertainties** affect the accuracy of the orbit determination and prediction?
- At what optimal **orbital altitude** and **inclination** must the system be positioned to obtain the best possible orbit determination and prediction accuracy?
- To what extent does the performance of the system **improve** if **extra tracking satellites** are introduced, and what would be the optimal geometric **configuration**?

### Answer:

A sensitivity analysis was performed, which identified the most crucial parameters for the optimisation problem. For instance, looking at Figure 7.17, it can be seen that debris of size 10 cm can be detected with a position accuracy of 10 m and a velocity accuracy of 0.1 m/s.

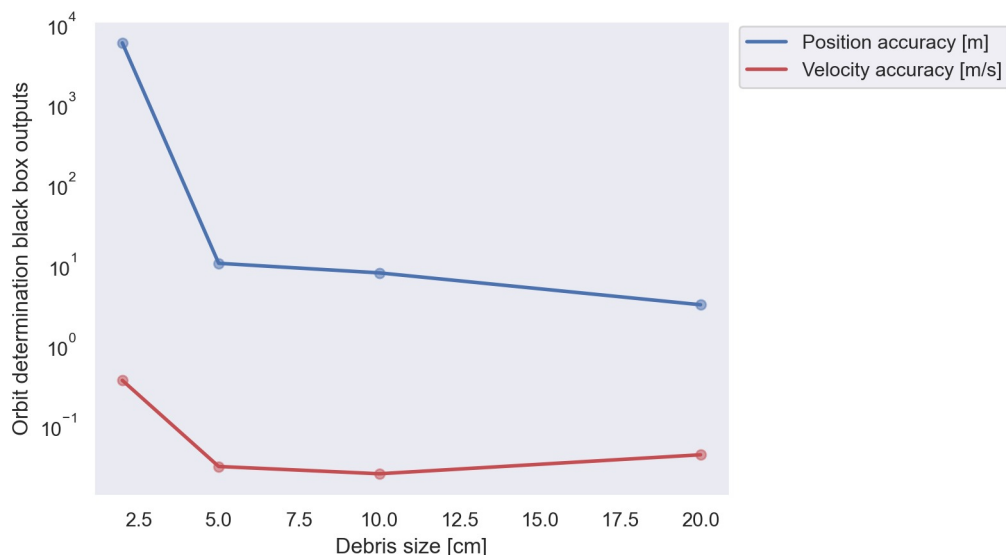


**Figure 7.17:** Variation of debris size with the orbit determination black-box outputs, which are uncertainty in position and velocity.

### Sub-question 1:

Adding noise and bias to the true measurements is to make them close to reality. The magnitude of the standard deviation of the noises added to the measurements was determined by the Cramer-Rao lower limit, which depends on the radar parameters. The bias values were chosen randomly in the same order of magnitude, which were used for generating the orbit determination results.

However, the exact magnitudes are still uncertainties in the model, for which the effect of changing the standard deviation values was studied in Section 6.7.2. By increasing the magnitude of bias and noise standard deviations, the orbit's accuracy in position and velocity worsened, along with growing errors in position and velocity.

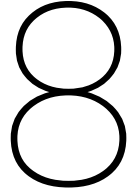
### Sub-question 2 and 3:

A grid search exercise was performed in Section 7.2, which went through 25 grid points and divided the space into five regions based on their combinations of  $\Delta h$  and  $\Delta i$ . Each best-performing case was selected from the five regions to perform another grid search optimisation and declare the most optimal configuration for those sets of grid points.

The most optimal configuration was Case 16, with three satellites in a triangulated configuration. The individual  $\Delta h$  and  $\Delta i$  parameters per satellite were  $\Delta h_1 = 500$  km and  $\Delta i_1 = 0^\circ$  for Satellite 1,  $\Delta h_2 = 500$  km and  $\Delta i_2 = 4^\circ$  for Satellite 2 and  $\Delta h_3 = 500$  km and  $\Delta i_3 = 176^\circ$  for Satellite 3.

After discussing the various elements from each chapter in the report, it is time for an overall conclusion, which summarises all key aspects for the reader. This is presented in Chapter 8.





---

# Conclusions and Recommendations

---

The earlier chapters extensively explored the required knowledge, methodology and results to achieve an answer to the research goal defined in Chapter 2. This chapter serves as a culmination of this research, presented in Section 8.1, which is aimed to summarise the key findings from the theory and numerical simulation results. Alongside, the areas requiring further investigation and work are highlighted in Section 8.2, which is aimed to highlight the limitations of the current study and make recommendations for further work.

## 8.1. Conclusions

Space debris poses significant challenges to current and future space missions, as even the tiniest fragments can pose serious threats to operational satellites and spacecraft. This study aimed to assess the space situational awareness capability of a space-based radar system, which surveys and detects small-sized debris objects in the geostationary orbital regime, to overcome the limitations posed by ground-based sensing systems. Three research questions were defined at the start of the study in Chapter 2, answered in this thesis report in Chapter 7.

The thesis methodology was based on numerically simulating the orbit of an observation satellite in a sub-GEO regime, such that it can observe a small-sized debris object in the GEO ring using a radar instrument. The INDIGO radar is selected as a pulsed waveform phased array radar with a planar surface. It has 20 antenna elements, with an individual power of 50 W, leading to a total power of 1 kW. Its operating frequency is 18 GHz, and it can target objects within 1 to 10 cm. It has a pulse compression ratio factor of 1000, which amplifies signals it receives, to receive a threshold Signal-to-Noise Ratio (SNR) value of 10 dB. The design process was explained in Chapter 4 of the report, which bases Chapter 3 as the theoretical framework for the methods used. The orbit propagation model is developed in Python, using standard NumPy and SciPy tools, which incorporate the relevant orbital accelerations of the GEO regime:  $J_2$  spherical harmonics,  $J_{2,2}$  spherical harmonics, third-body perturbations due to Sun and Moon and Solar radiation pressure. A fixed-step Runge-Kutta 4 integrator propagates the state of the debris object and the satellite every 25 seconds. The radar collects instantaneous measurements and adds Gaussian noise and bias to its measurements: range, range rate, azimuth, and elevation. It then uses the Weighted Least Squares method to estimate the debris's initial state by fitting the orbit through the observed measurements.

The methodology is validated using external software (TUDATPy and Poliastro) in Chapter 5. The

research results are explained in Chapter 6. Several test cases are analysed in that chapter by studying the effect on orbit determination quality due to varying integration step sizes, noise parameters, altitude difference, inclination difference, types of measurements, and the number of satellites in the constellation. Further, a sensitivity study was conducted to study the effect of uncertainties in the model and its results. In Chapter 7, the simulation was carried out for four months to demonstrate successful re-capturing of measurements upon revisit. This was followed by a simple optimisation process where a grid search was performed on 25 cases on a three-satellite triangulated configuration. The parameters varied were the satellite's relative altitude and inclinations, after which a second round of optimisation established the best performing or most optimal configuration. It was seen that Case 16, was the most optimal configuration compared to the remaining 24 grid points in that optimisation space. The individual  $\Delta h$  and  $\Delta i$  parameters per satellite were  $\Delta h_1 = 500$  km and  $\Delta i_1 = 0^\circ$  for Satellite 1,  $\Delta h_2 = 500$  km and  $\Delta i_2 = 4^\circ$  for Satellite 2 and  $\Delta h_3 = 500$  km and  $\Delta i_3 = 176^\circ$  for Satellite 3. This configuration was seen to have an accuracy of 19 m in position and 40  $\mu\text{s}$  in velocity, and is capable of sweeping the entire GEO orbit, therefore inventorying and updating the RSO catalogue.

Compared to the accuracy of TLE (27 km position error) obtained from ground-based systems, INDIGO performs better in orbit determination and prediction than most optical ground-based telescopes, which only use angular data to track small-sized GEO objects. This declares it as a feasible conceptual system, which can be taken to the next level of research before manifesting it in reality. Some recommendations were provided at the end of the study, which a future researcher could utilise to broaden this proof-of-concept study and contribute to the field of advanced space situational awareness.

## 8.2. Recommendations

This research was the first approach to the proof-of-concept study, which took a preliminary step towards obtaining the feasibility outcome. Certain aspects of the study were not addressed due to lack of time and resources, which I would like to mention as recommendations for future study, which can take this research to the next level.

The variational equations only incorporated the state transition matrix and did not account for the uncertainties of the model force parameters. Hence, including a sensitivity matrix would yield more accurate results. The effects of light-time and relativity have been ignored in this study, along with clock errors. Although their effects might seem small, they do influence the trajectory determination and initial state estimation by a few meters in position. This is a hindrance for POD, especially where the desired accuracy in position is less than a meter [44], and hence should be considered in the orbit estimation model. The radar module simply acts as a black-box but does not implement the phased array beam steering concept for more angular information. Moreover, there could be a study for a powerful radar that could function at lower altitudes to sweep the entire GEO ring quicker. A smaller sub-level study could be done to investigate a better radar configuration, which can perform better than INDIGO and also do so for low power and cost. This study was a proof-of-concept that assumed just one debris object. In reality, there will be debris clouds with different angular velocities and orbital properties. To see if the satellite configuration can sweep information on the entire debris ring is an interesting next-level task that could be done. Implementing the radar to cubesats or nanosatellites, such that there can be many such objects flying around in a formation flying, regularly tracking the object is one more exciting case that can be studied. In this case, however, for real-time applications, a Kalman Filter estimation method would be preferred to WLS method used here.

---

## References

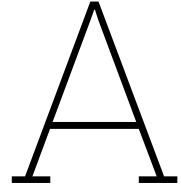
---

- [1] Sophie Kaineg. "The Growing Problem of Space Debris". In: *Hastings Environmental Law Journal* 26 (2020), pp. 277–288.
- [2] Nicholas L Johnson. "Evidence for historical satellite fragmentations in and near the geosynchronous regime". In: *Space Debris*. Vol. 473. 2001, pp. 355–359.
- [3] B. Lal et al. "Position Paper: Space Traffic Management". In: *Global trends in Space Situational Awareness (SSA) and Space Traffic Management (STM)*. IDA Science and Technology Policy Institute. 2018, pp. 1–153.
- [4] Delphine Cerutti-Maori et al. "Preliminary concept of a space-based radar for detecting mm-size space debris". In: *Proc. 7th European Conf. on Space Debris*. Vol. 7. 2017.
- [5] Loretta Hall. "The history of space debris". In: *Space Traffic Management Conference 19* (2014), pp. 2–14.
- [6] W. Flury and JM. Contant. "The updated IAA position paper on orbital debris". In: *Space Debris*. Vol. 473. 2001, pp. 841–849.
- [7] UNOOSA. 2023. URL: [https://www.unoosa.org/oosa/osoindex/search-ng.jsp?lf\\_id=](https://www.unoosa.org/oosa/osoindex/search-ng.jsp?lf_id=) (accessed: 30.07.2023).
- [8] Space Debris User Portal. 2023. URL: <https://sdup.esoc.esa.int/discosweb/statistics/> (accessed: 01.07.2023).
- [9] D. J. Kessler et al. "The Kessler syndrome: implications to future space operations". In: *Advances in the Astronautical Sciences* 137.8 (2010).
- [10] Brian Weeden. "2007 Chinese Anti-Satellite Test Fact Sheet". In: *Secure World Foundation*, Updated November 23 (2010), pp. 1–3.
- [11] Brian Weeden. "Iridium-Cosmos collision fact sheet". In: *Secure World Foundation* (2010), pp. 1–3.
- [12] Joseph S. Imburgia. "Space debris and its threat to national security: a proposal for a binding international agreement to clean up the junk". In: *Vanderbilt Law Review* 44 (2011), pp. 589–641.
- [13] Bohumil Doboš and Jakub Pražák. "Master spoiler: a strategic value of Kessler Syndrome". In: *Defence Studies* 22.1 (2022), pp. 123–137.
- [14] Stefan Frey, Stun Lemmens, et al. "Status of the space environment: current level of adherence to the space debris mitigation policy". In: *Journal of the British Interplanetary Society* 70.2-4 (2017), pp. 118–124.
- [15] P. Wegener et al. "Population evolution in the GEO vicinity". In: *Advances in Space Research* 34.5 (2004), pp. 1171–1176.
- [16] D.L. Oltrogge et al. "A comprehensive assessment of collision likelihood in Geosynchronous Earth Orbit". In: *Acta Astronautica* 147 (2018), pp. 316–345.
- [17] S. Riepl et al. "First results from an ESA study on accurate orbit determination with laser tracking of uncooperative targets". In: *Proceedings of the 7th European Conference on Space Debris*, Darmstadt, Germany. 2017, pp. 18–23.

- [18] Z. Li, Y. Wang, and W. Zheng. "Space-based optical observations on space debris via multi-point of view". In: *International Journal of Aerospace Engineering 2020* (2020). DOI: <https://doi.org/10.1155/2020/8328405>.
- [19] A Manis et al. "The Updated GEO Population for ORDEM 3.1". In: *International Orbital Debris Conference (IOC)*. JSC-E-DAA-TN73673. 2019.
- [20] Thomas Schildknecht. "Optical astrometry of fast moving objects using CCD detectors." In: *Geod.-Geophys. Arb. Schweiz* 49 (1994).
- [21] T. Flohrer et al. "Feasibility of performing space surveillance tasks with a proposed space-based optical architecture". In: *Advances in Space Research* 47.6 (2011), pp. 1029–1042.
- [22] H. Krag et al. "Preliminary concept of a space-based radar for detecting mm-size space debris". In: *Proceedings, 7th European Conference on Space Debris*, Darmstadt, Germany. 2017.
- [23] E. Schrama. "AE4872 Satellite Orbit Determination : Tracking, refraction and relativity". In: *TU Delft lecture Notes* (2021).
- [24] The United Nations Office for Outer Space Affairs. "Space Debris Mitigation Guidelines of the Committee on the peaceful uses of outer space". In: *Space Debris Mitigation Guidelines*. The United Nations. 2010.
- [25] James Murray and Timothy Kennedy. "Haystack Ultra-Wideband Satellite Imaging Radar Measurements of the Orbital Debris Environment: 2020". In: *National Aeronautics and Space Administration* (2020). URL: <https://ntrs.nasa.gov/citations/20220006634>.
- [26] R. Lupo et al. "Lighthouse: A spacebased mission concept for the surveillance of geosynchronous space debris from low earth orbit". In: *Advances in Space Research* 62.12 (2018), pp. 3305–3317.
- [27] Karel F. Wakker. "Fundamentals of Astrodynamics: Course AE4874". In: *Delft University of Technology Online Repository* (2015). URL: <http://resolver.tudelft.nl/uuid:3fc91471-8e47-4215-af43-718740e6694e>.
- [28] David A Vallado. *Fundamentals of astrodynamics and applications*. Vol. 12. Springer Science & Business Media, 2001.
- [29] Byron Tapley et al. "GGM02—An improved Earth gravity field model from GRACE". In: *Journal of Geodesy* 79 (2005), pp. 467–478.
- [30] Howard Curtis. *Orbital Mechanics for Engineering Students: Revised Reprint*. Butterworth-Heinemann, 2005.
- [31] D. Dirkx and K. Cowan. "AE4868 Numerical Astrodynamics - Acceleration Models - Spherical Harmonic Gravity". In: *TU Delft lecture notes* (2022). URL: <https://brightspace.tudelft.nl/d21/1e/content/398043/viewContent/2254243/View>.
- [32] Horizons NASA. 2023. URL: <https://ssd.jpl.nasa.gov/horizons/app.html#/>. (accessed: 14.05.2023).
- [33] D. Dirkx and K. Cowan. "AE4868 Numerical Astrodynamics - Acceleration Models - Non-Gravitational accelerations". In: *TU Delft lecture notes* (2022). URL: <https://brightspace.tudelft.nl/d21/1e/content/398043/viewContent/2254242/View>.
- [34] Troy L. Hacker. "Performance analysis of a space-based GMTI radar system using separated spacecraft interferometry". PhD thesis. Massachusetts Institute of Technology, 2000.
- [35] Heiner Klinkrad. *Space debris: models and risk analysis*. Springer Science & Business Media, 2006.

- [36] Robert M O'Donnell. "Introduction to radar systems". In: Massachusetts Institute of Technology: MIT OpenCourseWare, Primavera (2007).
- [37] Bassem R Mahafza. Introduction to radar analysis. CRC press, 2017.
- [38] G. Richard Curry. Radar system performance modeling. Artech House Radar Library, 2004.
- [39] Hsueh-Jyh Li, Yean-Woei Kiang, and W.K. Chen. "Radar and inverse scattering". In: The Electrical Engineering Handbook (2005), pp. 671–690.
- [40] Understanding Radar Antenna Beams, Half Power Beam Width (HPBW) and First Null Beam Wdth (FNBW). 2023. URL: <https://www.skyradar.com/blog/understanding-half-power-beam-width-hpbw-and-first-null-beam-width-fnbw>. (accessed: 14.08.2023).
- [41] Simon Kingsley and Shaun Quegan. Understanding radar systems. Vol. 2. SciTech Publishing, 1999.
- [42] Marc Fernandez Uson. "GeoSAR mission: Orbit determination methods and techniques". In: Universitat Politècnica de Catalunya. 2016. URL: <http://hdl.handle.net/2117/87556>.
- [43] Jehangir J. Pocha. An Introduction to Mission Design for Geostationary Satellites. Vol. 1. D. Reidel Publishing Company, 2012.
- [44] Byron Tapley, Bob Schutz, and George H. Born. Statistical orbit determination. Elsevier, 2004.
- [45] Oliver Montenbruck, Eberhard Gill, and F.H. Lutze. "Satellite orbits: models, methods, and applications". In: Appl. Mech. Rev. 55.2 (2002), B27–B28.
- [46] C.E. Livingstone. Radar systems for monitoring objects in geosynchronous orbit. Defence Research and Development Canada, 2013. URL: <https://publications.gc.ca/site/eng/9.821063/publication.html>.
- [47] Radar link budget analysis. 2023. URL: <https://nl.mathworks.com/help/radar/ug/radar-link-budget-analysis.html>. (accessed: 18.07.2023).
- [48] 4G | ShareTechnote – sharetechnote.com. [https://www.sharetechnote.com/html/Handbook\\_LTE\\_BeamForming.html](https://www.sharetechnote.com/html/Handbook_LTE_BeamForming.html). [Accessed 14-08-2023].
- [49] Documentation for Phased Array Toolbox. 2023. URL: [https://nl.mathworks.com/help/pdf\\_doc/phased/index.html](https://nl.mathworks.com/help/pdf_doc/phased/index.html). (accessed: 18.07.2023).
- [50] Frederik Michel Dekking et al. A Modern Introduction to Probability and Statistics: Understanding why and how. Vol. 488. Springer, 2005.
- [51] Mostafa Akbari et al. "Artificial neural network and optimization". In: Advances in friction-stir welding and processing 2 (2014), pp. 543–599.
- [52] Wouter van der Wal. "Introduction to VV and software verification". In: TU Delft lecture notes: Simulation, Verification and Validation (2020). URL: <https://brightspace.tudelft.nl/d21/1e/content/293150/viewContent/1908860/View>.
- [53] TUDAT API Documentation. 2023. URL: <https://py.api.tudat.space/en/latest/>. (accessed: 18.04.2023).
- [54] Poliastro API reference. 2023. URL: <https://docs.poliastro.space/en/stable/api.html>. (accessed: 18.04.2023).
- [55] Clare Martin, Hugh Lewis, and Roger Walker. "Studying the MEO & GEO space debris environments with the Integrated Debris Evolution Suite (IDES) model". In: Space Debris. Vol. 473. 2001, pp. 351–354.
- [56] Celestrak. 2023. URL: <https://celestrak.org/satcat/search.php>. (accessed: 29.06.2023).

- 
- [57] Celestrak documentation. 2023. URL: <https://celestrak.org/NORAD/documentation/tle-fmt.php>. (accessed: 18.07.2023).
  - [58] Carolin Früh and Thomas Schildknecht. "Accuracy of two-line-element data for geostationary and high-eccentricity orbits". In: *Journal of Guidance, Control, and Dynamics* 35.5 (2012), pp. 1483–1491. URL: [https://publik.tuwien.ac.at/files/PubDat\\_228872.pdf](https://publik.tuwien.ac.at/files/PubDat_228872.pdf).
  - [59] T.I. Fossen. "Lecture Notes TTK 4190 Guidance, Navigation and Control of Vehicles." In: Norwegian University of Science and Technology (2023).



# Frame transformations

Several frame transformations and relevant computations are provided in this appendix as a supplement to the theory provided in Chapter 3 and the methodology adopted in Chapter 4. This appendix is divided into three sections. Appendix A.1 lists the transformations between the reference frames used throughout the orbital simulation, followed by Appendix A.2 which lists the coordinate system transformations.

## A.1. Reference frame transformations

The three reference frames used in this thesis were provided in Section 3.1.1. They included the inertial Earth-Centred Inertial (ECI) frame, the non-inertial rotating Earth-Centred Earth-Fixed (ECEF) frame and the Local-Vertical Local-Horizontal (LVLH) frame. The transformation algorithm followed in our developed model will be described here.

### A.1.1. ECI to ECEF:

The relationship between the ECI and ECEF frames is that their Cartesian axes coincide at the starting epoch. Thereafter, the ECEF frame rotates about the common z-axis, with a fixed rate of  $\omega_{ie}$  with a value of  $7.2 \times 10^{-5}$  rad/s. This can be seen in Figure A.1.

Upon neglecting the effects of precession and nutation, an ECI Cartesian set of  $x_i$ ,  $y_i$  and  $z_i$  axes can be transformed into an ECEF Cartesian set of  $x_e$ ,  $y_e$  and  $z_e$  axes. The rotation angle about the z-axis is given by Equation A.1.

$$\begin{aligned}\theta_{ie} &= \omega_{ie}(t - t_0) \\ &= \omega_{ie}t + \theta_{GMST}\end{aligned}\tag{A.1}$$

where  $\theta_{GMST}$  refers to the mean equinox of the J2000 frame. The transformation for the position coordinates from ECI to ECEF can be seen in Equation A.2.

$$\begin{bmatrix} x_e \\ y_e \\ z_e \end{bmatrix} = \begin{bmatrix} \cos \theta_{ie} & -\sin \theta_{ie} & 0 \\ \sin \theta_{ie} & \cos \theta_{ie} & 0 \\ 0 & 0 & 1 \end{bmatrix} \begin{bmatrix} x_i \\ y_i \\ z_i \end{bmatrix}\tag{A.2}$$

Upon taking one more derivative w.r.t. time, the transformation of the velocity Cartesian coordinates can also be computed using the Chain Rule of differentiation. It is given by Equation A.3.

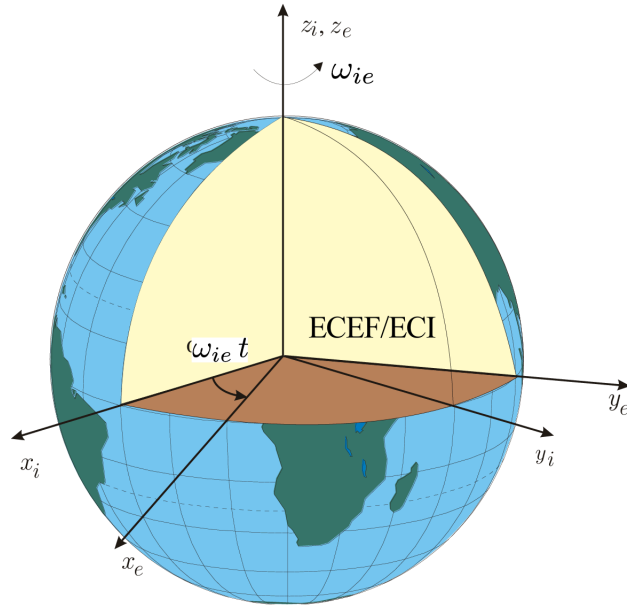


Figure A.1: Schematic for ECI and ECEF reference frames [59].

$$\begin{bmatrix} \dot{x}_e \\ \dot{y}_e \\ \dot{z}_e \end{bmatrix} = \begin{bmatrix} \cos \theta_{ie} & -\sin \theta_{ie} & 0 \\ \sin \theta_{ie} & \cos \theta_{ie} & 0 \\ 0 & 0 & 1 \end{bmatrix} \begin{bmatrix} \dot{x}_i \\ \dot{y}_i \\ \dot{z}_i \end{bmatrix} + \begin{bmatrix} \theta_{ie} & -\theta_{ie} & 0 \\ \theta_{ie} & \theta_{ie} & 0 \\ 0 & 0 & 0 \end{bmatrix} \begin{bmatrix} x_i \\ y_i \\ z_i \end{bmatrix} \quad (\text{A.3})$$

### A.1.2. ECEF to ECI:

Similarly, to go back to the inertial ECI frame, the inverse of the earlier transformation matrices can be used. Since the rotation matrix about z-axis is orthonormal and skew-symmetric, the inverse of the matrix is equal to its transpose. The conversion in position vector from ECEF to ECI is given by Equation A.4.

$$\begin{bmatrix} x_i \\ y_i \\ z_i \end{bmatrix} = \begin{bmatrix} \cos \theta_{ie} & \sin \theta_{ie} & 0 \\ -\sin \theta_{ie} & \cos \theta_{ie} & 0 \\ 0 & 0 & 1 \end{bmatrix} \begin{bmatrix} x_e \\ y_e \\ z_e \end{bmatrix} \quad (\text{A.4})$$

Similarly, the transformation in velocity coordinates from ECEF to ECI can be provided by Equation A.5.

$$\begin{bmatrix} \dot{x}_i \\ \dot{y}_i \\ \dot{z}_i \end{bmatrix} = \begin{bmatrix} \cos \theta_{ie} & \sin \theta_{ie} & 0 \\ -\sin \theta_{ie} & \cos \theta_{ie} & 0 \\ 0 & 0 & 1 \end{bmatrix} \begin{bmatrix} \dot{x}_e \\ \dot{y}_e \\ \dot{z}_e \end{bmatrix} - \begin{bmatrix} \theta_{ie} & -\theta_{ie} & 0 \\ \theta_{ie} & \theta_{ie} & 0 \\ 0 & 0 & 0 \end{bmatrix} \begin{bmatrix} x_e \\ y_e \\ z_e \end{bmatrix} \quad (\text{A.5})$$

### A.1.3. ECI to LVLH:

For the purpose of collecting measurements, a frame transformation is made from the inertial ECI frame to the satellite's center. Since the body frame coincides with the local orbital frame, a transformation from the ECI frame to the Local-Vertical Local-Horizontal frame is made.

There are three components of the LVLH frame. The x-axis is in the **radial** direction, followed by the y-axis, which is in the **tangential** direction of the orbit. The z-axis is **normal** to the orbit in the direction of angular momentum. This frame is also sometimes known as the RTN frame. The individual unit vectors in the radial, tangential, and normal directions are given by Equation A.6.

$$\begin{aligned}\vec{e}_R &= \frac{\vec{r}}{\|\vec{r}\|} \\ \vec{e}_N &= \frac{\vec{r} \times \vec{v}}{\|\vec{r} \times \vec{v}\|} \\ \vec{e}_T &= \vec{e}_R \times \vec{e}_N\end{aligned}\tag{A.6}$$

where  $\vec{r}$  is the position vector and  $\vec{v}$  is the velocity vector in the ECI frame.

Depending on their relative positions and velocities, these unit vectors are then transformed from the ECI to the LVLH frame. Assuming that point A refers to the satellite and point B refers to the debris, the relative position vector  $\vec{r}_{LVLH}$  of the debris as seen in the satellite LVLH frame can be given by Equation A.7.

$$\begin{aligned}\vec{r}_{BA} &= \vec{r}_B - \vec{r}_A \\ \vec{r}_{LVLH} &= \vec{r}_{BA} \begin{bmatrix} \vec{e}_R \\ \vec{e}_T \\ \vec{e}_N \end{bmatrix}\end{aligned}\tag{A.7}$$

where  $\vec{r}_B$  is the position vector of the debris and  $\vec{r}_A$  is the position vector of the satellite in the ECI frame w.r.t. the Earth's centre.

Similarly, the relative velocity vector  $\vec{v}_{LVLH}$  of the debris in the satellite LVLH frame can be given by Equation A.8.

$$\begin{aligned}\vec{v}_{BA} &= \vec{v}_B - \vec{v}_A - \left( \frac{\vec{r} \times \vec{v}}{\|\vec{r}_A\|^2} \times \vec{r}_{BA} \right) \\ \vec{v}_{LVLH} &= \vec{v}_{BA} \begin{bmatrix} \vec{e}_R \\ \vec{e}_T \\ \vec{e}_N \end{bmatrix}\end{aligned}\tag{A.8}$$

where  $\vec{v}_B$  is the velocity vector of the debris and  $\vec{v}_A$  is the satellite's velocity vector in the ECI frame w.r.t. the Earth's centre.

#### A.1.4. LVLH to ECI:

Starting from the satellite's LVLH frame, it is possible to switch the state of the debris back to the ECI frame. The inverse of the unit vector matrix was earlier given in Equation A.6. The debris position and velocity vector in the ECI frame can be calculated from Equation A.9.

$$\begin{aligned}\vec{r}_B &= \vec{r}_A + \vec{r}_{LVLH} \begin{bmatrix} \vec{e}_R \\ \vec{e}_T \\ \vec{e}_N \end{bmatrix}^{-1} \\ \vec{v}_B &= \vec{v}_A + \left( \frac{\vec{r}_{LVLH} \times \vec{v}_{LVLH}}{\|\vec{r}_A\|^2} \times \vec{r}_{LVLH} \begin{bmatrix} \vec{e}_R \\ \vec{e}_T \\ \vec{e}_N \end{bmatrix}^{-1} \right) + \vec{v}_{LVLH} \begin{bmatrix} \vec{e}_R \\ \vec{e}_T \\ \vec{e}_N \end{bmatrix}^{-1}\end{aligned}\quad (\text{A.9})$$

## A.2. Coordinate frame transformations

This thesis uses the three coordinate systems: Cartesian, spherical, and Kepler orbital. The transformations are given as follows:

### A.2.1. Cartesian to Spherical:

The spherical coordinate system can be seen by Figure A.2.

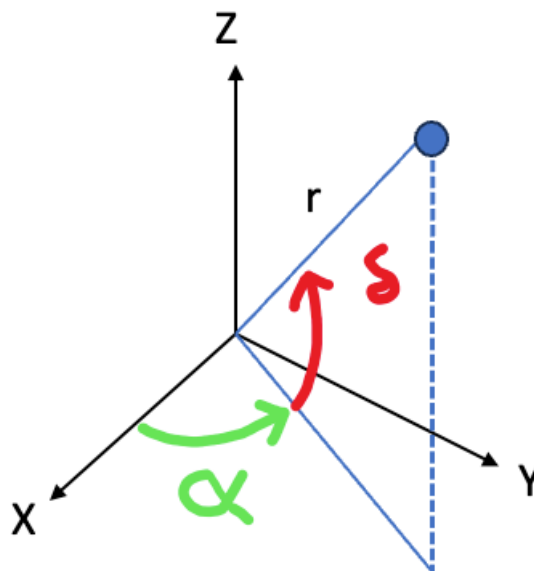


**Figure A.2:** Coordinate transformation visualised in Cartesian and spherical coordinates.

The spherical coordinate system can be described by the radius  $r$ , the geocentric latitude  $\delta$  w.r.t the x-y plane and the longitude  $\alpha$ . This is seen by Equation A.10.

$$\begin{aligned}r &= \sqrt{x^2 + y^2 + z^2} \\ \alpha &= \text{atan2}(y, x) \\ \delta &= \tan^{-1} \left( \frac{z}{\sqrt{x^2 + y^2}} \right)\end{aligned}\quad (\text{A.10})$$

### A.2.2. Spherical to Cartesian:

Similarly, from the spherical coordinate system, the Cartesian coordinates can be derived from Equation A.11.

$$\begin{aligned} x &= r \cos \delta \cos \alpha \\ y &= r \cos \delta \sin \alpha \\ z &= r \sin \delta \end{aligned} \quad (\text{A.11})$$

### A.2.3. Cartesian to Kepler elements:

The position and velocity vectors in Cartesian coordinates are given by  $\vec{r}$  and  $\vec{v}$ . The orbital momentum vector  $\vec{h}$  is given by Equation A.12.

$$\vec{h} = \vec{r} \times \vec{v} \quad (\text{A.12})$$

The orbital eccentricity vector is then derived from the orbital angular momentum vector and is given by Equation A.13.

$$\vec{e} = \frac{\vec{v} \times \vec{h}}{\mu} - \frac{\vec{r}}{\|\vec{r}\|} \quad (\text{A.13})$$

Thereafter, the vector  $\hat{n}$  in  $\text{m}^2/\text{s}$ , which represents the pointing direction towards the ascending node, is given by Equation A.14.

$$\hat{n} = \begin{bmatrix} 0 \\ 0 \\ 1 \end{bmatrix} \times \vec{h} = \begin{bmatrix} -h_y \\ h_x \\ 0 \end{bmatrix} \quad (\text{A.14})$$

The orbital inclination can be calculated as given by Equation A.15.

$$i = \arccos \frac{h_z}{\|\vec{h}\|} \quad (\text{A.15})$$

The orbital semi-major axis  $a$  and the eccentricity  $e$  are computed from Equation A.16.

$$\begin{aligned} a &= \frac{1}{\frac{2}{\|\vec{r}\|} - \frac{\|\vec{v}\|^2}{\mu}} \\ e &= \|\vec{e}\| \end{aligned} \quad (\text{A.16})$$

The longitude of the ascending node  $\Omega$  can be given by Equation A.17.

$$\Omega = \begin{cases} \arccos \frac{n_x}{\|\hat{n}\|} & n_y \geq 0 \\ 2\pi - \arccos \frac{n_x}{\|\hat{n}\|} & n_y < 0 \end{cases} \quad (\text{A.17})$$

The argument of periapsis can be found by Equation A.18.

$$\omega = \begin{cases} \arccos \frac{\hat{n} \cdot \vec{e}}{\|\hat{n}\| \|\vec{e}\|} & e_z \geq 0 \\ 2\pi - \arccos \frac{\hat{n} \cdot \vec{e}}{\|\hat{n}\| \|\vec{e}\|} & e_z < 0 \end{cases} \quad (\text{A.18})$$

The true anomaly can be calculated by Equation A.19.

$$\theta = \begin{cases} \arccos \frac{\vec{e} \cdot \vec{r}}{\|\vec{e}\| \|\vec{r}\|} & \vec{r} \cdot \vec{v} \geq 0 \\ 2\pi - \arccos \frac{\vec{e} \cdot \vec{r}}{\|\vec{e}\| \|\vec{r}\|} & \vec{r} \cdot \vec{v} < 0 \end{cases} \quad (\text{A.19})$$

#### A.2.4. Kepler orbital elements to Cartesian elements:

First, the eccentric anomaly  $E$  has to be calculated first, which is related to the true anomaly  $\theta$  by Equation A.20.

$$\tan\left(\frac{\theta}{2}\right) = \sqrt{\frac{1+e}{1-e}} \tan\left(\frac{E}{2}\right) \quad (\text{A.20})$$

This is then used to obtain the body's distance  $r_{pos}$  to the Earth at instant  $t$ . For this, the semi-major axis  $a$  and the eccentricity  $e$  are needed. The relation is given by Equation A.21.

$$r_{pos}(t) = a(1 - e \cos E(t)) \quad (\text{A.21})$$

The position and velocity vectors in the orbital frame are given by  $\mathbf{r}$  and  $\mathbf{r}\dot{\mathbf{r}}$ . They are defined by Equation A.22 and Equation A.23 respectively.

$$\mathbf{r}(t) = \begin{bmatrix} r_x(t) \\ r_y(t) \\ r_z(t) \end{bmatrix} = r_{pos}(t) \begin{pmatrix} \cos \theta(t) \\ \sin \theta(t) \\ 0 \end{pmatrix} \quad (\text{A.22})$$

$$\dot{\mathbf{r}}(t) = \begin{bmatrix} \dot{r}_x(t) \\ \dot{r}_y(t) \\ \dot{r}_z(t) \end{bmatrix} = \frac{\sqrt{\mu a}}{r_{pos}(t)} \begin{bmatrix} -\sin E \\ \sqrt{1-e^2} \cos E \\ 0 \end{bmatrix} \quad (\text{A.23})$$

After this, the orbital frame has to be transformed into the inertial frame at the centre of the Earth. This is done with transformation sequences with rotation matrixes.

$$\begin{aligned} \mathbf{R}(t) &= \underline{R}_z(-\Omega) \underline{R}_x(-i) \underline{R}_z(-\omega) \mathbf{r}(t) \\ &= \begin{bmatrix} r_x(t)(\cos \omega \cos \Omega - \sin \omega \cos i \sin \Omega) - r_y(t)(\sin \omega \cos \Omega + \cos \omega \cos i \sin \Omega) \\ r_x(t)(\cos \omega \sin \Omega + \sin \omega \cos i \cos \Omega) + r_y(t)(\cos \omega \cos i \cos \Omega - \sin \omega \sin \Omega) \\ r_x(t)(\sin \omega \sin i) + r_y(t)(\cos \omega \sin i) \end{bmatrix} \\ \dot{\mathbf{R}}(t) &= \underline{R}_z(-\Omega) \underline{R}_x(-i) \underline{R}_z(-\omega) \dot{\mathbf{r}}(t) \\ &= \begin{bmatrix} \dot{r}_x(t)(\cos \omega \cos \Omega - \sin \omega \cos i \sin \Omega) - \dot{r}_y(t)(\sin \omega \cos \Omega + \cos \omega \cos i \sin \Omega) \\ \dot{r}_x(t)(\cos \omega \sin \Omega + \sin \omega \cos i \cos \Omega) + \dot{r}_y(t)(\cos \omega \cos i \cos \Omega - \sin \omega \sin \Omega) \\ \dot{r}_x(t)(\sin \omega \sin i) + \dot{r}_y(t)(\cos \omega \sin i) \end{bmatrix}. \end{aligned} \quad (\text{A.24})$$

Hence, Kepler elements can be used to obtain the Cartesian position and velocity vectors in the ECI frame.